Quantum Dot Nanobioelectronics and Selective Antimicrobial Redox Interventions

by

Samuel Martin Goodman
B.S., University of Wisconsin – Madison, 2012

A thesis submitted to the
Faculty of the Graduate School of the
University of Colorado in Partial fulfillment
Of the requirements for the degree of
Doctor of Philosophy
Department of Chemical and Biological Engineering
2016

This Thesis entitled:
Quantum Dot Nanobioelectronics and Selective Antimicrobial Redox Interventions
written by Samuel Martin Goodman
has been approved for the Department of Chemical and Biological Engineering

_____
Chair: Prashant Nagpal

_____
Stephanie J. Bryant

_____
Anushree Chatterjee

_____
Barbara Demmig-Adams

_____
Wei Zhang

Date _____

The final copy of this thesis has been examined by the signatories, and we find that both the content and the form meet acceptable presentation standards of scholarly work in the above mentioned discipline

Goodman, Samuel M. (Ph.D., Department of Chemical and Biological Engineering)

Quantum Dot Nanobioelectronics and Selective Antimicrobial Redox Interventions

Thesis directed by Assistant Professor Prashant Nagpal

The unique properties of nanomaterials have engendered a great deal of interest in applying them for applications ranging from solid state physics to bio-imaging. One class of nanomaterials, known collectively as quantum dots, are defined as semiconducting crystals which have a characteristic dimension smaller than the excitonic radius of the bulk material which leads to quantum confinement effects. In this size regime, excited charge carriers behave like prototypical particles in a box, with their energy levels defined by the dimensions of the constituent particle. This is the source of the tunable optical properties which have drawn a great deal of attention with regards to finding appropriate applications for these materials.

This dissertation is divided into multiple sections grouped by the type of application explored. The first sectoin investigates the energetic interactions of physically-coupled quantum dots and DNA, with the goal of gaining insight into how self-assembled molecular wires can bridge the energetic states of physically separated nanocrystals. Chapter 1 begins with an introduction to the properties of quantum dots, the conductive properties of DNA, and the common characterization methods used to characterize materials on the nanoscale. In Chapter 2 scanning tunneling measurements of QD-DNA constructs on the single particle level are presented which show the tunable coupling between the two materials and their resulting hybrid electronic structure. This is expanded upon in Chapter 3 where the conduction of photogenerated charges in QD-DNA hybrid thin films are characterized, which exhibit different charge transfer pathways through the constituent nucleobases depending on the energy of the incident light and resulting electrons. Complementary investigations of energy transfer mediated through DNA are

presented in Chapter 4, with confirmation of Dexter-like transfer being facilitated through the oligonucleotides.

The second section quantifies the use of cadmium telluride quantum dots as light-activated therapeutics for treating multi-drug resistant bacterial infectoins. A review of the physiological effects of cadmium chalcogenide quantum dots is first presented in Chapter 5 which provides a foundation for understanding the inherent toxicity of these materials. The phototoxic effect induced by CdTe quantum dots is then introduced in Chapter 6 showing the reduction in growth of gram-negative bacteria. Additional insight is provided in Chapter 7 which discusses the therapeutic mechanism and the oxygen-centered radical species which are formed by the application of light in aqueous media. The section closes with Chapter 8 describing efforts to improve the stability and bio-compatibility of the dots using various surface treatments, and shows that stability can be improved by the passivation of the quantum dots' anionic facets, though at the cost of overall radical generation.

Dedicated in Memory of
Cleo J. Powers

Acknowledgements

Firstly, I would like to thank my parents Brian M. and Kathleen L. Goodman for their constant support throughout my time in graduate school. From the first week when you helped me move across the country until now you have always been there when I needed it, and I could not have done this without you.

I would next like to thank my advisor, Professor Prashant Nagpal, for always having an open door and for treating my questions and concerns with attention and respect. I greatly appreciate all the things you have done over the years to realize these projects, in addition to keeping me on track and helping me to pursue my ambitions. Thank you for the opportunity to work your lab.

I would also like to thank Professor Anushree Chatterjee who helped foster the fruitful collaboration which is reflected in Chapters 5-8. I appreciate being allowed a space to work in your lab, and the time you took to work with a novice in biology.

I would like to especially thank fellow graduate student Colleen M. Courtney with whom I collaborated with on the biological aspects of my thesis. Thank you for your patience and for your dedication both in and outside of the lab. Without your help this work would be greatly diminished.

During my time completing this thesis I had the opportunity to work with several outstanding undergraduate assistants. The first volunteer was Albert Siu, who worked with me on the cascade energy transfer project (Chapter 4). Thank you for the support which kept that project on track. Next, I want to recognize Jessica A. McDaniel who provided a great deal of assistance with preparing nanomaterials for integration with living systems (Chapter 6). Thank you as well for keeping the lab a fun place to be, and for forcing me to actually come in early.

I would like to express my gratitude to Dr. Annette Erbse for her training and assistance with the instruments of the biochem core, most importantly the EPR which yielded the data presented in Chapters 7 and 8. Thank you for dedicating the time to work with me on that project and I also appreciate the confidence and trust you placed in me using the instruments. On this subject, I would like to also extend my appreciation to Dr. David Mulder who hosted me at NREL while I analyzed the EPR data using their equipment.

One of the hurdles for finishing this project was being able to complete all of the different experiments which rely on strict time lines, so I would like to thank Dr. Feifei Li for running some of the cultures and assays presented in Chapter 8.

Additionally, I would like to thank the other Nagpal group members who contributed to work presented in this dissertation. For the DFT simulations of individual nucleobases presented in Chapter 2 I would like to thank Josep Casamada Ribot. To Yuchen Ding I would like to express my gratitude for performing the cyclic voltammetry measurements shown in Chapter 7, the charge-injection lifetime measurements shown in Chapter 8.

I would like to thank Professor Jennifer N. Cha and Dr. Hyunwoo Noh, with whom I collaborated on the QD-DNA project. I greatly appreciate the time spent working with me on quantum dot-DNA chemistry and for providing the devices used in Chapter 3. Thanks are also due to Glenn R. Halfenstein of the Cha lab who operated the NMR to obtain the spectra shown in Chapter 7.

During the first half of my tenure I received a great deal of assistance from Dr. Vivek Singh concerning instrumentation. Thank you for your training and assistance with the single particle measurements presented in Chapters 2 and 4.

The ICP-MS data presented in Chapter 8 were acquired by Dr. Fredrick G. Luiszer of the geology department. Thank you also for your counsel regarding sample analysis.

The actual process of completing my Ph.D. was sometimes ambiguous, so I would like to sincerely thank Dominique de Vangel for helping me navigate the ins and outs of keeping on top of my administrative requirements.

Finally, I would like to acknowledge the interlibrary loan staff at the University of Colorado Boulder Libraries for their prompt acquisition of paywall-blocked articles which proved important when constructing the review presented in Chapter 5.

Contents

List of Tables

List of Figures

Chapter 6

Chapter 7

Chapter 8

Appendix

Chapter 1
Introduction to Quantum Dots and DNA Conduction

1.1 Overview of Nanomaterials

When evaluating the literature concerning specific aspects of nanoparticle (NP) research it is easy to assume that the now commercialized field is still relatively new. While it is true that the beginning of the full exploration of these materials has been limited to the past twenty-five or so years, when the necessary imaging and characterization technology became sufficiently advanced, the field can trace its roots back much further. It is somewhat common to cite Richard Feynman's talk given to the 1959[1] annual meeting of the American Physical Society as the foundation of the field, though his points are mainly concerned with the potential of patterning on the nanoscale for information storage and electrical component manufacture. Many of the more interesting emergent properties of NPs only became apparent once they had actually been made.

Though all sharing the common (and somewhat broadly defined) feature of having at least one dimension below 100 nm, different categories of NPs can be defined by the bulk materials from which they are constituted which largely determine the specific properties observed on the nanoscale. There is cross-over, as some metals will begin to exhibit semiconducing properties at this scale. Since a defining development in nanotechnology has been the ability to colloidally synthesize nanoparticles at a large scale instead of relying on expensive, slow, and laborious epitaxial methods,[2] this chapter will focus on those dots which are primarily made and utilized in solution and their unique properties with regard to some applications.

As the focus of this dissertation is solely on the physics and chemistry of semiconductor quantum dots (QDs) other materials including metals (Section 1.1.1) and carbon (Section 1.1.2) are only briefly discussed. As morphological characterization methods are indispensable for

understanding QD properties, the most common techniques are described in Section 1.2. With this information, it is then possible to understand the fundamentals of QD optical and electronic properties, which are presented in Section 1.3 along with several prominent applications for these materials. This chapter concludes with a discussion of the interactions of QDs with conducting polymers (Section 1.4), which is the focus of the research presented in Chapters 2-4.

1.1.1 Metal Nanoparticles

One of the principle classes of NPs currently under investigation are those composed of metallic elements. Reliable and fascile syntheses have been established for a wide swath of the d-block including noble metals like gold[3] and palladium,[4] magnetic elements like iron,[5] and alloyed particles of two or more metals.[6] There are references to these kind of nanoparticles as early as the late 1960s/1970s (caution should be heeded though given the lack of systematic nomenclature at that time),[7] but many of the interesting properties and ideas for comonly recognizable applications have only arisen starting in the early 1990s.

One of the prototypical applications of metal NPs is their use as infrared and visible absorbers through surface plasmon resonance, with gold and silver being the primary workhorses. Surface plasmon resonance can generally be described as the interaction between surface electrons and absorbed light when the two are in energetic resonance.[8] Changes to the surface, such as with bound molecules, will alter the resonant energy whose shift can be used to track specific changes. This has attracted a great deal of attention primarily as a sensing and biological diagnostic tool[9] (similarly, magnetic particles have attracted attention in the context of magnetic resonance imaging).[10] This type of excitation should not be confused with exciton formation in QDs.

A consequence of plasmon absorption is usually concomitant localized heat generation, and has led to intensive investigation into their potential as activatable photothermal therapies.[11] In this scheme the metal NP is bound to targeting agents (usually through thiols in the case of gold) which direct the nanoparticle to a specific cell-type or tissue. Application of light is used to induce thermal stress which kills any adjacent cell. Due to the mamallian body's low transparency to visible light, infrared absorbing particles can by synthesized by altering the NP size, with larger sizes leading to longer absorbed wavelengths.[12]

In addition to altering the size to yield optically tuned NPs, other shape-based morphological changes can recommend metal NPs for both imaging and catalytic applications.[13] Because the rate of reaction can depend on the specific crystal facets that are exposed on catalytic active sites, controlling NP shape can provide an in-built method for enhacing activity over more traditional loading methods like insipient wetness and reduction. The ability to controllably alloy NPs also can lead to enhanced conversion using this class of materials.[14]

1.1.2 Carbon-Based Morphologies

At this point it may be reasonable to say that graphene is one of the most well-known developments in material science of the last few decades. Despite its saturation of several journals, to near buzzword status, and fascile scotch tape-based synthesis, graphene was one of the last morphologies of carbon to be widely studied.[15]

Discovered about 20 years earlier and also relevant to the nanoscale are the fullerenes, molecules most commonly composed of 60 carbon atoms (although other sizes are well-known).[16] In addition to possessing interesting properties on their own, derivatives of the base C-60 form are now commonly used in organic solar cells as electron acceptors in conjunction with

a range of polythiophenes acting as donors.[17] Efficiencies for these cells are typically maximized at ~10%.

A second close relative of graphene are the carbon nanotubes, whose attributes include an interesting case of disagreement over scientific priority due to a lack of transaction through the iron curtain.[18] While possessing some interesting electronic properties which impacts on sensing, the primary applications of nanotubes are mostly structural. More interesting are the carbon quantum dots, which behave more like semiconductors on the nanoscale than the graphene analogues, including bright and size-tunable emission.[19]

1.2 Characterizing Materials on the Nanoscale

There are a host of different techniques which can provide useful structural information for organic and biological molecues which are not necessarily applicable to nanomaterials. Nuclear magnetic resonance (NMR) spectroscopy will only allow the identification of stabilizing ligands or adsorbates on the QD surface, which is either known in the case of the former or likely of too low of concentration for the latter. Mass spectrometry in all of its forms is also limited due to the high weight and homogeneity of the core material. X-ray diffraction is also only useful for confirming the identity of the majority constituent compounds due to the large number of scattering bounries between individual particles.

What is most useful to know, and the starting point of any analysis of QDs, is the physical structure of the particles including the overall size, shape, and heterogeneity. These characteristics will then define the electronic structure, transport properties, and interactions with the local environment. The most concrete assessment of morphology is to directly image the particles and derive statistics for those dimensions. For this purpose, there are two techniques that accelerate electrons towards the sample, either measuring their transmission (Section 1.2.1)

through a thin sample or the effect of an electron beam on a surface (Section 1.2.2). With the advent of high-quality piezoelectric components, it is also possible to measure samples through physical contact (Section 1.2.3) or through quantum tunneling (Section 1.2.4).

1.2.1 Transmission Electron Microscopy

Because electrons are low enough in mass to exhibit significant wave-like character, they can be utilized for imaging in ways generally analogous to other forms of microscopy, only with a resolution measured in the tenths of an ångström. The use of transmission electron microscopy (TEM) was developed in the 1930s starting in Germany and later in the United States; early successes include the first direct imaging of viruses. In the basic scheme, a chamber is loaded with an appropriately thin sample under high vacuum (Figure 1.1). On one end of the chamber is the source electrode which during measurement is heated and subjected to a 60-100 kV potential, causing electrons to accelerate through the sample. These are then captured with a detector, formerly on film as evidenced by the modules on older instruments but now exclusively digital, to produce an image. Like an optical microscope, TEM requires focusing the electron beam onto the sample to obtain a clear image, though instead of solid lenses magnetic fields are used to direct the particles. The transmission adjective in TEM refers to the contrast in the resulting images resulting from different sample components absorbing different numbers of incident electrons. This corresponds to the total thickness of a sample section and also the atomic weights of the constituent elements, with lighter elements like carbon

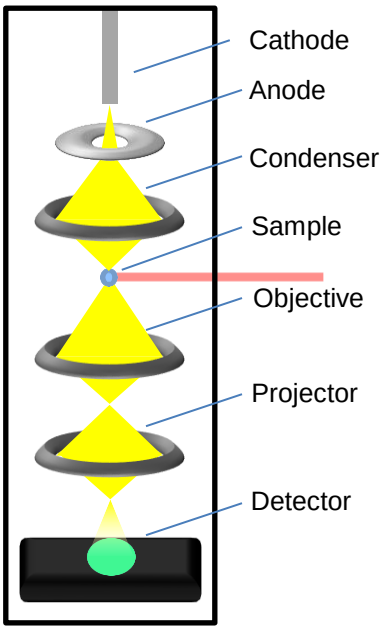

Figure 1.1 – Basic TEM schematic showing internal components.

having so little absorbance that it is commonly used as a substrate. Because the resolution of TEM allows the direct imaging of NPs, both NP size and shape can be readily identified and statistics about all of the particles in a field of view can be readily calculated (see Appendix). This technique was utilized to characterize the size and shape of all particles studied in this thesis regardless of the subsequent experiments.

Images of nanoparticles are not the only possible output of TEM experiemnts, with complementary measurements being able to provide direct compositional analysis. As an electron beam is already used to acquire a TEM image a logical extension is the measurement of an electron energy-loss spectrum (EELS) to determine local composition.[20] In this mode changes in the kinetic energy of the electron beam are measured after passing through the sample, which will be characteristic depending on the elements they pass through, and in this way, the distributions of atoms can be determined in an individual particle. Similarly, the x-ray emission profile of a sample can be measured under these conditions to yield similar data.

1.2.2 Scanning Electron Microscopy

While both operating using electron beams, scanning electron microscopy (SEM) offers different methods of analysis compared to TEM.[21] This first is that SEM in inherently non-destructive, in both sample preparation and accelerating voltage, and is capable of accepting much larger samples. However, there is an inherent loss of resolution compared to TEM, maximizing at about 1-5 nm, though it is still very useful for examining sub-micron scale features. This is evident from the SEM image shown in Figure 3.1 which while clearly shows the different layers of a thin film device. Unlike TEM, which moves the sample to acquire different areas, SEM utilizes a raster scan mechanism where the electron beam is moved across the sample and secondary effects are collected and correlated with position. These can include the collection

of secondary or Auger electrons, emitted x-rays, or a current in the sample. Due to the nature of the electron and x-ray methods similar elemental analyses as is possible with TEM can be collected, though only for the surface (≤1 μm penetration depth).

1.2.3 Scanning Tunneling Microscopy

The next nanoscale characterization apparatus to be introduced arrived in the early 1980s with the demonstration of the first scanning tunneling microscope (STM) in Switzerland.[22] Like TEM, STM utilizes a quantum mechanical principle to extract information. In this scheme a metal tip (usually a noble alloy like Pt-Ir) is etched to atomic sharpness and brought into close, but not physical, contact with a conductive surface. In the constant current mode, a bias is applied between the tip and the substrate allowing electrons to tunnel through the air/vacuum gap whose rate of transference is kept contant via piezoelectric elements as a raster scan is performed (Figure 1.2). In a constant height mode, topographic information is obtained by measuring the tunneling current as the tip is scanned across the surface, whose changing magnitude is then proportional to the feature size. The images presented in Chapters 2 and 4 were obtained in the former constant current mode.

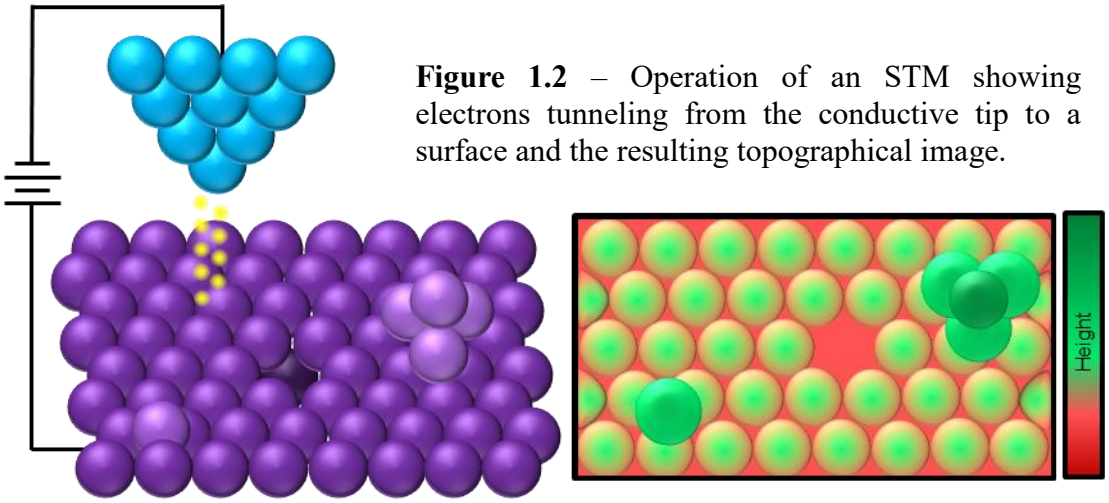

Figure 1.2 – Operation of an STM showing electrons tunneling from the conductive tip to a surface and the resulting topographical image.

The greatest advantage of STM is using it to obtain information on electronic structure with high spatial resolution. From an image perspective, this can be visualized by performing multiple constant height scans with different biases between the tip and substrate, which will change the level of tunneling current depending on the number of electronic states which align with the tip's potential. For NP characterization, it is possible to obtain more complete information using scanning tunneling spectroscopy (STS) whereby the tip is held in a constant position above a single particle and the bias is scanned constantly within the desired range. Because the tip and sample are not in physical contact, the derivative of the resulting current-voltage curve provides a direct measure of both the positions of the individual electronic states and the information about the bandgap of an individual QD. When the work function of the STM tip is known (based on its composition) the resulting spectrum can be corrected on appropriate redox scales to identify where the bandedge positions of the nanomaterial lie in regards to different electron transfer reactions, which is utilized in Chapter 7 to explain the aqueous radical production of certain QDs. In addition to measuring condensed matter, this technique is also applicable to measuring the HOMO/LUMO and higher energy states of molecules,[23] whose alignment and interaction with QD states are the subject of chapters 2-4.

1.2.4 Atomic Force Microscopy

Ariving several years after STM,[24] atomic force microscopy (AFM) instead utilizes direct contact with a sample in order to obtain topographical information. In the basic configuration, a reflective cantilever is etched, ideally to an atomic point, is brought into contact with a surface. As it moves across a designated surface the cantilever applies a constant force and so any deviations in the surface will cause its surface to bend (Figure 1.3). The resulting deflection is

measured by an incident laser which reflects onto a spatially-sensitive detector which records the change in surface height.

This variant of AFM involves direct contact with the substrate and so depending on the incident force may cause confounding changes during measurement.[25] For soft surfaces this can result in the tip deforming the sample leading to an incorrect topography. NPs resting on the surface of a hard substrate can also be moved by the action of the tip,[26] which while useful for attempting to engineering structures is sometimes an impediment for material characterization. The first alternate operating mode which can avoid these issues is to run the AFM in a non-contact mode whereby the tip is held held several nm above the substrate where motion towards the surface is induced by van der Waals forces. This may have a tendency to smear out any sharp features which are better seen in tapping mode, where a constant oscillation is applied to the tip so it only briefly contacts the surface.

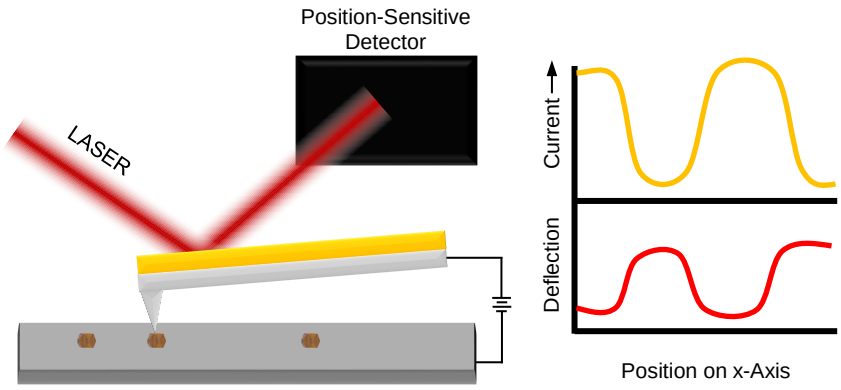

Figure 1.3 – Atomic force microscope in use to obtain a line scan of quantum dot topography (deflection) and current on a flat conductive surface.

In addition to imaging AFM can be useful for measuring nano-scale forces like bonding and friction, or as in the case of Chapters 4 and 9 of this work be used as single particle conductive probes. This requires the use of metal-coated tips and cantilevers to serve as electrodes, which when in contact with a semiconducing material resting on another conducting surface forms a Schottky junction. An applied bias between the tip and substrate can then allow current-voltage

characteristics to be measured under a variety of conditions, though the form is different and yields distinct information about the particles of interest (see Chapter 3 for the different mathematical descriptions). Such measurements are inherently difficult at room temperatures due to thermal fluctuations in the equipment, necessitating careful control of the tip position and applied force for consistent measurements. This is especially important for thermoelectric characterization of single nanoparticles which require significant temperature changes which will exacerbate the rate of drift.

1.3 The Properties and some Applications of Quantum Dots

Semiconductors on the nanoscale behave in significantly different ways than bulk morphologies, which has attracted a great deal of interest with reagards to their potential applications. The underlying physics of QDs are the result of the quantum confinement (QC) of the electrons which dictates their energetic structure and emergent properties (Section 1.3.1). One of the consequences of QC is the ability to tune the optical properties of QDs in a size-dependent manner which has engendered a great deal of interest in their use as fluorescent biological probes which avoid problems associated with photobleaching (Section 1.3.2). Like metal NPs, QDs can also be applied in catalytic contexts due to the way their redox potentials can be tuned to target reactions of interest, also as a result of QC (Section 1.3.3). The discretization of the QD energy levels which is concomitant with QC has also been predicted to aid the performance of themoelectric devices in addition to decreasing thermal conductivity through the plethora of scattering boundries natural to such configurations (Section 1.3.4). Finally, the use of QDs in solar cells is introduced, which is a significant enough endevour that the progress of the technology is closely tracked by NREL (Section 1.3.5).

1.3.1 Quantum Confinement

Significant changes to a material's electronic properties occur once the size of the particle is reduced below the Bohr excitonic radius (eq. 1.1).[27] Once a dimension is reduced below this value QC effect begin to become apparent, most readily is the blue-shifting of the optical properties with continually decreasing size.[28] This can be visualized as the classic quantum mechanical particle in a box system (Figure 1.4a), where solutions to the Schrödinger equation specify that energy levels are limited to higher energy modes as the dimensions of the potential well decrease. With size changes, there is also a breakdown of the bulk electronic structure in which the continuous electronic states become more discrete (Figure 1.4b), due to both QC and a reduction in the total number of atoms, which is a property that has engendered interest in QD utilization in solar cells (Section 1.3.5 and Chapters 2-4).

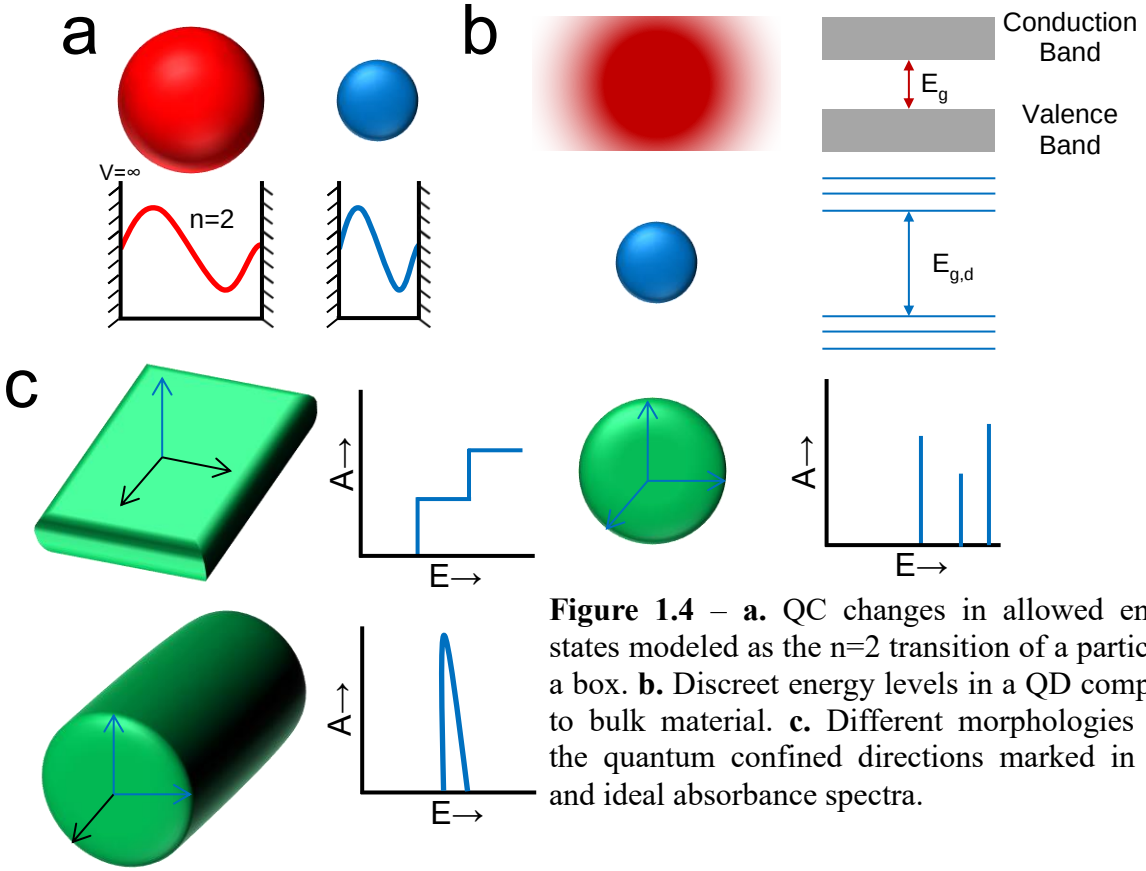

Figure 1.4 – **a.** QC changes in allowed energy states modeled as the n=2 transition of a particle in a box. **b.** Discreet energy levels in a QD compared to bulk material. **c.** Different morphologies with the quantum confined directions marked in blue and ideal absorbance spectra.

$$r_B = \varepsilon r_0 \frac{m}{m*} \quad (1.1)$$

QC is an inherently direction property with materials being defined by the number of un-confined degrees of freedom they possess. In the bulk case, where all directions are on a scale greater than r_B, there is no QC and is thus a three-dimensional material (3D, Figure 1.4c). While graphene is the most broadly known 2D material, such originally named quantum wells have been studied as early as the 1970s given their ability to be synthesized over comparatively large areas epitaxially. Modern procedures can synthesize such materials either through mechanical action, as with graphene and the VIB dichalcogenides,[29] directed colloidal growth like the II-VI semiconductors,[30] or through cation replacement of previously made structures. Reducing the dimensionality by one more degree enters the realm of nanowires which are quantum confined in two directions and are morphologically analogous to carbon nanotubes. The primary morphology discussed in this work is that where any dimension is quantum confined, which will be refered to specifically herein as QDs.

The different degrees of QC lead to different electronic and optical properties for each of the different morphologies, transitioning from a continuous increase in the bulk material, to stepwise increases for nanosheets, and to increasingly Dirac-like absporption lines in 1D and 0D materials (Figure 1.4c). As a consequence of the energy shifts associated with size decreases the optical properties of individual particles change significantly, undergoing pronounced blue shifts. This also corresponds to a blue-shifting of the emission properties as well, with ideal emission peaks showing a slightly lower energy than the absorbing state due to exciton binding energy of the excited electron and hole. Emission can also be strongly affected by the surface chemistry off the NPs, due to the high surface area to volume ratio, with more defects leading to further red-shifting Stoke's shifts.

1.3.2 Bio-Imaging

The bright and relatively stable emission properties of QDs lead to their utilization as biological probes and imaging agents.[31] This partially arises due to the instability of traditional small molecule fluorophores to photobleaching during prolongued measurements. In its developed form, the probe consists of a core QD which fluoresces at the wavelength desired for a specific imaging experiment. Around the core is typically grown an inert shell of bio-compatible material which serves to prevent the core for interacting the environment through redox reactions, and to stabilize it against any oxidation to maintain bright emission for long periods of time (Figure 1.5). Concerns over the toxicity of the core materials led to the first investigations of QD toxicity (Chapter 5) and further interest in their use then as therapeutics (Chapters 6-8). As probes, the QDs are further suface-functionalized with targeting factors like antibodies, proteins, or signaling molecules which will ensure they reach desired targets or structures of interest.[32] An important caveat of imaging with QDs is that their emission is not steady state, with individuals blinking at a slow enough rate to potentially interfere with highly time-resolved measurements. QDs can also serve as unique probes given their ability to engage with resonant energy transfer with surrounding biological molecules, so they themselves can be sued as stimulating agents or as secondary indicators of other energy transfer processes (this is the main phenomena investigated in Chapter 4).

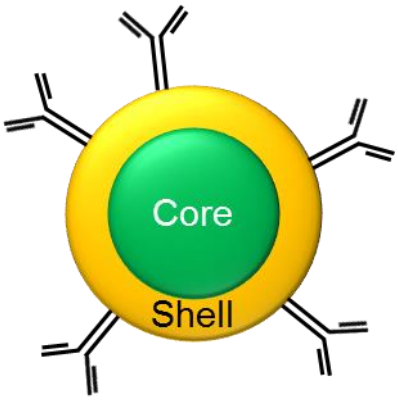

Figure 1.5 – Structure of an antibody-conjugated core-shell NP used for imaging.

1.3.3 Catalysis

While a great deal of attention towards QDs for inorganic applications has focused on light harvesting for photovoltaics (discussed below), reports investigating their use for photocatalytic reactions in a variety of cases has also been shown. In one general scheme cadmium chalcogenide quantum dots are adsorbed onto a wide-bandgap oxide such that excited electrons are transferred into the substrate which is at a proper potential for water splitting and hydrogen generation.[33] This is only an indirect usage of QC, for aligning the oxide and QD energies to sensitize the former, and similar structures are also capable of reducing atmospheric CO_2 to higher order alkanes when the redox capabilities of the visible-absorbing particles play an active role.[34] The inherent design criteria for direct action is again QC, with selectivity towards different reactions being possible by changes to the size or material, as discussed in Chapter 7 in the context of selective radical generation in aqueous environments.

1.3.4 Nanostructuring and Thermoelectrics

As a result of the discreet nature of the QD electronic states it has been predicted that they can offer improved thermoelectric performance compared to bulk materials.[35] However, the current methods of making superlattice structures from QDs for improved thermopower conversion rely instead on decreasing the overall thermal conductivity of the film through scattering at the numerous boundaries and junctions of such configurations. In this way, the potential benefits of QDs are lost as the inter-particle contact breaks the QC in the direction of transfer.

1.3.5 Photovoltaics

There are several different configurations a QD based solar cell can take that, to varying degrees, take advantage of their QC properties.[36] In one architecture analogous to dye-sensitized

solar cells QDs, are bound to a film of titanium dioxide, which is in a type-II alignment with the particles, into which their photoexcited electrons are injected. The ability to tune the position of the conduction band states such that this alignment is possible is an advantage of QC, which would allow this for a variety of different sensitizing materials. However, like in molecular dye-sensitized cells, this configuration relies on the use of an electrolyte to provide hole conduction to the other electrode, which offers significant design challenges for long-term stability. More traditional Schottky cells containing a QD layer in physical contact with two electrodes is the typically more efficient configuration, with QC allowing tailored allignment of the QD states with the respective work functions of the metals to increase the resulting voltage output of the cell.

As of 2016, the most efficient certified solar cell based on QDs can convert just over 11% of the incident light into electricity. While about half as efficient as traditional silicon cells and more recent materials like the perovskites, this is still an impressive improvement over the 3-4% obtained by the first certified cells in 2010. The first impediment to conversion efficiency was the long-chain aliphatic ligands that were used during early syntheses. While allowing high quality particles from an optical standpoint, the ligands would serve as an insulating barrier completely preventing the transport of current through a film. Efforts to improve conductivity have typically centered on decreasing the inter-particle spacing by switching to shorter ligands, linking ligands like dithio-ethane, using atomic ligands like iodine, or by removing the ligands all together. This latter case must be used carefully because of how the NPs can sinter together at moderate annealing conditions and thus result in an amorphous bulk film.

Ordering is also an issue when designing thin film photovoltaic devices as a deposition of colloidal QDs will usually result in a stochastically distributed film. One solution that has seen

prominence is the creation of superlattice strctures of ordered NPs through surface tension effects at the interface of a solvent-solvent interface.[37] In this way the particles will natively form an ordered film that can be transferred to a surface, and is capable of containing differently sized particles in unit cells resembling atomic lattices. One touted advantage of this architecture is the predicted wavefunction overlap of adjacent particles, which would create a coherent pathway for charge condution. However, in order to preserve the quantum confinement of the individual dots, they must still be physically separated which limits this overlap, and if they were touching the advantages of this structure over a homogenously-grown quantum well are not been conclusively demonstrated.

Another option for NP ordering is the use of polymers to fill the gap between the QDs for both ordering and to enhance conductance, with the inherent requirement that the polymer be able to conduct both charges.[36] DNA offers a non-traditional alternative to the polythiophenes for this configuration, which potentially provides several advantages. First, due to the way DNA selectively hybridizes to a complementary strand there is an in-built mechanism of directed assembly which allows the organization of QDs in a three-dimensional space.[38] There have also been reports that DNA can be conductive under some circumstances, a requirement for moving charges efficiently, which is discussed in the next section in the context of their applicability to QD-DNA hybrids.

1.4 The Conductive Properties of DNA

Charge transport through DNA is a topic which, while proven to occur under a variety of circumstances, is not yet fully understood and accurately modeled.[39-41] A primary design consideration is the distance over which charge transport is feasible, which will determine the feature size in solid state electronics. When on the order of several thousand base-pairs (μm

length), DNA is almost always seen as an insulating material. Once cleavedd to the scale of several nanometers though it has been observed that DNA will adopt a semiconducing profile. Reducing the length further to only a couple base pairs now enters the regime where direct tunneling between electrodes is possible, and where the DNA will play a reduced role.

It has also been noted that DNA can assume what appears to be Ohmic conductance when it is placed in solution environment rather than steady state. It has been proposed that this is in part due a change in the structural conformation of the nucleotide due to the influence of water molecules and salts which make it more amenable to conducting charges (although there may be a component of ionic conduction in those conditions which has a similar voltage dependence, see Chapter 3). A consideration which may have been overlooked however is that in a liquid environment it is much easier for an oligonucleotide to switch between conformational/vibrational energy levels thus allowing a higher probability of being in a proper alignment for an electron moving between the bases. These different states are only visible in the solid state where water can be reliably removed, where movement is more constrained and is discussed in Chapter 2 with regards to alignment with DNA states. Changes to the structure upon drying can potentially be mitigated through the use of high salt concentrations in the depositing solution which serve to maintain the hydrophilic areas.

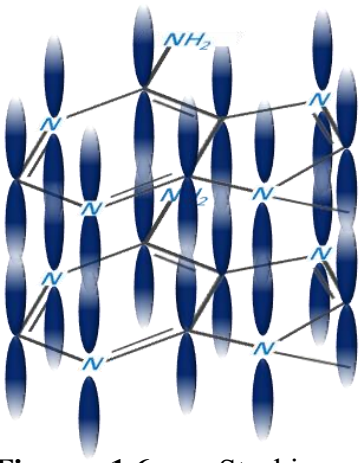

Figure 1.6 – Stacking *p* orbitals of closely adjacent adenine bases.

The overall interpretation of charge transport studies through DNA, despite the difficulty of modeling *ab initio*, is that it occurs through the π-stacking of adjacent bases which forms a coherent molecular orbital throughout the entire double-stranded molecule (Figure 1.6). This

predicts that the bases must be held in the configuration, so any single-stranded components will negatively affect the conduction, which is corroborated by no observed transport occurring through single-stranded DNA. This model also explains why heterogeneous sequences have a negative impact on the rate of charge transfer, with the odd base breaking the conjugated stack and serving as a barrier or defect. Base-mediated transport is likely the only source of conduction as it has been noted that damage to the backbone has negligible effect on the charge transport, which is corroborated the simulations presented in Chapter 2 which show minimal HOMO/LUMO wavefunction presence outside of the bases.

Outiside of the bio-sensing and medical fields (see Chapter 5), the interactions between QDs and DNA are largely limited to the use of DNA as an assembly template,[42] with almost no studies dedicated to the energetic interactions of the two materials. This information is critically important if DNA or other molecular wires are to be considered useful for nanoscale electronics, so the first several chapters (2-4) are dedicated to the photophysics of QD-DNA systems.

1.5 Symbols and Abbreviations

AFM	-	atomic force microscopy	
DNA	-	deoxyribonucleic acid	
EELS	-	electron energy-loss spectroscopy	
HOMO	-	highest occupied molecular orbital	
LUMO	-	lowest unoccupied molecular orbital	
m	-	electron rest mass	eq. 1.1
m^*	-	electron reduced mass	eq. 1.1
NMR	-	nuclear magnetic resonance	
NP	-	nanoparticle	
NREL	-	National Renewable Energy Laboratory	
QC	-	quantum confinement	
QD	-	quantum dot	
r_0	-	Bohr radius of the hydrogen atom	eq. 1.1
r_B	-	Bohr radius of a material	eq. 1.1
SEM	-	scanning electron microscopy	
STM	-	scanning tunneling microscopy	
STS	-	scanning tunneling spectroscopy	
TEM	-	transmission electron microscopy	
ε	-	dielectric constant	eq. 1.1

1.6 References

1) Feynman R P. *Engineering and Science* **1960**, 22-36.
2) Kubena R. L., et al. *Appl. Phys. Lett.* **1987**, *50*, 1589-1591.
3) Brust M., et al. *J. Chem. Soc., Chem. Commun.* **1994**, 801-802.
4) Kim S., et al. *Nano Lett.* **2003**, *3*, 1289-1291.
5) Hyeon T. *Chem. Commun.* **2003**, 927-934.
6) Liu Z., et al. *Chem. Mater.* **2006**, *18*, 4946-4951.
7) Kreibig U. *J. Phys. F: Metal Phys.* **1974**, *4*, 999-1014.
8) Willets K. A., van Duyne R. P. *Annu. Rev. Phys. Chem.* **2007**, *58*, 267-297.
9) Pattnaik P. *Appl. Biochem. Biotechnol.* **2005**, *126*, 79-92.
10) Sun C., et al. *Adv. Drug Deliv. Rev.* **2008**, *60*, 1252-1265.
11) Boisselier E., Astruc D. *Chem. Soc. Rev.* **2009**, *38*, 1759-1782.
12) Link S., El-Sayed M. A. *J. Phys. Chem. B* **1999**, *103*, 4212-4217.
13) Sun Y., Xia Y. *Science* **2002**, *298*, 2176-2179.
14) Zhang S., et al. *Angew. Chem. Int. Ed.* **2013**, *52*, 3681-3684.
15) Novoselov K. S., et al. *Science* **2004**, *306*, 666-669.
16) Kroto H. W., et al. *Nature* **1985**, *318*, 162-163.
17) Kim Y., et al. *Nat. Mater.* **2006**, *5*, 197-203.
18) Monthious M., Kuznetsov V. L. *Carbon* **2006**, *44*, 1621-1623.
19) Sun Y., et al. *J. Am. Chem. Soc.* **2006**, *128*, 7756-7757.
20) Egerton R. F. *Rep. Prog. Phys.* **2009**, *72*, 016502.
21) Vernon-Parry K. D. *III-Vs Rev.* **2000**, *13*, 40-44.
22) Binning G., et al. *Phys. Rev. Lett.* **1982**, *49*, 57-61.
23) Ribot J. C., et al. *J. Phys. Chem B* **2015**, *119*, 4968-4974.
24) Binnig G., et al. *Phys. Rev. Lett.* **1986**, *56*, 930-933.
25) Jalili N., Laxminarayana K. *Mechatronics* **2004**, *14*, 907-945.
26) Falvo M. R., et al. *Nature* **1999**, *397*, 236-238.
27) Yoffe A. D. *Adv. Phys.* **1993**, *42*, 173-262.
28) Norris D. J., Bawendi M. G. *Phys. Rev. B* **1996**, *53*, 16338-16346.
29) Eda G., et al. *Nano Lett.* **2011**, *11*, 5111-5116.
30) Bouet C., et al. *Chem. Mater.* **2013**, *25*, 639-645.
31) Bruchez M., et al. *Science* **1998**, *281*, 2013-2016.
32) Algar W. R., et al. *Anal. Chim. Acta.* **2010**, *673*, 1-25.
33) Wang G., et al. *Nano Lett.* **2010**, *10*, 1088-1092.
34) Singh V., et al. *Nano Lett.* **2014**, *14*, 597-603.
35) Balandin A. A., Lazarenkova O. L. *Appl. Phys. Lett.* **2003**, *82*, 415-417.
36) Kamat P. V. *J. Phys. Chem. C* **2008**, *112*, 18737-18753.
37) Murray C. B. et al. *Science* **1995**, *270*, 1335-1338.
38) Bui H., et al. *Nano Lett.* **2010**, *10*, 3367-3372.
39) Genereux J. C., Barton J. K. *Chem. Rev.* **2010**, *110*, 1642-1662.
40) Mallajosyula S. S., Pati S. K. *J. Phys. Chem. Lett.* **2010**, *1*, 1881-1894.
41) Kubař T., et al. *Phys. Status Solidi B* **2013**, *250*, 2277-2287.
42) Mitchell G. P., et al. *J. Am. Chem. Soc.* **1999**, *121*, 8122-8123.

Chapter 2
Single Particle Measurements of Quantum Dot-DNA Hybrids

Quantum dots (QDs) are currently being explored for the design of solution-processed thin films due to their size- and shape-tunable molecule-like energy levels, which provide potential advantages over bulk materials for a variety of applications.[1–12] One that has seen a great deal of interest is in increasing the efficiency of photoresponsive devices via better utilization of high-energy hot carriers. A hot carrier results when a semiconductor absorbs light with greater energy than its nominal bandgap, which excites an electron-hole pair into higher energy states. In a bulk material this extra energy is lost as the charge carriers shed this extra energy as heat and return to their nominal bandedge states, which happens rapidly (~fs) due to the continuous electronic density of states (Figure 2.1). QDs can potentially utilize these hot carriers before they have a chance to cool because of their more discreet, molecule-like energy levels which prevent the charge carriers from cooling for orders of magnitude longer (~ns).[13] However, moving charges out of a quantum dot, even in a densely packed film, is a relatively slow process which allows the extra energy to again thermalize.

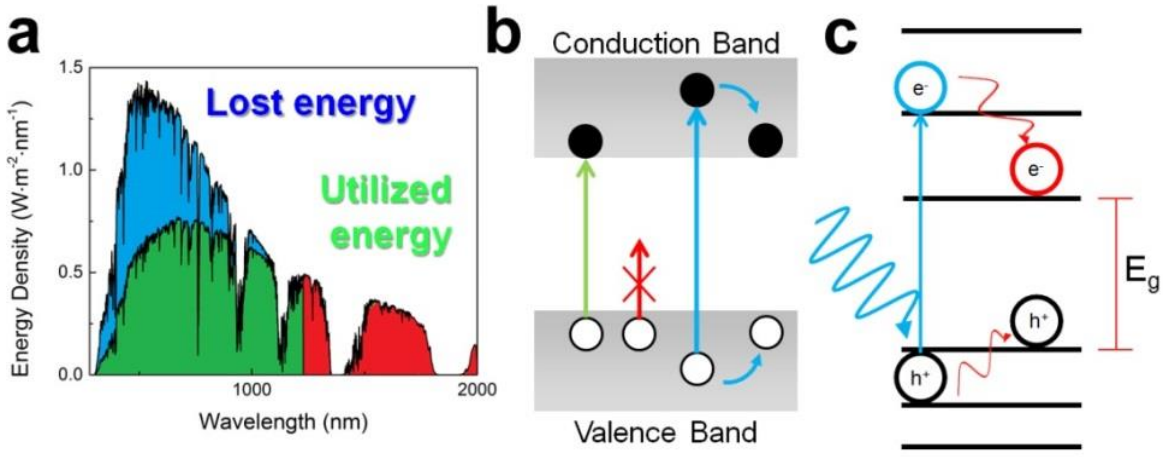

Figure 2.1 – **a.** Maximum solar energy conversion using single crystalline silicon (green). Blue region is energy lost to thermal relaxation, and red region is low energy light unable to excite an election.[14,15] **b.** Energy diagram of a bulk semiconductor with continuous bands of electronic states illustrating relaxation and absorption limitations. **c.** Electronic structure of a quantum dot with discreet energy levels.

Several strategies are being explored for the simultaneous conduction of multiple energy photogenerated charges, such as band-like conduction in self-assembled superlattice structures instead of glassy QD films.[16–18] DNA-mediated bottom-up assembly provides an alternative for arranging these semiconductor nanostructures in desired 3-D architectures with nanometer scale precision to yield desired electronic and photonic properties.[19–23] While charge conduction studies in DNA have identified the role of conjugation in nucleobases, it has not been

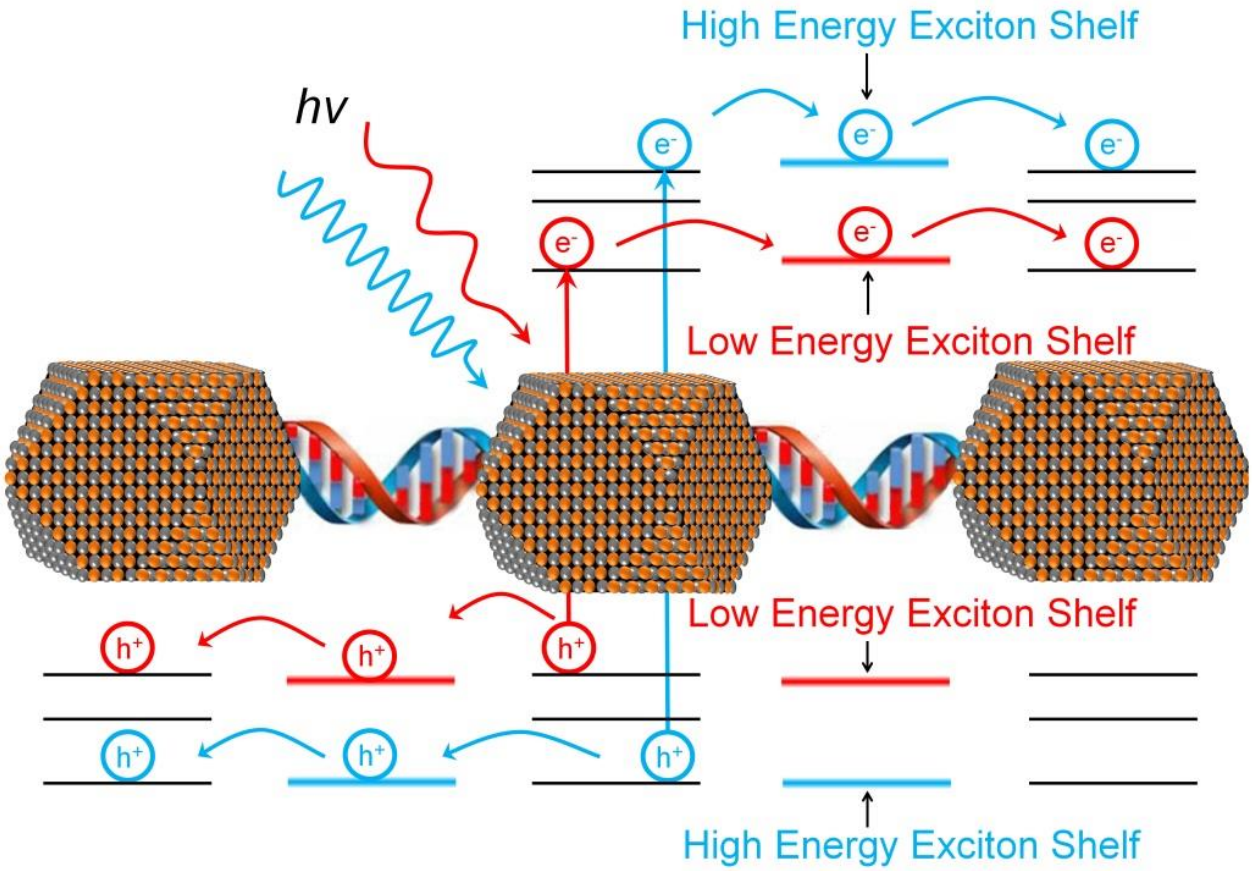

Figure 2.2 – Schematic illustrating the concept of an exciton shelf. QDs are chemically coupled to dsDNA to energetically combine the different energy molecular orbitals (low energy red, high energy blue) of the constituent nucleic acids with the molecule-like energy states of QDs and create pathways for simultaneous conduction of bandedge and excited-state carriers.

investigated for the conduction of photogenerated charges when coupled with quantum dots.[24-28] A molecular wire with multiple HOMO/LUMO (highest occupied molecular orbital, lowest unoccupied molecular orbital) energy levels, like DNA, can provide an active pathway for efficiently utilizing broadband solar radiation if these energy levels are aligned with the respective bandedge and hot-carrier QD states. This concept is outlined in Figure 2.2, which provides a schematic of the conduction pathways for different energy charge carriers. Depending

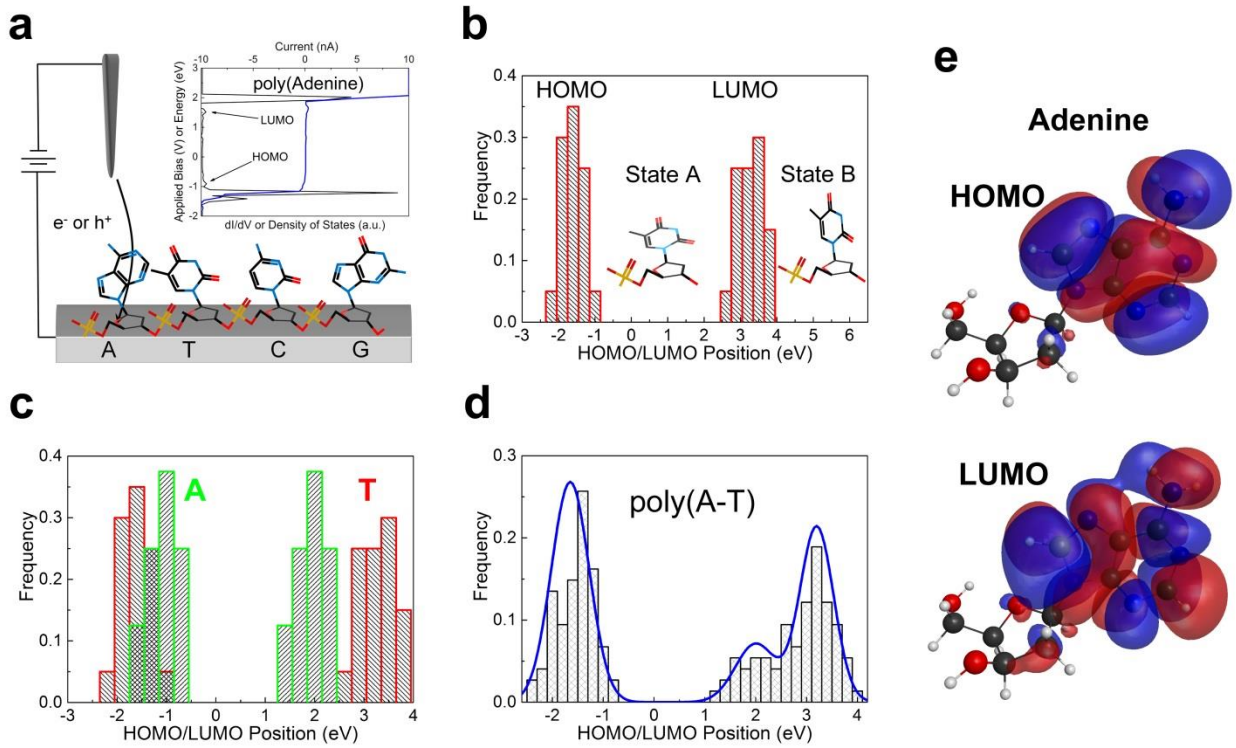

Figure 2.3 – **a.** Schematic showing STS measurements of single nucleotides. Inset shows a typical measurement of an adenine nucleotide, blue curve is the current−voltage (I−V) characteristics, and the black curve (dI/dV) is proportional to the electronic density of states. **b.** Statistical distribution of HOMO/LUMO positions of poly(thymine) as determined by STS. Histograms show the energetic dispersion in the measured data due to conformational entropy of the DNA molecule represented as states A and B. **c.** Histograms showing measured HOMO/LUMO positions of adenine and thymine DNA nucleotides relative to STS tip ionization energy (0 eV). **d.** Measured electronic states of a double-stranded oligonucleotide composed of A and T. **e.** First-principle quantum-chemical density functional theoretical (DFT) calculations for adenine nucleotide, showing confinement of the wave function of the highest occupied molecular orbital and the virtual orbital on the first unoccupied state to the nucleobases, with the sugar backbone acting as a spatial and energetic separation between the electronic molecular orbitals of the hybridized nucleobases.

on the energy of absorbed photons, electrons can be promoted to bandedge states (red) or high-energy states (blue) in a QD. The DNA molecules joining the QDs form an energetic bridge that provides an efficient conduction pathway for the different energy carriers, including capturing the hot electron before it can cool to the bandedge via nonradiative relaxation. Therefore, these different coupled energy states, here referred to as exciton shelves (ES), present in QD-DNA constructs can provide a simultaneous route for the transport of different energy charge carriers. To achieve this desired energetic alignment, the electronic structures of different cadmium chalcogenide QDs (CdSe, CdS, and CdTe) and QD-DNA constructs were characterized using scanning tunneling spectroscopy (STS).

The DNA molecule is composed of a negatively charged phosphate−sugar backbone and four naturally occurring nucleobases (guanine, thymine, cytosine, and adenine). To understand the electronic properties of each base, STS measurements quantified the energetic structure of homogeneous polynucleotides. This allows a direct measurement of electron and hole tunneling probability, and a map of the electronic density of states (DOS) for the nanoscaled material (Figure 2.3a). At room temperature, DNA molecules can acquire different conformations, leading to a dispersion of electronic DOS.[29] Therefore, the DNA energy states have a larger energetic dispersion than a solid-state QD and are shown using histograms that map the spatial and vibrational entropy of the molecule (Figure 2.3b). While there is dispersion, the energy and potential of the molecular orbitals of each conformation is discrete (shown as states in Figure 2.3b). Comparing the HOMO/LUMO probability density functions of the nucleotides reveals their energetic separation and the relative positions for each base (Figure 2.3c). The measurements of HOMO position are in good quantitative agreement with studies of nucleotides

performed in the gas phase using UPS given the poly-dispersity of conformations in the examined samples.[30-33]

$$P(V) = \sum_i \left\{ N_i \exp\left[\frac{-(V-\mu_i)^2}{2\sigma_i^2} \right] \right\} \tag{2.1}$$

The clearest differences are between the LUMO levels of adenine and thymine, which implies that it is possible to create a two-level system for transporting different energy electrons, and one for holes, using A−T double-stranded DNA (dsDNA) as a molecular wire. This is predicted to be feasible as there is no measured convolution of the complementary nucleobases' energies as measured by STS, leaving each energetically sequestered (an A−T double-stranded oligonucleotide here, functional form of fit shown in equation 2.1, Figure 2.3d). If they were

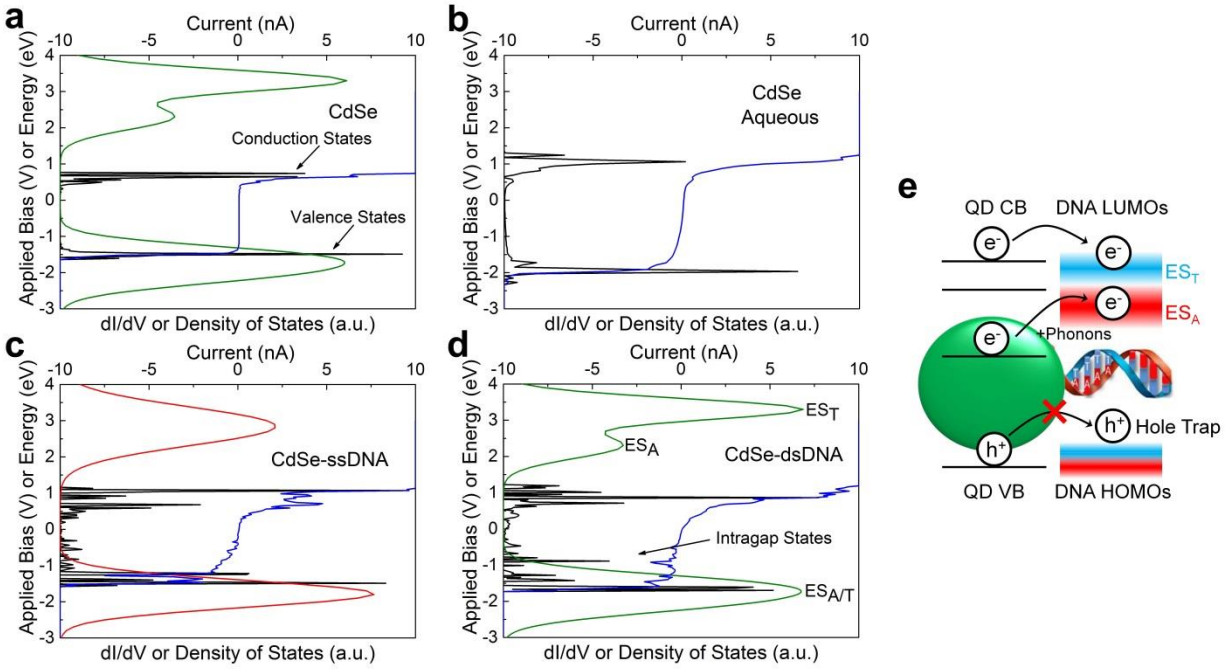

Figure 2.4 – **a.** DOS of a CdSe quantum dot with overlaid DNA HOMO/LUMO distributions (green). **b.** DOS of CdSe after aqueous ligand exchange showing a similarly clear bandgap. **c.** DOS of a CdS-ssDNA construct exhibiting intragap states. **d.** DOS of a CdS-dsDNA construct exhibiting intragap states. **e.** Predicted charge injection properties of an architectures utilizing CdS including the probable hole trapping behavior.

energetically mixed, the measured distribution would reflect that new hybrid LUMO level instead of overlaying with the un-hybridized states. The apparent preference for the thymine level likely reflects the necessity of tunneling though both bases depending on the physical positioning of the dsDNA molecule relative to the surface. The observed separation was supported using first-principle quantum-chemical density functional theoretical (DFT) calculations (Figure 2.3e). The electron and hole wave functions are mostly confined in the nucleobases with some extension of the LUMO into parts of the deoxyribose sugar. The entire

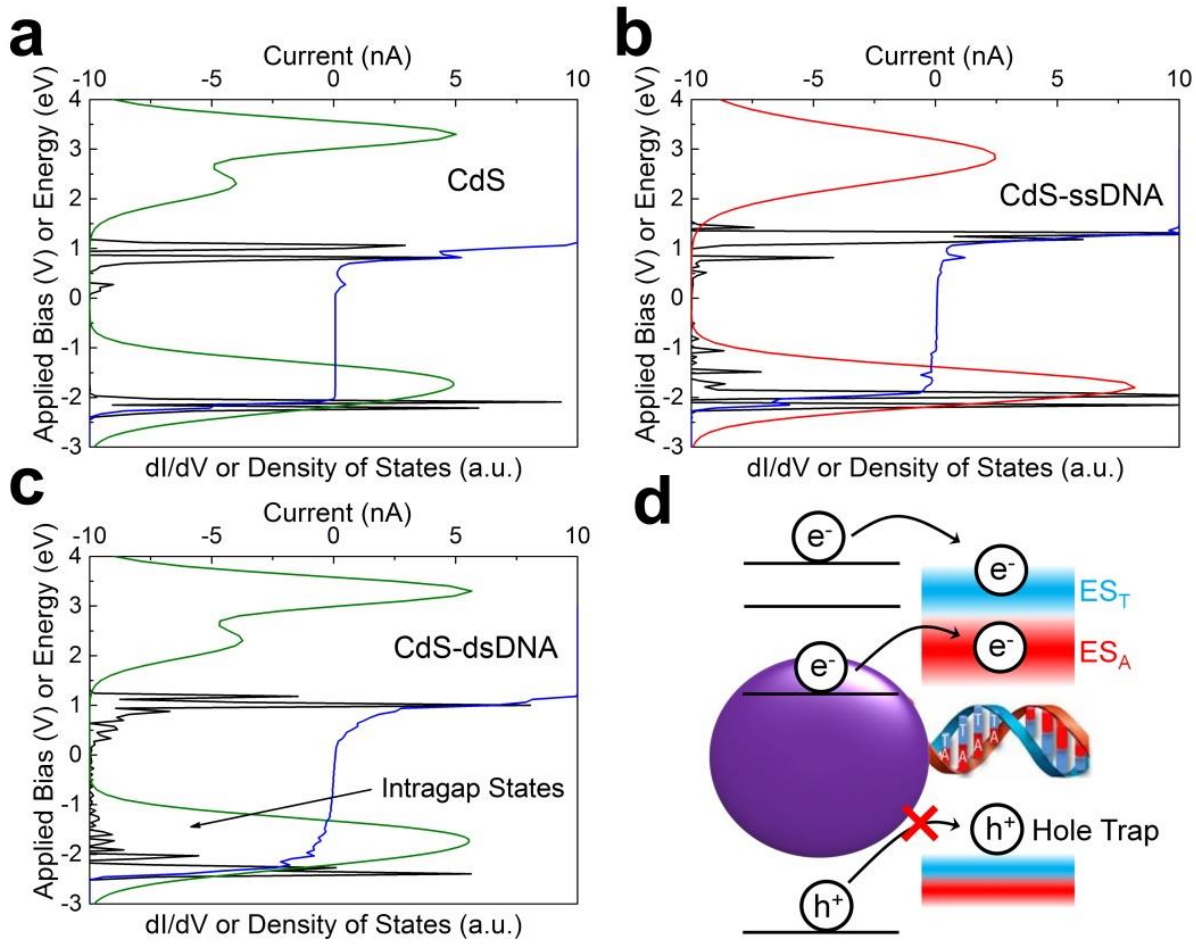

Figure 2.5 – **a.** DOS of a CdS quantum dot with overlaid DNA HOMO/LUMO distributions (green). **b.** DOS of a CdS-ssDNA construct exhibiting intragap states. The DNA states are representative of the thymine nucleotide only. **c.** DOS of a CdS-dsDNA construct exhibiting intragap states. **d.** Predicted charge injection properties of an architectures utilizing CdS including the probable hole trapping behavior.

backbone is not conjugated at this level though, which adds additional energetic and spatial separation between subsequent nucleotides, and supports the π-π stacking model as the source of the conductivity.[26]

To fulfill the roll of a molecular, wire the HOMO/LUMO levels of the DNA will have to be properly aligned with the electronic states of the linked QDs, which were also measured here using STS. Unmodified CdSe QDs exhibit clear conduction "band" (CB) and valence band (VB) states as well as a bandgap free of defects or traps (Figure 2.4a). When the DNA DOS is overlaid on these measurements (solid green curve, Figure 2.4a), a clear overlap of the DNA states into the bandgap of the CdSe QD is observed. This implies that if the two materials are energetically coupled, the presence of intra-bandgap states can be expected in the DOS of the composite material because of the DNA molecules' influence. dsDNA was chemically bound to the surface of the CdSe QDs via aqueous ligand exchange and conjugation (see Methods). As a control the exchanged dots without DNA were tested and found to be free of defect states which may arise from increased oxidation of the surface due to the shorter ligands (Figure 2.4b). Initially, the QDs were reacted with thiol-terminated single stranded DNA, which binds to the cadmium rich facets of the QDs, yielding QD-ssDNA constructs, the double strand being formed upon the addition of the hybrid strand. Measuring the STS of the CdSe-ssDNA and CdSe-dsDNA constructs clearly reveals a composite DOS that is different from the unmodified QDs (Figure 2.4c, d), especially the presence of new states within the nominal bandgap. These new intragap states correlate with the overlap of the DNA energy levels into the bandgap and show that the two materials can energetically couple. These intrabandgap states in the CdSe-dsDNA constructs will likely act as hole traps and lead to nonradiative recombination of photogenerated charge carriers.[34] Moreover, the CB states are much lower than the DNA LUMO levels, leading to a

high barrier for conduction of the bandedge electron, requiring a multi-phonon injection process. Therefore, the misaligned energy levels will likely lead to poor charge transport efficiency in architectures using such QD-DNA constructs (Figure 2.4e).

While the bandgap of nanoscaled semiconductors can be altered by simply changing the nanoparticle size via quantum confinement, the heavy hole mass of CdX QDs primarily moves the position of the CB, while the VB position remains relatively unchanged. Therefore, to attempt to eliminate the overlap between the QD valence states and DNA HOMO level, and the resulting trap states, the chalcogenide will have to be changed. In CdS, a higher band gap

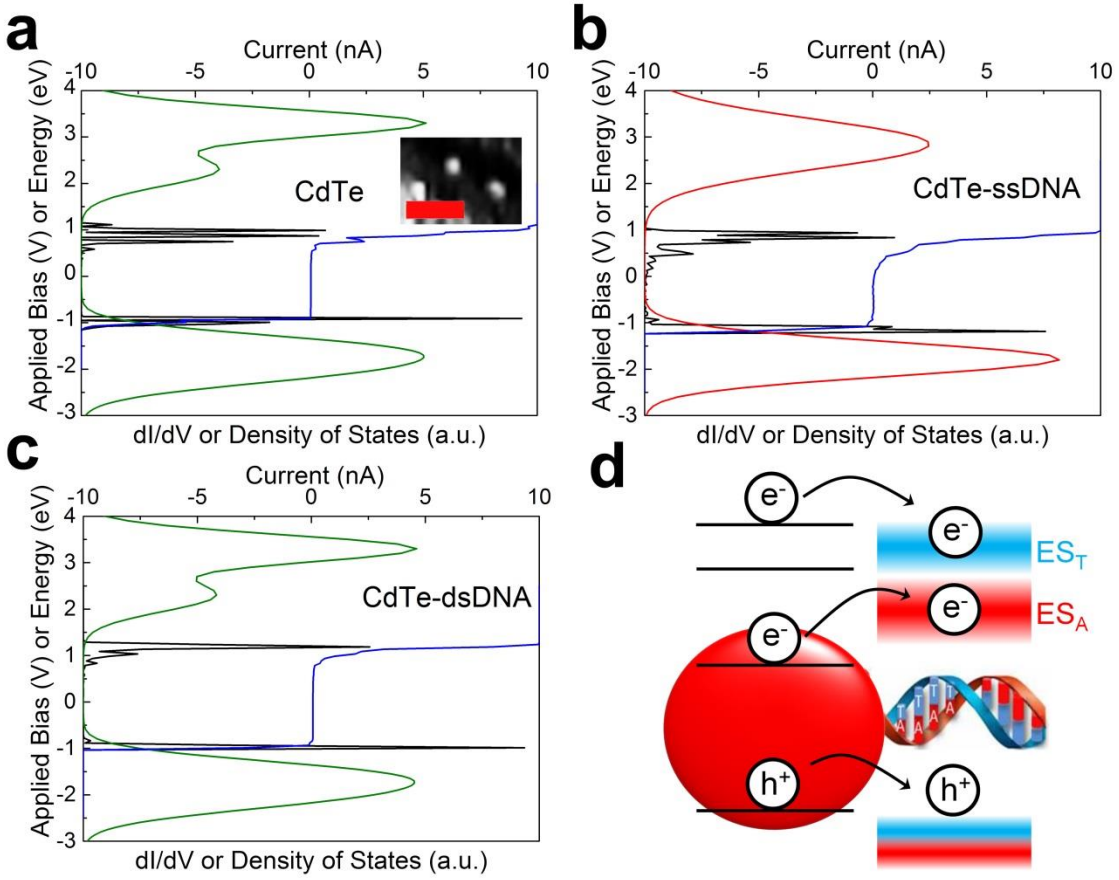

Figure 2.6 – **a.** DOS of a CdTe quantum dot with overlaid DNA HOMO/LUMO distributions (green). Inset shows an STM micrograph of two CdTe quantum dots (20 nm scale bar). **b.** DOS of a CdTe-ssDNA construct. The DNA states are representative of the thymine nucleotide only. **c.** DOS of a CdTe-dsDNA. **d.** Predicted charge injection properties of an architectures utilizing CdTe.

material, the CB and LUMO levels are better-matched compared to CdSe, allowing more efficient electron injection (Figure 2.5a, b, c). However, there is an ever-greater predicted overlap between the valence and HOMO states, which results in similar intrabandgap states as seen for CdSe, which will again lead to charge trapping (Figure 2.5d).

Of the three CdXs, CdTe has the lowest bulk bandgap and the highest relative VB position (Figure 2.6a). There are still some intra-bandgap states in the CdTe-ssDNA constructs, likely due to the greater dispersity of states in the un-sterically hindered form of DNA (Figure 2.6b) Measurements of CdTe-dsDNA constructs though show minimal intragap states and a better alignment between the CB and LUMO levels for efficient charge/exciton transport (Figure 2.6c, d). The closer alignment of the VB/HOMO levels indicate hole injection will be a more

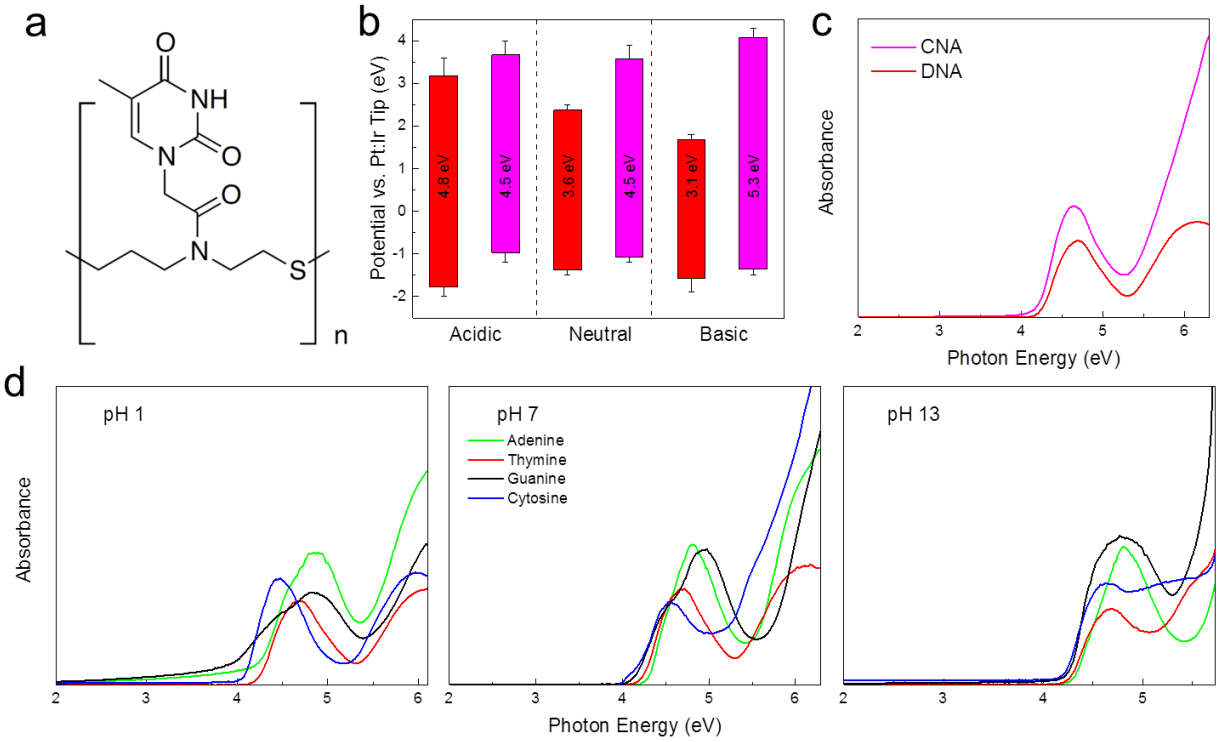

Figure 2.7 – **a.** Structure of a CNA polymer with a thymine nucleobase. **b.** HOMO/LUMO level comparison for CNA- and DNA-thymine as determined by STS after different pH treatments. **c.** Absorbance spectra of thymine with different backbones. **d.** Effect of pH on the absorbance of homogeneous DNA.

energetically favorable process, with injection into the LUMO levels requiring either photons or an energetically favorable conformation on the part of the accepting DNA.

Besides the standard form of DNA found in living systems there are a variety of different synthetic nucleic acids which utilize different backbone structures, like the well-known peptide nucleic acids[35] or, more recently, nucleobases which are polymerized using thiol-ene/thiol-Michael chemistry called click-nucleic acids (CNA).[36] The structure of these polymers is quite different from traditional DNA in that the backbone is uncharged, and which is connected to the nucleobase using an amide group instead of a pentose sugar (Figure 2.7a). The lack of charge makes this type of molecule more attractive for use as a molecular wire as it can be easily dissolved in non-polar solvents, where the bulk of quality nanomaterials are current synthesized. To evaluate its properties, similar STS characterization was performed on poly(CNA-thymine) molecules at various conditions and compared to poly(DNA-thymine). In acidic conditions the HOMO/LUMO states are quite similar, despite some offset, with statistically similar band gaps (Figure 2.7b). However, while the band gap for DNA-thymine decreases with basicity, the CNA-thymine remains the same at neutral conditions and increases at basic. While the perpetually wide bandgap makes this an unattractive molecular wire, the band gap positions raise some additional questions about nucleobase electronic structure in general.

Comparing the absorbance spectra at neutral conditions, the peak arising from thymine's absorbance is largely the same for the two polymers (Figure 2.7c). As the measured HOMO/LUMO gaps for the DNA-thymine was lower than the absorbance transition, the backbone is likely playing a role in a non-optically allowed transition state being formed (Figure 2.3e), and as the CNA backbone is unconjugated such intra-gap levels are not possible. The non-optically allowed transitions in all of the DNA nucleotides were confirmed via extinction

measurements which exhibit similar HOMO/LUMO gaps between 4 or 5 eV (Figure 2.7d) and shows that all of the exciton shelves used in Chapters 2 and 3 depend on the modulation of the nucleobase electronic states by the backbone for proper charge conduction.

In this chapter, single-particle measurements of DNA, QDs, and QD-DNA constructs have yielded information on the electronic properties of the individual and hybridized materials. The different chemical structure of purines and pyrimidines energetically separates the LUMO levels of adenine and thymine, which opens the possibility of creating a multilevel QD-DNA molecule bridge that can simultaneously transport energetically diverse charge carriers. It was shown that it is possible to control the electronic structure of hybrid materials by designing energy-matched pairings of QDs conduction/valence and DNA HOMO/LUMO. The resulting exciton shelves may provide a new alternative for charge or exciton transport of in nanoscale electronic devices. This possibility is further investigated in Chapter 3, which examines the electric characteristics of QD-DNA thin films.

Methods

Materials. Cadmium oxide (99.95%) and tellurium powder (-325 mesh, 99.99%) were purchased from Alfa Aesar. 2-mercaptoethanol (≥99.0%), trioctylphosphine oxide (99%), trioctylphosphine (97%), stearic acid (puriss., ≥98.5%), sulfur (puriss., 99.5-100.5%), oleic acid (technical grade, 90%), selenium powder (-100 mesh, 99.99%), octadecylamine (≥99.0%), octadecylphosphonic acid (97%), and 1-octadecene (technical grade, 90%) were purchased from Sigma Aldrich. TCEP·HCl was purchased from Thermo Scientific. All materials were used as provided.

DNA was purchased from Integrated DNA Technologies and used as provided. Aqueous DNA solutions were kept at -20°C for storage. The cytosine and guanine nucleobases were

added to prevent the formation of energetically coupled DNA-linked networks from forming and facilitate complete hybridization of the two complementary ss-DNA sequences (using only A and T polynucleotides can cause random alignment and some non-hybridized nucleobases).

Thiolated Strand: 5' – HS–TTT TTT TTT TTT TTT TCC TTT CTC – 3'

Complementary Strand: 3' – AAA AAA AAA AAA AAA AGG AAA GAG – 5'

CdSe quantum dot synthesis. An oven dried 100 mL 3-necked flask was filled with CdO (25.6 mg, 0.20 mmol), stearic acid (227 mg, 0.80 mmol), 1-octadecene (8 mL), and a stir bar. The flask was connected to a Schlenk line and the remaining necks were fitted with rubber septa. A thermocouple was inserted through one septum and used for temperature control (J KEM Scientific Model 210 temperature controller) via heating mantle. Three purge cycles of vacuum for 5 min followed by refilling with nitrogen were completed. The temperature was increased to 90°C and the flask was placed under vacuum for 1 h. The flask was then re-filled with nitrogen and the reaction mixture was heated to 210°C and stirred until the solution became optically transparent and colorless. The flask was cooled to room temperature and was charged with octadecylamine (1 g, 3.7 mmol) and trioctylphosphine oxide (1 g, 2.6 mmol). The solution was heated to 80°C and purged in the previous manner. Once the flask was purged the solution was heated to 300°C and allowed to reach a stable equilibrium. TOP-Se injection solution was made by dissolving selenium powder (39 mg, 0.49 mmol) in trioctylphosphine (500 mg, 600 μL, 1.3 mmol) using sonication (Bransonic Ultrasonic Cleaner 1510R-MTH). A syringe was purged with nitrogen and used to inject the entire TOP-Se solution rapidly. The temperature was reduced to 280°C for quantum dot growth. The flask was immediately quenched to room temperature using a cold water bath following growth, and 15 mL of toluene was added. The entire reaction mixture was transferred to a centrifuge tube. Bulk centrifugation (Beckman Coulter Allegra X-

22R) at 5,000 rpm for 3 min resulted in a QD rich liquid which was decanted, and unreacted solid materials which were discarded. An equal volume of acetone was added to the QD suspension, mixed, and centrifuged at 5,000 rpm for 3 min. The liquid was decanted and the precipitated QDs were re-dispersed in 15 mL toluene. The washing process was repeated twice. The final product was dispersed in 4 mL toluene for storage. 30 min of reaction time yielded quantum dots with an excitonic absorption peak at 592 nm, a photoluminescence red shift of 4.7 nm, and an average diameter of 4.2 nm, matching publish correlations (see Figure 2.8).[37-39]

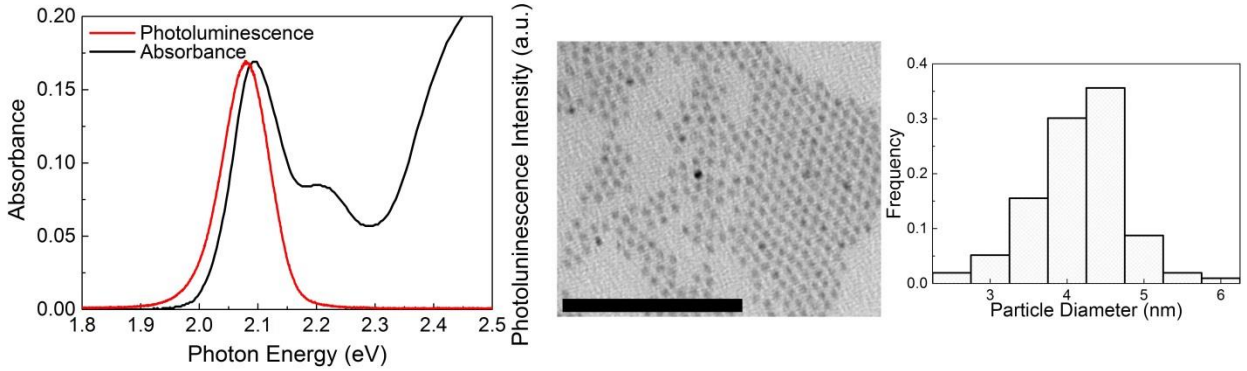

Figure 2.8 – Absorbance and photoluminescence spectra of the synthesized CdSe QDs with TEM image and size distribution analysis (scale bar is 100 nm).

CdS quantum dot synthesis. An oven dried 100mL 3-necked flask was charged with CdO (25.0 mg, 0.195 mmol), oleic acid (165 mg, 185 µL, 0.584 mmol), and 1-octadecene (10 mL). The flask was connected to a Schlenk line and the remaining necks were fitted with rubber septa. A thermocouple was inserted and used for temperature control via heating mantle. Three purge cycles of vacuum for 5 min followed by refilling with nitrogen were completed. The temperature was increased to 90°C and the flask was placed under vacuum for 1 h. The injection solution was made by dissolving sulfur (6.4 mg, 0.20 mmol) in 1-octadecene (2 mL). The flask was then re-filled with nitrogen and the reaction mixture was heated to 210°C and stirred until the solution became optically transparent. The temperature was increased to 250°C and allowed to equilibrate. The sulfur solution was rapidly injected and the reaction was allowed to progress

for 45 min. The reaction was ceased by quenching the flask in water until it cooled to room temperature. The product was transferred to a centrifuge tube then mixed with hexane (10 mL) and acetone (30 mL). The unreacted products remained in the liquid phase and were decanted. Washing (same volumes) was repeated once more and the QDs were dispersed in hexane for storage. Procedure yielded QDs with an absorption peak of 2.9eV, a large Stoke's shift common in CdS, and an average diameter of 4.5 nm (Figure 2.9).

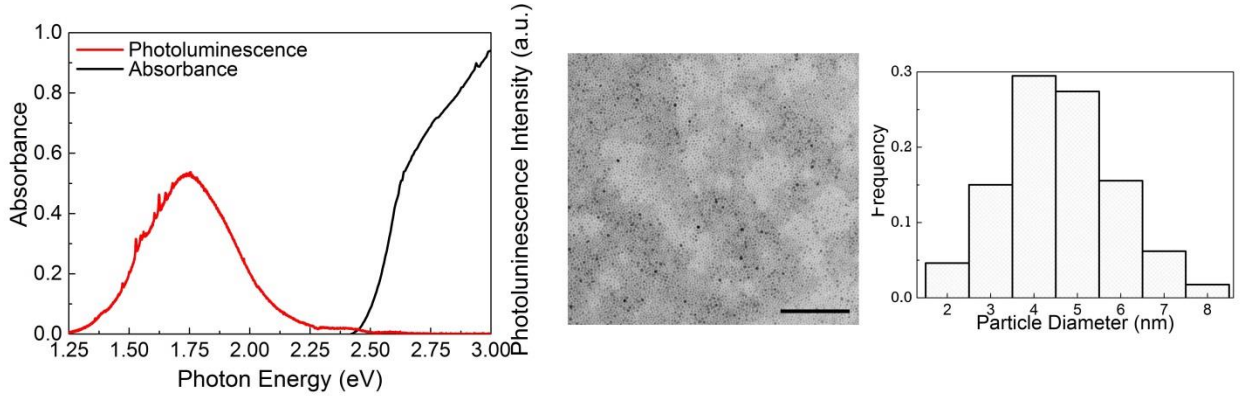

Figure 2.9 – Absorbance and photoluminescence spectra of the synthesized CdS QDs with TEM image and size distribution analysis (scale bar is 200 nm).

CdTe quantum dot synthesis. An oven dried 100 mL 3-necked flask was charged with CdO (35.0 mg, 0.273 mmol), octadecylphosphonic acid (0.275 g, 0.822 mmol), and trioctylphosphine oxide (3.725 g, 9.704 mmol). The solution was then heated to 80°C and purged with nitrogen for 3 h. The flask was heated to 325°C and allowed to equilibrate. TOP-Te injection solution was prepared by mixing tellurium powder (35.0 mg, 0.274 mmol) in trioctylphosphine (0.313 g, 377 μL, 0.844 mmol) at 325°C under nitrogen for 3 h (solution turns light yellow). The TOP-Te was rapidly injected, and the reaction mixture taken to 315°C for growth. Following growth, the flask was cooled to 60°C at which point toluene was added. The reaction mixture was transferred to a centrifuge tube, and centrifuged at 5,000 rpm for 3 min (to remove unreacted solids). The supernatant was collected and an equal volume of methanol was added to the QD dispersion. The suspension was then centrifuged at 5,000 rpm for 3min. The

liquid phase was decanted and the QDs were re-dispersed in toluene. Washing was repeated three times and the final product was stored in toluene. Growth for 8 min resulted in QDs with an absorption peak of 1.8 eV (Figure 2.10).

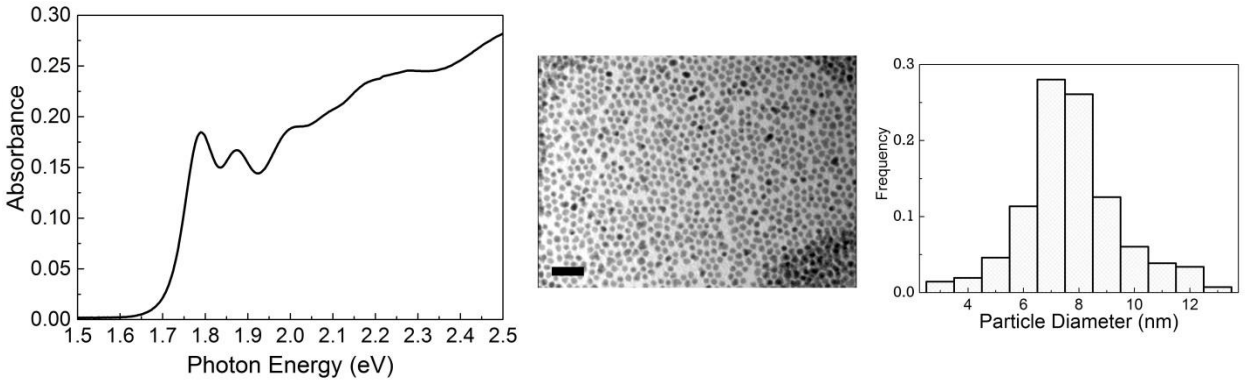

Figure 2.10 – Absorbance spectrum of the synthesized CdTe QDs with TEM image and size distribution analysis (scale bar is 20 nm).

Quantum dot-DNA conjugation. The long, non-polar ligands coating the QDs were first exchanged with 2-mercaptoethanol (ME). A small amount (~75 pmol, stock solution concentration determined optically) of quantum dots were initially vacuum dried and re-dispersed in chloroform (100 μL). An aqueous solution of water (90 μL), ME (100,000:1 ME:QD), and NaOH (10 μL, 1 M) was layered on top. The biphasic ligand exchange system was stirred at room temperature for 3 h, and then centrifuged for complete phase separation. The aqueous phase was then filtered through an Omega 30K Nanosep centrifuge filter (OD030C33), and washed with water. Thiolated single stranded (ss) DNA (200:1 DNA:QD) was reduced with excess tris(2-carboxyethyl)phosphine hydrochloride (TCEP•HCl) for 1 h, then centrifuge filtered with a desalting column if greater than MW 6000 (Thermo Scientific Zeba spin desalting columns), or otherwise with a 2000 MWCO dialysis membrane for 1 h (Thermo Scientific Slide-ALyzer mini dialysis units). The filtered DNA solution was then used to re-disperse the QDs. 1 M NaOH solution was added to the mixture (10 vol%), and the solution was placed on a rotating mixer (Labquake Shaker Rotisserie) for at least 4 h. The resulting QD-ssDNA constructs were

filtered and washed using a 30K filter, then re-dispersed and stored in 5 mM phosphate buffer. The complementary strand to the thiolated DNA was attached by heating a mixture containing it and the QD-ssDNA constructs above the melting point of the DNA (55°C) in a PCR machine for 3 h (Applied Biosystems GeneAmp PCR System 9700). ssDNA without QDs was hybridized with a stoichiometric amount of complimentary strand and reacted for 3 h at 55°C in a PCR machine for the density of states determination for dsDNA. The QD-dsDNA constructs were filtered and washed in a 30K filter and stored in 5 mM pH 7 phosphate buffer. Hybridization was confirmed by optically measuring the concentration of DNA in the filtrate.[40]

Instrumentation. Scanning tunneling microscopy/spectroscopy (STM/STS) measurements were taken using a modified Molecular Imaging PicoSPM II microscope and controller with a Pt−Ir (80:20) tip (Agilent Technologies). Indium-tin-oxide (ITO) substrates (Delta Technologies) were prepared prior to use by washing with ethanol, then cleaning by O_3 plasma for 45 min (Jelight Company INC UVO Cleaner Model No. 42). Each QD/DNA sample was dropcast onto the ITO substrates (2−5 μL of 100 nM to 10 μM solution). Scanning tunneling spectra were acquired by varying the bias between the substrate and Pt-Ir tip. The DOS is calculated from the first derivative of the current-voltage curve. The energy dispersion curves due to different conformations of DNA nucleotides shown in Figure 2.3, are the statistical distributions of >30 independent measurements represented as histograms

Transmission electron microscopy images were taken with a Philips CM 100 and were used for confirmation of QD shape and size. Images were analyzed using the built-in functions of ImageJ for determining the particle size distribution.

UV-VIS spectra were acquired on a Beckman Coulter DU 730 from 190-1100nm at 1 nm resolution. Photoluminescence spectra were measured by illuminating the sample with a UV

lamp (UVP UVGL-25) and collecting the resulting emission spectrum with an Ocean Optics USB 4000 detector.

Density Functional Theory Simulations. Electronic structure calculations were done using density functional theory with B3LYP functional and 6-311G(2d,2p) basis set on the GAMESS software package using restricted Hartree-Fock method. For neutral nucleobases, a 6-311G(2d,2p) basis set was used which provides accurate results as it is a split-valence triple zeta description of the Gaussian orbitals. Addition of diffuse functions on both hydrogens and heavy atoms provides a better description for charged molecules. The structure of each nucleobase/nucleoside was initially optimized using Jmol software integrated feature. Further geometry optimization was calculated during electronic calculation on GAMESS. Molecular orbitals were drawn using MacMolPlt.[41,42]

Symbols and Abbreviations

DFT	-	density functional theory	
dsDNA	-	double-stranded DNA	
e^-	-	electron	
E_g	-	bandgap	
ES_A	-	adenine exciton shelf	
ES_T	-	thymine exciton shelf	
h^+	-	hole	
i	-	all observed Gaussian peaks	eq. 2.1
ITO	-	Indium-doped tin oxide	
N	-	Gaussian pre-factor	eq. 2.1
P	-	probability density	eq. 2.1
QD(s)	-	quantum dot(s)	
ssDNA	-	single stranded DNA	
STM	-	scanning tunneling microscopy	
STS	-	sanning tunneling spectroscopy	
TEM	-	transmission electron microscopy	
TOP	-	trioctylphosphine	
V	-	applied bias	eq. 2.1
μ	-	peak position	eq. 2.1
σ	-	peak standard deviation	eq. 2.1

References

1) Murray C. B., et al. *J. Am. Chem. Soc.* **2005**, *115*, 8706.
2) Coe S., et al. *Nature* **2002**, *420*, 800-803.
3) Gur I., et al. *Science* **2005**, *310*, 462-465.
4) Talapin D. V., Murray C. B. *Science* **2005**, *310*, 86-89.
5) Sun B., et al. *Nano Lett.* **2003**, *3*, 961-963.
6) Law M., et al. *J. Am. Chem. Soc.* **2008**, *130*, 5974-5985.
7) Talapin D. V., et al. *Chem. Rev.* **2010**, *110*, 389-458.
8) Nozik A. J. *Physica E* **2002**, *14*, 115-120.
9) Schaller R. D., Klimov V. I. *Phys. Rev. Lett.* **2004**, *92*, 186601.
10) Sukhovatkin V., et al. *Science* **2009**, *324*, 1542-1544.
11) Tisdale W. A., et al. *Science* **2010**, *328*, 1543-1547.
12) Semonin O. E., et al. *Science* **2011**, *334*, 1530-1533.
13) Pandey A., Guyot-Sionnest P. *Science* **2008**, *322*, 929-932.
14) Shockley W., Queisser H. J. *J. Appl. Phys.* **1961**, *32*, 510-519.
15) National Renewable Energy Laboratory. Reference Solar Spectral Irradiance: Air Mass 1.5. http://rredc.nrel.gov/solar/spectra/am1.5/ (accessed Aug 15, 2013).
16) Urban J. J., et al. *J. Am. Chem. Soc.* **2006**, *128*, 3248-3255.
17) Dong A., et al. *Nature* **2010**, *466*, 474-477.
18) Choi J. H., et al. *Nano Lett.* **2012**, *12*, 2631-2638.
19) Han D., et al. *Science* **2011**, *332*, 342-346.
20) Noh H., et al. *Small* **2011**, *7*, 3021-3025.
21) Park S. Y., et al. *Nature* **2008**, *451*, 553-556.
22) Hung A. M., et al. *Nat. Nanotechnol.* **2010**, *5*, 121-126.
23) Nykypanchuk D., et al. *Nature* **2008**, *451*, 549-552.
24) Kelley S. O., Barton J. K. *Science* **1999**, *283*, 375-381.
25) Endres R. G., et al. *Rev. Mod. Phys.* **2004**, *76*, 195-214.
26) Genereux J. C., Barton J. K. *Chem. Rev.* **2010**, *110*, 1642-1662.
27) Slinker J. D., et al. *Nat. Chem.* **2011**, *3*, 228-233.
28) Cohen H., et al. *Proc. Natl. Acad. Sci. U.S.A.* **2005**, *102*, 11589-11593.
29) Ahmed T., et al. *Nano Lett.* **2012**, *12*, 927-931.
30) Urano S., et al. *J. Mol. Struct.* **1989**, *214*, 315-328.
31) Dougherty D., et al. *J. Electron. Spectrosc. Relat. Phenom.* **1978**, *13*, 379-393.
32) Dougherty D., et al. *J. Am. Chem. Soc.* **1976**, *98*, 3815-3520.
33) Peng S., et al. *Proc. Natl. Acad. Sci. U.S.A.* **1976**, *73*, 2966-2968.
34) Nagpal P., Klimov V. I.. *Nat. Commun.* **2011**, *2*.
35) Nielsen P. E., et al. *Science* **1991**, *254*, 1497-1500.
36) Xi W., et al. *Angew. Chem. Int. Ed.* **2015**, *54*, 14462-14467.
37) Yu W. W., et al. *Chem. Mater.* **2003**, *15*, 2854-2860.
38) Chen Z., et al. *J. Am. Chem. Soc.* **2007**, *129*, 15702-15709.
39) Peng A. A., Peng X. *J. Am. Chem. Soc.* **2001**, *123*, 183-184.
40) Noh H., et al. *RSC Adv.* **2014**, *4*, 8064-8071.
41) Schmidt M. W., et al. *J. Comput. Chem.* **1993**, *14*, 1347-1363.
42) Bode B. M., Gordon M. S. *J. Mol. Graph. Model.* **1998**, *16*, 133-138.

Chapter 3
Multiple Charge Conduction Pathways for Hot Carriers

Reproduced in part with permission from H. Noh, S. M. Goodman, P. Mohan, A. P. Goodwin, P. Nagpal, J. N. Cha. Direction conjugation of DNA to quantum dots for scalable assembly of photoactive thin films. *RSC Adv.* **2014**, *4*, 8064-8071. Copyright 2014 Royal Society of Chemistry; S. M. Goodman, H. Noh, V. Singh, J. N. Cha, P. Nagpal. Charge transport through exciton shelves in cadmium chalcogenide quantum dot-DNA nano-bioelectronic thin films. *Appl. Phys. Lett.* **2015**, *106*, 083109. Copyright 2015 AIP Publishing LLC.

One of the most investigated applications of quantum dots (QDs) is their use in solution-processable device fabrication, which utilize the size-dependent multiple quantum-confined electronic states of the materials for utilizing broadband radiation in photodetectors, photovoltaic cells, and photocatalytic systems.[1–6] While some strategies involving the assembly of more ordered or annealed QD films is being investigated to improve conduction in these devices,[8-10] an alternative is the use of molecular wires to improve electrical properties while maintaining the benefits of quantum confinement. DNA-mediated self-assembly provides a route for arranging semiconductor nanostructures in desired three-dimensional architectures, using bottom-up fabrication.[10–13] As described in Chapter 2, the highest occupied and lowest unoccupied molecular orbitals (HOMO-LUMO) states of complementary nucleobases adenine (A) and thymine (T) may also provide a pathway for the simultaneous conduction of bandedge and hot carriers without cooling from the QD states energetically aligned with the DNA levels, termed exciton shelves (ES, Figure 3.1).[7]

The energy level alignment of different cadmium chalcogenide QDs with DNA was shown using scanning tunneling spectroscopy (STS) measurements in Chapter 2. Hybridized dsDNA (double-stranded DNA) nucleotides show energetic separation of the LUMO levels of the constituent nucleotides arising from their different chemical structure which is the impetus for the testing of different energy ES (Figure 3.1b). Chemically coupling dsDNA to CdSe QDs reveals a mismatch between the DNA HOMO states and the valence band (VB) of the QDs, leading to the formation of intra-bandgap states, likely causing charge trapping and recombination, similarly with CdS-dsDNA. As the hole states are heavy relative to the electron in CdX nanoparticles (Figure 3.2), the valence band/HOMO level overlap cannot be removed by changing the size of the particles, so the hypothesis is that neither CdS or CdSe will be promising

candidates for photoresponsive devices. In contrast, the well-matched energy levels of the CdTe bandsand respective DNA LUMO-HOMO states form are much better aligned, which minimal overlap leading to trap states. This chapter investigates the macro-effects of the STS measurements presented in Chapter 2, examining the electrical characteristics of QD-DNA thin films and their responses to different photostimulation to test the viability of moving different energy charge carriers through the different adenine and thymine LUMO levels (Figure 3.1b). A focus on CdTe-based devices[14] (Figure 3.1c) is presented given the more favorable energetic alignment with DNA which was measured previously.

The first step in characterizing these devices was testing whether the observed interactions on a single particle level translate to macroscopic effects. The charge transport properties of electrically injected electrons and holes in the QD-DNA films without illumination

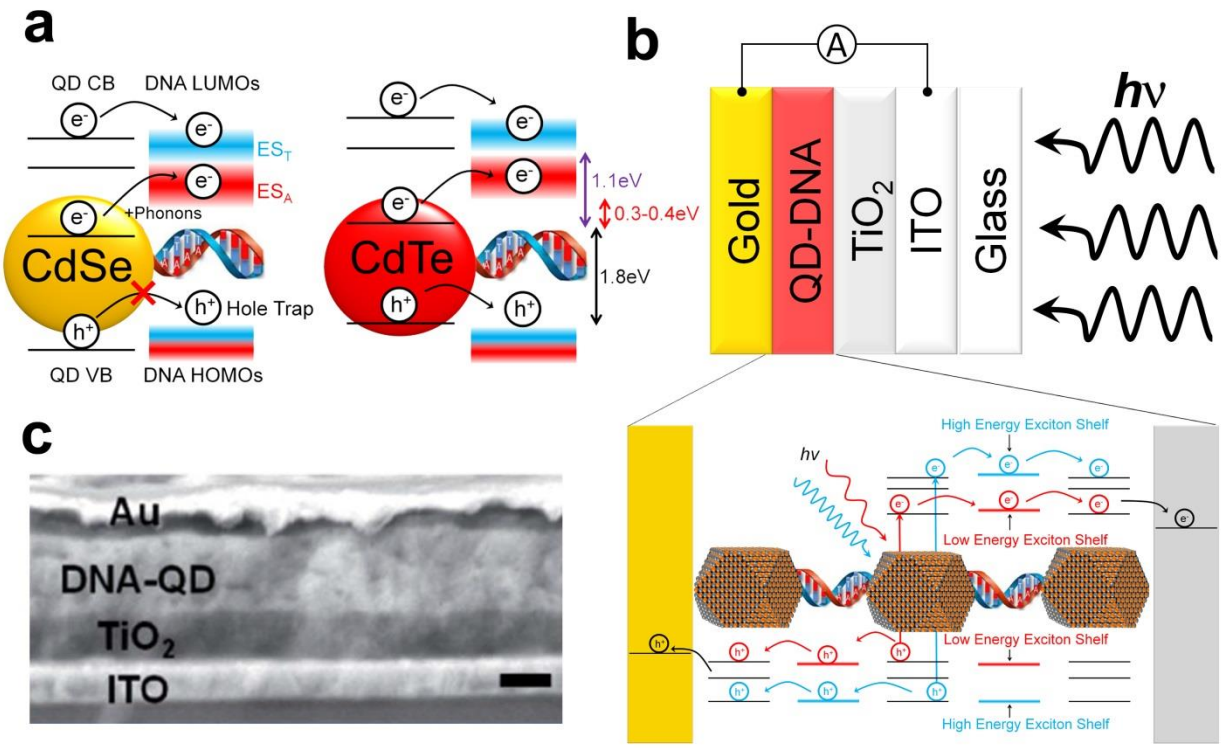

Figure 3.1 – **a.** Energetic alignments between A-T dsDNA and CdTe quantum dots with predicted spacings marked. **b.** Schematic of a thin film QD-DNA photoresponsive device. **c.** SEM image of the fabricated device (200 nm scale bar).

were first probed by monitoring the current-voltage (I-V) characteristics at different temperatures. The barriers (ϕ) for electron and hole transport were calculated from the change in conductivity (equation 3.1, see end of chapter for symbol definitions in all equations), with and Richardson's plot (equation 3.2, Figure 3.3).[15] Using both methods, the barrier for electron transport was measured as ~0.37 eV, which matches well with the STS measurements which predict the energetic spacing between the CB of the CdTe QDs and the LUMO level of the adenine nucleobases to be 0.3–0.4 eV (Figure 3.1a). The hole transport barrier was much lower (0.01–0.1 eV) and is also consistent with the STS measurements showing a close overlap between the CdTe QD VB and the HOMO levels of the dsDNA.

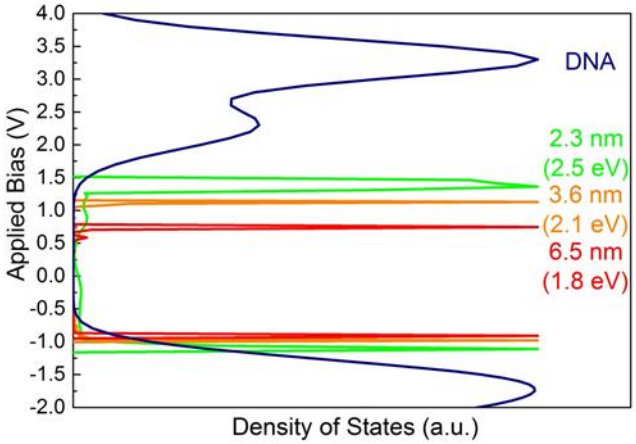

Figure 3.2 – Bandedge state position as a function of CdTe particle size with overlaid dsDNA states for comparison.

$$I \propto V \exp\left[-\frac{e\phi}{k_B T}\right] \tag{3.1}$$

$$I \propto T^2 \exp\left[-\frac{e\phi}{k_B T}\right] \tag{3.2}$$

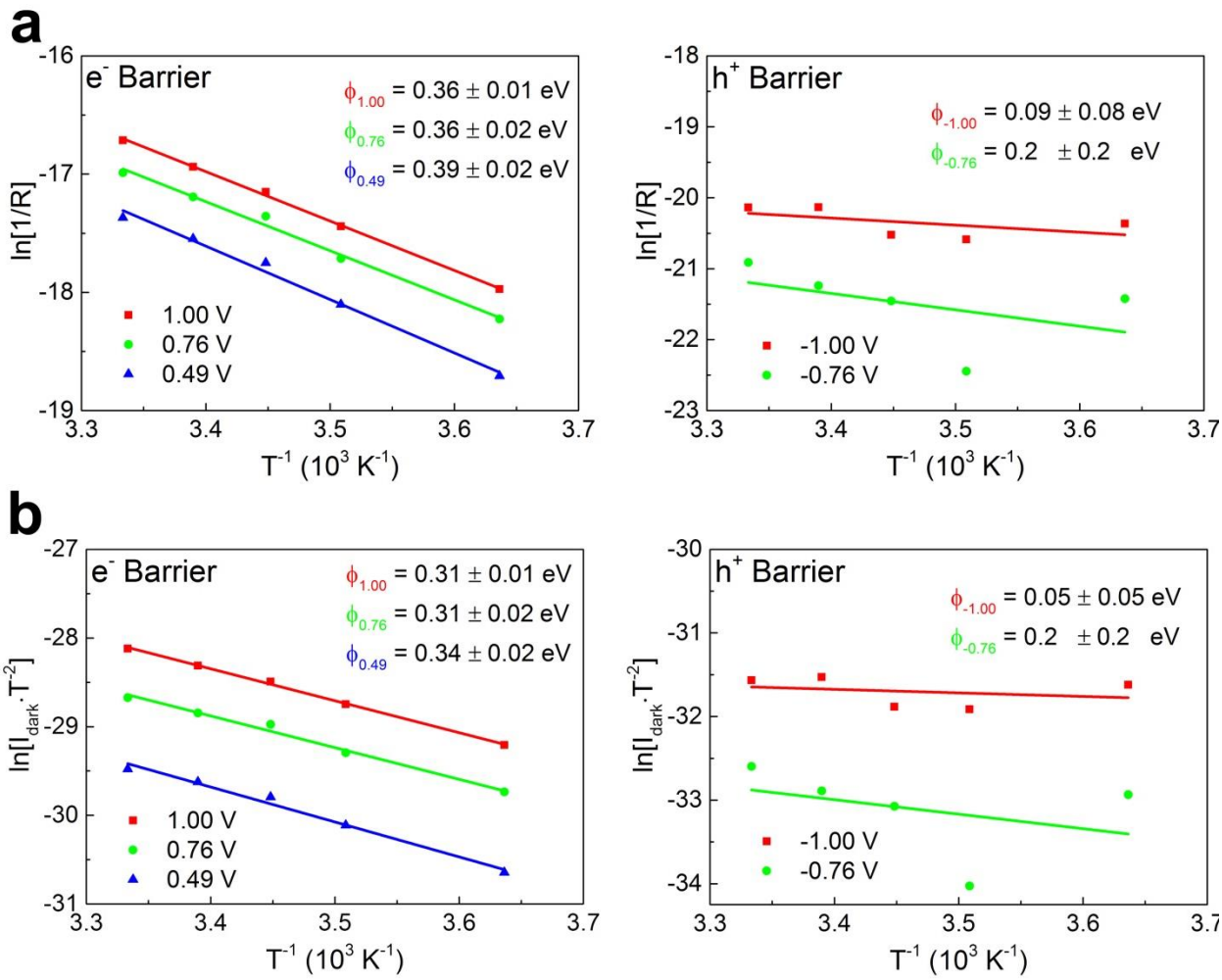

Figure 3.3 – Barrier height determination using **a.** conductivity as a function of temperature, and **b.** Richardson's plot.

To gain further understanding of the charge conduction mechanism for electrically injected charge carriers, Fowler-Nordheim analysis was applied to the individual characteristics (equation 3.3) to identify the different regimes of charge transport under the application of external bias (Figure 3.4a).[16] From this, two different regions can be easily identified: a high bias region where $I \cdot V^{-2}$ is independent of the applied bias, and a linear region with low applied bias where ln[I/V2] is proportional to ln[1/V]. The current dependence on external bias in high bias region ($I \propto V^2$) is characteristic of space-charge limited current (SCLC, equation 3.4).[17–20] The linear dependence of current on voltage (I/V) at low bias is indicative of Ohmic transport, which

is also common to SCLC conduction. While these qualitative features support this mechanism, more rigorous analysis was performed using other known mechanisms (Figure 3.4b).

$$I \propto V^2 \exp\left[-\frac{C(\phi)}{V}\right] \tag{3.3}$$

$$I = \frac{8\varepsilon\mu V^2}{9d^3} + \frac{V}{R} \tag{3.4}$$

If the electronic states of DNA played no role in charge conduction, and DNA only acts as a trap-free insulator, charge tunneling between QDs would be the likely transport mechanism. There are two regimes for tunneling, with the first occurring at low biases (direct tunneling) where the applied voltage is less than the barrier height (eq. 3.5). The second occurs at high biases (field emission) where the applied bias is greater than the barrier (eq. 2.6). From the FN plots there appears to be a growing feature in the intermediate bias regime (250-400 mV) as the temperature decreases which has a negative slope that is similar to what is observed in the high bias regime for tunneling mechanisms (Figure 3.4a). This may indicate that at lower temperature some DNA states are frozen out and are inaccessible to moving charges, requiring tunneling between available nucleotides, or directly between quantum dots. The primacy of the SCLC

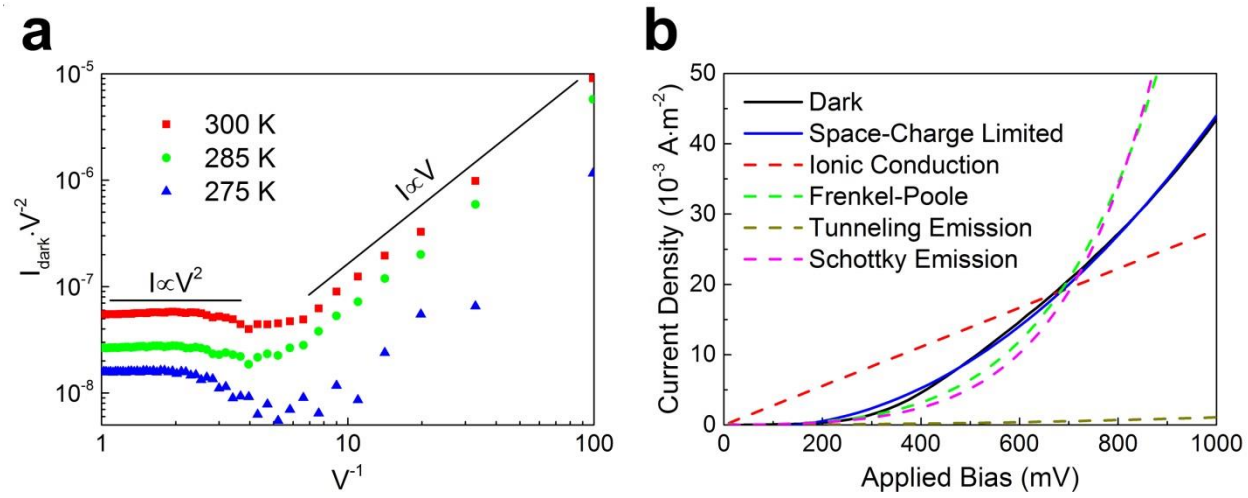

Figure 3.4 – **a.** Fowlder-Nordheim plot for the CdTe device in dark conditions at various temperatures. **b.** Fits of various charge transport mechanisms (eq. 3.4-3.8) compared to the experimentally measured data.

feature at higher biases largely precludes this from being a major factor at or above ambient conditions.

$$I \propto V \exp\left[-\frac{2d\sqrt{2m^*\phi}}{\hbar}\right] \tag{3.5}$$

$$I \propto V^2 \exp\left[-\frac{4d\sqrt{2m^*\phi^3}}{3e\hbar V}\right] \tag{3.6}$$

Another possible charge transport mechanism where the DNA plays a limited role could be ionic conduction (equation 3.7). In this mechanism, the DNA is inert and the metal ions (Na^+, Mg^{2+}, etc.) which counter the negatively charged phosphate backbone, would act as mobile charge carriers through the film. A pronounced hysteresis is usually observed under these conditions, which was absent from the measurements. Furthermore, this functional dependence of electronic current on bias and temperature does not match the observed charge transport measurements outside of the low-bias regime.

$$I \propto \frac{V}{T} \exp\left[-\frac{\Delta E_a}{k_B T}\right] \tag{3.7}$$

If the dsDNA is the charge conduction medium, but the HOMO-LUMO electronic states do not permeate the entire molecule such that each nucleotide is energetically separate, a mechanism resembling Frenkel-Poole emission may be expected (equation 3.8). If this is the case, the HOMO-LUMO levels which are capable of accepting charge would be analogous to trap states in an insulator and require the electrons or holes to hop across the sequence instead of being smoothly conducted. This is inconsistent with the charge transport characteristics observed here though.

$$I \propto V \exp\left[-\frac{e}{k_B T}\left(\phi - V^{1/2}\sqrt{\frac{q}{\pi\varepsilon}}\right)\right] \tag{3.8}$$

Another alternative is if the QD-DNA thin film acted as a composite semiconductor. Charge separation following Schottky emission-like behavior would then be observed (equation

3.9), however the difference between the CB and LUMO levels largely preclude a complete interaction of this type.

$$I \propto T^2 \exp\left[-\frac{e}{k_B T}\left(\phi - V^{1/2}\sqrt{\frac{q}{4\pi\varepsilon}}\right)\right] \tag{3.9}$$

When compared against different potential charge transport mechanisms (Figure 3.4b) these studies consistently indicate SCLC as the primary transport mechanism which matches the observed I-V-T characteristics. In these QD-DNA thin films, QDs likely act as charge centers with the moving charges likely distributed over the surface of the quantum dot. When the charge carrier attains enough energy or a bound DNA molecule assumes an energetically favorable conformation it is then injected into the nucleobase sequence and conducted to the next QD in the chain. Thus this model predicts that hot electrons will be more favorably conducted through the system due to their higher energy.

While measurements of electrically injected charges in dark corroborate the band alignment observed by STS measurements and provide insights into the role of DNA, the transport of photogenerated charge carriers was next investigated to evaluate the potential of utilizing the predicted different energy exciton shelves. The transparent ITO-side of the devices were illuminated with monochromatic light (Figure 3.1b) and the photocurrent response of different energy charge carriers was quantified. Photocurrent was chosen as the representative parameter, because while hot electrons would ideally yield an increased voltage as their extra energy is maintained through conduction, the output voltage is governed by the work function of the metal electrodes, which is a constant property of the device. Thus, while it is possible to probe the the exciton shelves as conduction pathways in these exploratory devices, a more optimized configuration with multiple-work function electrodes would be required to fully use both bandedge and hot carriers.

The I-V curves under illumination yielded a clear photovoltaic response above the bandgap of the CdTe QDs, and a significant increase in current with light illumination (Figure 3.5a). Comparing the photocurrent normalized by light intensity (*P*) across the UV-VIS spectrum, a several orders of magnitude increase in photocurrent was observed for ultraviolet photons (Figure 3.5b). Nominally in thin film QD devices, the photocurrent is limited by light absorption, and hence mimics the QD absorbance (Figure 3.5b, inset) as there is only one pathway for charge conduction. While the absorbance of the QDs does increase with the photon energy, it does not match the observed orders of magnitude increase.

To gain a better understanding of the charge conduction of photogenerated charges, a figure-of merit was developed for analyzing energetically diverse charge carriers (eq. 3.10, Figure 3.5c) Using this figure-of-merit, the photoresponse is normalized by QD absorbance (*A*) and is analyzed using the Fowler-Nordheim functional form to separate the effect of different charge conduction regimes. When plotted as a function of incident photon energy for a given applied bias, this parameter represents a measure of the relative barrier for charge transport as a function of charge carrier energy.

$$F(\lambda) = V \ln\left[\frac{I(\lambda) - I_{dark}}{V^2 \cdot P(\lambda) \cdot A(\lambda)}\right] \tag{3.10}$$

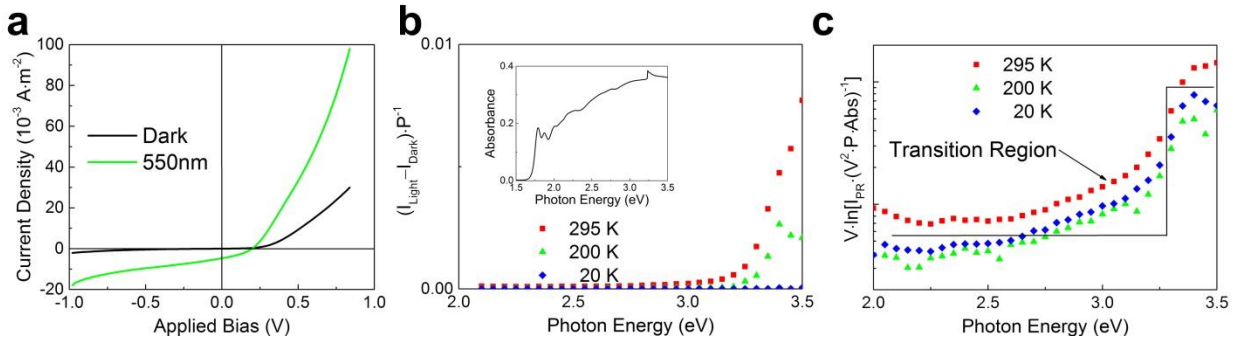

Figure 3.5 – **a.** I-V characteristics of the CdTe-dsDNA thin film in light and dark. **b.** Linear scale photoresponse with inset absorbance spectrum. **c.** Figure of merit for photogenerated charges. **d.** Photoresponse of the TiO_2 substrate.

In traditional QD thin films, this functional form would yield a flat curve due to the presence of a single pathway for charge conduction through the QD bandedge states. Based on the shape of the observed response, there are two distinct regions of charge conduction in this system for the same applied bias. The first region, at low photon energies, corresponds to a relatively high barrier for charge transport, where the lower energy photogenerated charge carriers in CdTe are being injected into the lower energy adenine LUMO level. After a transition (~2.8 eV), there is a second region corresponding to lower barrier for injection of photogenerated charges into the complementary thymine LUMO level. The inflection point of the transition region matches the separation of the QD CB and the thymine LUMO level measured by STS. While the TiO_2 layer will begin absorbing at ~3.3eV the observed transition is sufficiently low in energy that this would not be a confounding factor, especially given titanium dioxide's indirect transition. Taken together, these observed charge conduction pathways match the presented STS measurements and are an evidence of different energy conduction pathways using exciton shelves in QD-DNA thin films.

While CdTe provides the best potential alignment of the three cadmium chalcogenide materials tested, the robustness of the architecture was tested using a CdSe device. This was fabricated in the same manner as described for the CdTe device, only with a much less ideal pairing of DNA. In addition to increasing the number of nucleotides between constituent dots the nucleotides are now for the most part single stranded, and the double stranded component is heterogeneous. Combined this should have the effect of decreasing the device performance by limiting the number of possible adenine level states for moving bandedge charges and by interfering with the formation of exciton shelves via uneven electronic levels in the linking region of the DNA.

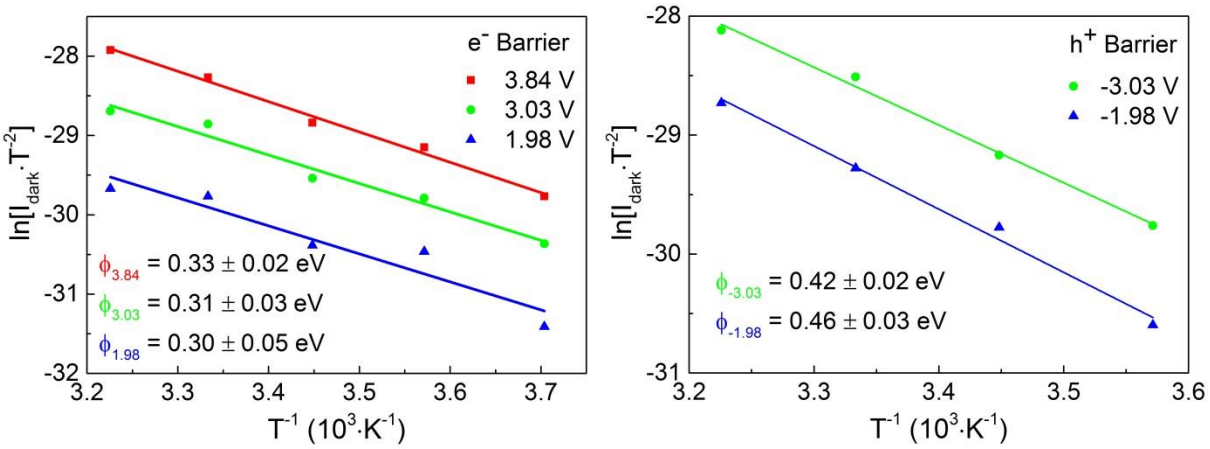

Figure 3.6 – Charge conduction barriers determined using Richardson's plot for the CdSe devices.

Compared to the previous measurements in dark a much larger hole barrier for charge transport is expected due to the energetic overlap between the QDs and DNA, which will attempt to trap the charge carriers in the lowest energy DNA states, requiring additional energy to move between quantum dots (Figure 3.1a). Evaluating the CdSe devices in dark across a range of temperatures yields the same type of barrier data as obtained for CdTe (Figure 3.6). While the electron barrier is comparable due to the similar CB alignment of CdSe and CdTe, the hole

barrier has dramatically increased to ~0.45 eV which matches the predicted alignment of the VB/HOMO states.

Additionally, a change in the conduction mechanism was observed for electrically injected charges. From the Fowler-Nordheim plot a flat region as previously observed for SCLC is no longer observed (Figure 3.7a). Fitting individual I-V curves yields Schottky emission as the mostly likely charge transport mechanism (Figure 3.7b). From a linearized form of eq. 3.9 the barrier height can be extracted directly from the I-V curve, and yields a value of 0.37 eV for electrons and 0.48 eV for holes. These values compare well with the temperature dependent data acquired in Figure 3.6. The altered mechanism likely arises from the larger degree of energetic interaction between the DNA and quantum dots in the thin film. As evidenced by the STS measurements of individual complexes the CdSe-DNA interaction is dictated by the overlap of the HOMO level with the VB, leading the observed intra-bandgap states. The close alignment and energetic similarity of the two thus has the effect of rendering the photoactive layer in the device to be a quasi-composite semiconductor, primarily for hole transport.

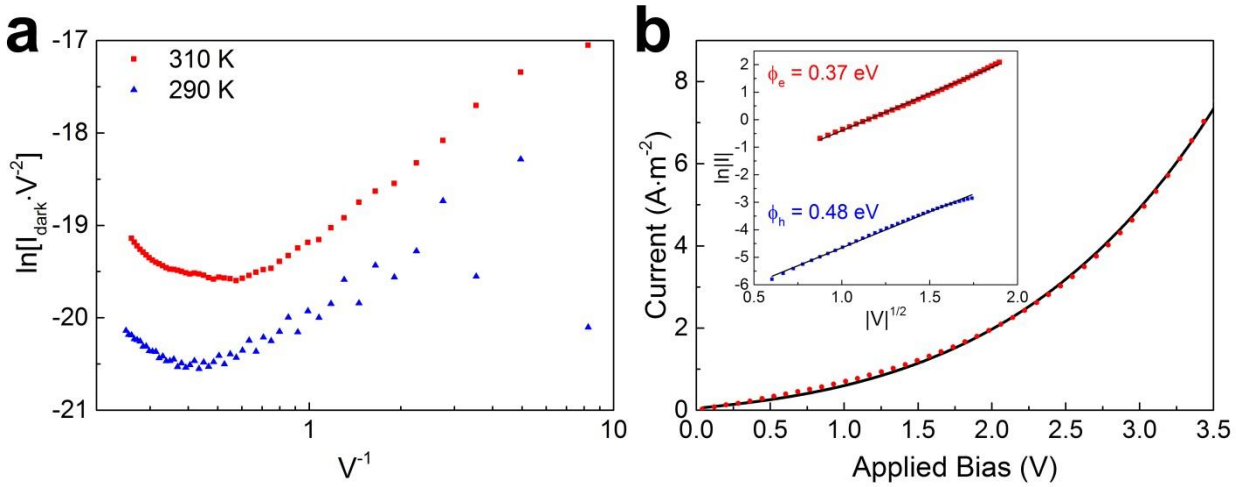

Figure 3.7 – **a.** Fowlder-Nordheim plot for the CdSe device at room temperature in dark. **b.** IV curve with Schottky emission fit at 310 K. Inset shows linearized curve used to extract the barrier height.

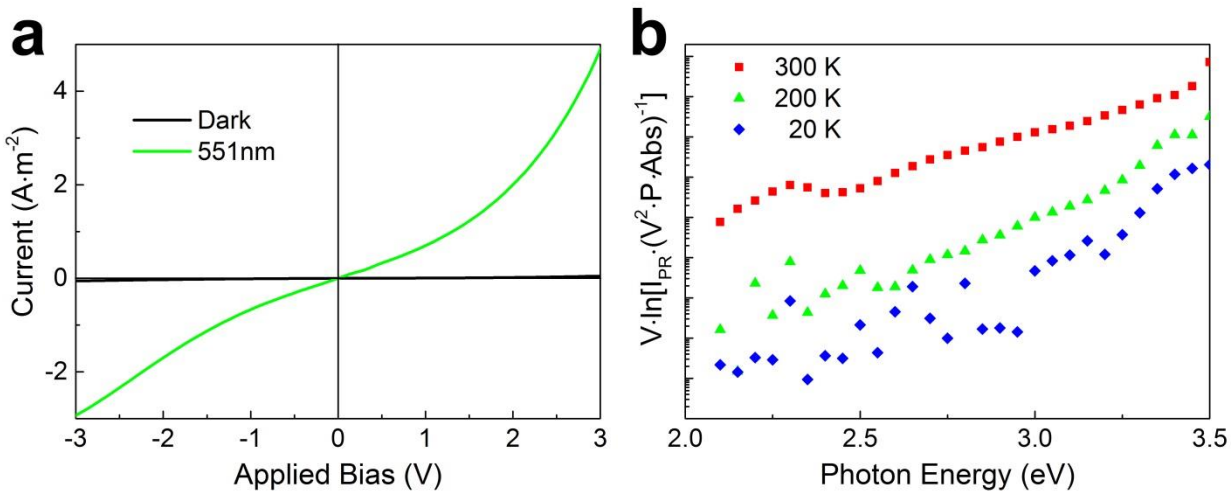

Figure 3.8 – **a.** I-V characteristics of the CdSe device in dark and under illumination. **b.** Photoresponse figure of merit.

As the temperature decreases the FN plot shifts to reflect the increasing contribution of tunneling to the system as evidence by the sharper transition voltage (V_{trans}) and subsequent change in barrier (eq. 3.11). Such tunneling configurations are typical of unlinked QD thin films, where charges have to move across a barrier determined by the inter-particle spacing and surface ligands.[21,22] Long-chain molecules largely eliminate the ability of charges to move in such devices, requiring devices to be ligand exchangedor treated with a bidentate ligand like hydrazine to induce cross linking.[23-25] Therefore, the change in mechanism from Schottky to tunneling likely indicates the decreasing ability of DNA to accept or conduct charges at lower temperatures due to the freezing of the necessary conducting states, which has a larger effect on the ssDNA because of the greater number of conformation it can assume compared to sterically constrained dsDNA.

$$\phi = \sqrt{\frac{3}{16} V_{trans} \cdot b} \tag{3.11}$$

When exposed to light the CdSe device differs from its CdTe analogue firstly in the change of photoresponse type (Figure 3.8a). Instead of a clear photovoltaic characteristic the CdSe only shows a photodiode I-V curve for all wavelengths tested. Additionally, when plotted

using the figure of merit (eq. 3.10) the photoresponse does not exhibit the previously observed energetically-separated exciton shelf-like behavior of the CdTe (Figure 3.8b). Instead of a constant region and transition to the second shelf there is only a constantly increasing value representing a different barrier for each wavelength. Thus it appears that an addition caveat for proper exciton shelf formation is the requirement that the linking DNA must be homogenous, and be primarily composed of dsDNA.

As the photon energy increases towards 4 eV (310 nm) and beyond, the DNA itself can begin absorbing light as well. While the devices are designed to be air and water free in the active region, any impurities could begin to react with and damage the DNA and thus limit device longevity in a realistic setting with broadband radiation. When these devices were exposed to high energy light a strong photocharging effect was observed, such that longer exposure continued to increase the current without reaching a steady state. After the light was remove the current would slowly relax to its nominal dark level following a first order kinetic expression (eq. 3.12, Figure 3.9a, b). The extracted time constants are on the order of hours,

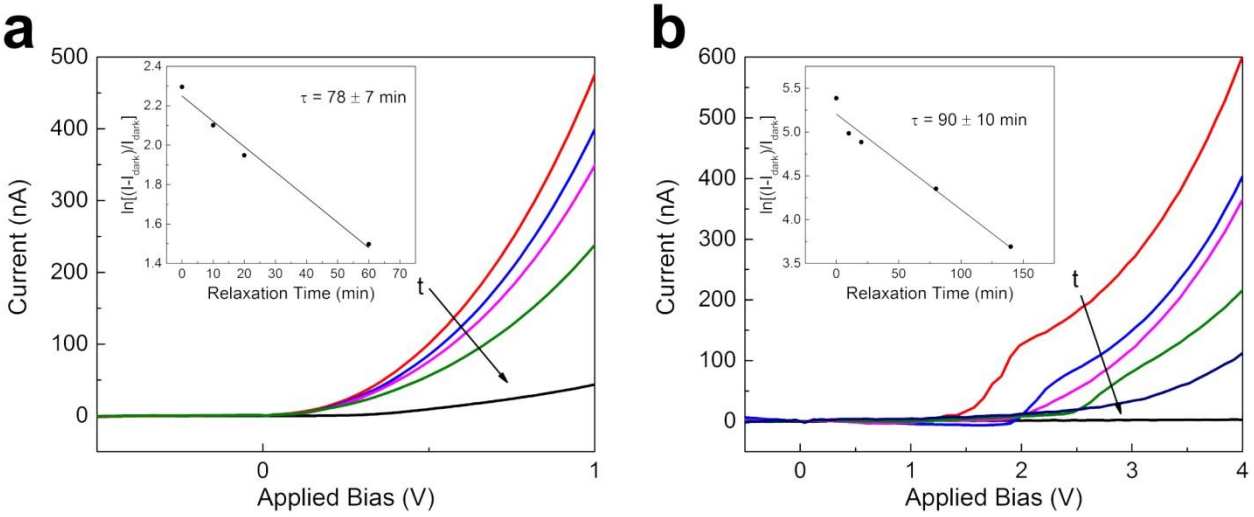

Figure 3.9 – Photocharging effect of high energy light for **a.** the CdTe and **b.** CdSe devices. Insets show the tracked kinetics and extracted time constants for the systems.

requiring over twelve hours to fully return to the nominal dark current. The chemical or physical changes to the devices under these conditions are not entirely clear, though they did not appear to have a detrimental impact on device performance after relaxation and return to visible wavelengths.

$$\frac{I - I_{dark}}{I_{dark}} \propto \exp\left[-\frac{t}{\tau}\right] \tag{3.12}$$

In this chapter, the electronic properties of QD-DNA thin films were investigated. Quantifying the temperature- and external bias-dependence of transport of electrically injected charges in dark, it was shown that charge conduction likely proceeds through a space-charge limited mechanism of injection from the QDs into the DNA. It was also shown that it is possible to transport different energy photogenerated charge carriers in the QDs through the predicted exciton shelves of the energetically distinct adenine and thymine nucleobases. While providing a proof of concept for such architectures, the potential charge trapping due to the negatively charged phosphate-sugar backbone, the improvements required in device architecture, DNA's low relative conductivity and temperature tolerance, and a high manufacturing ost limits the potential application of these devices. However, the insights gained from measurements of DNA electronic levels and its integration with optoelectronic nanomaterials opens up opportunities to integrate them as biological transducers and provide a pathway to intervene with electronic or optical stimuli, while building a foundation for investigating other conjugated polymers as molecular wires for the formation of exciton shelves with QDs.

Methods

Device Fabrication. Titanium(IV) chloride (≥98.0%), and magnesium chloride (≥98%) were purchased from Sigma Aldrich. TiO_2 nanoparticles (Ti-Nanoxide HT/SC) were purchased from Solaronix. Gold (99.999%) was purchased from Kurt J. Lesker Company. DNA was

purchased from Integrated DNA Technologies. Aqueous DNA solutions were kept at -20°C for storage. All materials were used as provided.

CdTe Device

Thiolated Strands: 5’ – HS-TTT TTT TTT T – 3’

5’ – TTT TTT TTT T-SH – 3’

Linker Strand: 3’ – AAA AAA AAA A – 5’

CdSe Device

Thiolated Strands: 5’ – HS-TTT TTT TTT TTT TTT TTC CTC TTT CCT – 3’

5’ – CTC TCT TCT TTT TTT TTT TTT TTT-SH– 3’

Linker Strand: 5’ – AGA GAG AGT AGG AAA GA – 3’

A layer of TiO_2 nanoparticles were initially spin-coated on a piece of indium-tin-oxide substrate at 3,000 rpm for 15 s.[14] A strip of the substrate was then wiped clean of TiO_2 with ethanol. The remaining film was annealed at 450°C for 10 min. A treatment with 50 mM $TiCl_4$ at 70°C for 30 min preceded a second annealing at the same conditions. To deposit the QD layer, 5’ and 3’ thiolated DNA coated QDs were mixed in 10 mM $MgCl_2$ with the linking DNA strand. An area of the substrate was defined by exposing it to ultraviolet light under O_2 using a shadow mask. The QD-DNA mixture was then drop cast on the substrate and allowed to adsorb for 1 h under humid conditions. A vacuum treatment was used to remove excess solvent. Excess salts were removed with a brief wash of 90vol% ethanol. The order of the QD-DNA film was improved by annealing at 60°C for 1 h under humid conditions, with a slow cooling rate of 30 K/h. Any remaining water was removed by vacuum drying at 80°C for 40 min. The gold contact was deposited on the QD-DNA film via vacuum evaporation at rates between 0.4-1.5 Å/s, and

was annealed at 80°C for 40 min. CdTe QDs were synthesized, ligand-exchanged, and coated with DNA as described in chapter 2.

Instrumentation. The thin films were measured in an Advanced Research Systems vacuum cryostat chamber (DE202AE with an ARS-2HW compressor) with temperature controlled by a Lakeshore 335 Temperature Controller. Current-voltage (I-V) curves were obtained with a Keithley 2612A System SourceMeter. A tungsten lamp (GE 35200-EKE) provided sample illumination with wavelength controlled by a monochromator (Princeton Instruments Action SP2150) with filters to remove 2^{nd} order wavelengths (Thor Labs 315-710 nm band pass filter). Light intensity was recorded after each set of measurements (Newport Power Meter Model 1918-R). The film was left in complete darkness for at least 12 h before measurement at each temperature. Dark Measurements were taken first, with five replicates each. When measuring each wavelength, the thin film was exposed to the light for 5 s before measuring the I-V curves. After taking each I-V curve the light beam was physically blocked.

Symbols and Abbreviations

A	-	adenine, absorbance	eq. 3.10
b	-	slope of the F-N plot in the field emission regime	eq. 3.11
CB	-	conduction band	
ES	-	exciton shelf	
d	-	tunneling separation	eq. 3.5-6
dsDNA	-	double stranded DNA	
e	-	elementary charge	eq. 3.1,2,6,8-9
F	-	normalized photoresponse figure of merit	eq. 3.10
F-N	-	Fowler-Nordheim	
HOMO	-	highest occupied molecular orbital	
I	-	current	eq. 3.1-10,12
I_{dark}	-	dark current	eq. 3.10,12
k_B	-	Boltzmann constant	eq. 3.1,2,7-9
LUMO	-	lowest unoccupied molecular orbital	
m^*	-	Reduced electron/hole mass	eq. 3.5-6
P	-	light intensity	eq. 3.10
QD(s)	-	quantum dot(s)	
ssDNA	-	single stranded DNA	
STS	-	scanning tunneling spectroscopy	
T	-	thymine, or temperature	eq. 3.1,2,7-9
t	-	elapsed relaxation time	eq. 3.12
V	-	voltage or applied bias	eq. 3.1,3-10
VB	-	valence band	
ΔE_a	-	activation energy	eq. 3.7
ε	-	dielectric constant	eq. 3.4,8-9
λ	-	wavelength	eq. 3.10
μ	-	mobility	eq. 3.4
τ	-	relaxation time constant	eq. 3.12
ϕ	-	barrier for charge transport	eq. 3.1-3,5-9,11

References

1) Coe S., et al. *Nature* **2002**, *420*, 800-803.
2) Gur I., et al. *Science* **2005**, *310*, 462-465.
3) Talapin D. V., Murray C. B. *Science* **2005**, *310*, 86-89.
4) Semonin O. E., et al. *Science* **2011**, *334*, 1530-1533.
5) Sukhovatkin V., et al. *Science* **2009**, *324*, 1542-1544.
6) Singh V., et al. *Nano. Lett.* **2014**, *14*, 597-603.
7) S. M. Goodman, et al. *J. Phys. Chem. Lett.* **2014**, *5*, 3909-3913.
8) Nagpal P., Klimov V. I. *Nat.Commun.* **2011**, *2*.
9) Urban J. J., et al. *J. Am. Chem. Soc.* **2006**, *128*, 3248-3255.
10) Mirkin C. A., et al. *Nature* **1996**, *382*, 607-609.
11) Han D., et al. *Science* **2011**, *332*, 342-346.
12) Noh H., et al. *Small* **2011**, *7*, 3021-3025.
13) Park S. Y., et al. *Nature* **2008**, *451*, 553-556.
14) Noh H., et al. *RSC Adv.* **2014**, *4*, 8064-8071.
15) Sze S. M. Physics of Semiconductor Devices, 2nd ed. Wiley-Interscience **1981**.
16) Fowler R. H., Nordheim L. *Proc. R. Soc. London* **1928**, *119*, 173-181.
17) Choi S. H., et al. *Science* **2008**, *320*, 1482-1486.
18) Rose A. *Phys. Rev.* **1955**, *97*, 1538-1544.
19) Beebe J. M., et al. *Phys. Rev. Lett.* **2006**, *97*, 026801.
20) Lampert M. A. *Phys. Rev.* **1956**, *103*, 1648-1656.
21) Dao T. D., et al. *Bull. Korean. Chem. Soc.* **2014**, *35*, 457-465.
22) Chu I. H., et al. *J. Phys. Chem. C* **2011**, *115*, 21409-21415.
23) Konstantatos G., et al. *Nature* **2006**, *442*, 180-183.
24) Tang J., et al. *Nat. Mater.* **2011**, *10*, 765-771.
25) Tang J., et al. *ACS Nano* **2010**, *4*, 869-878.

Chapter 4
Energy Transfer in DNA-Linked Quantum Dot Cascades

The use of homogenous thin film architectures for quantum dot based devices receive a great deal of attention in the literature and were the focus of Chapter 3.[1-7] A different configuration which can serve as an alternative light harvesting structure is what is known as a cascade.[8] Cascades use different-sized quantum dots linearly linked, and arranged in order of decreasing bandgap, such that the bandedge states of the constituent QDs align to create an energetically favorable gradient for exciton transfer (Figure 4.1). In such device architectures, when a smaller QD absorbs light, the resulting exciton can move down the cascade to the largest dot, where they can either recombine to enhance the photoluminescence of the large dot by several fold, which would be useful for LED devices, or dissociate and inject the charges into a substrate for photodetection or photovoltaic devices. Energy transfer (ET) in this manner can potentially allow the utilization of energetically diverse photons to improve the conversion efficiencies of QD devices several fold. An important advantage of using ET for exciton transport in QD devices is that transport in the opposite direction does not happen appreciably, with carriers moving up the cascade gradient, allowing the fabrication of devices with a selective inbuilt pathway for charge capture.[9] As QDs of the same material can be made with bandgaps throughout the

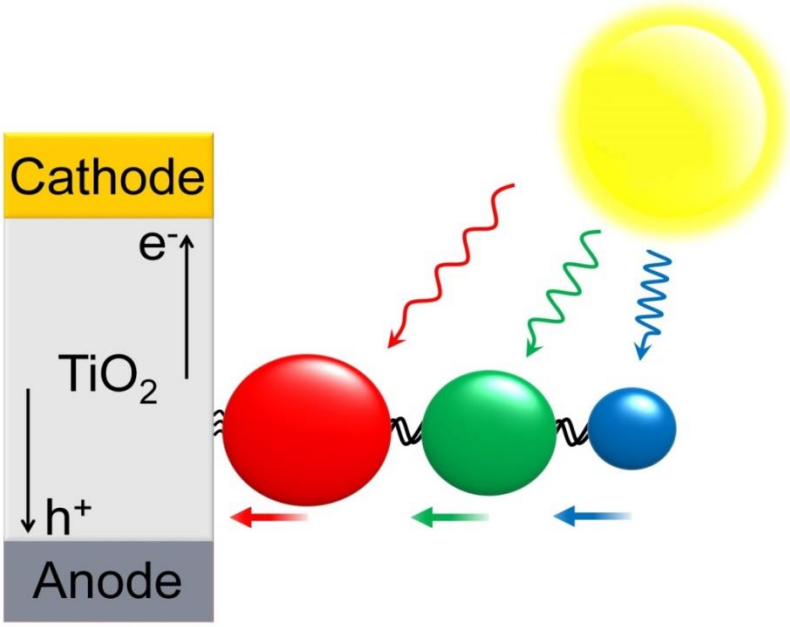

Figure 4.1 – Schematic showing a light harvesting quantum dot cascade utilizing inter-dot energy transfer, followed by exciton dissociation and charge transfer in a TiO_2 nanotube.

visible and near-infrared, devices can compose a naturally aligned cascade which is photoactive in the primary regimes of the solar spectrum.

Typically, non-radiative long-range ET occurs via a Förster mechanism by dipole-dipole coupling through space, and can be enhanced by near-field electronic effects.[10] The other primary observed mechanism in coupled system is Dexter ET which is short range, occurring via bonds and the energetic overlap of wave functions. While perfectly spherical nanoparticles can have desired dipole orientations due their isotropic shape, slight anisotropy and the resulting

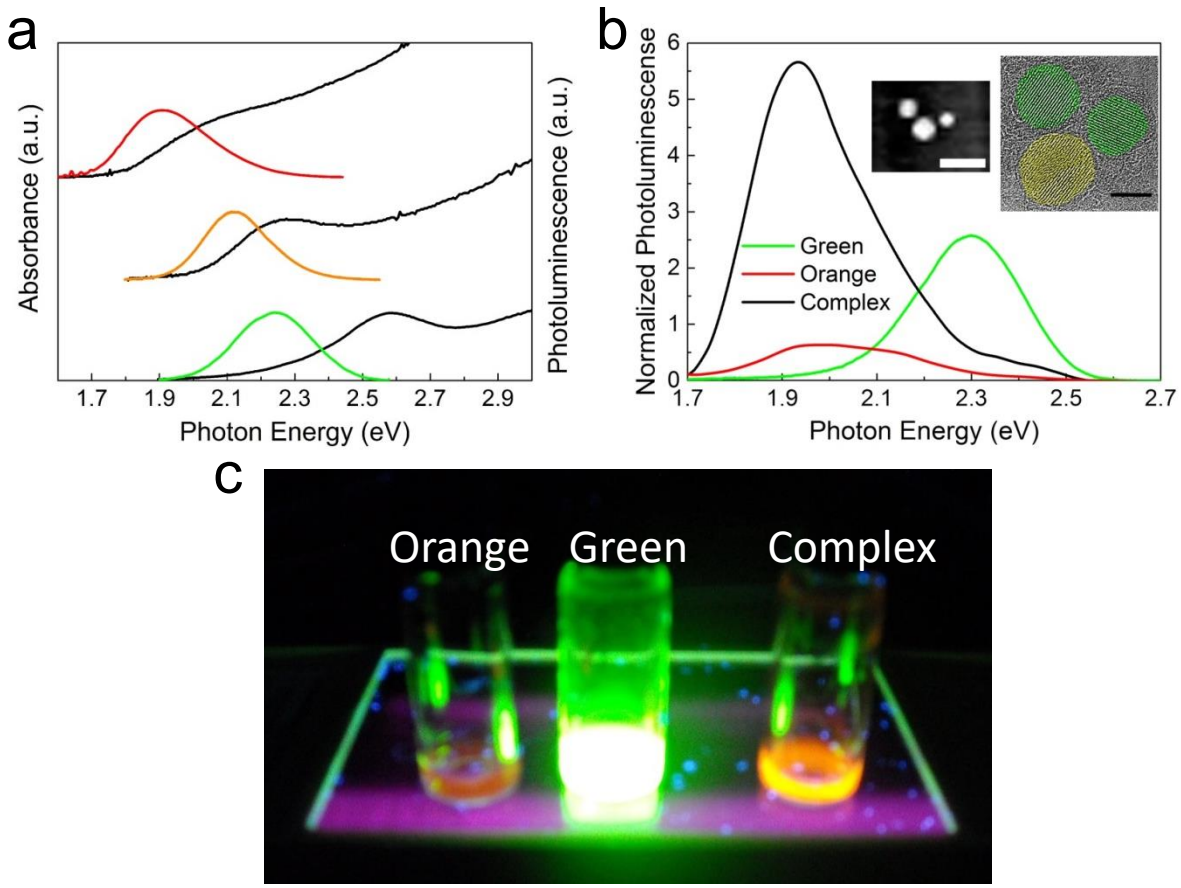

Figure 4.2 – **a.** Absorbance/photoluminescence spectra of aqueous synthesized CdTe quantum dots of different sizes. The color of the photoluminescence spectra corresponds to the observed color upon excitation. **b.** Photoluminescence spectra comparing solutions of orange and green quantum dots to a complex composed of green and orange DNA-linked dots in a 2:1 ratio. Insets show a high-resolution TEM image (4 nm scale bar) and an STM image (20 nm scale bar) of the complex. **c.** Photograph of the complex and constituent quantum dots shown in **b**.

mismatch of dipole orientations can reduce Förster coupling.[11,12] Dexter ET is relatively insensitive to dipole orientations, formation of charged species, or trapped charges[13] (e.g. formation of singlet species in QDs), and thus is potentially the more selective and efficient of the two in this context. Given the required sub-angstrom scale spatial accuracy which is necessary for architectures based on Dexter ET, such devices are cost prohibitive on a large scale without a reliable colloidal method for assembling cascades in desired configurations. In this Chapter, DNA is again used as a templating agent for the selective assembly of CdTe QDs. The energy transfer properties of the resulting complexes are described on both a single particle level and in macroscopic devices.

CdTe quantum dots were synthesized in a wholly aqueous procedure to avoid the necessity of ligand exchanges (see Methods). Size was easily controlled, yielding particles which emit green, orange, or red light (Figure 4.2a). The DNA was conjugated during the nanoparticle growth, which facilitates the assembly of ET complexes (Figure 4.2b inset). An initial proof-of-concept for enhancing light emission in such systems is the observation of complexes exhibiting photoluminescence shifts, such that the emission of the largest QDs in a cascade are enhanced at the expense of the smaller dots via down conversion (Figure 4.2b). In one such configuration where an orange dot is linked to two satellite green QDs the emission of the orange is visibly enhanced by a significant amount (Figure 4.2c). When normalized for concentration, the orange emission is enhanced by twice the intensity of the original green emission while higher energy photoluminescence is strongly attenuated, and provides direct evidence of inter-particle energy transfer (Figure 4.2b). This indicates near complete ET from the two small QDs to the larger QD, and also points to the feasibility of using these constructs for light-emission by improving the

photoluminescence quantum yields of a desired light color using this type of QD-DNA cascade/construct.

While such ensemble measurements provide an estimate of the overall efficiency of the ET processes, in order to better evaluate and understand the underlying photophysics, current-sensing atomic force microscopy (CS-AFM) was utilized to measure energy transfer within individual complexes (Figure 4.3). Unlike the STS measurements presented in Chapter 2, the gold-coated tip is in direct contact with the particles of interest, forming a Schottky junction instead of a tunneling barrier. This allows the photoresponse to be quantified, like in Chapter 3, but on a single particle level. The spatial separation and sharpness of the tip in soft-contact allows the junction to only be formed between the contacted dot, the tip, and the conductive substrate, with any interaction coming from attached dots being measured as perturbations of the measured dots photocurrent.

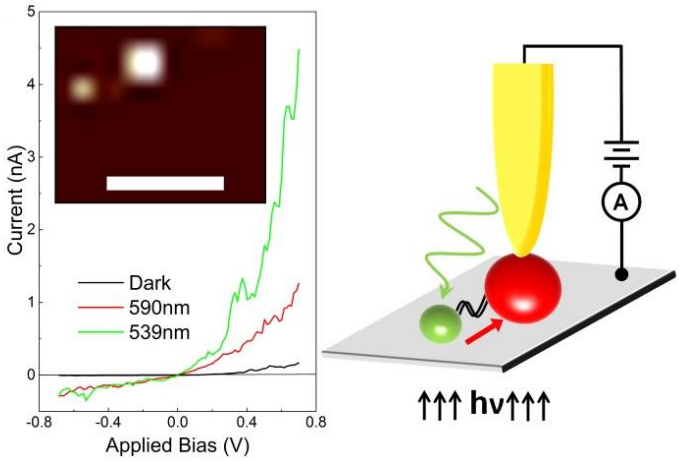

Figure 4.3 – Schematic illustrating the CS-AFM measurement architecture used to obtain the photoresponse of single dots and complexes, and I-V curves for an orange-green binary complex. Inset shows a CS-AFM micrograph of a complex taken at a scan bias of -0.1 V (20 nm scale bar).

To provide a baseline for comparison, the photoresponse of non-complexed dots was initially measured in this way. The photoresponse quantity (R) is defined in eq. 4.1 as the measured dark current (I_{dark}) subtracted from the light current (I_{λ}) which is then normalized by the incident light power at that wavelength (P_{λ}). Plotted as a function of photon energy, the

resulting curves match the bandedge positions identified by solution phase absorption, and more clearly show individual higher-order transitions (Figure 4.4a).

$$R = \frac{I_\lambda - I_{dark}}{P_\lambda} \tag{4.1}$$

Based on data from individual dots, binary complexes were designed to have a difference between the band-edge states (ΔE_{DA}) from 0.1-0.3 eV to allow for sufficient peak resolution and to avoid convolution of the donor states with the higher order peaks of the acceptors. QD-DNA complex spectra, measured via metal-coated tip placement on the largest dot for exciton dissociation and charge collection, show two primary peaks: a low energy response correlating with the bandgap of the larger dot and a second response of equal or greater intensity corresponding with the smaller dot's bandgap (Figure 4.4b). Placing the tip on the smaller dot only reveals the second transition and is equivalent to the single nanoparticle measurements. In theory, this second peak should have at most a photoresponse approaching twice that of the first if both dots are absorbing and the smallest is transferring all of its energy. The observation of

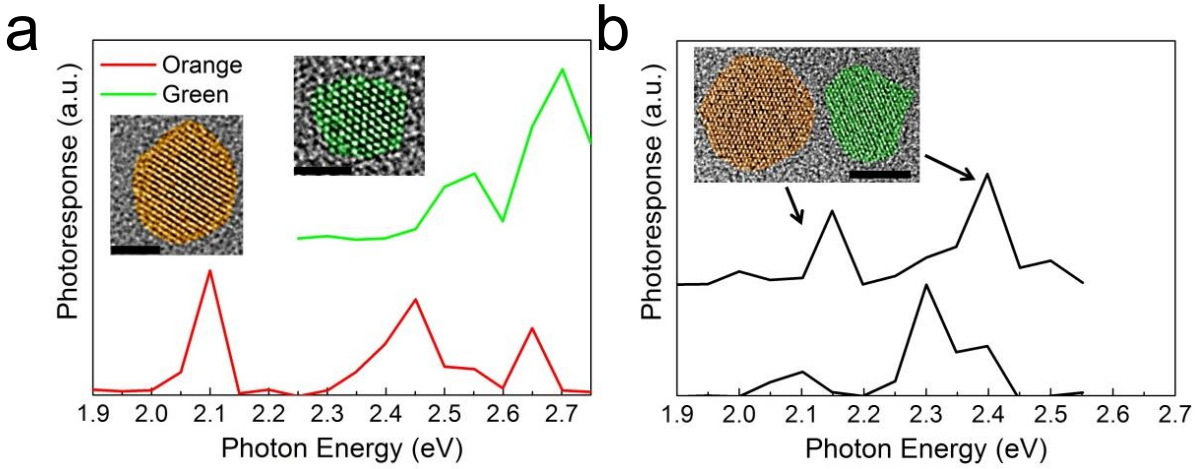

Figure 4.4 – **a.** Energy resolved photoresponse measurements of single dots (non-complexed, no DNA) with high-resolution TEM images inset (2 nm scale bars). **b.** Photoresponse spectra of binary complexes with TEM images inset (4 nm scale bar).

enhancements approaching a 5-fold increase is therefore indicative of of the gold-coated CS-AFM tip's influence, which exhibits plasmon resonances in the visible spectrum, and increases the effective absorbance cross-section of the smaller QD. Similar structures have been shown in the literture to act as absorption enhancers for closely adjacent QDs,[14-16] while the QDs in physical contact with tip are not significantly enhanced since they form a Schottky junction.

Using the ratio of the two donor-acceptor bandedge peaks as a measure of the ET in these single construct measurements, there appears to be an ideal energetic separation between the QDs in the binary complexes, occurring at $\Delta E_{DA} \approx 0.2$ eV (Figure 4.5a). The observed trend is qualitatively consistent with resonance energy transfer between the bandedge absorption state of the large QD and the emission state of the small QD, which has been shown to occur in other nanoscaled systems.[17]

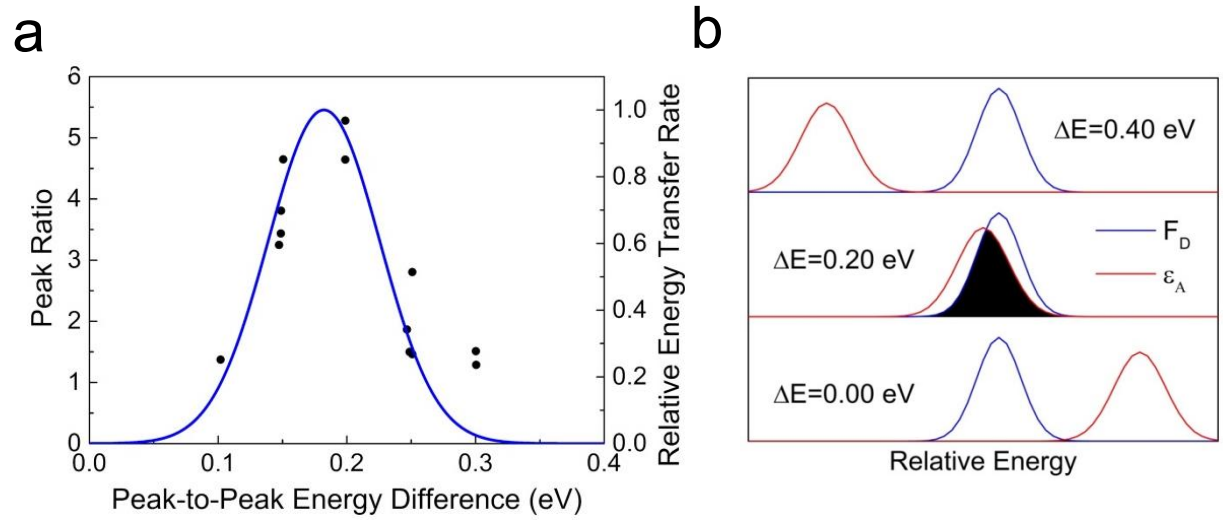

Figure 4.5 – **a.** Plot summarizing the ratio of bandedge photoresponse beaks in binary complexes as a function of the energy difference between the QDs as well as the model curve. **b.** Visualization of the donor and acceptor state convolutions for binary complexes predicted by the model within the measured peak separation range.

The relative ET rate in binary complexes of were modeled based on the convolution of the bandedge donor and acceptor states (Figure 4.5b, eq. 4.2, F_D: emission spectrum of donor, ε_A: first excitonic transition of acceptor).[18] Both parameters were described as Gaussian distributions

(eq. 4.3, 4.4) with variances calculated from the full-width at half-maximum (Γ) of the CS-AFM photoresponse peaks for non-complexed QDs (eq. 4.5). The relative rates of energy transfer were calculated by numerically evaluating the integral in eq. 4.2 holding E_D constant and varying ΔE_{DA} from 0.1-0.4 eV, assuming an unchanging inter-particle distance and constant material dependent properties between the two differently sized QDs. The calculated rates of energy transfer matche the CS-AFM responses, and the predicted curve only deviates from experimental observations at high ΔE_{DA}, likely due to the increasing influence of higher order QD states for which the model does not account. These results show that while energy transfer is possible for a range of bandgap separations, the energetic spacing between the constituents must be carefully controlled to produce a properly tuned cascade which maximizes efficiency.

$$r_{ET} \propto \int_0^\infty F_D \varepsilon_A \lambda^4 d\lambda \tag{4.2}$$

$$F_D = \left(2\pi\sigma_D^2\right)^{-1/2} \exp\left\{\frac{-\left[E(\lambda) - \left(E_D - \Delta E_S\right)\right]^2}{2\sigma_D^2}\right\} \tag{4.3}$$

$$\varepsilon_A = \left(2\pi\sigma_A^2\right)^{-1/2} \exp\left\{\frac{-\left[E(\lambda) - \left(E_D - \Delta E_{DA}\right)\right]^2}{2\sigma_A^2}\right\} \tag{4.4}$$

$$\sigma_{A,D} = \Gamma_{A,D}\left[8\ln(2)\right]^{-1/2} \tag{4.5}$$

To correlate these charge transfer measurements with ensemble studies, large QDs were chemically bound to the surface of electrochemically etched 4-8 μm tall TiO_2 nanotubes via the capping MPA ligands (Figure 4.6).[19] The smaller dots were then allowed the complementary dot to hybridize to the first. Using a closed-loop helium cryostat the temperature-dependence of the energy resolved photoresponse of these ensemble films was tracked as a measure of the ET kinetics. A red-yellow sensitized device (ΔE_{DA} = 0.15-0.20 eV) exhibited a response consistent with the CS-AFM measurements at room temperature, albeit without the plasmon enhanced absorption. As the temperature decreased, the signal from the high energy smaller dot was

observed to attenuate until it appeared that all energy transfer had effectively shut down (Figure 4.7a).

This behavior differs from typical Förster resonance energy transfer processes which are largely temperature independent in the measured temperature range.[20] To confirm this hypothesis, the donor and acceptor states were modeled using data on exciton-phonon coupling[21] and the temperature dependence of the Stokes shift[22] in CdTe QDs, to simulated changes in ET as a function of temperature assuming a Förster mechanism (eq. 4.6 and 4.7. Γ_0: contribution of inhomogeneous broadening, γ_{Ph}: exciton-acoustic phonon coupling, Γ_{LO}: exciton-optical phonon coupling, E_{LO}: phonon energy, $E_{A,D}$: exciton energy at 0 K for the acceptor and donor states, X: exciton-phonon interaction, θ: phonon temperature; see Chapter X for optoelectronic characterization descriptions).

$$\sigma_{A,D} = \left(8\ln 2\right)^{-1/2}\left[\Gamma_0 + \gamma_{Ph}T + \frac{\Gamma_{LO}}{\exp\left(\frac{E_{LO}}{kT}\right)-1}\right] \tag{4.6}$$

$$\Delta E_S = E_A - E_D + 2\left[\frac{X_D}{\exp\left(\frac{\theta_D}{T}\right)-1} - \frac{X_A}{\exp\left(\frac{\theta_A}{T}\right)-1}\right] \tag{4.7}$$

For cascades with an energetic spacing from 100 to 300 meV this model predicts a slight increase in energy transfer efficiency with decreasing temperature in the measured range (Figure 4.7b). Thus the strong decreases observed in the ET photoresponse points to Dexter-like energy transfer due to energetic overlap, which was shown to possess a similar functional dependence in metal complexes.[23] This is in contrast to some previous studies which relied on long range Förster dipole coupling in order to overcome the insulating ligand layers between constituent quantum dots.[24] In the previous chapter it was shown that the HOMO/LUMO levels of DNA are

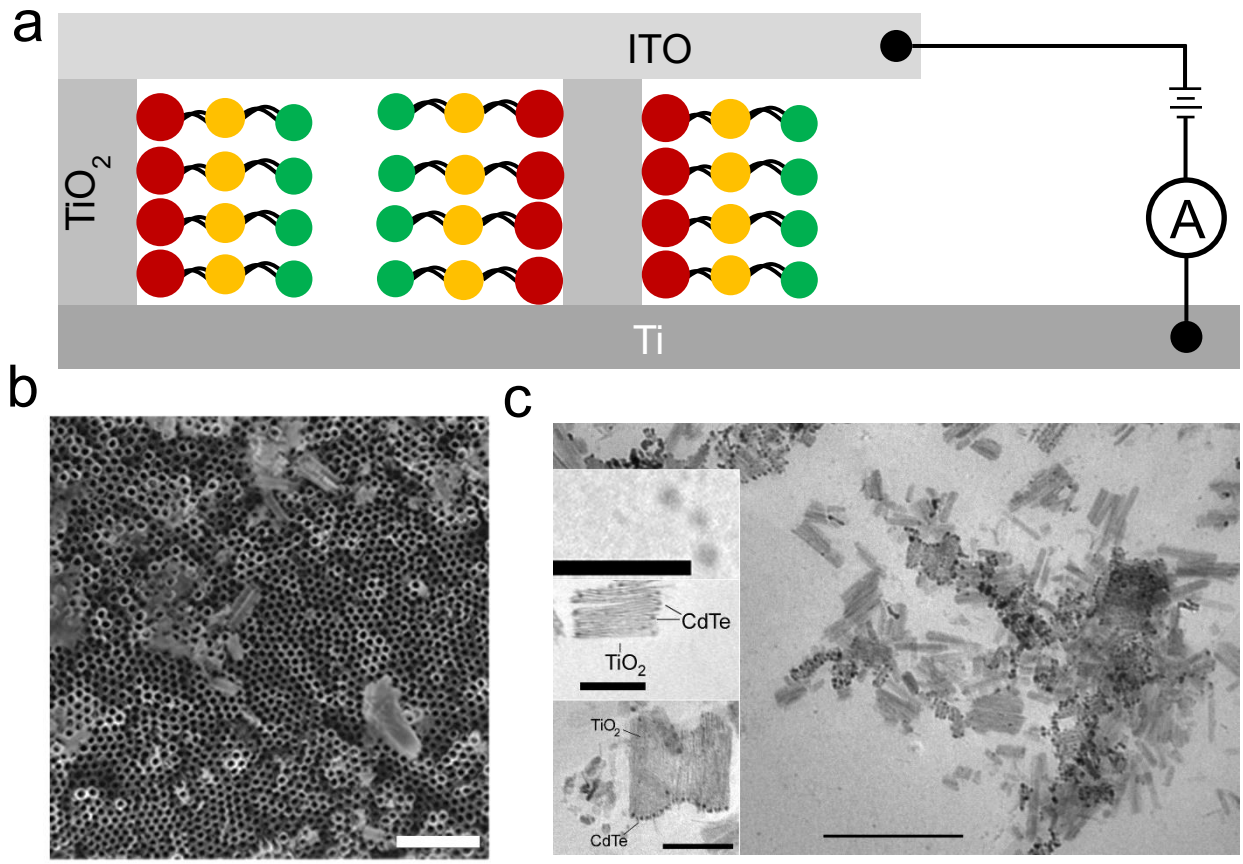

Figure 4.6 – **a.** Schematic of the devices used in low temperature characterization. **b.** SEM micrograph of the TiO_2 nanotubes used in the devices (500 nm scale bar). **c.** TEM images of nanotubes scraped from the surface of the titanium substrate showing nanoparticle decoration (500 nm scalebar). Inset images from top to bottom are a single ternary complex (50 nm scalebar), and two sections of nanotubes showing primary nanoparticle attachment to the termini (100 nm scalebars).

aligned with the CdTe states and can energetically interact with QDs, which thus likely serves as the pathway for the transfer of electrons and holes, and leads to the observed energy transfer behavior.[25,26] There is precedent for such Dexter-like energy transfer mechanisms in other conjugated polymers, including those connected to quantum dots.[27,28] For DNA, In such a configuration the lower temperatures constrain the conformational entropy of the DNA molecules and significantly reduce the spread in the HOMO/LUMO states of the DNA[27] which can prevent the energetic coupling for exciton transfer, thereby leading to decrease in collection of photogenerated charges and charge trapping in these QD-DNA constructs. A similar effect was noted in Chapter 3, with the increasing prevalence of tunneling at lower temperatures in the thin films.

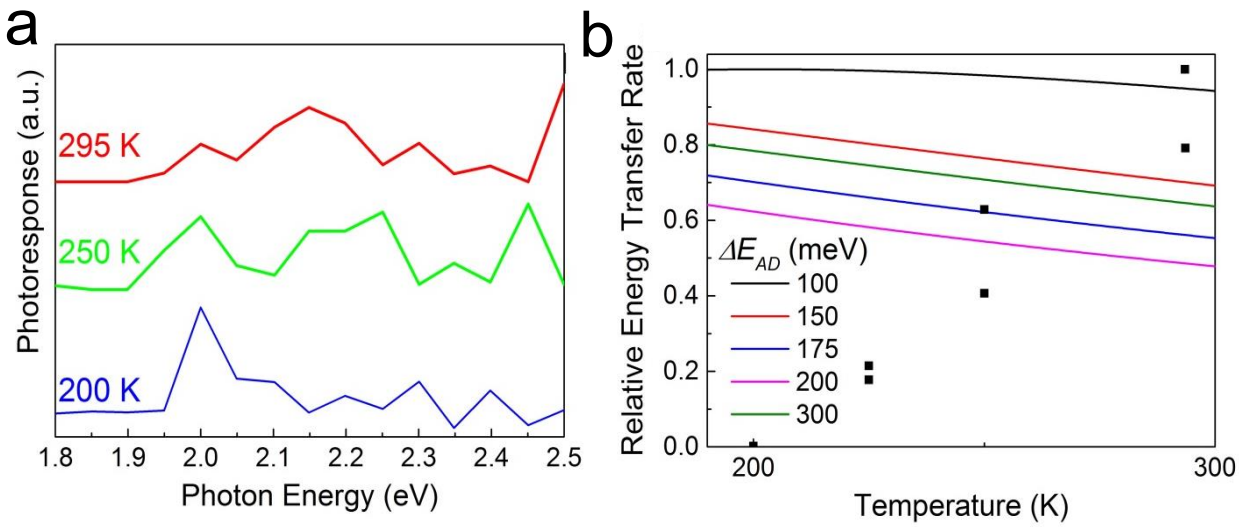

Figures 4.7 – **a.** Photoresponse spectra of an ensemble of red-yellow (ΔE_{DA} = 0.15-0.20 eV) QD-DNA constructs attached to TiO2 thin film with decreasing temperature. **b.** Predicted rates of Förster energy transfer modeled as a function of temperature and donor-acceptor bandgap spacing (colored lines) compared to experimentally measured data (solid points).

A final test of this architecture was to sensitize a device with a ternary red-orange-green cascade (Figure 4.8). The bandgap differences were kept at ΔE_{DA} = 0.1 eV in order to allow the resolution of the third QD bandedge from the higher order transitions of the first and second QD.

All three peaks are clearly visible in the wavelength-resolved photoresponse at room temperature, and the same strongly temperature dependent behavior is again observed, which confirms that the same physical principles hold for binary as well as higher order complexes. The third peak has a lower relative response likely due to the requirement of an additional energy transfer step, indicating that the overall energy transfer efficiency of each dot decreases with position in the cascade. Going beyond a quaternary complex would not likely yield a large increase in efficiency due to the attenuated energy transfer from the smallest constituent and the increasing competition with the larger dots' higher order absorbing states.

In this chapter near complete long-range ET in QD-DNA cascades was demonstrated using photoluminescence, single construct CS-AFM measurements, and temperature dependent ensemble photocurrent measurements of cascades attached to TiO_2 nanotubes. The analysis indicates that the long-range ET likely occurs due to Dexter ET, with the overlapping energy levels of DNA aiding ET from smaller QDs to larger QDs in an energy matched QD-DNA cascade. These results can have important implications of using broadband radiation to improve the poor transport observed in QD devices, and for real optoelectronic device architectures for light-absorption and emission based on quantum dots.

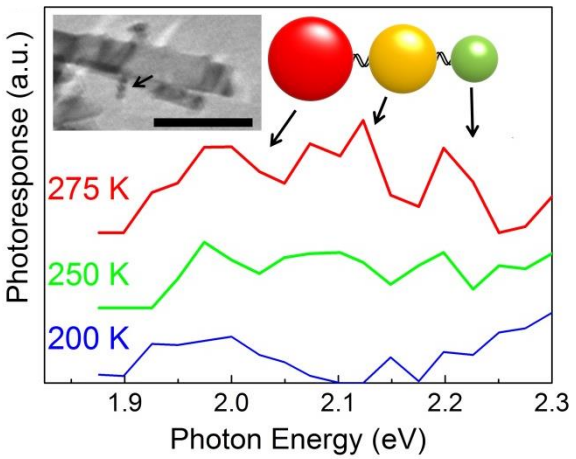

Figure 4.8 – The energy-resolved photoresponse spectra of a ternary QD-DNA construct sensitized device at different temperatures. Inset shows a TEM image of a ternary complex bound to the surface of a TiO_2 nanotube (100 nm scalebar).

Methods

Synthesis Chemicals. 3-Mercaptopropionic acid (≥99%) was purchased from Acros Organics. Cadmium(II) chloride (technical grade), ammonium fluoride (≥98%), and hexamethylenetetramine (≥99.0%) were purchased from Sigma Aldrich. Tellurium -325 mesh powder (99.99% metal basis) was purchased from Alfa Aesar. Sodium borohydride (98%), sodium hydroxide (≥97.0%), and ethylene glycol (certified) were purchased from Fisher Scientific. Compressed nitrogen (pre-purified) and oxygen (ultrahigh purity) were purchased from Airgas. Ethanol (200 proof) was purchased from Decon Laboratories INC. DNA sequences were custom ordered from Integrated DNA Technologies. All purchased materials were used as provided without further purification.

DNA Sequences. Oligonucleotides are labeled according to the position of the conjugated QD in a ternary complex L-M-O (L - largest dot, M - middle dot, O - outer dot), the number of possible connections with other dots (1 or 2), and which strand is complementary (for the outer dots). For example, a ternary complex consisting of a red dot, yellow dot, and green dot would be described as R(L1)-Y(M2)-G(O1M), while a central red dot connected to two green dots would be described as G(O1L)-R(L2)-G(O1L). A * in a sequence refers to a phosphorothioate linkage which is the binding moiety for conjugation to the QD surface. In the case of L2, the 2 refers to the ability of the large QD to accommodate two different DNA strands.

L_1: 5’ – $(G^*)_{20}$ A_{10} AAA GGA A – 3’
L_2: 5’ – $(G^*)_{10}$ A_{10} AAA GGA A – 3’
M_2: 5’ – TCC GCT GCA G A_{10} $(G^*)_{17}$ A_{10} TTC CTT T – 3’
O_1L: 5’ – $(G^*)_{10}$ A_{10} TTC CTT T – 3’
O_1M: 5’ – CTG CAG CGG A_{10} A* $(G^*)_9$ G – 3’

CdTe Quantum Dot Synthesis. Deionized water was initially degassed using bubbling nitrogen for 30 min. 1 mL degassed water was used to dissolved $NaBH_4$ (35 mg, 0.93 mmol),

and the resulting solution was transferred to a septum-capped 2 mL vial (Thermo Scientific) containing Te powder (40 mg, 0.31 mmol). A needle was inserted into the septum for outgassing during the reaction, which was allowed to proceed until the tellurium precursor solution became optically clear and colorless. A cadmium precursor solution was created by dissolving $CdCl_2$ (3.7 mg, 0.020 mmol) and 3-mercaptopropionic acid (1.8 µL, 2.2 mg, 0.021 mmol) in 10 mL of degassed water. The reaction solution was made by mixing 250 µL of the cadmium precursor solution, 200 µL degassed water, 1 µL of the tellurium precursor solution, 10 µL of 0.5 M NaOH, and 50 µL of 1 mM DNA solution (total volume 511 µL). 100 µL aliquots of the reaction solutions were divided into 5 PCR tubes (Life Science Products INC), and placed in a thermocycler (Applied Biosystems GeneAmp PCR System 9700). The tubes were held at 98°C for the reaction duration. The quantum dots were then filtered (Omega 30K Nanosep OD030C33), and washed with pH 10 water. The purified dots were re-dispersed in 150 µL pH 10 water for storage. Quantum dots without DNA were synthesized in the same manner, replacing the 50 µL DNA solution with 50 µL degassed water. DNA conjugated QDs exhibited long term stability over several months while non-DNA conjugated QDs became non-luminescent within

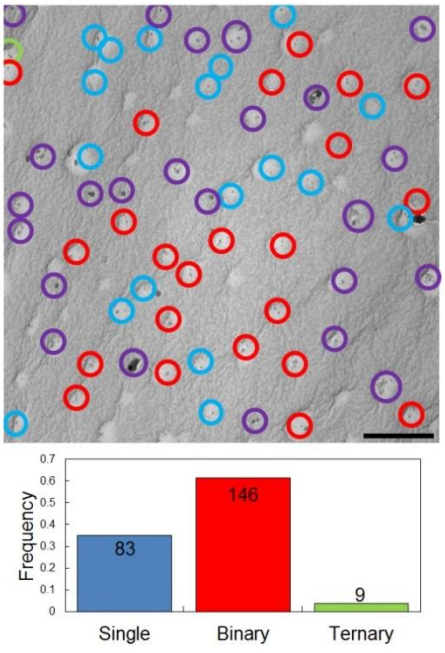

Figure 4.9 – Low magnification TEM image of a sample of yellow-red binary complexes (scale bar is 500 nm) with binary complexes circled in red, ternary complexes circled in green, and unbound dots circled in blue. A histogram showing the total number of dots in each configuration is included below the image. The total number of observed dots in each configuration is included with the histogram. About 65% of the dots are part of a binary or ternary complex in this sample. Ambiguous features not counted in the analysis are circled in purple.

several weeks. Procedure adapted from Tikhomirov et al.[29]

Complex Formation. QD complexes were formed by mixing dots with complementary DNA strands in a stoichiometric ratio, and heating the mixture to 70°C for 1 h in the thermocycler. QD concentrations were determined from optical absorption as described in Yu et al.[30]

Titanium Dioxide Nanotube Devices. TiO_2 nanotubes were grown via anodization in a solution of ethylene glycol containing 1wt% NH_4F at room temperature.[19] A titanium sheet, cut to desired dimensions, served as the anode and a platinum electrode as the cathode. The voltage was kept at 30 V by a DC power supply throughout the etching process. Nanotubes between 4-8 μm served as substrates in the device experiments.

Substrates were initially sensitized by exposure to ozone plasma for 10 min. They were then immersed in 400 μL of the stock QD solution such that the liquid level was 10 mm above the bottom of the substrate. The solution was then heated in a temperature controlled oil bath at 70°C for one hour. The substrate was then removed from the QD solution and rinsed with 200 μL pH 10 water. Successive sizes were added by immersing the sensitized substrate in a solution of the next QD to form the desired sequence, and repeating the above procedure.

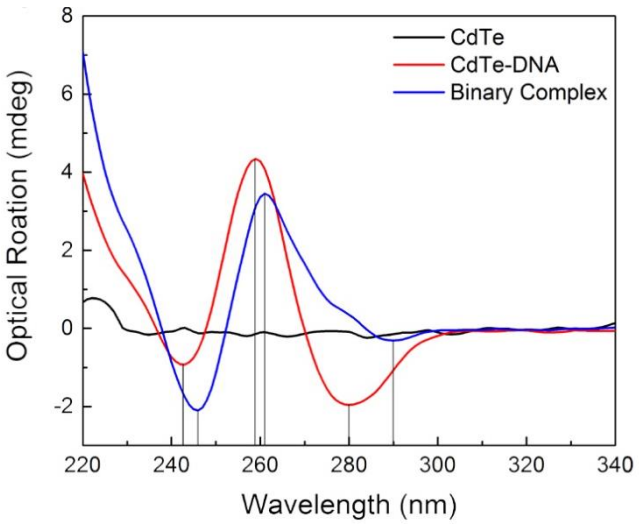

Figure 4.10 – Circular dichroism spectra of CdTe quantum dots with and without DNA, and of binary complexes.

Optical Spectroscopy. UV-VIS spectra were acquired on a Beckman Coulter DU 730 at 1 nm resolution. Photoluminescence spectra were measured by illuminating the

sample with a UV lamp (UVP UVGL-25) and collecting the resulting emission spectrum with an Ocean Optics USB 4000 detector.

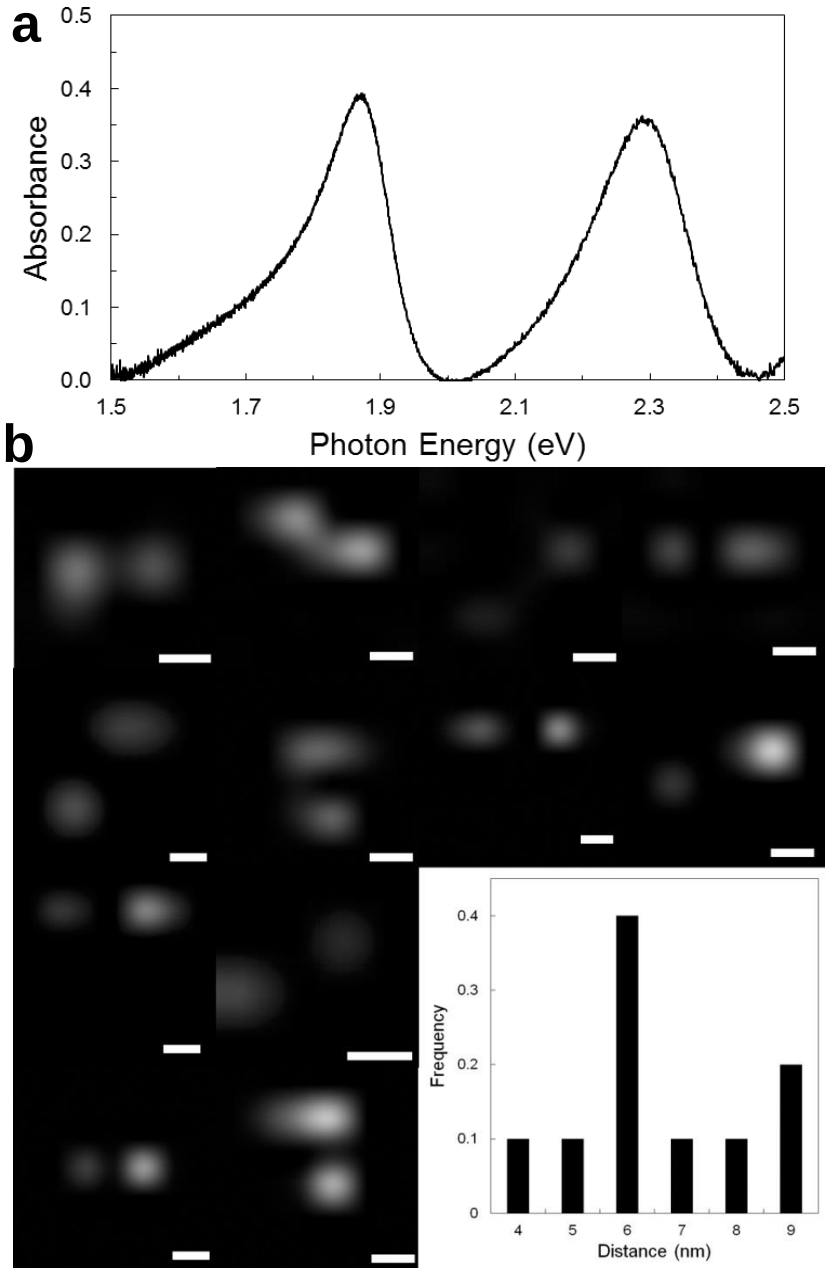

Figure 4.11 – **a.** Plasmon absorbance spectra of the gold-coated CS-AFM tips. **b.** Complexes as seen by CS-AFM (scale bars are 5 nm). Histogram showing the distribution of interparticle distances for 20 independent complexes is included.

Transmission Electron Microscopy. High resolution TEM images were acquired by the CAMCRO facility at the University of Oregon. Low magnification images of complexes (Figure 4.9) and QD-decorated nanotubes were obtained at the University of Colorado with a Philips CM 100 at 80 kV accelerating voltage.

Circular Dichroism. The complete hybridization of the DNA using these procedures was confirmed by measuring the polarization spectra of the quantum dots, QD-DNA constructs, and complexes (Figure 4.10). Spectra were acquired using an Applied

Photophysics Chirascan Plus Circular Dichroism and Fluorescence Spectrometer maintained by the Biochemistry Instrument Core at the University of Colorado. Comparing the obtained spectra show feature shifts and a loss of negative rotation from 280-290 nm, indicating a high degree of DNA hybridization. For these tests the DNA was composed of A_{10} binding segments on the constituent dots which were linked by a T_{20} oligomer to better visualize hybridization.

Current Sensing Atomic Force Microscopy. CS-AFM measurements were taken using gold coated (5 nm Cr / 15 nm Au, in house, Figure 4.11a plasmon absorbance) silicon AFM tips (NanoDevices INC). Dilutes samples were drop cast on ITO substrates, which allowed illumination with monochromatic light to measure the photoresponse, with wavelength controlled by a Princeton Instruments Action SP2150 monochromator with filters to remove 2nd order diffraction (Thor Labs 315-710 nm Band Pass filter). Light intensity was measured by a Newport Power Meter Model 1918-R after each set of measurements. Individual complexes were located in soft contact mode to avoid perturbing their separation (Figure 4.11b). The average distance between particles was measured as 6±2 nm (theoretical maximum of 9.7 nm assuming 3.6 Å separations between individual bases).[31]

The I-V curves were analyzed in order to determine the likely charge transport mechanism, and were found to conform to Schottky emission (Figure 4.12, eq. 4.8). Based on these fits the residual (*r*, eq. 4.9) was calculated at each point to estimate the error of the photocurrent. For example, for the curves shown in Figure 4.3, the 590 nm photocurrent (I_λ-I_{dark}) has a value of 1.09±0.06 nA (eq. 4.10) while the 539 nm photocurrent has a value of 4.3±0.3 nA at 700 mV, implying the photoresponse will have an uncertainty of ~5-7% (the light power measurement is an order of magnitude more precise and will not be a dominant contributor to the

photoresponse error). Repeating this calculation using the average of all residuals ($\bar{r}$) for each curve predicts an uncertainty of ~3-5%.

$$I \propto \exp\left[a\sqrt{V} - b\right] \tag{4.8}$$

$$r = \left|I_{measured} - I_{fit}\right| \tag{4.9}$$

$$\sigma_R = r_{I_\lambda} - r_{I_{dark}} \tag{4.10}$$

Low Temperature Measurements. Devices were measured in an Advanced Research Systems vacuum cryostat chamber (DE202AE with an ARS-2HW compressor) with temperature controlled by a Lakeshore 335 Temperature Controller. Current-voltage curves were measured with a Keithley 2612A System SourceMeter. A tungsten lamp (GE 35200-EKE) provided sample illumination with wavelength controlled by a monochromator with filters to remove 2nd order wavelengths. Light intensity was recorded after each set of measurements. Dark Measurements were taken first, with five replicates each. When measuring each wavelength the device was exposed to the light for five seconds before measuring the I-V curves. Each I-V curve

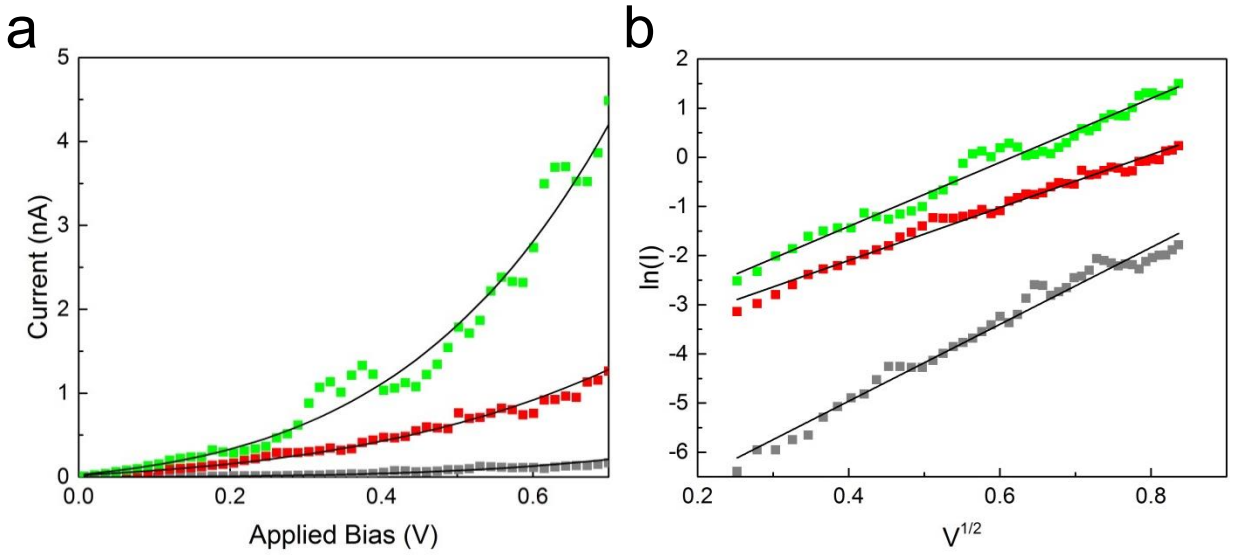

Figure 4.12 – Fits of the measured I-V curves to Schottky emission **a.** and the linearized forms used to fit the data **b**.

consists of 101 total points with a scan rate of 50 ms per point. After taking each I-V curve the light beam was blocked by placing a physical barrier between the device and monochromator. I-V curves within the standard error of the dark measurements were treated as having zero response.

Symbols and Abbreviations

a	-	constant	eq. 4.8
A	-	accepting state	eq. 4.7
b	-	constant	eq. 4.8
D	-	donor state	eq. 4.4,7
CS-AFM	-	current sensing atomic force microscopy	
E	-	photon energy	eq. 4.3-4
$E_{a,e}$	-	exciton energy at 0 K	eq. 4.7
E_D	-	bandgap of the donor quantum dot	eq. 4.3-4
E_{LO}	-	phonon energy	eq. 4.6
ET	-	energy transfer	
F_D	-	donor quantum dot emission spectrum	eq. 4.2-3
G*	-	guanine with a phosphorothioate group	
I	-	current	eq. 4.1,8-9
I-V	-	current-voltage	
k	-	Boltzmann constant	eq. 4.6
MPA	-	3-mercaptopropionic acid	
P	-	light power	eq. 4.1
QD	-	quantum dot	
r	-	residual	eq. 4.9,10
R	-	photoresponse	eq. 4.1
r_{ET}	-	rate of energy transfer	eq. 4.2
T	-	temperature	eq. 4.6,7
UV-VIS	-	ultra violet-visible	
V	-	applied bias	eq. 4.8
Γ	-	full-width at half maximum	eq. 4.5
Γ_0	-	inhomogeneous broadening	eq. 4.6
Γ_{LO}	-	exciton-optical phonon coupling	eq. 4.6
γ_{Ph}	-	exciton-acoustic phonon coupling	eq. 4.6
ΔE_{DA}	-	donor-acceptor bandgap difference	eq. 4.4
ΔE_S	-	Stoke's shift	eq. 4.3,7
ε_A	-	first excitonic absorption peak of the acceptor	eq. 4.4
$\theta_{a,e}$	-	Debye temperature	eq. 4.7
λ	-	wavelength of light	eq. 4.1-4,10
σ_x	-	standard error or variance of x	eq. 4.3-6,10
X	-	exciton-phonon interaction energy	eq. 4.7

References

1) Tang S. F., et al. *Appl. Phys. Lett.* **2001**, *78*, 2428-2430.
2) Coe S., et al. *Nature* **2002**, *420*, 800-803.
3) Nozik A. J. *Phys. E* **2002**, *14*, 115-120.
4) Murray C. B., et al. *Annu. Rev. Mater. Sci.* **2000**, *30*, 545-610.
5) Choi J. H., et al. *Nano Lett.* **2012**, *12*, 2631-2638.
6) Urban J. J., et al. *J. Am. Chem. Soc.* **2006**, *128*, 3248-3255.
7) Sun B., et al. *Nano Lett.* **2003**, *3*, 961-963.
8) Kongkanand A., et al. *J. Am Chem. Soc.* **2008**, *130*, 4007-4015.
9) Lee Y., Lo Y. *Adv.Funct. Mater.* **2009**, *19*, 604-609.
10) Sun Q., et al. *Nano Lett.* **2014**, *14*, 101-106.
11) Padilha L. A., et al. *ACS Nano* **2011**, *5*, 5045-5055.
12) Diaconescu B., et al. *Phys. Rev. Lett.* **2013**, *110*, 127406.
13) Nagpal P., Klimov V. I. *Nat. Commun.* **2011**, *2*, 486.
14) Pillai S., et al. *J. Appl. Phys.* **2007**, *101*, 093105.
15) Schaadt D. M., et al. *Appl. Phys. Lett.* **2005**, *86*, 063106.
16) Singh V., et al. *Nanoscale* **2014**, *6*, 14643-14647.
17) Kagan C., et al. *Phys. Rev. Lett.* **1996**, *76*, 1517-1520.
18) Lakowitcz J. R. Principles of Fluorescence Spectroscopy, 3rd ed. Springer **2006**.
19) Alivov Y., et al. *Nanoscale* **2014**, *6*, 10839-10849.
20) Förster T. *Discuss. Faraday Soc.* **1959**, *27*, 7-17.
21) Morella G., et al. *J. Phys. Chem. C* **2007**, *111*, 5846-5849.
22) Achtstein A. W., et al. *Nano Lett.* **2012**, *12*, 3151-3157.
23) Soler M., McCusker J. K. *J. Am. Chem. Soc.* **2008**, *130*, 4708-4724.
24) Franzl T., et al. *Nano. Lett.* **2004**, *4*, 1599-1603.
25) Goodman S. M., et al. *J. Phys. Chem. Lett.* **2014**, *5*, 3909-3913.
26) Goodman S. M., et al. *Appl. Phys. Lett.* **2015**, *106*, 083109.
27) Murphy C. B., et al. *J. Chem. B* **2004**, *17*, 1537-1543.
28) Zhang Y., Xu Z. *Appl. Phys. Lett.* **2008**, *93*, 083106.
29) Tikhomirov G., et al. *Nat. Nanotechnol.* **2011**, *6*, 485-490.
30) Yu W. W., et al. *Chem. Mater.* **2003**, *15*, 2854-2860.
31) Goodman S. M., et al. *Nanoscale* **2015**, *7*, 18435-18440.

Chapter 5
Review of CdX Quantum Dot Cytotoxicity

5.1 Introduction

Quantum dots are semiconductor nanocrystals which possess at least one dimension less than the Bohr excitonic radius of the constituent material. Decreasing the size below this point changes the electronic structure such that the bandgap begins to increase. A simplified visualization is the simple one-dimensional particle in a box model, which predicts that a more confined space limits the available states to higher energy modes.[1,2] On the macro level these changes are reflected in the observed optical properties of the nanomaterials, such that different sized particles absorb and emit different energy radiation, thus making them useful for a variety of applications from catalysis,[3,4] to bio-imaging.[5]

One visible class of nanomaterials which already see use in applications for disinfection is the high-band gap metal oxides like TiO_2 and ZnO.[6–9] When these materials absorb ultraviolet light an electron is excited from the valence bandedge state to the lowest conduction state, while the compliment to the excited electron, the hole, remains in the valence band. In this excited state both charge carriers can interact with their chemical environment through oxidation/reduction (redox) reactions which depend on the specific potentials of the bandedge states.[10] As anti-microbial agents, these materials can thus directly interfere with cellular function and redox homeostasis. This type of effect is distinct from plasmonic metal nanoparticles, which rely on heating the surrounding medium.[11,12]

While potentially useful when there is a sufficient flux of ultraviolet photons, they are precluded from *in vivo* integration due to the opacity of tissue to that spectral region.[13,14] Penetration depth is significantly increased at higher wavelengths, up to several millimeters for visible light,[15] which could potentially allow the stimulation of lower energy materials. The traditional first choices for visible absorbing quantum dots have been the cadmium

chalcogenides (CdS, CdSe, and CdTe) due to their bright luminescence, easily tunable excitonic transition, and ease of reliable synthesis[16] whose properties have encouraged their use as biological labeling agents.[5] Concerns have logically been raised about using these particles in living systems due in large part to the toxicity of the constituent elements. Cadmium is recognized as a hepatotoxin and carcinogen,[17–19] which directly damages DNA through proposed reactive oxidative species (ROS) mechanisms and indirectly damages via protein interference.[20] Selenium, while an essential trance nutrient, causes selenosis in high doses,[21] and tellurium has limited natural biological function in exotic amino acids in certain organisms.[22,23]

Evaluation of nanoparticle bio-compatibility has been convoluted by a wide breadth of reports which yield sometimes conflicting results over many different experimental conditions. It is the goal of this review to analyze the available information on quantum dot cytotoxicity to determine their applicability as potential antimicrobial agents. While there is data on non-cadmium based quantum dots, they are in the overall minority due to the primary reliance on the cadmium chalcogenides as imaging agents while the field was nascent. Thus, there is not the same breadth of studies which examine comparable and systematic conditions for other nanomaterials. The purposes of this review will be to first use the deep but incoherent literature available on the CdX's to gain better understanding of the effects of quantum dots in living systems, especially their toxicity, and secondly to determine the potential of quantum confined particles as light-stimulated therapeutic interventions.

5.2 Designing Studies

Before commencing a toxicological evaluation of nanomaterials there are several important features without traditional analogue which must be accounted for and controlled. A degree in the wide dispersity in the reported toxicities and effects can likely be attributed to the

inconsistent application of protocols including purification (Section 5.2.1), concentration uncertainty (Section 5.2.2), the use of different assays (Section 5.2.3), and the application of different illumination conditions (Section 5.2.4). In this section to goal is to highlight these aspects of nanoparticle assays which have traditionally suffered from a lack of critical consideration in the available literature.

5.2.1 Quantum Dot Purification

A consideration which is sometimes lacking in the available literature is the purification methods used for preparing QDs for cell culture. No synthesis uses all of the individual components stoichiometrically resulting in excess metal salts or intermediates being left behind. As Cd^{2+} is typically used in excess, this means that there may be a significant number of free ions in solution which inherently have a deleterious effect. While these can be removed from solution using various centrifuge or filtering procedures, it is necessary to maintain sterility to avoid having to use ethanol to directly sanitize the dots. Measurements have shown that ethanol tends to catalyze the aggregation of short ligand aqueous QDs, and has the ability to strip the ligands off and thus decrease stability.

5.2.2 Determining Concentrations

For any kind of toxicological evaluation one must know how much of a given material is present.[24] Quantum dots present a unique challenge in this respect due to the inherent morphological dependence of their properties. The first available method is to use molarity to describe the total number of particles per volume. The main difficulty with this method is that it primarily relies on optical extinction coefficient correlations which have been primarily derived for particles synthesized in organic media to determine the particle concentration. Almost every paper which uses molarity to describe the concentration of CdS, CdSe, or CdTe uses the size-

excitonic peak correlation method,[25] wherein the position of the first absorbance peak is used to determine the diameter of the particle and extinction coefficient, from which the concentration is calculated (Figure 5.1a). This method is strongly dependent on the size distribution and resolution of the first excitonic peak, which presents problems for aqueous samples.

The dispersity of the dots resulting from a water-based synthesis is generally much greater then when made through high temperature organic routes. Due to this size dispersion, the most populous synthesized size will constitute a lower overall fraction of the total dots, and using the absorbance at that peak will tend to underestimate the true concentration. A second confounding effect is the generally greater overlap of the first excitonic transition with higher order absorbing states in the aqueous derived populations, and without sufficient information about the extinction spectrum at lower wavelengths, subtracting out these other peaks to extract the primary transition becomes increasingly subject to error (Figure 5.1b). Using the observed peak without this subtraction through will tend to overestimate the quantum dot concentration, and may not be reproducible between samples or between groups.

A potential solution can be found in correlations for nanomaterials which do not have a clear transition peak. For example, $CuInS_2$ have been compared against the absorbance well above the bandgap transition to calculate concentration, thus both peak identification and broadness will have a diminished contribution to error.[26] However, this assumes that the extinction for all sized particles will be comparable at that wavelength or that particle sizes on either side of the mean exhibit a proportional response, neither of which have been rigorously proven. This type of correlation is still also dependent on the precise knowledge of the mean particle size, which in this case was accomplished using the emission maximum as a reference

(Figure 5.1c). However, emission is even more strongly dependent on the synthetic route due to the large effect defects have on the position and intensity of the spectrum.

An extension of concentration-based measurements recognizes the large proportion of surface atoms, which will have the greatest impact on the possible chemistry. It has been proposed in several reports to use the number of cadmium atoms on the nanoparticle surface (or total exposed atoms in solution) as the metric for comparison.[27–29] This makes the resulting quantification more similar to the characterization of catalytic materials, however with additional sources of uncertainty due to estimation. It is presumed with this method that one can know precisely the surface content of a nanoparticle a priori or with costly characterization which precludes the rapid screening of the material. Quicker methods such as adsorption to determine the number of surface sites[30] is complicated by the need to remove the stabilizing ligands first, the methods of which usually leads to sintering through the formation of aggregates and a change

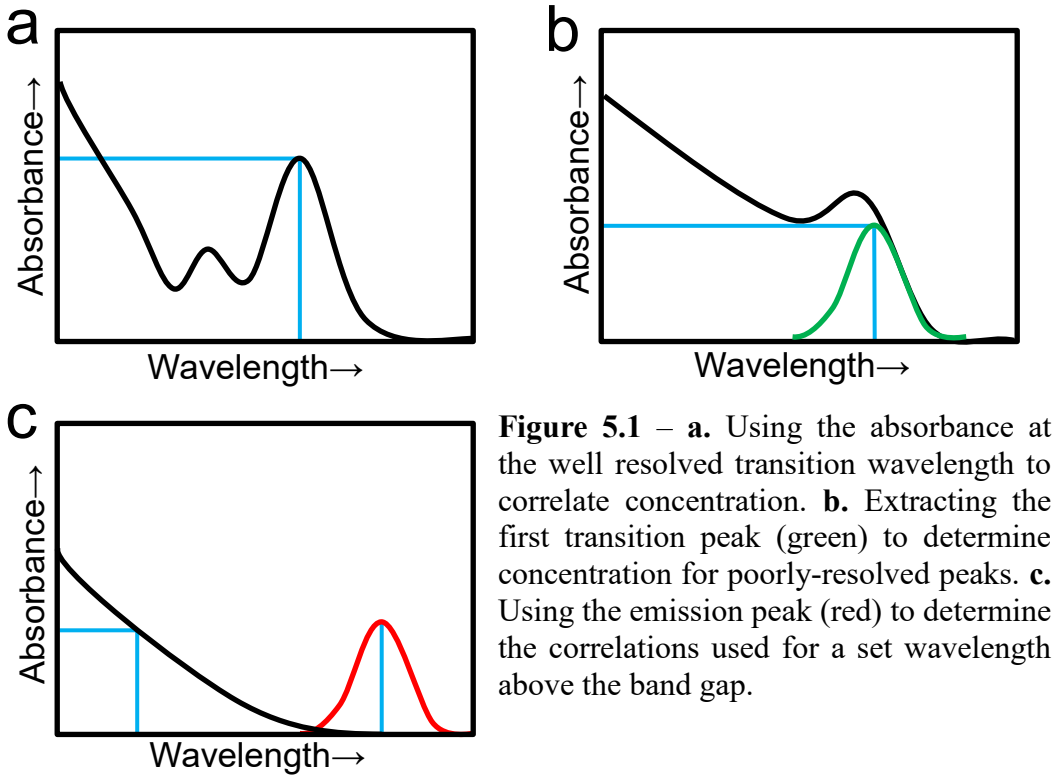

Figure 5.1 – **a.** Using the absorbance at the well resolved transition wavelength to correlate concentration. **b.** Extracting the first transition peak (green) to determine concentration for poorly-resolved peaks. **c.** Using the emission peak (red) to determine the correlations used for a set wavelength above the band gap.

in surface area for nano-dispersed colloids.[31] This metric also does not facilitate comparisons between sizes, which due to quantum confinement can have different properties, and complicates any attempted analysis when studying core-shell structures.

It may seem then that using the mass concentration would be a superior method of comparison. However, while gravimetric analysis is generally easier and can be performed with high accuracy, such analysis makes comparison between different capping ligands difficult. For a 3 nm quantum dot coated with a short chain molecule like 3-mercaptopropionic acid, the ligand contribution to the molecular weight will be less than 5%. The same dot with a polymer coating like a poly(ethylene glycol) derivative will have a substantially greater molar mass due to the greater bulk of stabilizing material, thus making the overall mass a potentially poor predictor of concentration-dependent toxicity. It is also potentially misleading to compare differently-sized dots with this metric given that a one monolayer size difference will significantly impact the molecular weight, and number of particles in solution,[32] while only changing the average particle diameter by 200-300 pm.

In vivo studies of toxicity should report toxicities in units of mol/kg or g/kg of the studies animal's body weight to be in line with the standard reporting of chemical toxicities, either of which can be calculated from the above methods of determining the concentration of the injected solution. It is also important to remember that the isolated or cultured tissue response does not necessarily represent the toxicity and effects of QDs *in vivo*[33–35] given the modes of distribution and sequesteration observed in whole organisms which is discussed later.

5.2.3 Common Methods

While there have been efforts to standardize protocols for establishing QD toxicity[36] the wide range of possible bacteria and eukaryotic cells largely precludes one form of culturing from

becoming applied in all situations. This is of potential importance due to observations that the choice of media will have a large impact on the observed nanoparticle toxicity. For example, minimal media (M9 + 0.4% glucose) yielded a significantly lower toxic threshold than a complex media (LB). This could be an additional confounding factor when trying to correlate different reports in the literature. Efforts *in vivo* are somewhat more defined given the necessary steps of evaluating specific organ toxicity and effects.[37] The following paragraphs provide an introduction to the most commonly observed assays used in determining nanoparticle toxicity.

For bacteria, an efficient method of examining toxicity is to measure the optical density (OD) of individual cultures as a function of time to obtain a growth curve, which can be used to obtain the saturation level, growth rate, and lag time for the comparison of different conditions.[38,39] While Beer's law allows for the correlation of the measured OD to the total concentration of cells, this technique suffers from a high detection limit and does not differentiate between living cells and un-lysed dead cells. Colony forming unit (CFU) assays offer a more quantitative result in this respect. For slower dividing eukaryotic cells live/dead counting assays are typically required to determine toxicity which can be accurately completed using probes which measure the integrity of the cellular membrane like fluorescent DNA-binding propidium iodide, optical staining trypan blue, or lactate dehydrogenase assays (LDH).

Another broadly used class of colorimetric assays measures the overall metabolic activity of the target cells (both prokaryotes and eukaryotes). The most common of these reported is the MTT assay which changes color upon reduction in a living cell via enzymes, the magnitude of which is proportional to the number of viable cells.[40,41] MTT typically refers to the use of the 3-(4,5-dimethylthiazol-2-yl)-2,5-diphenyltetrazolium cation, though the same principle is used for other dyes like resazurin (sodium salt).[42] Non-metabolic dyes have also been used extensively to

determine the presence of certain redox active species which may perturb the redox homeostasis of cell.[43-45]

5.2.4 Light Conditions

Because the cadmium chalcogenides are semiconductors with transitions in the visible band, they are naturally photoresponsive at ambient conditions. This is relevant to living systems as it has been shown that QDs can transfer their photoexcited charges or energy to biological molecules,[46,47] potentially leading to unintended consequences. These interactions can also interfere directly with colorimetric assays, like those using propidium iodide, leading to false or misleading results.[48] Only a minority of the available studies specifically address the effect of illumination (see Section 5.5.2),[48–51] or even describe in the methods how or if this was controlled. Ideally, for studies only concerned with the inherent toxicity of the nanoparticles under study, all cultures would be kept in as low light intensity as possible during treatment. This omission from the literature may be a significant cause for the observed spread in quantum dot toxicity between various reports. Care must also be taken when investigating the light-based toxicity due to the inherent toxicity of UV light[52] and heating effect of infrared light, which is why it is recommended to use light at or near the bandgap only to better control the experiments. As photodegradation of the quantum dots is also possible natively it is important to maintain them in dark conditions as well prior to use (see Section 5.4.3).

5.3 Parameters Affecting Toxicity

Due to the great variation in reported toxicities for the three materials, with unique IC_{50} values numbering in the hundreds,[53] it is necessary to decouple the different parameters which may be having significant effects.[54,55] Due to the complexity of the parameter space affecting quantum dot toxicity,[56] articles on this subject typically relate that comprehensive analysis of the

available data is not feasible, summarized as one author[57] states "At this point, it should be noted that because most toxicity studies were carried out independently, each one under specific experimental conditions, any comparison to identify a particular relationship between a QD structural features and a particular trend in its toxicity is quite impossible." This section is dedicated to dispute this hypothesis and to determine what factors contribute to CdX toxicity and how they can be modulated. First the choice of material is considered (Section 5.3.1) as this will determine their chemical character, then the size (Section 5.3.2) which controls the electronic structure, and finally the choice stabilizing ligand is examined (Section 5.3.3) which will have a large impact on the particle's interaction with a biological environment.

The only notable parameter not discussed in this section is the effect of particle shape on toxicity. While shape has shown some effect on interactions with cells (HeLa),[58] those particles were much larger than the quantum confinement regime of interest to the CdXs. Other materials have shown highly angled structures as more toxic than blunted versions (*E. coli*),[59] and that high aspect ratios decrease uptake.[60] However, there is a lack of data concerning the effect of nanoparticle shape on CdX toxicity specifically, so previous observations for other particles are assumed to hold.

5.3.1 Material

The primary consideration thus far for biological integration of nanomaterials has been their optical properties due to the popularity of imaging studies. Of the four cadmium chalcogenides CdSe and CdTe have been the primary recipients of this attention because their bulk bandgaps (Table 5.1) result in quantum confined emission in the visible spectrum. CdS is largely unused in this respect due to its higher bandgap and broad emission profile due to surface states which can interfere with other emitters. CdO is similar with the caveat that it is almost

entirely un-emissive. While cadmium itself is inherently toxic that does not mean that all of the Cd-based quantum dots are equally toxic. Unfortunately, there are deficiencies in the available literature which complicate the comparison of material-dependent toxicities *ceteris paribus*.

Firstly, there is the natural deviation between studies of even the same material in the same cell type (Table 5.2),[61–64] or even between techniques used in the same study.[65] Thus, all directly compared particles listed in the remainder of the review are limited to those which are reported in the same study to maintain consistency and to draw appropriate qualitative conclusions. For example, problems begin to arise when materials are compared which are different sizes[74] or are capped with different ligands[75] because those properties will have significant impacts on how the particles interact with cells (see Sections 5.3.2 and 5.3.3). So even while it is likely that TiO_2, as an approved food additive,[76] will be similarly less toxic than CdTe on the nanoscale, the different physical characteristics of the utilized particles do not allow a definite conclusion. This limitation precludes the compilation of all possible results in absolutely quantitative terms, with the overall goal being to determine which attributes of the different nanomaterials have a significant impact on their toxicity. An internally consistent study is one which maintains all other aspects of the nanoparticles equal except for the parameter of interest. For example, a study[66] which examined different bulk oxides reports that MnO_2 is significantly less toxic than CdO, while CdO itself is less toxic than similarly micron sized CdS (human renal cells).[67] Though such findings are inherently un-comparable to quantum confined results, such studies can provide information on the inherent or chemical toxicity of the different materials.

Table 5.1

	Bulk Bandgap (eV)	(nm)
CdO[68]	2.2-2.3	540-560
CdS[69]	2.4	520
CdSe[69]	1.7	730
CdTe[69,70]	1.4-1.5	830-890
MnO_2[71]	2.1-2.7	460-590
TiO_2[72]	3.2	390
$CuInS_2$[73]	1.4	830
ZnS[69]	3.6	340
ZnSe[69]	2.6	480
ZnTe[69]	2.2	560

Table 5.2

Material	Cell Type (Assay)	Diameter (nm)	Ligand (Charge)	MSTC or LC_{50}†
CdTe	*E. coli* (OD, 33 h)[61]	3*	MPA (-)	50-100 nM†
	(CFU, 2 h)[62]	3.3*	MSA (-)	120-160 nM†
CdTe	HUVEC (MTT, 24 h)[63]	4	MSA	10-20 μg/mL†
	(MTT, 12 h)[64]	3.7	MPA	>50 μg/mL†
CdO	Rat Liver[66] (MTT, 24 h)	$1\text{-}2\times10^3$	none	0.8 μg/mL†
MnO_2				>250 μg/mL†
CdO	*B. subtilis*[74] (CFU, 7 h)	22	None[80]	15 μg/mL†
CdS		3		8 μg/mL†
CdTe	*C. reinhardtii*[75] (count, 86 h)	3.5-4.5	TGA (-)	5 μg/mL†
TiO_2		22	none	10 μg/mL†
CdS	HEC[77] (trypan blue, 72 h)	4-6	MPA (-)	1-10 μM
ZnS				>10 μM
$CuInS_2$	HeLa[78] (resazurin, 72 h)	2.3ᵏ	OCMC (+/-)	>250 μg/mL
$CuInS_2$/ZnS				>250 μg/mL
CdSe	Fibroblast[28] (attachment, 48 h)	3.3ᵏ	MPA (-)	0.7 μM‡
CdSe/ZnS				6 μM‡
CdSe	Neuroblastoma[79] (MTT, 24 h)	3.5ᵏ	TGA (-)	150 nM
CdSe/ZnS				>300 nM
CdTe	Macrophage[81] (MTT, 24 h)	3ᵏ	CYS (+/-)	25-50 μg/mL†
CdTe/ZnTe				>160 μg/mL†
CdTe	K562[82] (MTT, 24 h)	3.5ᵏ	MPA (-)[83]	0.19 μM†
CdTe/CdS				0.75 μM†
CdTe/CdS/ZnS				>16 μM†
CdTe	HEK[82] (MTT, 24 h)	3.5ᵏ	MPA (-)[83]	0.19 μM†
CdTe/CdS				0.38 μM†
CdTe/CdS/ZnS				>3 μM†
CdTe	PC12[84] (MTT, 24 h)	2.6ᵏ	MPA (-)[85]	4-18 nM†
CdTe/CdS/ZnS				74 nM†

*Size estimated from reported optical data. ‡ Reported concentration of Cd surface atoms. ᵏ Core diameter.

Due to the perceived toxicity of the CdX elements the primary materials objective has been to replace them with non-toxic alternatives. By changing the cation to zinc, for example, the toxicity of the nanoparticles can be greatly reduced.[77] However, due to the lack of correlations for determining the concentration of these other QDs, the issue of comparability arises again when attempting to screen different materials due to the uncertainty of just how many particles are in solution. A potential work-around is the use of core-shell materials, whereby an uncoated

core is tested against one which has a hetero-layer grown on top of it. Provided the shell is limited to several monolayers, the otherwise same characteristics of the particles should allow the direct comparison of different materials. For example, coating copper indium disulfide with zinc sulfide has little effect on the overall toxicity of the particles implying the two materials are of comparable biological compatibility.[78] In contrast, coating cadmium selenide with zinc sulfide greatly attenuates the toxicity of the cores, confirming the previously mentioned observations of the individual homo-particles.[28,79]

Table 5.3

	Hydrodynamic Diameter (nm)		
Core	3.4±0.6	5.0±0.8	10±1
MUA	5±1	7.6±0.9	46±9
MPA	5±1	16±5	60±20
AUT	10±1	122±9	90±20
CA	4±1	15±3	40±20

A note on terminology used herein. The convention of referring to core-shell particles with the form (core material)/(shell material) is used throughout. For example, a CdSe core coated with a layer of ZnS is referred to as CdSe/ZnS. For ternary particles, the same convention is used with the intermediate layer listed between the core and shell, such as CdSe/CdS/ZnS. Core-shell structures will only refer to particles with multiple condensed phases, with all capping molecules and polymers being treated separately as ligands (see Section 5.3.3).

While most reports[86] have used ZnS as a shell due to its inherent stability and proposed type-I alignment with the CdXs,[87] the chemistry and crystal structure of other zinc chalcogenides do not preclude their ordered growth. Both CdTe/ZnTe[81] and CdTe/ZnSe[88] show decreased toxicity relative to the nominal cores, which indicates the presence of a certain anion on the surface will not determine toxicity (see Section 5.4.1). The presence of cadmium on the surface itself is also not a determining factor, as core shells composed of CdTe/CdS also show significantly attenuated toxicity relative to the cores.[82] These observations imply that in addition

to the elemental composition of the nanomaterial of interest the toxicity will also be determined in part due to the electronic structure of the specific semiconducting material (see Section 5.5.2).

It is also possible to tentatively rank the toxicity of the four chalcogenides in order of increasing toxicity as CdO < CdS < CdSe < CdTe given the available data.[89]

If the goal is to completely sequester the optically active core from the intracellular medium it is possible to grow increasingly thick shells.[90,91] A general weakness in the literature on core-shell structures is the actual thickness of the shell, which confounds comparison between studies, and should be viewed as another critical characterization parameter to always be reported. Ternary core-shell-shells offer a potentially more controlled growth as they reduce the lattice strain in each hetero-layer, and do not change the compatibility of the outer layer, in most cases ZnS.[82–85,92,93] It is of course also possible to completely sequester the core in a shell of silica.[94,95]

5.3.2 Size

It is accepted that the toxicological profile for bulk-regime materials is different from nanoparticles,[96] for example CdS lacks oxidative product formation when micron-sized, but generates radicals on the nanoscale.[97] However, when attempting to extract useful conclusions for quantum confined particles the same confounding factors described for materials apply with additional caveats.

The first necessary consideration is the effect of hydrodynamic size, which can obscure the specific effect of changing the core nanocrystal radius (Table 5.3). The core and hydrodynamic diameters are not linearly dependent, preventing the comparison over a wide size range. Additionally, there is the influence of the ligand which has a strong effect on the effective

size of the particles, necessitating the comparison of particles with the same ligands only in this section as well.

Table 5.4

Material	Cell Type (Assay)	Diameter (nm)	Ligand (Charge)	MSTC or LC_{50}†
CdS[97]	CHL (MTT, 24 h)	5-7	none	10 ppm†
		>1,000		10-20 ppm†
CdSe[98]	NHBE (LDH, 24 h)	3	MUA (-)	20 μg/mL
		5		20 μg/mL
		10		>160 μg/mL
		3	MPA (-)	>160 μg/mL
		5		>160 μg/mL
		10		>160 μg/mL
CdTe[65]	*E. coli* (μ-calor.)	2.7*	MPA (-)	74 nM†
		3.1*		77 nM†
		3.8*		88 nM†
CdTe[99]	RPC (MTT, 24 h)	2.3	CA (+)	10-50 μg/mL†
		5.7		100 μg/mL†
CdTe[103]	HEPG2 (MTT, 48 h)	2	TGA (-)	3 μM†
		4		4.8 μM†
		6		19.1 μM†
CdSe/ZnS[κ,100]	Vero (MTT, 24 h)	3	MUA (-)	0.2 mg/mL†
		4-5		0.3 mg/mL†
		6-7		>0.4 mg/mL†
	HeLa (MTT, 24 h)	3		0.1-0.15 mg/mL†
		4-5		0.1-0.15 mg/mL†
		6-7		0.15-0.2 mg/mL†
	PHH (MTT, 24 h)	3		0.15 mg/mL†
		4-5		0.25 mg/mL†
		6-7		0.35 mg/mL†

* Size estimated from reported optical data. κ Sizes based on cited methods and core optical properties.[106]

A second factor which not comes into greater focus is the use of mass concentrations to describe nanoparticle concentrations (Table 5.4). While it may appear from the available data that increasing size decreases toxicity, this does not take into account the total decrease in particle number per mass as the diameter enlarges.[98–100] This has led to the conclusion that the smaller particles are more toxic because a greater fraction of their constituent atoms are on the

surface.[101] While a larger surface area to volume ratio will present more surface area on a per-mass basis, it does not hold true on a per-mole basis due to the nature of geometry requiring a greater absolute number of atoms on the surface of a larger particle.[102] Because the studies which operate using molarity also show a decreasing toxicity with particle size,[65,89,103] it can be concluded that the total surface area is not a primary factor. The only exception being those conjugated to positive ligands,[98] which have a higher overall association with the cell surface (see Section 5.3.3).

It thus remains that smaller CdX particles are in general more toxic than their larger analogues.[104] For CdTe, this is evident as a gradient within the quantum confined region with significant differences likely due in part to the changing electronic structure (see Section 5.5.2). In contrast, CdSe is more consistent during size comparison tests, with minimal differences in toxicity being observed for short ligands.[98] Only slight differences in the magic-size regime have been previously shown to have a considerable effect with CdSe, with 1.1 nm particles being almost twice as toxic as 1.2 nm particles in HeLa cells.[105] The available literature on CdS and CdO is not as robust as CdSe and CdTe, so specific conclusions about their size-dependent changes are currently unavailable.

While the surface-area changes with sizes are not a primary toxicological factor, there is evidence that the total size modulates the particle uptake in this size regime. In general increasing the size of the particles has been observed to decrease the overall uptake (for a detailed discussion see Section 5.5.1), and thus limits the number of particles which can interact with the intracellular medium.[107,108] Additionally, there are size-exclusion effects within mammalian cells which determine their sub-cellular distribution (rat PC12 and murine M9).[99] Smaller particles have shown greater interaction with organelles, like mitochondria (human

mesochymal stem cells),[109] while larger particles appear confined to the cytoplasm with specific size thresholds depending on the specific cell type.[99,108,110] Perhaps most importantly, small (2.1 nm) CdTe have been observed to enter the nuclear region through a histone-regulated transporter while slightly larger (3.4 nm) are excluded (PANC-1[111] and other human cell lines[112]). While the nuclear accumulation is not necessarily toxic, it has the potential of directly damaging the genome through the mechanisms described later (see Section 5.5.3).

Taken together the size-dependent toxicity of a nanoparticle would appear to depend first on the electronic structure, which determines what reactions it is available to conduct, the rate at which it enters a cell, and the specific intra-cellular location it is able to access. All of these factors can in turn be modulated by the capping ligands which will be discussed in the next section.

5.3.3 Ligand

The vast majority of CdX quantum dots are colloidally stabilized by the conjugation of surface-stabilizing ligands, which are generally more reliable than relying on advantageous surface charge, though the wide variety of employed molecules complicates comparisons (Figure 5.2). In order to make them compatible with an aqueous/biological environment they must either be synthesized natively with water-soluble ligands, or undergo various substitutions.[113] The specific ligand choice has been proposed as a primary way of controlling the toxicity due to the observation of varying toxicity when only changing that aspect of the nanoparticle (Table 5.5), including altered gene expression (Vero/WTK1).[114,115]

The ligand property which appears to primarily affect toxicity is the stabilizing charge, with positive ligands having higher toxicity than negatively charged ligands of comparable sizes.[98,116–118] This has been attributed to the attraction between the negatively charged cellular

membrane and the positive ligand, which increases the relative uptake and association, reflected in morphological changes. It was shown for small gold nanoparticles that the surface charge will modulate membrane potential and fluidity, with positive charges having more of an effect.[119] Thus, the observed toxicity is likely not specific to the core material for well-passivated QDs, but due to the inherent interactions and disruptions caused by ligand binding to different portions of the cellular exterior. This is not to say that the ligands desorb to do this, given that the free ligands themselves are orders of magnitude less toxic than the quantum dots, but that the accumulation of QDs on a cell's exterior is an inherently toxic outcome.

Table 5.5

Material	Cell Type (Assay)	Diameter (nm)	Ligand (Charge)	MSTC or LC_{50}[†]
CdSe[98]	NHBE (LDH, 24 h)	3	MUA (-)	20 µg/mL
			MPA (-)	>160 µg/mL
			AUT (+)	0.5 µg/mL
			CA (+)	20 µg/mL
CdSe[116]	NHBE (LDH, 24 h)	2.8-2.9	MPA (-)	>160 µg/mL
			CA (+)	80 µg/mL
CdTe[121]	*E. coli* (OD, 10 h)	2*	MPA (-)	0.8 µM
			NAC (-)	>2.4 µM
			GSH (+/-)	2.4 µM
CdSe/ZnS[123]	NEK (MTT, 24/48 h)	4.6	PEG	>20 / 20 nM
			PEG-N (+)	>20 / 20 nM
			PEG-A (-)	20 / 2 nM
CdSe/ZnS[124]	BCF (MTT, 24/48 h)	4.6	PEG	20 / >20 nM
			PEG-N (+)	20 / 10 nM
			PEG-A (-)	20 / 5 nM
CdSe/CdS/ZnS[128]	BCG (count, 72 h)	5-6	MPA (-)	>2.75 µg/mL
			PEG-PPL (-)	1.38 µg/mL
CdSe/CdS/ZnS[118]	MAM (LDH, 24 h)	5[130]	MPA (-)	500 nM[‡]
			TCL (+)	125 nM[‡]

*Size estimated from reported optical data. [‡]LC_{40}.

The presence of multiple groups possessing charge also exhibit this behavior, including those which contain both positive and negative characteristics. As an illustrative example, particles coated with CYS have been observed to be more toxic than those conjugated with TGA

or DHLA (*Photobacterium phosphoreum*).[120] Using the acetylated form (NAC) however results in overall less toxicity than the smaller molecules, likely due to the electron withdrawing properties of the carbonyl attenuating the acid/base character of the amide nitrogen relative to an amine which yields an overall negative charge at relevant pHs.[121] Another way of counteracting this effect is by adding additional negative charges so that the net effect is a negative ligand, as shown by GSH.

The effect of ligand charge appears to have a diminishing effect with overall size (higher mass/charge), with negligible differences between positive and negatively charged PEG-coated CdSe/ZnS over twenty four hours,[122–124] and reflect the overall lower uptake of this type of coating (human breast cancer[125] and BALB/3T3 fibroblasts[126]) This begins to change over time, with negatively charged PEG exhibiting greater toxicity at forty eight hours likely due to endocytosis and breakdown of the ligand shell (see Sections 4.2 and 5.4).

While increased stearic bulk does generally confer greater compatibility,[121,127] this depends on the presence or absence of largely aliphatic regions of the capping ligands. Even though it possesses the same charge as MPA, MUA induces an order of magnitude higher toxicity, as does AUT relative to CA.[98] This holds even when the particles are fully encapsulated in a lipid micelle structure, which should completely segregate the core from the cellular environment,[128] or with the organic phase ligands pre-exchange inducing higher levels of toxicity than short chain hydrophilic ligands (murine macrophage).[129] This may be due to the ability of these ligands to facilitate entry into lipid bilayers, causing membrane fluidity and permeability as a primary toxic mechanism.

The high-level design rules for ligand choice can thus be summarized as follows. Unless high inherent toxicity is desired, positively charged small molecules and primarily-aliphatic

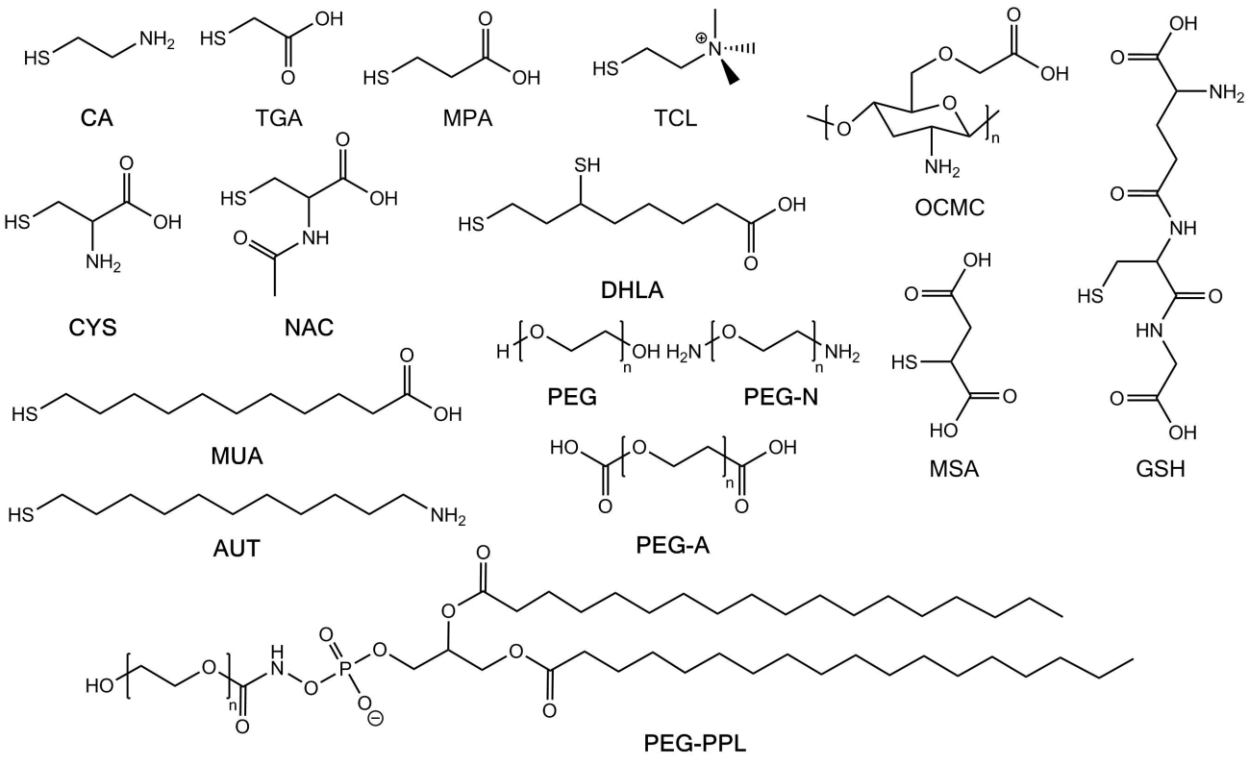

Figure 5.2 – Chemical structures of all discussed ligands. See section 5.9 for a list of all abbreviations.

ligands should be avoided. If it is desirable to segregate the core from the cellular environment completely, bulky ligands which contain multiple negative charges should be used, while polymeric ligands should be used with caution given their lack of QD-QD repulsion. This last caveat relating to aggregation, and other stability considerations of ligands, are further examined in Section 5.4.1.

5.4 Particle Stability

In addition to the toxicity of nanoparticles a primary concern is their time dependent stability both *in vitro* and *in vivo*, which will ultimately determine their useful or efficacious lifespan. The degradation and deactivation of quantum dots will primarily rely on two factors:

the ability of the ligand to provide colloidal stability, and the chemical stability of the core itself. Colloidal stability (Section 5.4.1) is important as it will determine the aggregation and diffusion kinetics of the particles in addition to the exposure of surface facets which can interact with the cellular environment. Chemical stability (Section 5.4.2) dictates the optical and redox properties of the core over time. Included in this section is a discussion of the hypothesis originally put forward to explain quantum dot toxicity, positing that elemental release from the quantum dots during degradation is of paramount importance (Section 5.4.3), which is currently un-supported by the available data.

5.4.1 Colloidal

While the properties described in section 5.3.3 will directly modulate toxicity, there remains other considerations related to stability which are also determined by the ligand choice. When using thiol-cadmium linkages to anchor ligands on the QD surface the pH susceptibility of this bond becomes a primary factor, with dissociation arising from re-protonation of the thiol group at neutral or acidic pHs (equation 5.1). Measurements have shown that at physiological pH the ligand bond occupies a somewhat meta-stable state, being vulnerable to protonation and dissociation.[131] As evidenced by one study, non-thiol based polymers were more stable capping ligands than MUA over 48 h of exposure to relevant media.[32] Desorption of ligands under acidic conditions is supported by the observation that the rate of fluorescence quenching increases, implying greater access to the surface by the quencher.[132] Studies have shown that particles which have been treated with a Cd over-coating step, which have a larger number of potential ligand binding sites, are much more stable than their as-synthesized analogues.

$$^{-}O_2C(CH_2)_2S^{-} + H^{+} \longrightarrow {}^{-}O_2C(CH_2)_2SH \qquad pK_A = 10.8^{133} \qquad (5.1)$$

Exposure to UVC light (254 nm) has also been observed to catalyze the dimerization of the bound thiol ligands via the photogenerated hole as a route of removing surface ligands.[134] Unlike their dark controls, these particles eventually precipitate and the core material becomes oxidized as the ligand oxygen-diffusion barrier is lost, as evidenced by a blue-shifting emission. Similar measurements using visible light (488 and 532 nm) reveal the same breaking of Cd-S bonds and particle aggregation.[135,136] Instability in the presence of chemical oxidizers are also indicative of this mechanism of degradation, especially for hypochlorous acid[137] which is present in certain phagocytes.[138] Thus for studies only interested in the inherent toxicity of nanoparticles measures should be taken to ensure as little light reaches the cultures as possible, and for all studies to limit the exposure of QDs to light before integration with cultures.

There are several controllable characteristics of the non-polymer ligands which can offer greater stability, the first of which being the presence of positively charged groups. CA-coated particles have been observed to increase oxidative stress compared to the same dots with MPA, indicating either more rapid desorption of the ligands or a decreased level of diffusion protection separating the core from the cellular environment.[116] Observations show complete aggregation by 3 and 5 h in light and dark when using CA, compared to 7 and 10 h using MPA. They are also less stable at elevated temperatures, following the same toxicity trend of CYS being less stable than GSH, which is less stable than TGA.[136] To increase stability via ligands it has generally been observed that bulkier ligands are more effective (e.g. MSA compared to TGA) which is likely due to the greater surface protection they offer which inhibits either oxidative species or protons from diffusing.[136,139,140]

It has also been observed that cores with larger diameters are inherently less stable compared to those even a few nanometers smaller.[32,102] This is reflected in terms of pH stability,

with larger dots precipitating at higher pH values.[131] An explanation of this observation involves two potential contributions. The first is the presence on every nanoparticle of anion rich facets which have a lower overall ligand density, which are greater in area on larger diameter particles. Fewer ligands would then allow more favorable proton trajectories directly to the thiol group to more rapidly desorb ligands from the surface. The second effect would be the increased mass to charge ratio for larger dots, and the greater destabilization with the loss of a comparative fraction of ligands.

An additional consideration is the number of binding sites joining the ligand the QD surface. Bi-dentate ligands like DHLA are generally more stable than those of the same size and character with one thiol.[102] This would be a greater factor for non-photoactive particles for improving the re-protonation kinetics, while the inherent close proximity would aid the catalytic oxidation of the adjacent thiols. A final factor influencing the aggregation and precipitation of all particles is the ionic strength of the medium, with higher salinity decreasing stability.[117,141–143]

5.4.2 Chemical

Both CdSe[144] and CdTe have been observed to undergo degradation in aqueous environments, which is evidenced by changes in the optical properties of the materials.[145] This is usually observed as a blue-shifting of the core emission over time, which due to quantum confinement effects indicates a shrinking overall diameter. This has been traditionally interpreted as the direct release of material from the core (see Section 4.3 for toxicological evaluation of this hypothesis). From a physical perspective, the likelihood of direct leaching or dissociation is quite small given that the Ksp values of these materials are vanishingly small (Table 6), thus indicating more complex pathways.

A feature in the optical changes of CdTe which is sometimes not reported is the presence of an initial red-shift in the emission early in the degradation accompanied by a general decrease in quantum yield. While this may be interpreted as energy transfer in bulk aggregates, the lack of significant scatter until well into the blue-shifting regions makes this unlikely. This is instead indicative of the oxidation of the tellurium facet, reflected in XPS measurements as the formation of TeO_2.[49] Similarly the initial CdSe oxidation occurs on the Se-rich facets forming SeO_2.[150] The solubility of bulk CdTe strongly depends on the concentration of dissolved oxygen, and only weakly on pH, indicating O_2 is the primary oxidizing agent in solution.[151]

Table 5.6

	pK_{sp}
CdS	33[146]
CdS[A]	16[146]
CdSe	35[131]
CdTe	36[147]
ZnO	17[148]
ZnS	25-30[146]
ZnS[A]	8-12[146]
ZnSe	31[149]
ZnTe	34[146]

[A]: in an acidic environment

These observations have then lead to the assumption that the oxidized form of the core material is what is leaching. However, tellurium dioxide has a generally low solubility in aqueous environments,[152] with a saturation concentration of 150 μM at buffered pH 7.[153] Selenium dioxide would be the more unstable of the two chalcogenides given its ability to react with water to form selenious acid at ambient conditions, which is itself quite soluble,[154] but measurements show that overall CdSe particles are more stable than CdTe.[89] While being proposed as a barrier against further dissolution,[155] CdO has been previously reported to be the most soluble chalcogenide form (5.4 μM) due to its ability to hydrolyze to $Cd(OH)_2$ and its by-products (eq. 5.2-4).[146] However, the subsequent solubility of this mineral is still too low outside of basic environments to yield the proposed levels of leaching.

$$Cd(OH)_{2(s)} \longrightarrow Cd^{2+}_{(aq)} + 2OH^-_{(aq)} \qquad K = 7\times10^{-15}\ M^3 \qquad (5.2)$$

$$Cd(OH)_{2(s)} \longrightarrow Cd(OH)_{2(aq)} \qquad K = 3\times10^{-7}\ M \qquad (5.3)$$

$$Cd(OH)_{2(s)} + 2OH^-_{(aq)} \longrightarrow Cd(OH)_{4(aq)} \qquad K = 2\times10^{-6}\ M^{-1} \qquad (5.4)$$

An observation though to support chemically assisted leaching via phosphate complexes in biologically relevant media (PBS) is the decreased stability of the particles under those conditions.[116] From a thermodynamic perspective, the formation of cadmium hydrogen phosphate at physiological pH is favored (eq. 5.5-6), though this is based upon the presence of liberated Cd^{2+} already being available. The high temperatures (~300°C) required during organic syntheses to form phosphate complexes from CdO also would seem to preclude a direct leaching effect near ambient.[156]

$$Cd^{2+}_{(aq)} + HPO^{2-}_{4(aq)} \longrightarrow CdHPO_{4(aq)} \qquad K = 479\ M^{-1} \qquad (5.5)$$

$$Cd^{2+}_{(aq)} + H_2PO^{-}_{4(aq)} \longrightarrow CdHPO_{4(aq)} + H^{+}_{(aq)} \qquad K = 10^{-4} \qquad (5.6)$$

A likelier mechanism involves the re-protonation of the capping ligands, which is thermodynamically favorable at neutral pH, which then would allow the surface to be more susceptible to acid attack as the other chalcogenides are generally more soluble by acid (Table 5.6).[157] This would seem to be borne out under acidic conditions, where higher levels of leaching have been shown.[116] However, there are negligible differences in the reported leaching of MPA-coated particles at neutral and acidic conditions, which should be the most susceptible, compared to the longer-chain ligands who's leaching is reportedly significantly increased at lower pH. Thus, this is either emblematic of a ligand-based effect again or is an artifact of incomplete QD precipitation during the preparation of the samples for elemental analysis.

The rate of particle degradation can be controlled with several factors. The first is the observation that smaller particles generally degrade slower than larger ones,[145] which is an extension of the colloidal instability presented in Section 5.4.1. An increase rate of ligand desorption opens up greater areas of the particle surface for oxidative attack. Controlling for the incident light intensity also can improve the lifetime of particles due to the attenuated formation of more reactive species (see Section 5.5.2).

To protect the emissive core adding a shell layer of a more resistant material like ZnS has been shown to greatly attenuate the rate of oxidation over weeks *in vitro*,[85,158,159] including under intense UV stimulation.[92] The larger anions are increasingly unstable when bound to cadmium, thus this treatment is therefore most useful for CdTe[160] which can increase the stability by an order of magnitude.[161]

The shell provides increased stability due to both the greater relative chemical stability and the imposition of a diffusion barrier for further interaction with the core, as evidenced by the use of pre-oxidized shells also conferring higher stability.[162] This last observation may indicate that the oxidized surface species do not dissociate and further oxidation is due to the slow diffusion of oxygen into the particle volume.

Overall, the precise mechanism and kinetics of the chemical degradation of these QDs is not well understood and characterized. While direct dissolution is unlikely, whether the oxidized surface species dissociate or additional oxygen has to diffuse though them is not satisfactorily settled based on the available literature. Clarifying studies would be of assistance in designing particles which degrade as slowly as possible, which is useful for QD therapeutics as it has been observed that particle degradation allows previously treated cultures to recover.[48]

5.4.3 Toxicity Compared to Salts

A prominent hypothesis for the source of CdX toxicity points to cadmium or other heavy element leaching due to time-dependent oxidation or dissolution, which is one of the reasons for the wide interest in core-shell structures.[67,163–166] This is a logical concern as cadmium is widely recognized as a toxin, and whose release into the environment has caused wide-spread human health problems in the past.[167] However, the vast majority of studies both *in vivo* and *in vitro* which use divalent cadmium as a control observe dissimilar concentration-dependent responses

between the quantum dots and free ion, such that salts are orders of magnitude less toxic than the particles.[52,98,121,127,142,165,168–175] Controlling for free ligands, soluble selenium ions, and aqueous tellurium actions shows similar behavior.[28,48,142] Only a minority of reports[176] have shown salts as more toxic than a tested quantum dot, which may be reflective of ligand stability,[177] or the use of a more highly oxidized form of tellurium ($NaTeO_3$) than what is typically stable in aqueous media.[142]

Several early investigations pointed to the increased toxicity of partially oxidized particles as evidence that toxicity is dependent on the leaching of chemically degraded surface species. This was shown for both CdTe, in the form of oxygen-free synthetic conditions leading to lower toxicity,[178] and for CdSe particles which were purposefully exposed to a combined oxidizing environment of air and UV stimulation.[164] The observed blue-shifting optical properties were then taken as evidence of core leaching. But this does not take into account that increased oxygen on the surface would prevent stabilizing ligands from binding efficiently to the cationic facets, which allows greater degrees of aggregation, itself a potentially toxic outcome,[179] and exposes greater surface areas to the cellular environment for QD-mediated chemical reactions.[49]

Several caveats of the presented controls counter the above justification (in addition to the potentially low solubility of oxides as previously discussed, and support the observation of differential toxicity between particles, their degradation products, and free salts. First, when matching the concentration of introduced $CdCl_2$ to the total amount of Cd^{2+} being added by the particles, rather than QD concentration, the greater QD toxicity was again observed. The mechanism of toxicity is also clearly different between the two conditions. Surface-charge stabilized particles, which should be the most susceptible to leaching due to the lack of ligands,

induce significant morphological changes while Cd^{2+} salts do not.[168] Similarly in one study using *Chlamydomonas reinhardtii* different transcriptome level responses were observed with QDs compared to Cd^{2+} salts, indicating different perturbations of the cellular homeostasis.[180] Specific intracellular effects have also been observed, such as the increased actin content of cells exposed to CdSe/ZnS particles, while the addition of Cd^{2+} led to de-polymerization.[181] In perhaps the clearest demonstration, it was shown that a strain of *Pseudomonas aeruginosa*, which was specifically resistant to Cd^{2+} (LC_{50} of $CdCl_2$ greater than 5 mM), was susceptible to un-shelled CdTe quantum dots, the least stable of the CdXs, at nanomolar concentrations.[48]

The claim of salt toxicity also does not factor in the various methods of cells have of removing Cd^{2+} and tellurium oxides.[182] Certain organisms, including various fungi,[183] yeasts,[184] and bacteria,[185] have been reported to take cationic cadmium and sequester it as CdS nanocrystals, implying an innate tolerance to the materials.[185,186] This has also been found to occur for CdTe, CdSe, the lead chalcogenides,[187] and even mercuric telluride.[188] Unlike in laboratory synthesis, these particles form due to interactions involving peptide-cation complexes that nucleate into nanoparticles.[184] In addition to dealing with intracellular stress, some organisms can pre-emptively sequester toxic metals with the release of extra-cellular enzymes.[189,190] The particles formed in this way are also more inherently bio-compatible due to protein coatings which effectively exclude the core from the cellular environment.[191] Similar behavior has also been observed for chalcogen oxides which would form from leaching.[192] Combining the observation of the eventual effluxing of these auto-synthesized particles and the already in-built pathways for removing toxic ions it is clear that exposed cells have the ability to respond to perturbations induced by salts,[117,193–195] though the eventual accumulation of Cd^{2+} in the kidneys via metallothionein proteins is of potential concern in humans.[196]

Regardless of the precise mechanism of cellular response to Cd^{2+}, the lack of correlation of free cadmium salts with the observed toxicity and morphological changes observed in cells exposed to QDs indicates that leaching is not a prime biological effect. This is reflected in different transcriptome changes reflecting differing mechanisms of sequestering the stress.[171,175] A different hypothesis put forward is that the overall toxicity of cadmium chalcogenides is due to the formation of reactive oxygen species (ROS), which is discussed in Section 5.5.1.

5.5 Therapeutic Considerations

While the bulk of the literature on quantum dots in living systems is concerned with imaging and potential toxicity, some researchers have hypothesized the potential benefits of using QD toxicity as a therapeutic tool[62,197,198] beyond metal nanoparticles.[199,200] This antimicrobial intervention would utilize the redox properties of the semiconductor materials to directly induce oxidative stress upon the application of light as a triggering mechanism (Section 5.5.1). Some mechanisms that attenuate this form of stress (Section 5.5.2) result from the ability of aerobic cells to prevent oxidative damage to DNA (Section 5.5.3) and membranes (Section 5.5.4). Membranes themselves may serve as significant barriers to general applicability given the differential toxicity between gram negative and positive bacterial strains (Section 5.5.5), which can be countered by the inclusion of additional small molecule antibiotics in combination therapies (Section 5.5.6).

5.5.1 Species Formed

The first evidence that particles are generating a potentially phototoxic response is that photobleaching occurs when they are exposed to light,[112] which can be accomplished even with visible wavelengths.[136,201] Such bleaching must be the result of oxidation of the particles in some form, which indicates that there are highly-reactive chemical species formed upon stimulation.

Additionally, those few studies which do control for light exposure report some toxic effects only under light stimulation,[52] or significantly enhanced toxicity upon stimulation (Table 5.7).[49] Both green (2.6 nm) and red (3.4 nm) emitting CdTe have been observed to decrease *E. coli* viability when exposed to 365 nm light, which was significantly different than UV only controls.[112] The observation of phototoxicity in sa range of different organisms, from the bacterium *E. coli* to seeds of wheat (*Triticum aestivum*)[202] imply a generally applicable mechanism of action.

Table 5.7

Material	Cell Type (Assay)	Diameter (nm)	Ligand (Charge)	MSTC
CdTe - Dark	*E. coli*[49] (OD)	3-4	TGA (-)	10 nM
CdTe - Light				1 nM

To gain a qualitative understanding of the type of reactive species formed by QDs upon light stimulation, different redox active dyes have been used,[90,203,204] most commonly dichloro-dihydrofluorescein-diacetate (DCFH-DA).[64,79,205,206] Upon exposure to various radicals and other oxidizing species, DCFH-DA is de-protected and oxidized to a fluorescent form of fluorescein. This is observed primarily during light exposure, which indicates the light-activated mechanism involves electron transfer from a photoexcited QD to other targets to form reactive oxygen-based species.[206] For more in depth information, electron paramagnetic resonance (EPR) measurements have typically been employed for both identification and quantification of the resulting radicals.

Briefly, EPR measures the spin transitions of un-paired electrons in an analogous way as NMR, but using microwave radiation and a sweeping magnetic field to obtain a spectrum.[207] The lock-in signal is typically left as the first derivative of the absorbance to facilitate the identification of characteristic coupling features for specific species. The lifetimes of these

species, which range on the order of micro seconds,[208] are indicative of their high reactivity in a biological environment in addition to requiring the use of trap molecules like DMPO[209,210] to make light-generated radicals[211] visible on EPR measurement timescales.

Beginning with CdS, EPR measurements reveal the significant production of both superoxide ($^{\bullet}O_2^-$) and hydroxyl ($^{\bullet}OH$) radicals, both derived from dissolved oxygen (eq. 5.7).[212,213] Superoxide itself is known to engage in a chain of reactions in aqueous environments, from forming the uncharged perhydroxyl radical which can more easily penetrate membranes (eq. 5.8), to ultimately form hydroxyl radicals at even neutral pHs through Fenton chemistry (eq. 5.9-11).[214] This last step likely means that the source of the hydroxyl radicals is partly the decomposition of initially formed superoxide, in addition to proposed direct oxidation of water. It should be noted that even highly stable CdS is susceptible to hydroxyl radical attack,[215] suggesting auto-photooxidation is a likely contributor to the observed chemical instability of CdTe in aqueous media under light stimulation[216] via tellurium oxidation.[217] Of the two radical species, it has been proposed that superoxide on its own is overall less toxic than hydroxyl radicals,[218] implying that the formation of the latter should be maximized in phototherapeutic schemes.

$$O_2 \longrightarrow {}^{\bullet}O_2^- \qquad \text{-0.15 V}^{212} \qquad (5.7)$$

$$^{\bullet}O_2^- + H^+ \longrightarrow HO_2^{\bullet} \qquad (5.8)$$

$$2\,^{\bullet}O_2^- + 2H^+ \longrightarrow H_2O_2 + O_2 \qquad (5.9)$$

$$^{\bullet}O_2^- + 2H^+ \longrightarrow H_2O_2 \qquad (5.10)$$

$$H_2O_2 \xrightarrow{M^{2+}} {}^{\bullet}OH + OH^- \qquad (5.11)$$

Unlike CdS, CdSe only weakly produces hydroxyl radicals visible by EPR,[212] which correlates with the much-reduced levels of observed phototoxicity.[120] This has been attributed to the difference in reduction potential between the CdS and CdSe particles preventing charge transfer to oxygen. However, the conduction bands, which determine the reduction potential, are

quite similar between the two both in bulk[87] and the quantum confined regimes,[219] the valence bands (oxidation potentials) are more offset. The low levels of radical formation in EPR studies (low signal to noise) may have obscured superoxide formation which has been supported using colorimetric assays,[57] implying the position of the oxidation potential must also align with a target so that a complete redox cycle can form. The high potential required to directly oxidize water to form hydroxyl radicals largely precludes direct formation by these nanomaterials (eq. 5.12). Even though CdSe is largely incapable of directly producing radicals, when coupled to an appropriate organic sensitizer it has been observed to indirectly produce excited singlet oxygen ($^1O_2$) through resonance energy transfer (eq. 5.13),[220,221] even through a ZnS shell.[222]

$$H_2O \longrightarrow {}^{\bullet}OH + H^+ \qquad 2.31\ V^{223} \qquad (5.12)$$

$$^3O_2 \longrightarrow {}^1O_2 \qquad 1.95\ V^{224} \qquad (5.13)$$

CdTe in contrast readily transfers its photoexcited electron to from superoxide, which can then go on to form hydroxyl radicals.[48,225] Due to the much lower oxidation potential of CdTe the only apparent source of ·OH is the decomposition of superoxide, which measurements confirmed using superoxide dismutase to attenuate both radical signals. There is certainly a quantum confinement effect for the production of superoxide, as measurements show an attenuation going from green emitting particles to red when normalized by concentration which squares with previous observations.[98] Thus, as the band gap changes and reduction potential shifts it is no longer in the proper range for transferring an electron to dissolved oxygen.

In addition to superoxide, one report suggested singlet oxygen formation as measured by transient florescence spectroscopy.[127] However, the lack of signal in EPR studies indicate that if formed it is only a very minor photogenerated product.[48] Other minor products observed by EPR include the decrease in radical-susceptible TEMPO signal by CdSe/ZnS QDs, but identification

of the causal species was not provided and whatever the source it did not appear to have a large impact on the tested cells.[226]

5.5.2 Attenuating Toxicity

Several methods of attenuating the impact of redox species have been demonstrated in living organisms. Depending on the thickness of certain core-shell QD materials the production of radicals can be strongly attenuated. While this can dampen observed morphological changes in bacteria,[107] shells that are too thin still allow intracellular damage.[57,212,227,228] This implies that the chemically inert shell acts as a tunneling barrier for moving photoexcited electrons to the relevant chemical species,[79,229] and that studies which initially attributed the shell acting as a leaching barrier were actually observing the effect of decreasing the core electronic interaction with the cellular chemistry. Core-shells can change electronic structure of the dots, as evidenced by the previously mentioned red-shifts and quenching due to trap formation of cationic binding to chalcogen-rich facets,[136] which may move the redox potentials out of the necessary range.

The addition of anti-oxidants like n-acetyl cysteine (NAC) also has been shown to improve cellular viability upon QD addition.[64,98,230,231] Adding anti-oxidants does not always restore viability, and depends on the specific molecules chosen, especially when they are added concurrently with QDs instead of during a pre-treatment. There also appears to be a ligand effect whereby shorter ligands lead to lower oxidative signal,[98] which is likely due to the aliphatic nature and higher mass to charge ratio of longer ligands.

The organism itself has a multitude of different mechanisms to deal with this type of stress, the usurpation of which implies the high potency of QDs for overwhelming them. All aerobic organisms possess pathways that counter the formation of the radical species discussed, such as the superoxide dismutase enzyme which has been shown *ex vivo* to strongly attenuate the

radical signal produced by QDs. Curiously, the up-redulation of redox genes is not always observed *in vivo* for higher organisms (*Hydra vulgaris*).[173]

5.5.3 Genotoxicity

The ability to produce oxidative species has naturally raised concerns about nanomaterials as DNA-damaging and developmental toxins,[232] which is legitimized by the ability of small particles to enter the nuclear space.[111,112] In *ex vivo* experiments, DNA damage has been shown for both CdSe[233] and CdTe[234] in a light-dependent manner, indicating the low-level of production by CdSe is still sufficient to cause some damage, though the use of QD-degrading UV light complicates the conclusion. A study using a green laser to excite CdSe/ZnS did report damage to both purine and pyrimidine bases in addition to strand breaking attributed to oxidative damage.[235] Similarly, DNA damage has been reported below the LD_{50} concentrations of small CdS (*Danio rerio*),[236] CdSe (bronchial epithelial cells),[116] and CdTe in living cells (murine[237] and human breast cancer[238]) and *in vivo* (*Elliption complanata*),[239] indicative of genotoxicity as a potentially potent mechanism of action. Interestingly, CdSe doped with 1% Co^{2+} was significantly more genotoxic *in vivo*, which may reflect a change in electronic structure.[240]

Specific interactions with DNA have been proposed to center on the prevalence of hydroxyl radicals generated in solution.[235] All four of the DNA nucleobases are susceptible to attack by these radicals, which includes carbon-centered radical formation from proton abstraction, adduct formation to the ring structure through reactions with double bonds, and resulting ring breaking and strand cleavage (see cited reviews for in-depth reaction pathways).[241,242] Damage from superoxide radicals has been reported to occur from attack of the deoxyribose sugar leading to scission, though its greater impact lies in its ability to form

hydroxyl radicals. Any singlet oxygen formed has selectivity for forming adducts with guanine, with some implication in strand breaking.[243]

5.5.4 Uptake and Membrane Damage

In order for a nanotherapeutic to be effective at targeting DNA it will have to cross a cell membrane in order to reach its proper targets given the typical ns-μs lifetimes of radical species. For mammalian cells, this is relatively straight forward, as it has been shown that eukaryotes will readily uptake QDs via endocytotic mechanisms.[60,244–246] Some studies have even shown that certain cells will actively uptake quantum dots, with the specific intracellular distributions depending on cell type.[109,201,247,248] It has been noted in HeLa cells that, in addition to endocytosis, there is a slow net exocytosis of about 50% of the internalized dots at equilibrium for zwitterionic CdSe/ZnS, implying non-permanent accumulation in certain cells.[249]

Ligands have an effect on interactions, both in terms of disrupting endosomes to enter the cytoplasm (HeLa),[250] and with previously described charge dependencies. Positively charged ligands potentially complicate endocytosis due to exterior membrane adhesion and aggregation (*E. coli*).[61,65,121] Such association is inherently damaging, disrupting membrane fluidity and permeability which is reflected in the deformation of the cell shape. This has also been shown for QDs that have entered cells and become associated with mitochondria, additionally causing depolarization and permeability (neuroblastoma,[79] HepG2,[251] rat liver,[252,253] murine renal adenocarcinoma[254]). While membrane association may lead directly to cell lysis at high concentrations (various bacteria),[49] is also a potential vector for QDs entering the cells. This is especially true for prokaryotes that in only rare instances possess endocytotic processes[255] and instead rely on either sub 10 nm pores or membrane damage to allow QD entry.[169]

It has been proposed that the redox-active species formed by QDs contribute to membrane damage as observed in *S. aureus* and *E. coli*.[256] This is reflected is several instances where lipid peroxidation was observed after QDs were introduced *in vivo* to freshwater mussels (*Elliption complanata*),[239] and in cultures of *E. coli* [62] and human neuroblastoma cells.[257] Like the damage to DNA, lipid peroxidation stems from the photogeneration of hydroxyl radicals that abstract protons from CH_2 groups adjacent to the double bonds of unsaturated fatty acids, which ultimately forms disrupting peroxide groups on the damaged molecule.[258] Though unlike DNA damage, this begins a self-propagating chain reaction which increases the effective reactivity of each hydroxyl radical several fold, which can explain how CdSe can have a disproportionate effect. Both the damage to the cellular membrane and the toxicity of the end products imply a generally broad toxicity.

5.5.5 Gram-Positive Versus Gram-Negative Bacteria

An additional caveat when designing nanoparticles to treat bacterial infections is the apparent difference in susceptibility between gram positive and gram negative strains to light-induced oxidative stress (Table 5.8).[48,259,260] While more quantum dots have been observed to be physically associated with positive strains, inducing greater levels of membrane de-polarization, gram-negative strains are typically an order of magnitude more susceptible to CdTe. It was also noted that CdTe can engage in energy transfer generally with the gram-positive strains but not the negative, which indicates different mechanisms of interaction which are dependent on the cell or membrane type. Measurements of photocatalytic TiO_2 also show a lower effect on gram-positive bacteria compared to gram-negative,[261] which may either represent a greater resistance to hydroxyl radical stress or more robust pathways for excluding quantum dots from the intracellular environment.

Table 5.8

Material (Assay)	Cell Type (Gram +/-)	Diameter (nm)	Ligand (Charge)	LC_{50}
CdTe[48] (OD)	*E. coli* (-)	3.6	MPA (-)	40 nM
	P. aeruginosa (-)			140 nM
	S. aureus (+)			2.1 μM
	B. subtilis (+)			3.0 μM

5.5.6 Combination Therapies

While sometimes considered as drug delivery vehicles,[262,263] few studies have considered using the optical properties of QDs in concert with molecular medicines. For example, while CdSe is incapable of delivering a phototherapeutic effect on its own, it was shown in one study that cinnamates can be photolysed to coumarin, allowing directed and selective application.[264] There was a pronounced benefit from the QDs insofar as visible light could be used to for the activation instead of UV.

In one study, 3 nm thioglycolic acid-coated CdTe QDs were combined with the antibiotic rocephin.[205] While the minimum inhibitory concentrations (MICs) for the rocephin and QDs were 20 and 1,200 μg/mL in *E. coli* separately, a new combinatorial MIC at 0.5 and 120 μg/mL when rocephin were administered together. Performing a combinatorial analysis showed that the two were acting in a synergistic manner to kill the bacteria. It was postulated that the two work in concert, where the rocephin damages the outer bacterial membrane to allow the QDs inside, which then induce intracellular oxidative stress.

5.6 Effect of Higher Organisms

If any nanoparticles are to be considered as antimicrobial agents they must, by definition, be less toxic to the host than the target bacteria. While experiments with co-cultures of bacteria and human cells could serve as a preliminary indicator of this ability, only a minimal number of

reports have executed such experiments.[89] This then necessitates examining the different impacts of nanomaterials on various cell types and organs (Section 5.6.1) to which particles may be distributed *in vivo* (Section 5.6.2). However, because *in vitro* toxicity may not be an accurate prediction of oxidative toxicity,[265] studies published thus far on the impact of QDs on whole organisms are also considered (Section 5.6.3), something which is also inherently required for regulatory approval.[266]

5.6.1 Effects on Cells and Organs

In this section, case studies are presented which examine the effect of quantum dots on specific cell types, including those that would be primarily contacted during acute exposure. Tissue specific responses are emphasized over the previously discussed mechanisms of toxicity. This section is not intended to be a comprehensive assessment of all possible outcomes, but illustrative of the considerations required when considering the systemic introduction of quantum dots.

5.6.1.1 Pulmonary

The effect of inhaled nanoparticles has traditionally received a higher level of attention due to the presence of carbon-based materials in combustion exhaust,[267] with some attention being given specifically to quantum dots.[268] *In vitro*, the particles exhibit the same kind of cell damage as described previously, which *in vivo* is reflected as tissue damage and inflammation, and in some instances the formation of temporary granulomas (murine).[237,269] There is also an issue of lung clearance with some reports showing very long half-lives (rat) [270] depending on the coating, with negatively charged particles being removed at greater rates than positively charged ones (rat).[271]

5.6.1.2 Reproductive and Developmental

For those particles that do escape their initial capture by an organ or tissue there are concerns that they may then go on to do systemic damage, especially causing reproductive impairment. Exposure to QDs has been shown to reduce the regenerative and reproductive capability of various aquatic organisms (*Hydra vulgaris*,[173] *Lymnaea luteola*[272]), including direct toxicity in embryonic zebrafish (*Danio rerio*).[174] Concerns about developmental toxicity is not limited to aquatic life as it has been shown that Cd-containing QDs can cross the murine placental barrier in a size-dependent manner.[273] One study tracked the inhalation of ligand-less aerosolized CdO, which proceeded to leave the lungs and cause damage to fetal mice *in utero*.[274] Developmental changes were also detected in murine models *in vitro* as changes in estrogen levels, dependent on the CdTe particle size, with an *in vivo* effect of increased uterine size.[275] Trans-generational damage has also been documented in *Caenorhabditis elegans* that ingested CdTe, which was attenuated with a ZnS coating.[276]

5.6.1.3 Dermal

One concern for topical treatments of superficial infections would be skin penetration and subsequent systemic exposure. Experiments with poly(ethylene glycol)-coated (PEG) CdSe/ZnS show minor penetration of the QDs through the human epidermis over 24 h.[277] In contrast, other studies concluded that significant skin penetration was possible (porcine),[278] and that QDs can penetrate the skin *in vivo* and accumulate in target organs (murine).[279] It was also shown that while intact skin greatly attenuates passage, damaged skin (physical and UV) is much more permeable to QDs (rat,[280] murine[281]), which is important for potential superficial exposure. As these studies focus on different animal tissues, further work needs be done to study the

penetrative power of CdX particles in human skin for a true assessment of penetration, and with more consistency over the capping structure and ligands.[282,283]

5.6.1.4 Neural

While the blood brain barrier typically screens out most circulating foreign bodies, the observed preferential uptake of nanomaterials may lead to some distribution to this organ. *In vitro* examinations of neurons exposed to CdSe and CdTe indicate a disruption of calcium homeostasis through increased cytoplasmic concentrations, potentially via interference with cation channels (rat hippocampal).[231,284] In *C. elegans* it was noted that exposure to CdTe led to behavioral changes, which was attributed to the influence of the particles on the nervous system, likely due to oxidative damage as evidenced by attenuation via ZnS shells and altered neurotransmitter levels.[160,285,286] A murine *in vivo* study showed that both CdSe and CdSe/ZnS altered synaptic transmission and plasticity, which was attributed to the brain's inherent sensitivity to oxidative species.[287] Fortunately, it does not appear that QDs will preferentially distribute or accumulate in the mammalian brain unless administered there deliberately (see Section 5.6.2).

5.6.1.5 Immunological

A systematic introduction of nanomaterials will invariably put them in contact with an organism's systems for clearing foreign bodies.[288] *In vitro* damage to immune cells by CdTe has been shown to impair the ability of a co-culture of murine macrophages and epithelial cells to resist a *P. aeruginosa* infection.[289] However, has been noted in an *in vivo* murine study that the presence of CdTe leads to an increase in white blood cell count which may indicate an overall stimulation of the immune system.[290]

5.6.1.6 Osteogenic

An *in vitro* study was conducted testing the effect of CdSe/ZnS particles on human bone marrow mesenchymal stem cells, though ostensibly for imaging applications.[291] While no specific morphological or proliferative changes were observed at the tested concentrations, there was a significant decrease in osteogenic differentiation and mineralization. It was suggested that this is due to signaling interruption via inhibited osteogenic markers. This may have implications for those treated with nanoparticles whose growth plates are still active.

5.6.1.7 Corneal

Though safety glasses are ideally worn in laboratory and manufacturing settings, a primary route of accidental nanomaterial exposure is through the eye. As the primary route of mitigating such exposure is though access to proper eye-wash stations the penetration kinetics of the cornea are of potential importance. One *in vitro* study measured the distribution of CdSe/ZnS in both intact and injured bovine corneas, and showed a penetration depth of 20 μm over 80 min for intact tissue.[124] However, a damaged epithelium allows much more rapid penetration into the stroma. Like the lungs, there is also a notably slow clearance of directly injected QDs *in vivo* (murine). Given the long residence lifetime and general irreparability of the optic system, QDs may not be candidates for treating conjunctivitis.

6.2 *In Vivo* Distributions

One of the paramount concerns of using intravenous QD therapeutics is the kinetics of organ localization. In BALB/c mice it has been shown that most injected QDs are cleared from circulation within 1-3 h, accumulating in the liver, spleen, bone marrow, kidneys,[292] and lymph nodes[293] to varying degrees depending on exact ligand.[294] The heart and lungs show some accumulation, but to a lesser degree, with minimal presence in the brain which indicates the

integrity of the blood brain barrier to nanomaterials.[176,295] Typically, particles are ultimately located in the spleen and liver due to processing by macrophages.[296]

It is interesting to note that there is a size-dependent distribution, with smaller particles accumulating in the kidney, while larger diameters are found in the spleen. A common feature *in vivo* is the rapid clearance from circulation with no detectable systemic clearance after many days (*in vitro* included).[124,297–300] Blood clearance also appears to strongly depend on the stabilizing charge of the nanoparticles, with neutral particles having the longest half-lives and positively charged the shortest.[301] Efficient excretion of applied dots also appears to be size dependent, with small hydrodynamic radius particles (<5.5 nm) being removed more effectively than larger ones (rat).[302] Similarly, positively charged particles have been shown to cleared much more rapidly than negatively charged (murine).[303]

Generally, all cadmium chalcogenide nanoparticles can form thermodynamically favorable aggregates with proteins in biological media due to sulphur-cadmium chemistry,[304] which makes them increasingly large obstacles for capture and sequestration, requiring a ligand shell that does not allow such interaction if systemic therapy is the ultimate goal. The increased specific-association and uptake with various cells has been shown to be possible with the inclusion of targeting molecules or peptides on the nanoparticle surface.[305,306] In one proof of concept demonstration, CdSe/ZnS particles coated with various peptide targeting factors could direct particles to the lung endothelium or tumor vasculature in mice, with the addition of PEG co-ligands increasing the selectivity by preventing hepatic-accumulation,[307] while specific antigens QDs can also be used to selectively target certain cancer cells.[308] While targeting factors and inclusion of co-polymers to reduce non-specific binding are useful for targeting for imaging applications,[309] the large polymer coating limits the effectiveness of any redox therapeutic.

5.6.3 Acute and Chronic Effects

In some early studies of core-shells for imaging it was noted that even at what would be high *in vitro* concentrations (> 1μM blood serum concentration), there were not immediatly detectable deleterious effects in mice.[310,311] However, it was noted in another murine study that high concentrations cause coagulation-induced acute toxicity, with negatively charged particles being more damaging, though the physical and chemical properties of the dots and ligands in this study were poorly characterized.[312] It has also been suggested there is a size-dependent effect of particle interactions with the bloodstream, with smaller particles showing less interaction in an invertebrate model (*Bombyx mori*).[204]

Given the observed tendency to accumulate, the long-term effects of QD injection are of equal importance to acute toxicity. PEG-stabilized CdSe/ZnS have been tracked *in vivo* for two years in a murine model, and while still emissive, the observed emission was significantly blue-shifted which indicates that even with such robust capping the core can still slowly degrade over potentially years of residence.[313] It should be noted that only a ZnS shell without bulky ligands does not confer months of stability (murine),[161] and that bare cores are quickly bleached (*Bombyx mori*).[204] Though the particles *in vivo* have been observed to break down, no toxicological effects are generally observed at low QD doses (rat).[314]

The clearest predictor of the impact of a certain nanoparticle on human health would be clinical trials involving other primate species.[315] However, the cost of these experiments is prohibitive, which exceedingly limited examples in the available literature. The one known study using cadmium containing nanoparticles in rhesus macaques (*Macaca mulatta*) employed a CdSe/CdS/ZnS doubled shell with thick ligand encapsulation.[316] As may be predicted, the thick

sequestering layers yielded no acute toxicological effects at 25 mg/kg doses, though there was significant accumulation in the same target organs as observed in mice.

5.7 Particles which Promote Growth

There have been reports in the literature where the addition of seemingly toxic nanoparticles had the statistically significant effect of increasing bacterial proliferation.[98] Given the inherent complexity of the intra-cellular redox environment, it stands to reason that photoactive nanoparticles can feed into various metabolic cycles or other pathways that can lead to an increase in proliferation or production of certain molecules.[317] In one example, energy transfer from CdTe QDs[318] or CdS nanorods[319] was able to stimulate a hydrogenase enzyme from *Clostridium acetobutylicum* for the photoreduction of protons, both being effective likely due to the similarity of the CdTe and CdS conduction band potentials.[87]

One way to indirectly promote bacterial growth is the use of high band gap particles as a type of sunscreen. In one study examining *Klebsiella aerogenes*, the presence of biologically synthesized CdS in the culture provided protection from UVA radiation (320 – 400 nm) for several hours, though this was eventually lost due to photodegradation of the particles.[320]

In a recent article it was shown that CdS can act as both a co-catalyst for the reduction of carbon dioxide in *Moorella thermoacetica*, and allow further proliferation under illuminated conditions.[321] In the proposed scheme, biologically derived CdS with diameters less than 10 nm transfer photogenerated electrons to reduce dissolved CO_2, while cysteine provides a sacrificial reducing agent for the photogenerated holes. The synergy between the two was shown by comparing cultures with and without CdS, with untreated populations losing viability over time and treated bacteria proliferating with a standard doubling time. Thus, by including the appropriate sacrificial redox species the phototoxic effects of these particles can be turned into a

net positive for the treated organisms. This would also appear to be material and organism dependent, as it has been shown that CdSe/ZnS particles can inhibit photosynthesis in *Chlamydomonas* algae.[322]

5.8 Conclusions

After surveying the available literature on quantum dot toxicity, there are multiple common deficiencies in the reported methods, which greatly limits the comparison of different pieces of work. All reports studying the toxicity of nanomaterials should include several key pieces of information in a standardized and clear way in their main text methods.[24,323–325] 1) The size distribution of the particles themselves, not just the hydrodynamic radius, should be quantified. For core-shells, the average shell thickness should be clearly determined. 2) The capping ligands need to be expressly defined. 3) The optical properties, absorbance and emission, should be presented along with the method used of quantifying concentration based on those spectra or other means. 4) The methods employed to purify and sterilize the QDs prior to integration with biological systems should be detailed. 5) Aspects of the *in vitro* or *in vivo* experiments should be defined, like cell culture media, or controlled for, like light exposure.

There is also a sub-set of reports that rely on commercial manufacturers for their supply of nanomaterials, which creates potential issues in two respects. The first is incomplete characterization provided by the manufacturer, which may arise due to their desire to protect the details of their product. Secondly, if that manufacturer changes methods, or becomes acquired by a different company, there is no guarantee of reproducibility by future investigators. Ideally, all groups investigating the biological impact of nanomaterials would synthesize their own, or work with a collaborator, so the methods and characterization can be made consistent and fully understood.

Despite these problems, it is possible to determine several guiding principles for controlling the toxicity of quantum dots from the available data. 1) The core semiconducting material will impact the overall toxicity due to its electronic structure and the intracellular reactions and redox species it can thus form upon light stimulation. 2) This is controllable through size control and quantum confinement. 3) Size also plays a role in uptake and intracellular distribution, with larger particles being progressively excluded from a greater number of intracellular spaces. 4) The choice of ligand has a profound impact on the toxicity first through charge, with positive amine groups leading to much higher toxicity, and through degree of aliphatic character, which also progressively increases toxicity.

There is also a lack of support for some of the proposed mechanisms of toxicity that were developed when the field was nascent. 1) While quantum dots do progressively degrade due to ligand loss and oxidation, there is no evidence that any leached salts lead to primary toxicity. As a corollary, the reduced toxicity of core-shell structures is not due to their oxidation resistance, but to an increased tunneling barrier for moving charges out of the core. 2) The total surface area per particle is not a toxicity determinant outside of the changes in electronic structure with size. Instead, the primary mechanisms of toxicity appear to be either membrane damage due to aggregation of positive particles or the many effects of redox species, which for the cadmium chalcogenides is reflected in the strong production of hydroxyl radicals through electron transfer to dissolved oxygen.

The ability to form these species upon light stimulation in a temporal and spatially controlled manner has led to the possibility of using QDs as anti-microbial agents. The primary mechanisms of action depend on the sub-cellular localization of the particles, but there is ample evidence that they can both target genetic stability and membrane integrity. The major drawback

is that the particles are susceptible to their own products and lose effectiveness over time. Longer stability could open up possibilities for visible light absorbing analogues of auto-disinfecting surfaces currently reliant on TiO_2, though only one known report has explored this possibility for embedded QDs.[326]

While work has been done examining the effect of nanoparticles on higher organisms, there are still significant gaps in the available knowledge. The long-term effects and accumulation of particles should be addressed *in vivo*, and not just for completely segregated core-shells with polymeric ligands but for bare charge-stabilized cores as well. A great deal of work should also be done on the differential toxicity of nanomaterials on human tissues compared to bacteria to addressthe question of antimicrobial potential.

Finally, greater attention should be given to the ultimate environmental impact of the release of QDs if they are to become an important and mass produced commodity. This includes further studies of where they ultimately accumulate, and in what form when released.[236] While important as the likely point of initial impact, moving beyond aquatic toxicity studies to terrestrial populations. To date, there are a handful of studies which explore this, showing accumulation in plants[202] and transference up food chains in microbe populations.[327–329] Ideally, the interest in toxicological studies will result in the necessary protocols being developed before mass production, preventing some of the oversights that have historically plagued certain product deployments in the chemical industry.

5.9 Symbols and Abbreviations

AUT - amino undecanethiol
BCF - bovine corneal fibroblasts
BCG - Stomach adenocarcinoma cells
CA - cysteamine
CdX - X = O, S, Se, Te
CFU - colony forming unit
CHL - Chinese hamster lung cells
CYS - cysteine
DCFH-DA - 2',7'-dichlorofluorescin diacetate
DHLA - dihydrolipoic acid
DMPO - 5,5-dimethyl-1-pyrroline-N-oxide
EC_{50} - 50% effective inhibitory concentration
EPR - electron paramagnetic resonance
GSH - glutathione
HEC - human endothelial cells
HEK - human embryonic kidney cells
HeLa - human cervical cancer cells
HEPG2 - human liver carcinoma cells
HUVEC - human umbilical vein endothelial cells
K562 - human erythroleukemia cells
pK_{sp} - negative log of the solubility product constant
LB - Luria broth
LC_{50} - 50% lethal dose/concentration
LDH - lactate dehydrogenase
MAM - murine alveolar macrophage
MPA - 3-mercaptopropionic acid
MTT - 3-(4,5-dimethylthiazol-2-yl)-2,5-diphenyltetrazolium
MSA - mercaptosuccinic acid
MSTC - Minimum significantly toxic concentration
MUA - mercaptoundecanoic acid
NAC - N-acetylcysteine
NEK - neonatal epidermal keratinocytes
NHBE - primary human pulmonary epithelial cells
NMR - nuclear magnetic resonance
OCMC - o-carboxymethylchitosan
OD - optical density

PEG - poly(ethylene glycol)
PEG-N - amine-functionalized PEG
PEG-A - acid-functionalized PEG
PEG-PPL - PEG-modified phospholipid
PHH - primary human hepatocyte
QD - quantum dot
RPC - rat pheochromocytoma cells
TEMPO - 2,2,6,6-tetramethyl-1-piperidinyloxyl
TGA - thioglycolic acid
TCL - thiocholine
UV - ultra-violet
XPS - X-ray photoelectron spectroscopy

5.10 References

1) Alivisatos A. P. *Science* **1996**, *271*, 933-937.
2) Brus L. E. *J. Chem. Phys.* **1983**, *79*, 5566-5571.
3) Kang Z., et al. *J. Am. Chem. Soc.* **2007**, *129*, 12090-12091.
4) Singh V., et al. *Nano Lett.* **2014**, *14*, 597-603.
5) Michalet X., et al *Science* **2005**, *307*, 538-545.
6) Brayner R., et al. *Nano Lett.* **2006**, *6*, 866-870.
7) Rengifo-Herrara J. A., et al. *J. Sol. Energy Eng.* **2007**, *129*, 135-140.
8) Jin T., et al. *J. Food Sci.* **2009**, *74*, M46-M52.
9) Wei C., et al. *Environ. Sci. Technol.* **1994**, *28*, 934-938.
10) Amelia M., et al. *Chem. Soc. Rev.* **2012**, *41*, 5728-5743.
11) Huang X., et al *J. Am. Chem. Soc.* **2006**, *128*, 2115-2120.
12) Hu M., et al. *Chem. Soc. Rev.* **2006**, *35*, 1084-1094.
13) Jaques S. L. *Phys. Med. Biol.* **2013**, *58*, R37-R61.
14) Smith A. M., et al. *Nat. Nanotechnol.* **2009**, *4*, 710-711.
15) Moulick A., et al. *Photochem. Photobiol.* **2015**, *91*, 417-423
16) Landry M. L., et al. *J. Chem. Educ.* **2014**, *91*, 274-279.
17) Rikans L. E., Yamano T. *J. Biochem. Mol. Toxicol.* **2000**, *14*, 110-117.
18) Oh S., Lim S. *Toxicol. Appl. Pharmacol.* **2006**, *212*, 212-223.
19) Michael P. W. *J. Inorg. Biochem.* **2000**, *79*, 241-244.
20) Bertin G., Averbeck D. *Biochimie* **2006**, *88*, 1549-1559.
21) Schroeder H. A., et al. *J. Chronic Dis.* **1970**, *23*, 227-243.
22) Ramadan S. E., et al. *Biol. Trace Elem. Res.* **1989**, *20*, 225-232.
23) Ba L. A., et al. *Org. Biomol. Chem.* **2010**, *8*, 4203-4216.
24) Rzigalinski B. A., Stobl J. S. *Toxicol. Appl. Pharmacol.* **2009**, *238*, 280-288.
25) Yu W. W., et al. *Chem. Mater.* **2003**, *15*, 2854-2860.
26) Booth M., et al. *Chem. Mater.* **2012**, *24*, 2064-2070.
27) Oberdörster G., et al. *Environ. Health Perspect.* **2005**, *113*, 823-839
28) Kirchner C., et al. *Nano Lett.* **2005**, *5*, 331-338.

29) Crane M., et al. *Ecotoxicology* **2008**, *17*, 421-437.
30) Kruk M., Jaroniec M. *Chem. Mater.* **2001**, *13*, 3169-3183.
31) Lopez-Sanchez J. A., et al. *Nat. Chem.* **2011**, *3*, 551-556.
32) Pace H. E., et al. *Environ. Toxicol. Chem.* **2010**, *29*, 1338-1344.
33) Sayes C. M., et al. *Nano Lett.* **2007**, *7*, 2399-2406.
34) Tsoi K. M., et al. *Acc. Chem. Res.* **2013**, *46*, 663-671.
35) Sayes C. M., et al. *Toxicol. Sci.* **2007**, *97*, 163-180.
36) McMahan R. S., et al. Quantum dots: applications in biology. Springer **2014**.
37) Scoville D. K., et al. Quantum dots: applications in biology. Spring **2014**.
38) Zwietering M. H., et al. *Appl. Environ. Microbiol.* **1990**, *56*, 1875-1881.
39) Mytilinaios I., et al. *Int. J. Food Microbiol.* **2012**, *154*, 169-176.
40) Mosmann T. *J. Immunol. Methods* **1983**, *65*, 55-63.
41) Gerlier D., Thomasset N. *J. Immunol. Methods* **1986**, *94*, 57-63.
42) Erb R. E., Ehlers M. H. *J. Dairy Sci.* **1950**, *33*, 853-864.
43) Kalyanaraman B., et al. *Free Radic. Biol. Med.* **2012**, *52*, 1-6.
44) LeBel C. P., Bondy S. C. *Neurochem. Int.* **1990**, *17*, 435-440.
45) Aranda A., et al. *Toxicol. In Vitro* **2013**, *27*, 954-963.
46) Willard D. M., et al. *Nano Lett.* **2001**, *1*, 469-474.
47) Clapp A. R., et al. *J. Am. Chem. Soc.* **2004**, *126*, 301-310.
48) Dumas E., et al. *Environ. Sci. Technol.* **2010**, *44*, 1464-1470.
49) Schneider R., et al. *Nanotechnology* **2009**, *20*, 225101.
50) Bailon-Ruiz S., Perales-Perez O. *J. Exp. Nanosci.* **2014**, *9*, 942-956.
51) Viana O., et al. *Molecules* **2015**, *20*, 8893-8912.
52) Bakalova R., et al. *Nano Lett.* **2004**, *4*, 1567-1573.
53) Oh E., et al. *Nat. Nanotechnol.* **2016**, *11*, 479-486.
54) Oberdörster G., et al. *Part. Fibre Toxicol.* **2005**, *2*, 8.
55) Hardman R. *Environ. Health Perspect.* **2006**, *114*, 165-172.
56) Bottrill M., Green M. *Chem. Commun.* **2011**, *47*, 7039-7050.
57) Kauffer F. A., et al. *J. Hazard. Mater.* **2014**, *268*, 246-255.
58) Gratton S. E. A., et al. *Proc. Natl. Acad. Sci. U. S. A.* **2008**, *105*, 11613-11618.
59) Pal S., et al. *Appl. Environ. Microbiol.* **2007**, *73*, 1712-1720.
60) Zhao F., et al. *Small* **2011**, *7*, 1322-1337.
61) Wang Q., et al. *J. Colloid Interface Sci.* **2011**, *363*, 476-480.
62) Lu Z., et al. *Langmuir* **2008**, *24*, 5445-5452.
63) Yan M., et al. *Toxicology* **2011**, *282*, 94-103.
64) Wang L., et al. *J. Nanosci. Nanotechnol.* **2010**, *10*, 8591-8596.
65) Fang T., et al. *Toxicol. In Vitro* **2012**, *26*, 1233-1239.
66) Hussain S. M., et al. *Toxicol. In Vitro.* **2005**, *19*, 975-983.
67) L'Azou B., et al. *Toxciol. Res.* **2014**, *3*, 32-41.
68) Dou Y., et al. *Surf. Sci.* **1998**, *298*, 241-258.
69) Bube R. H. *Proc. IRE* **1955**, *43*, 1836-1850.
70) Jenny D. A., Bube R. H. *Phys. Rec.* **1954**, *96*, 1190-1191.
71) Pinaud B. A., et al. *J. Phys. Chem. C* **2011**, *115*, 11830-11838.
72) Vratny F., Micale F. *Trans. Faraday Soc.* **1963**, *59*, 2739-2749.
73) Henderson D. O., et al. *Mater. Des.* **2001**, *22*, 585-589.
74) Hossain S. T., et al. *Toxicol. Environ. Chem.* **2013**, *95*, 1748-1756.

75) Wang J., et al. *Chemosphere* **2008**, *73*, 1121-1128.
76) *21CFR73.575*; **2015**.
77) Li H., et al. *J. Nanosci. Nanotechnol.* **2011**, *11*, 3543-3551.
78) Chen C., et al. *J. Phys. Chem. C* **2015**, *119*, 2852-2860.
79) Chan W., et al. *Toxicol. Lett.* **2006**, *167*, 191-200.
80) Hossain S. T., Mukherjee S. K. *Langmuir* **2012**, *28*, 16614-16622.
81) Law W., et al. *Small* **2009**, *5*, 1302-1310.
82) Su Y., et al. *Biomaterials* **2009**, *30*, 19-25.
83) He Y., et al, *Chem. Mater.* **2007**, *19*, 359-365.
84) Li X., et al. *Adv. Healthc. Mater.* **2014**, *3*, 354-359.
85) He Y., et al. *Adv. Mater.* **2008**, *20*, 3416-3421.
86) Yong K., et al. *Chem. Soc. Rev.* **2013**, *42*, 1236-1250.
87) Van De Walle C. G., Neugebauer J. *Nature* **2003**, *423*, 626-628.
88) Yong K., et al. *Chem. Commun.* **2010**, *46*, 7136-7138.
89) Courtney C. M., et al. *Nat. Mater.* **2016**, *15*, 529-534.
90) Lee H., et al. *Toxicol. Appl. Pharmacol.* **2009**, *238*, 160-169.
91) Park C., et al. *Bull. Korean Chem. Soc.* **2008**, *29*, 303-304.
92) Ulusoy M., et al. *RSC Adv.* **2015**, *5*, 7485-7494.
93) Ulusoy M., et al. *Toxicol. Res.* **2015**, *5*, 126-135.
94) Zhang T., et al. *Nano Lett.* **2006**, *6*, 800-808.
95) Selvan S. T., et al. *Adv. Mater.* **2005**, *17*, 1620-1625.
96) Jiang W., et al. *Environ. Pollut.* **2009**, *157*, 1619-1625.
97) Li K. G., et al. *Toxicol. In Vitro* **2009**, *23*, 1007-1013.
98) Nagy A., et al. *ACS Nano* **2012**, *6*, 4748-4762.
99) Lovrić J., et al. *J. Mol. Med.* **2005**, *83*, 377-385.
100) Shiohara A., et al. *Microbiol. Immunol.* **2004**, *48*, 669-675.
101) Winnik F. M., Maysinger D. *Acc. Chem. Res.* **2013**, *46*, 672-680.
102) Zhu Z., et al. *Nat. Chem.* **2011**, *3*, 963-968.
103) Zhang Y., et al. *J. Nanosci. Nanotechnol.* **2007**, *7*, 497-503.
104) Lewinski N., et al. *Small* **2008**, *4*, 26-49.
105) Silva A. C. A., et al. *Nano. Lett.* **2014**, *14*, 5452-5427.
106) Dabbousi B. O., et al. *J. Phys. Chem. B* **1997**, *101*, 9463-9475.
107) Kleopfer J. A., et al. *Appl. Environ. Microbiol.* **2005**, *71*, 2548-2557.
108) Su Y., et al. *Biomaterials* **2010**, *31*, 4829-4834.
109) Seleverstov O., et al. *Nano Lett.* **2006**, *6*, 2826-2832.
110) Williams Y., et al. *Small* **2009**, *5*, 2581-2588.
111) Nabiev I., et al. *Nano Lett.* **2007**, *7*, 3452-3461.
112) Chang S., et al. *Toxicol. Lett.* **2009**, *188*, 104-111.
113) Fan H., et al. *Nano Lett.* **2005**, *5*, 645-648.
114) Hoshino A., et al. *Nano Lett.* **2004**, *4*, 2163-2169.
115) Hoshino A., et al. *Arch. Toxicol.* **2011**, *85*, 707-720.
116) Nagy A., et al. *ACS Nano* **2013**, *7*, 8397-8411.
117) Al-Hajaj N. A., et al. *ACS Nano* **2011**, *5*, 4909-4918.
118) Nagy A., et al. *Chem. Res. Toxicol.* **2011**, *24*, 2176-2188.
119) Arvizo R. R., et al. *Nano Lett.* **2010**, *10*, 2543-2548.
120) Wang L., et al. *J. Hazard. Mater.* **2010**, *177*, 1134-1137.

121) Lai L., et al. *J. Colloid Interface Sci.* **2013**, *389*, 61-70.
122) Slaveykova V. I., et al. *Environ. Sci. Technol.* **2009**, *43*, 5117-5122.
123) Ryman-Rasmussen J. P., et al. *J. Invest. Dermatol.* **2007**, *127*, 143-153.
124) Kuo T., et al. *Chem. Res. Toxicol.* **2011**, *24*, 253-261.
125) Chang E., et al. *Small* **2006**, *2*, 1412-1417.
126) Mahto S. K., et al. *Toxicol. In Vitro* **2010**, *24*, 1070-1077.
127) Cho S. J., et al. *Langmuir* **2007**, *23*, 1974-1980.
128) Liu J., et al. *Mater. Sci. Eng. C* **2015**, *57*, 222-231.
129) Clift M. J. D., et al. *Toxicol. Appl. Pharmacol.* **2008**, *232*, 418-427.
130) Schumacher W., et al. *J. Phys. Chem. C* **2009**, *113*, 12132-12139.
131) Aldana J., et al. *J. Am. Chem. Soc.* **2005**, *127*, 2496-2504.
132) Adegoke O., et al. *J. Fluoresc.* **2012**, *22*, 771-778.
133) Keire D. A., et al. *J. Org. Chem.* **1992**, *57*, 123-127.
134) Aldana J., et al. *J. Am. Chem. Soc.* **2001**, *123*, 8844-8850.
135) Ma J., et al. *J. Phys. Chem. B* **2007**, *111*, 12012-12016.
136) Zhang Y., et al. *Appl. Surf. Sci.* **2009**, *255*, 4747-4753.
137) Mancini M. C., et al. *J. Am. Chem. Soc.* **2008**, *130*, 10836-10837.
138) Pullar J. M., et al. *IUMB Life* **2000**, *50*, 259-266.
139) Warnement M. R., et al. *Bioconjug. Chem.* **2008**, *19*, 1404-1413.
140) Algar W. R., Krull U. J. *ChemPhysChem* **2007**, *8*, 561-568.
141) Zhang Y., et al. *RSC Adv.* **2015**, *5*, 57082-57089.
142) Bruneau A., et al. *Environ. Toxicol.* **2013**, *30*, 9-25.
143) Zhou C., et al. *Ecotoxicol. Environ. Saf.* **2016**, *123*, 26-31.
144) Cordero S. R., et al. *J. Phys. Chem. B* **2000**, *104*, 12137-12142.
145) Boldt K., et al. *J. Phys. Chem. B* **2006**, *110*, 1959-1963.
146) Clever J. L., et al. *J. Phys. Chem. Ref. Data* **1992**, *21*, 941-1004.
147) Sinha P., et al. *Environ. Toxicol. Chem.* **2012**, *31*, 1670-1675.
148) Dirkse T. P. *J. Electrochem. Soc.* **1986**, *133*, 1656-1657.
149) Doña J. M., Herrero J. *J. Electrochem Soc.* **1995**, *142*, 764-770.
150) Katari J. E. B., et al. *J. Phys. Chem.* **1994**, *98*, 4109-4117.
151) Biver M., Filella M. *Environ. Sci. Technol.* **2016**, *50*, 4675-4681.
152) Dutton W. A., Cooper W. C. *Chem. Rev.* **1966**, *66*, 657-675.
153) Issa I. M., Awad S. A. *J. Phys. Chem.* **1954**, *58*, 948-951.
154) Waitkins G. R., Clark C. W. *Chem. Rev.* **1945**, *36*, 235-289.
155) Zeng C., et al. *J. Environ. Manage.* **2015**, *154*, 78-85.
156) Peng Z. A., Peng X. *J. Am. Chem. Soc.* **2001**, *123*, 183-184.
157) Mahendra S., et al. *Environ. Sci. Technol.* **2008**, *42*, 9424-9430.
158) He Y., et al. *Biomaterials* **2011**, *32*, 2133-2140.
159) van Sark W. G. J. H. M., et al. *J. Phys. Chem. B* **2001**, *105*, 8281-8284.
160) Zhao Y., et al. *Toxicol. Res.* **2015**, *4*, 399-408.
161) Liu N., et al. *Part. Fibre Toxicol.* **2013**, *10*, 37.
162) Aldeek F., et al. *Eur. J. Inorg. Chem.* **2011**, 794-801.
163) Kirchner C., et al. *Talanta* **2005**, *67*, 486-491.
164) Derfus A. M., et al. *Nano Lett.* **2004**, *4*, 11-18.
165) Xu M., et al. *Metallomics* **2010**, *2*, 469-473.
166) Chen F., Gerion D. *Nano Lett.* **2004**, *4*, 1827-1832.

167) Emmerson B. T. *Ann. Inter. Med.* **1970**, *73*, 854-855.
168) Hossain S. T., Mukherjee S. K. *J. Hazard. Mater.* **2013**, *260*, 1073-1082.
169) Priester J. H., et al. *Environ. Sci. Technol.* **2009**, *43*, 2589-2594.
170) Brayner R., et al. *J. Nanosci. Nanotechnol.* **2011**, *11*, 1852-1858.
171) Gagné F., et al. *J. Environ. Monit.* **2010**, *12*, 1556-1565.
172) Migita S., et al. *In Vitro Cell. Dev. Biol. Anim.* **2014**, *50*, 367-372.
173) Ambrosone A., et al. *Biomaterials* **2012**, *33*, 1991-2000.
174) King-Heiden T. C., et al. *Environ. Sci. Technol.* **2009**, *43*, 1605-1611.
175) Kim J., et al. *Aquat. Toxicol.* **2010**, *97*, 116-124.
176) Kensova R., et al. *Int. J. Electrochem. Sci.* **2015**, *10*, 3623-3634.
177) Katsumiti A., et al. *Aquat. Toxicol.* **2014**, *153*, 39-52.
178) Liu Y., et al. *J. Phys. Chem. B* **2006**, *110*, 16992-17000.
179) Lankoff A., et al. *Toxicol. Lett.* **2012**, *208*, 197-213.
180) DOmingos R. F., et al. *Environ. Sci. Technol.* **2011**, *45*, 7664-7669.
181) Zhang L. W., Monteiro-Riviere N. A. *Toxicol. Sci.* **2009**, *110*, 138-155.
182) Silver S. *Gene* **1996**, *179*, 9-19.
183) Ahmad A., et al. *J. Am. Chem. Soc.* **2002**, *124*, 12108-12109.
184) Dameron C. T., et al. *Nature* **1989**, *338*, 596-597.
185) Sweeney R. Y., et al. *Chem. Biol.* **2004**, *11*, 1553-1559.
186) Crookes-Goodson W. J., et al. *Chem. Soc. Rev.* **2008**, *37*, 2403-2412.
187) Jacob J. M., et al. *Microb. Biotechnol.* **2016**, *9*, 11-21.
188) Green M., et al. *Sci. Rep.* **2016**, *6*, 20480.
189) Prasad K., Jha A. K. *J. Colloid Interface Sci.* **2010**, *342*, 68-72.
190) Sanghi R., Verma P. *Chem. Eng. J.* **2009**, *155*, 886-891.
191) Bao H., et al. *Acta Biomater.* **2010**, *6*, 3534-3541.
192) Lampis S., et al. *J. Hazard. Mater.* **2016**, *in press*.
193) Bai H. J., et al. *Colloids Surf. B Biointerfaces* **2009**, *70*, 142-146.
194) Nies D. H., Silver S. *J. Ind. Microbiol. Biotechnol.* **1995**, *14*, 186-199.
195) Klaassen C. D., et al. *Toxicol. Appl. Pharmacol.* **2009**, *238*, 215-220.
196) Nordberg M. *Environ. Res.* **1978**, *15*, 381-404.
197) Samia A. C. S., et al. *Photochem. Photobiol.* **2006**, *82*, 617-625.
198) Xu G., et al. *Front. Pharmacol.* **2013**, *4*, 140.
199) Gogoi S. K., et al. *Langmuir* **2006**, *22*, 9322-9328.
200) Kim Y., et al. *J. Phys. Chem. B* **2006**, *110*, 24923-24928.
201) Ma J., et al. *Nanotechnology* **2006**, *17*, 2083-2089.
202) Chen H., et al. *PLoS One* **2014**, *9*, e110400.
203) Peshavariya H. M., et al. *Free Radic. Res.* **2007**, *41*, 699-712.
204) Liu T., et al. *Biomaterials* **2014**, *35*, 2942-2951.
205) Luo Z., et al. *J. Colloid Interface Sci.* **2011**, *362*, 100-106.
206) Tang M., et al. *Biomaterials* **2008**, *29*, 4383-4391.
207) Bleaney B., Stevens K. W. H. *Rep. Prog. Phys.* **1953**, *16*, 108-159.
208) Bhattacharjee S. *Curr. Sci.* **2005**, *89*, 1113-1121.
209) Buettner G. R., Mason R. P. *Methods Enzymol.* **1990**, *186*, 127-133.
210) Buettner G. R. *Free Radic. Biol. Med.* **1987**, *3*, 259-303.
211) Dvoranová D., et al. *Molecules* **2014**, *19*, 17279-17304.
212) Ipe B. I., et al. *Small* **2005**, *1*, 706-709.

213) Harbour J. R., Hair M. L. *J. Phys. Chem.* **1977**, *81*, 1791-1793.
214) Gill S. S., Tuteja N. *Plant Physiol. Biochem.* **2010**, *48*, 909-930.
215) Baral S., et al. *J. Am. Chem. Soc.* **1986**, *108*, 375-378.
216) Gaponik N., et al. *J. Phys. Chem. B* **2002**, *106*, 7177-7185.
217) Resch U., et al. *Langmuir* **1989**, *5*, 1015-1020.
218) Watts R. J., et al. *Adv. Environ. Res.* **2003**, *7*, 961-968.
219) Goodman S. M., et al. *J. Phys. Chem. Lett.* **2014**, *5*, 3909-3913.
220) Samia A. C., et al. *J. Am. Chem. Soc.* **2003**, *125*, 15736-15737.
221) Zenkevich E. I., et al. *J. Phys. Chem. C* **2011**, *115*, 21535-24545.
222) Clarke S. J., et al. *Nat. Mater.* **2006**, *5*, 409-417.
223) Buettner G. R. *Arch. Biochem. Biophys.* **1993**, *300*, 535-543.
224) Li Y., et al. *ACS Nano* **2012**, *6*, 5164-5173.
225) Neibert K. D., Maysinger D. *Nanotoxicology* **2012**, *6*, 249-262.
226) Cooper D. R., et al. *Nanoscale* **2010**, *2*, 114-121.
227) Mei J., et al. *Chemosphere* **2014**, *112*, 92-99.
228) Green M., Howman E. *Chem. Commun.* **2005**, 121-123.
229) Thuy U. T. D., et al. *Opt. Mater.* **2016**, *53*, 34-38.
230) Lovrić J., et al. *Chem. Biol.* **2005**, *12*, 1227-1234.
231) Wu T., et al. *Toxicol. Res.* **2015**, *4*, 1613-1622.
232) Ema M., et al. *Toxicol. Appl. Pharmacol.* **2016**, *299*, 47-52.
233) Liang J., et al. *Talanta* **2007**, *71*, 1675-1678.
234) Wang C., et al. *Talanta* **2010**, *80*, 1228-1233.
235) Anas A., et al. *J. Phys. Chem. B* **2008**, *112*, 10005-10011.
236) Ladhar C., et al. *Nanotoxicology* **2014**, *8*, 676-685.
237) Jacobsen N. R., et al. *Part. Fibre Toxicol.* **2009**, *6*, 2.
238) Choi A. O., et al. *J. Mol. Med.* **2008**, *86*, 291-302.
239) Gagné F., et al. *Aquat. Toxicol.* **2008**, *86*, 333-340.
240) Khalil W. K. B., et al. *Chem. Res. Toxicol.* **2011**, *24*, 640-650.
241) Cadet J., et al. *Mutat. Res. Fund. Mol. Mech. Mut.* **1999**, *424*, 9-21.
242) Burrows C. J., Muller J. G. *Chem. Rev.* **1998**, *98*, 1109-1152.
243) Epe B. *Chem. Biol. Interact.* **1991**, *80*, 239-260.
244) Jaiswal J. K., et al. *Nat. Biotechnol.* **2003**, *21*, 47-51.
245) Fan J., et al. *Biomaterials* **2016**, *78*, 102-114.
246) Peynshaert K., et al. *Chem. Rev.* **2014**, *114*, 7581-7609.
247) Gomes S. A. O., et al. *Sensors* **2011**, *11*, 11664-11678.
248) Xiao Y., et al. *J. Nanobiotechnology* **2010**, *8*, 13.
249) Jiang X., et al. *ACS Nano* **2010**, *4*, 6787-6797.
250) Duan H., Nie S. *J. Am. Chem. Soc.* **2007**, *129*, 3333-3336.
251) Nguyen C. C., et al. *Toxicol. Sci.* **2015**, *146*, 31-42.
252) Lai L., et al. *J. Membr. Biol.* **2015**, *248*, 727-740.
253) Li J., et al. *J. Hazard. Mater.* **2011**, *194*, 440-444.
254) Luo Y. H., et al. *Chem. Res. Toxicol.* **2013**, *26*, 662-673.
255) Lonhienne T. G. A., et al. *Proc. Natl. Acad. Sci. U.S.A.* **2010**, *107*, 12883-12888.
256) Tyagi A., et al. *Anal. Methods* **2016**, *8*, 1060-1068.
257) Choi A. O., et al. *J. Nanobiotechnology* **2007**, *5*, 1.
258) Mylonas C., Kouretas D. *In Vivo* **1999**, *13*, 295-309.

259) Dumas E., et al. *IEEE Trans. Nanobioscience* **2009**, *8*, 58-64.
260) Yang C., et al. *J. Colloid. Interface Sci.* **2015**, *450*, 388-395.
261) Rincón A., Pulgarin C. *Catal. Today* **2005**, *101*, 331-344.
262) Manabe N., et al. *IEEE Trans. Nanobioscience* **2006**, *5*, 263-267.
263) Johari-Ahar M., et al. *J. Drug Target.* **2015**, *24*, 120-133.
264) Wijtmans M., et al. *J. Am. Chem. Soc.* **2006**, *128*, 11720-11726.
265) Klaper R., et al. *Analyst* **2014**, *139*, 882-895.
266) Pelley J. L., et al. *Toxicol. Sci.* **2009**, *112*, 276-296.
267) Donaldson K., et al. *Part. Fibre Toxicol.* **2005**, *2*.
268) Wu T., Tang M. *Inhal. Toxicol.* **2014**, *26*, 128-139.
269) Ho C., et al. *Nanotoxicology* **2013**, *7*, 105-115.
270) Ma-Hock L., et al. *Toxicol. Lett.* **2012**, *208*, 115-124.
271) Roberts J. R., et al. *Part. Fibre Toxicol.* **2013**, *10*.
272) Verma S., et al. *J. Biomed. Nanotechnol.* **2011**, *7*, 197-198.
273) Chu M., et al. *Small* **2010**, *6*, 670-678.
274) Blum J. L., et al. *Toxicol. Sci.* **2012**, *126*, 478-486.
275) Jain M. P., et al. *Nanomedicine* **2012**, *7*, 23-37.
276) Liu Z., et al. *RSC Adv.* **2015**, *5*, 94257-94266.
277) Zhang L. W., et al. *Toxicol. Appl. Pharmacol.* **2008**, *228*, 200-211.
278) Ryman-Rasmussen J. P., et al. *Toxicol. Sci.* **2006**, *91*, 159-165.
279) Chu M., et al. *Nanotechnology* **2007**, *18*, 455103.
280) Zhang L. W., Monteiro-Riviere N. A. *Skin Pharmacol. Physiol.* **2008**, *21*, 166-180.
281) Mortensen L. J., et al. *Nano Lett.* **2008**, *8*, 2779-2787.
282) Baroli B. *J. Pharm. Sci.* **2010**, *99*, 21-50.
283) Schneider M., et al. *Dermatoendocrinol.* **2009**, *1*, 197-206.
284) Tang M., et al. *Environ. Health Perspect.* **2008**, *116*, 915-922.
285) Zhao Y., et al. *J. Hazard. Mater.* **2015**, *283*, 480-489.
286) Wu T., et al. *Nanoscale* **2015**, *7*, 20460-20473.
287) Tang M., et al. *Biomaterials* **2009**, *30*, 4948-4955.
288) Dobrovolskaia M. A., McNeil S. E. *Nat. Nanotechnol.* **2007**, *2*, 469-478.
289) Nguyen K. C., et al. *Nanotoxicology* **2013**, *7*, 202-211.
290) Sadaf A., et al. *J. Nanosci. Nanotechnol.* **2012**, *12*, 8287-8292.
291) Hsieh S., et al. *Biomaterials* **2006**, *27*, 1656-1664.
292) Su Y., et al. *Biomaterials* **2011**, *32*, 5855-5862.
293) Gopee N. V., et al. *Toxicol. Sci.* **2007**, *98*, 249-257.
294) Ballou B., et al. *Bioconjug. Chem.* **2004**, *15*, 79-86.
295) Han Y., et al. *J. Nanoparticle Res.* **2011**, *13*, 5373-5380.
296) Garnett M. C., Kallinteri P. *Occup. Med.* **2006**, *56*, 307-311.
297) Fischer H. C., et al. *Adv. Funct. Mater.* **2006**, *16*, 1299-1305.
298) Dubertret B., et al. *Science* **2002**, *298*, 1759-1762.
299) Yang R. S., et al. *Environ. Health Perspect.* **2007**, *115*, 1339-1343.
300) Hoshino A., et al. *Biochem. Biophys. Res. Commun.* **2004**, *314*, 46-53.
301) Albanese A., et al. *Annu. Rev. Biomed. Eng.* **2012**, *14*, 1-16.
302) Choi H. S., et al. *Nat. Biotechnol.* **2007**, *25*, 1165-1170.
303) Liang X., et al. *ACS Nano* **2016**, *10*, 387-395.
304) Mu Q., et al. *Chem. Rev.* **2014**, *114*, 7740-7781.

305) Clarke S. J., et al. *Bioconjug. Chem.* **2008**, *19*, 562-568.
306) Delehanty J. B., et al. *Bioconjug Chem.* **2006**, *17*, 920-927.
307) Åkerman M. E., et al. *Proc. Natl. Acad. Sci. U.S.A.* **2002**, *99*, 12617-12621.
308) Gao X., et al. *Nat. Biotechnol.* **2004**, *22*, 969-976.
309) Bentzen E. L., et al. *Bioconjug. Chem.* **2005**, *16*, 1488-1494.
310) Voura E. B., et al. *Nat. Med.* **2004**, *10*, 993-998.
311) Larson D. R., et al. *Science* **2003**, *300*, 1434-1436.
312) Geys J., et al. *Environ. Health Perspect.* **2008**, *116*, 1607-1613.
313) Fitzpatrick J. A. J., et al. *Nano Lett.* **2009**, *9*, 2736-2741.
314) Hauck T. S., et al. *Small* **2010**, *6*, 138-144.
315) Chen G., et al. *Chem. Rev.* **2016**, *116*, 2826-2885.
316) Ye L., et al. *Nat. Nanotechnol.* **2012**, *7*, 453-458.
317) King P. W. *Biochim. Biophys. Acta* **2013**, *1827*, 949-952.
318) Brown K. A., et al. *J. Am. Chem. Soc.* **2010**, *132*, 9672-9680.
319) Brown K. A., et al. *J. Am. Chem. Soc.* **2012**, *134*, 5627-5636.
320) Holmes J. D., et al. *Photochem. Photobiol.* **1995**, *62*, 1022-1026.
321) Sakimoto K. K., et al. *Science* **2016**, *351*, 74-77.
322) Lin S., et al. *J. Phys. Chem. C* **2009**, *113*, 10962-10966.
323) Dhawan A., Sharma V. *Anal. Bioanal. Chem.* **2010**, *398*, 589-605.
324) Warheit D. B. *Toxicol. Sci.* **2008**, *101*, 183-185.
325) Díaz E. C., Cases M. V. *Trends Anal. Chem.* **2016**, *84*, 160-171.
326) de Souza G. C. S., et al. *RSC Adv.* **2016**, *6*, 8563-8571.
327) Werlin R., et al. *Nat. Nanotechnol.* **2011**, *6*, 65-71.
328) Bouldin J. L., et al. *Environ. Toxicol. Chem.* **2008**, *27*, 1958-1963.
329) Chae Y., et al. *Chemosphere* **2016**, *151*, 101-107.

Chapter 6
CdTe as a Light-Activated Antibiotic

Multidrug-resistant (MDR) bacteria are a prominent example of rapid evolution induced from intense selective pressure, through the widespread adoption of antimicrobials, which when coupled with the lack of new antibiotics in development portents a future of increasingly devastating pathogens.[1-4] Antibiotic-resistant infections now affect nearly two million people in the United States annually, killing at least 23,000, which will only become worse as increasingly resistant organisms become more common.[5-9] Thus, it is imperative to develop new antimicrobial or disinfection strategies. One strategy is to induce intracellular physical or chemical changes within the cells that are not derived from a biological source or strategy. As it has been noted that redox changes are usually concomitant with bactericidal antibiotics, inducing this form of stress may be one such option (though there is some debate).[10-12] Because quantum dots have been shown to engage in electron transfer reactions for catalysis, they provide a useful model system for such studies as they can be turned on and off using light stimulation (Figure 6.1). Investigations into the development of nano-therapeutics for use *in vitro* as a treatment have tended to focus on metal nanoparticles which induce cell death by heating the surrounding medium through surface plasmon resonance.[13-15] However, as demonstrated in Chapter 5, such particles require specific antibodies or other targeting factors to be conjugated to the surface to ensure delivery to the intended targets while avoiding collateral damage to the host tissue. Thus, while it is unlikely that widespread adoption of QDs as direct therapeutics is

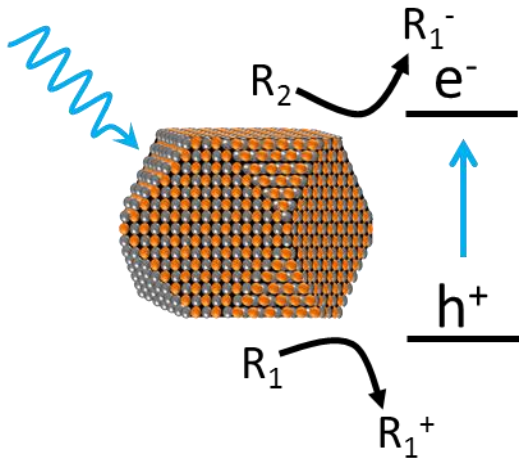

Figure 6.1 – Schematic showing photoexcitation of a quantum dot and charge transfer to molecules aligned with the QD redox potentials.

possible, the studies presented in these chapters can help identify what mechanisms of redox perturbations are most effective against bacteria, while yielding further evidence for the source and mechanism of CdX quantum dot toxicity.

Cells growing in aerobic environments possess natural mechanisms to mitigate oxidative species as their generation can lead to tissue damage and cell death.[16-20] Antibiotics like ampicillin, gentamicin, and ciprofloxacin, perturb the cellular redox environment as their mode of action, indicating the potential of this route using nanomaterials.[21,22] Ultraviolet absorbing quantum dots (Eg>3.1 eV) have been previously tested for their ability to induce oxidative stress in this manner.[23,24] However, ultraviolet stimulation is inherently toxic itself due to resulting DNA damage, making a shift to lower energy radiation, especially wavelengths which falls into the biological window of transparency, a pre-requisite for developing effective therapeutics.[25,26]

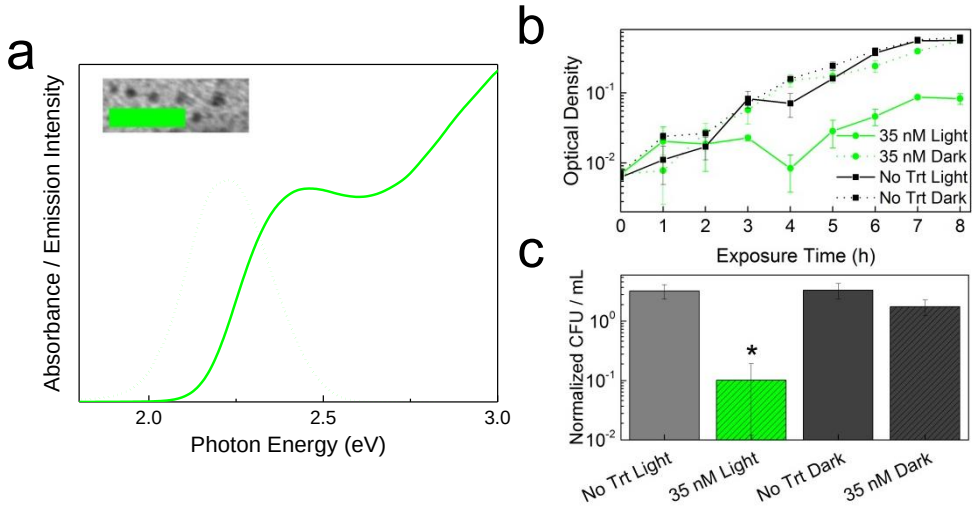

Figure 6.2 – **a.** Optical spectra of the CdTe-2.4 quantum dots with TEM image inset (scale bar: 25 nm). **b.** Optical density growth curves of *E. coli* exposed to the QDs in light and dark conditions. **c.** Colony forming unit analysis at 6 h (normalized to 0 h) at the different conditions.

The electronic properties of semiconductor nanomaterials can be tuned to provide specific perturbations in redox environments by simply altering their size-, shape- or composition-dependent electronic states. The most commonly encountered class of visible light-

stimulated quantum dots are the cadmium chalcogenides, which have the added benefit of being directly synthesizable in aqueous media;[27] although as described in Chapter 5 there are important considerations regarding the inherent toxicity of these elements. Of the three options, CdTe is the most applicable, as CdS has a bandgap too near the ultraviolet to provide much benefit over metal oxides, while CdSe is not emissive in aqueous environment which indicates some form of quenching mechanism that would limit the ability of the photoexcited electrons and holes to interact with the necessary targets. Thus, in this chapter, measurements focused on the phototoxic impact of green emitting CdTe quantum dots (CdTe-2.4, Figure 6.2a) in different pathogenic bacteria and HEK-293T cells is described.

As a first trial of these nanoparticles' potential, their effect on a lab strain of *E. coli* (MG1655) was tested in both light and dark conditions. Using the optical density of the cultures as a measure of bacterial growth there is a clear difference between the treated and untreated populations, and the treated populations in light and dark (Figure 6.2b). There are negligible differences between the untreated cultures, which is the result of only visible light being used through the use of filters to cut off everything outside of the 400-700 nm range. This removes both DNA damaging UV light and infrared radiation which would cause greater thermal stress in the light-exposed cells were it not removed. In light, there is a clearly antimicrobial photoeffect, such that at appropriate concentrations the growth can be completely attenuated within the measured timespan. As optical density is insensitive to differentiating live and dead cells, a confirmation of the decreased viability was performed using colony forming unit analysis (CFU, Figure 6.2c). Compared to the initial loading there is an order of magnitude fewer viable cells after treatment for six hours, while there is no significant difference between the no treatment and dark conditions at this concentration of quantum dots. Thus, with a significant observed

photoeffect, it was decided to test the general applicability of this therapy mode to other, more dangerous pathogens.

MDR bacteria were obtained from Dr. Nancy Madinger at the University of Colorado – Anschutz Medical Campus, and were all isolated from clinical cases. To confirm their high degree of resistance, the strains were exposed to a panel of nine antibiotics at concentrations corresponding to CLSI breakpoints where applicable, and nearly all of the strains were resistant at some level to all antibiotics tested.[29] Only the strain of *Salmonella typhimurium* had a merely intermediate resistance to ciprofloxacin and was susceptible to kanamycin. In addition to the tested resistances, the strain of *Klebsiella pneumoniae* expressed extended-spectrum β-lactamases (ESBLs), and one strain of *E. coli* is classified as a carbapenem-resistant Enterobacteriaceae (CRE). These treatments reflect a variety of different antibacterial mechanisms and their resistance underscores the increasing urgency of combating MDR infections in a clinical environment.

In the presence of CdTe- 2.4 and light stimulation the same photoeffect observed in MG1655 was seen in the MDR strains (Figure 6.3). In order to quantify the relative contributions of CdTe-2.4 in light and dark two different parameters were defined to quantify the inherent- (I_I) and photoinhibitions (I_P) relative to the untreated controls at specific time points (eq. 6.1, 6.2). A significant photoeffect is therefore distinguished from an inherent effect by the comparison of these two parameters using standard statistical tests. This was used as a metric for cell growth due to potentially incomplete growth curves for the treated populations within the measured time frame, limiting the accuracy of derived parameters for calculating further values. The photoeffect is clearly illustrated using these metrics for CdTe-2.4 in the sub-100 nM concentration regime

with significant differences between the light and dark treated cultures being observed (Figure 6.3).

To better visualize the differences in cell density between the treatment conditions, cells were plated out after 7 h of treatment with CdTe-2.4, revealing that after treatment there are many fewer cells. All of the strains exhibited different susceptibilities to the treatment, and are not directly comparable with the absolute values observed for MG1655 due to the different culture medium, though several trends can be observed to be present. To help visualize comparisons, these growth curves were fit using a modified Gompertz function (eq. 6.3) which uses the saturation population (S), lag-time (λ), and growth rate (μ) to model pre-death phase growth curves.[28] In both *E. coli* populations and the *K. pneumoniaea* there appear to be two growth phases observed in the normalized OD curves. The first consists of a lag time where the therapeutic is not readily effective and growth tracks with the control samples, which is followed by a saturation level which is maintained until seven or eight hours of exposure. After that point, the growth appears to resume and the OD begins to approach that observed in the other conditions. This likely reflects degradation of the particles over time in a biological medium, which ultimately renders them unable to produce the necessary phototherapeutic action (see Chapter 8 for an in-depth discussion of degradation). *S. typhimurium* appears to be an exception in that it ultimately reaches a lower overall saturation level in a monotonic phase. Another exception is MRSA which is much less susceptible to both the particles inherently and their phototoxic stimulation. Of the species tested MRSA is the only gram-positive bacterium which may indicate that toxicity depends on the membrane-structure.

$$I_I = 1 - \frac{\mathrm{OD}_{DT,t} - \mathrm{OD}_{DT,0}}{\mathrm{OD}_{DNT,t} - \mathrm{OD}_{DNT,0}} \tag{6.1}$$

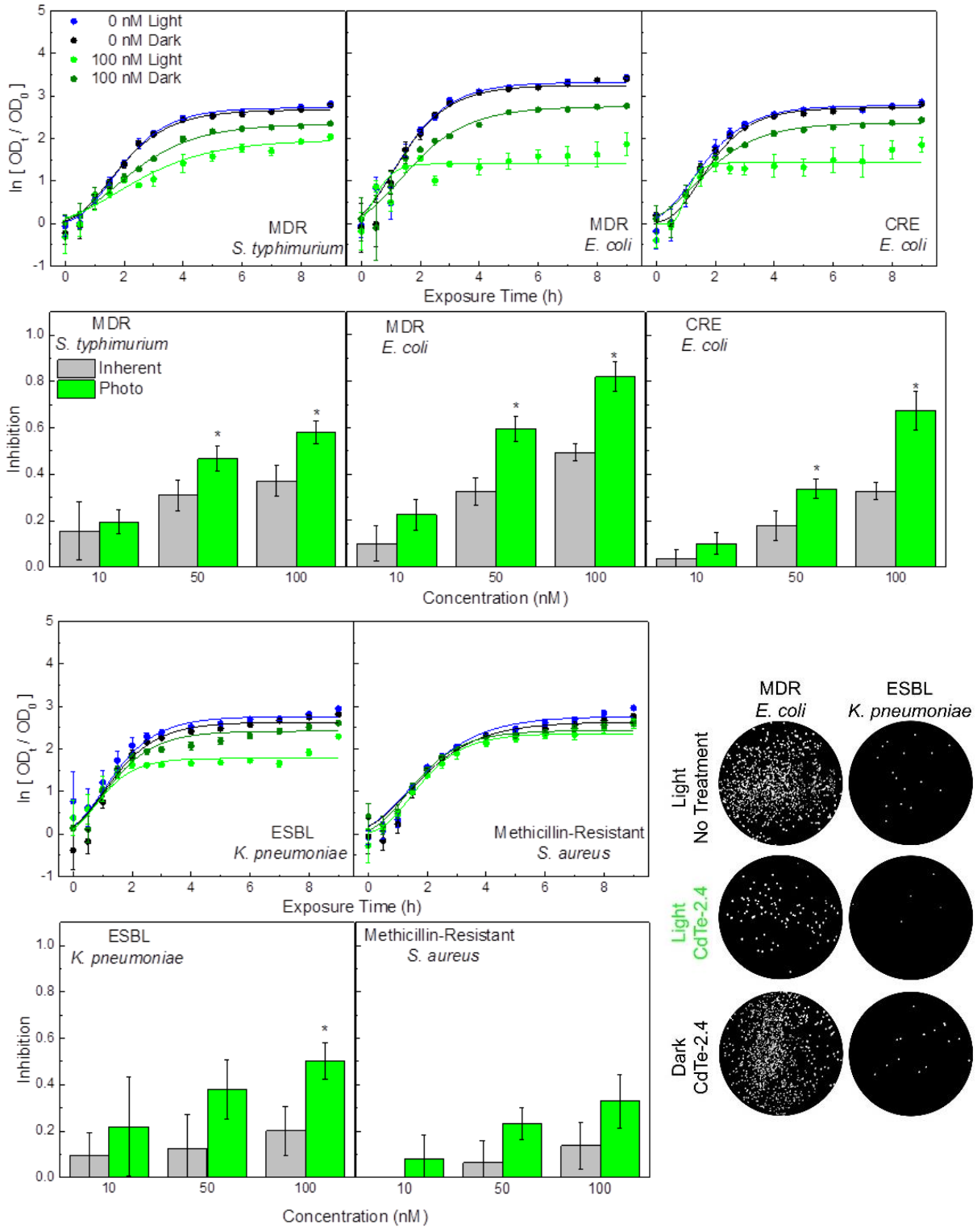

Figure 6.3 – Optical density growth curves and calculated inherent and photoinhibition for the pathogenic strains of bacteria. Significant differences between the inhibitions in light and dark are denoted by an asterisk. Plate images at the different treatment conditions for two strains are provided for better visualization of the effects.

$$I_P = 1 - \frac{\mathrm{OD}_{LT,t} - \mathrm{OD}_{LT,0}}{\mathrm{OD}_{LNT,t} - \mathrm{OD}_{LNT,0}} \tag{6.2}$$

$$\ln\left(\frac{\mathrm{OD}_t}{\mathrm{OD}_0}\right) = S \cdot \exp\left\{-\exp\left[\frac{\mu \cdot \exp(1)}{S}(\lambda - t) + 1\right]\right\} \tag{6.3}$$

As was previously shown in Chapter 5, different cell-types exhibit different tolerance to QDs, including a difference between eukaryotes and prokaryotes. To evaluate this possibility, experiments were performed where HEK-293T cells served as a model human cell-type, which were grown to 80% confluency and then inoculated with the nanoparticle treatments. Cell

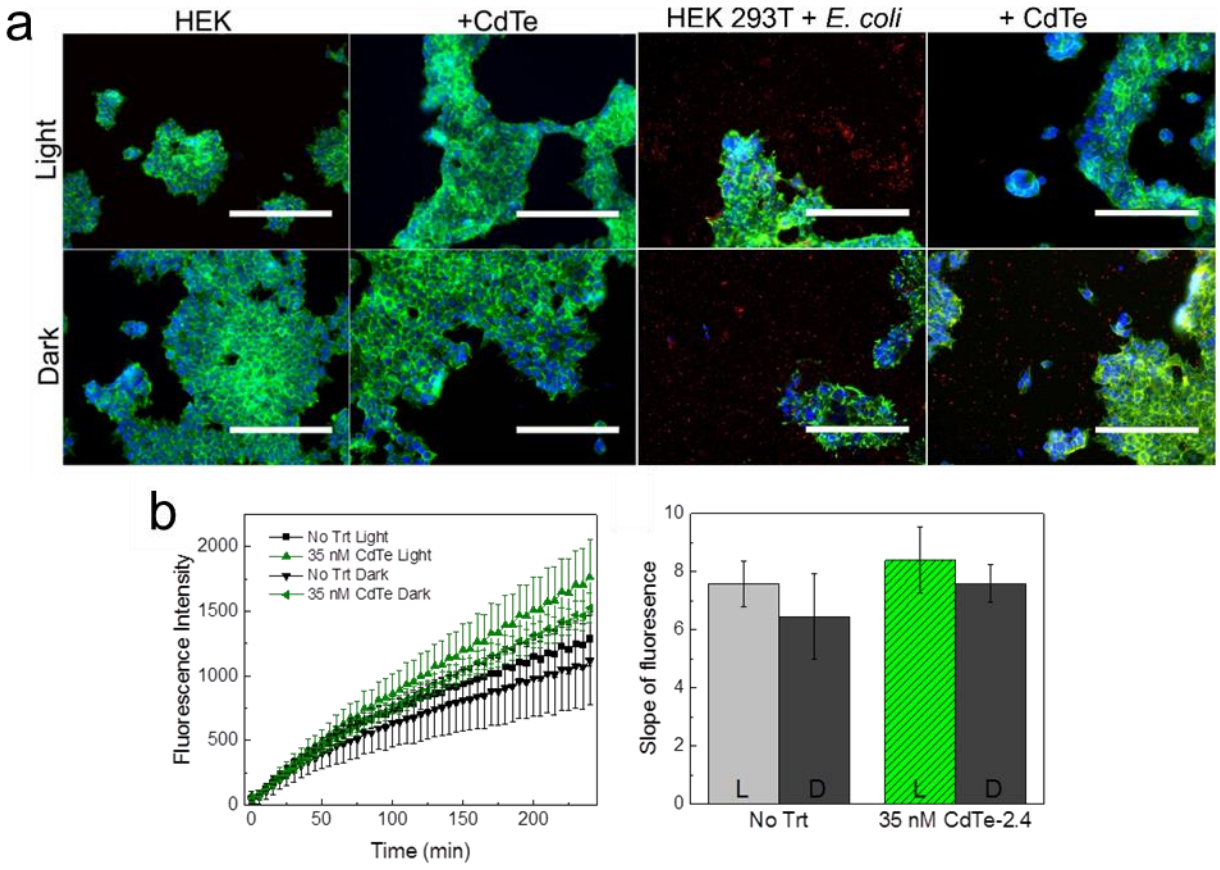

Figure 6.4 – **a.** Composite fluorescence images of HEK-293T cells in mono- and co-culture after exposure to 35 nM quantum dots. Scale bars are 200 µm. **b.** Time dependent Resazurin fluorescence of HEK 293T cells exposed to CdTe-2.4 in light and dark. Slopes of the measured fluorescence during the initial linear phase, where bars labeled "L" were under light exposure and bars labeled "D" were in dark, showing no significant difference in cell viability between treated and untreated cells ($p>0.05$).

viability was observed visually using DAPI (nuclear) and Phalloidin Cruzfor 488 conjugate (actin) stains to better observe cell morphology. At the QD concentrations required to eliminate *E. coli* the HEK-293T cells were able to tolerate the treatment, and were morphologically similar to untreated populations (Figure 6.4a). They were confirmed as viable using a resazurin metabolic assay that showed insignificant changes after 24 h of nanoparticle exposure (Figure 6.4b).

As a next step, co-culture experiments were performed whereby the HEK-293T cultures were inoculated with an mCherry protein (red) expressing strain of *E. coli* and then treated with nanoparticles in light and dark conditions (Figure 6.4a). Both celly types in the untreated controls remained viable and there was a proliferation of the invading bacteria. For the treated cells in dark there was some decrease in the absolute number of viable bacteria. In contrast, the light-treated cultures exhibited almost complete elimination of the bacteria population, leaving behind the human cells. These experiments demonstrate a significant difference in susceptiblility between certain bacteria and eukaryotic cells.

In this chapter, the potential utility of CdTe QDs as light-activated antimicrobial agents was presented and discussed. It was shown that this effect was due to the application of visible light and arrested the growth of both lab strains and MDR bacteria. The applicability as a therapy was investigated by quantifying the effect of the nanoparticles on human cells in both mono- and co-culture conditions, with the latter providing a proof-of-concept for the therapy. Additional work on the mechanism behind these therapeutic agents is discussed in Chapter 7, and attempts to improve QD stability and biocompatibility are presented in Chapter 8.

Methods

Synthesis Chemicals. 3-Mercaptopropionic acid (≥99%) was purchased from Acros Organics. Cadmium(II) chloride (technical grade), 10 mM phosphate-buffered saline, oleic acid (90%), copper(II) acetylacetonoate (≥99.99%), indium(III) acetate (99.99%), sulfur (99.5%), and oleylamine (technical grade) were purchased from Sigma Aldrich. Tellurium -325 mesh powder (99.99% metal basis), and selenium -325 mesh powder (99.5%) were purchased from Alfa Aesar. Sodium borohydride (98%), and sodium hydroxide (≥97.0%), were purchased from Fisher Scientific. Compressed nitrogen (pre-purified), and oxygen (ultra-high purity) were purchased from Airgas. Ethanol (200 proof) was purchased from Decon Laboratories INC. All purchased materials were used as provided without further purification.

CdTe Quantum Dot Synthesis and Sterilization. Deionized water was initially degassed using bubbling nitrogen for 30 min. 1 mL degassed water was used to dissolve $NaBH_4$ (35 mg, 0.93 mmol), and the resulting solution was transferred to a septum-capped 2 mL vial (Thermo Scientific) containing Te powder (40 mg, 0.31 mmol). -325 mesh was used for the reaction as coarser Te does not react well. A needle was inserted into the septum for outgassing during the reaction, which was allowed to proceed until the Te precursor solution became optically clear and light pink, and ceased sustained bubbling (~90 min). A cadmium precursor solution was created by dissolving $CdCl_2$ (3.7 mg, 0.020 mmol) and 3-mercaptopropionic acid (MPA, 1.8 µL, 2.2 mg, 0.021 mmol) in 10 mL of degassed water. The quoted values for MPA refer to a minimum, with more stable dots requiring three or four times more of the ligand. The reaction solution was made by mixing 250 µL of the cadmium (Cd) precursor solution, 250 µL degassed water, 1 µL of the Te precursor solution, and 10 µL of 0.5 M NaOH (total volume 511 µL). Batches were scaled up to a maximum of 1.5 mL total volume. 100 µL aliquots of the

reaction solutions were divided into PCR tubes (Thermo Scientific), and placed in a thermocycler (Bio-Rad T100). The tubes were held at 98°C for the reaction duration (approximately 1.5 h for CdTe-2.4, 2.5-3 h for CdTe-2.3, >5 h for CdTe-2.2). CdSe was prepared using the same procedure using Se (25 mg, 0.32 mmol) and $NaBH_4$ (25 mg, 0.66 mmol). The reaction between the two occurs at a much higher rate and the resulting solution is generally clear and colorless. The resulting dots are sterile and range in concentration from 2-3 μM. Two batches were always prepared in parallel in order to ensure a sample with the desired optical transition was obtained.

Prior to integration with cells, the CdX quantum dots were washed in the following manner. The stock was initially bulk centrifuged at 10,000 rpm for 5 min to precipitate unreacted materials and poorly stabilized QDs. An Omega 4K Nanosep filter was then sterilized with 100 μL 100% ethanol and centrifuged at 10,000 rpm for 6 min, and washed with 100 μL of sterile pH 11 water to remove any entrained ethanol. 200 μL of the stock QD solution was then filtered to dryness (about 6-7 min). Using more than 400 μL in the filter causes membrane failure in ~25% of cases. The dots were then washed twice with 100 μL of sterile pH 11 water (4 min centrifugation). The cleaned dots are then re-dispersed in pH 11 water and the concentrations were measured before incorporation with cells.[30]

Transition Electron Microscopy. TEM images of the nanoparticles were obtained on a Philips CM 100 at 80 kV for the CdTe. Particle size distributions were determined using ImageJ (Fig. 6.5).

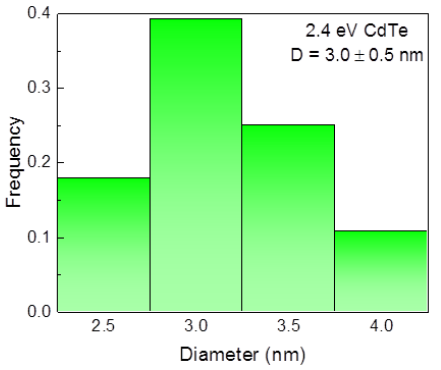

Figure 6.5 – Size distribution histogram of the CdTequantum dots.

Light Source for Cell Studies. Cells were illuminated using a tungsten lamp (GE 35200-EKE) placed externally of the incubator via a fiber optic cable. The lamp was equipped with filters to remove UV (Thorlabs FEL0400) and IR light, creating a bandpass filter from 400-700 nm (Fig. 6.6). The lamp spectrum was quantified using a Princeton Instruments Action SP2150 monochromator with filters to remove 2nd order diffraction (Thor Labs 315-710 nm Band Pass filter) with absolute intensities recorded with a NIST calib rated Newport Power Meter Model 1918-R (full lamp intensity entered the monochromator and the detector was paced 6 cm from the exit aperture). The spectrum was scaled based on readings using the fiber optic cable.

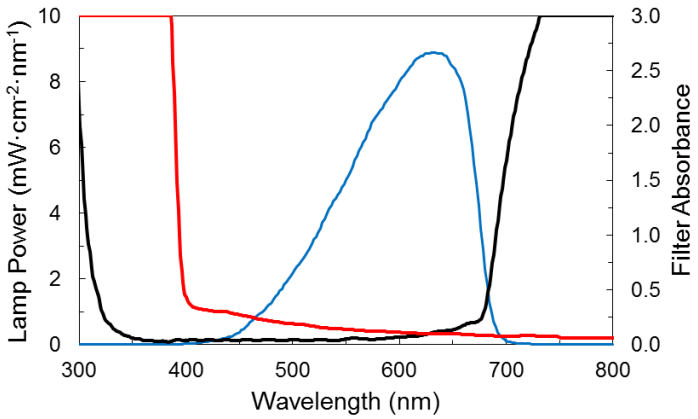

Figure 6.6 – Lamp emission spectrum (blue) and filter absorbance spectra (IR – black, UV – red) at 100% light intensity.

Statistical Analysis of Data. All biological replicate data was analyzed using single factor ANOVA with a significance of $p<0.05$ represented with an asterisk (*). Significance was analyzed in comparison to the no treatment populations. Error bars are standard deviation from average values. When transforming the optical density growth curves to a semi-log scale the initial reference (OD_0) was taken to be the average of all staring OD values for a give strain if the values were less than 0.1 due to the inherent error when measuring low optical densities. As all cultures were seeded with the same number of cells OD_0 deviations must be the result of this error at the initial time point. The error of this average was propagated throughout the

photoeffect parameter calculations in those instances. This was not done for the proliferation calculations due to the higher inter-replicate variability.

Bacterial Culture Conditions. MG1655 *E. coli* (ATCC 700926) was grown overnight in 1 mL 2% Luria Bertani broth (LB, Sigma Aldrich) at 37°C with shaking at 225 rpm. All MDR strains were cultured in 1 mL cation-adjusted Mueller Hinton broth (CAMHB, DIFCO). Individual replicates were grown from individual colonies grown on solid media. The strains were grown on 1.5% agar (Bectron Dickson) and their respective medium. MG1655 and MDR freezer stocks were stored in 40% and 10% glycerol at -80°C.

In vitro experiments were performed by diluting the overnight cultures 1:100 in 50 or 100 μL transparent flat-bottomed wellplates into their respective medium and QD concentrations. At least three wells contained only the medium to confirm sterility and subtract the background OD. Two plates were prepared for light and dark conditions, with the dark plate being wrapped in aluminium foil, and the light plate sealed with parafilm to prevent water loss. Both plates were secured into a shaking incubator at 37°C and 225 rpm. The fiber optic cable was placed directly above the center of the pate such that an even intensity was achieved over all cultures (measured and adjusted before each experiment). Optical density measurements were taken every 30 min for the first 3 h, and every hour following with a Tecan GENios at 562 nm (35 nm bandwidth).

Antibiotic Susceptability Testing. MDR strains were grown overnight in CAMHB and diluted to a 0.5 McFarland standard into corresponding antibiotic concentration. Some antibiotics were tested at two concentrations based on an intermediate resistance level reported in the CLSI breakpoints (Table 6.1). All antibiotics were purchased from Sigma Aldrich. The cultures were grown for 24 h at 37°C with shaking at 225 rpm. Resazurin sodium salt (Sigma Aldrich) solution was added at 24 h and allowed to react for 4 h, after which a color change to pink was used as an indicator of cell growth, and therefore, resistance.

Table 6.1

	Conc. ($mg \cdot mL^{-1}$)
AMP	8
FRX	1, 2
CHL	8
CLI	0.25, 0.5
GEN	1, 4
KAN	10
RIF	0.06, 0.5
STR	10
TET	1, 2

Colony-Forming Unit Analysis. Cultures were sampled at respective time points during a bacterial toxicity study and serial dilutions were performed ranging from 10^1-10^9. Dilutions were plated on respective solid media and grown at 37°C for 24 h. Images of cells on petri dishes shown in Figure 6.5 were treated for 7 h and diluted 10^3-fold before plating 10 μL on solid media. These images were processed to provide better contrast between the colonies and solid medium.

Mammalian Cell Culture. HEK-293T cells (ATCC CRL-3216) were recovered from freezer stocks in high glucose Dulbecco's Modified Eagle Medium (DMEM, HyClone) supplemented with glutamine and fetal bovine serum (HyClone). Cultures were grown at 37°C in 5% CO_2 with controlled humidity. Cells were passaged at 80% confluency with 0.25% trypsin (HyClone) with seeding densities calculated using a hemocytometer. HEK-293T cells were used between passages 11-20. Cells were stored in liquid nitrogen for long term storage.

Cells were seeded at 6,000 cells per well into a tissue culture treated 96-well plate (Cellstar). Media was supplemented with penicillin/streptomycin solution to minimize the

chance of contamination, however the penicillin/streptomycin solution was omitted in co-culture studies. Transmission (Figure 6.7) and fluorescence images of these cells were acquired on an EVOS FL microscope after 24 h of treatment. Three replicate images were taken by randomly imaging different locations in each well. After imaging, resazurin sodium salt solution was added and the fluorescence was measured using a Tecan GENios with an excitation and emission wavelength of 485 nm and 610 nm. The slope of the linear range of fluorescence was used as an evaluator of cell viability.

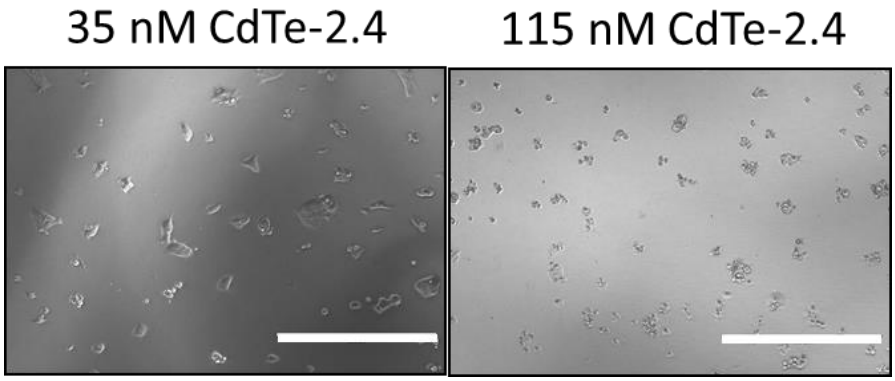

Figure 6.7 – HEK 293T cells at non-toxic (35 nM) and toxic (115 nM) concentrations of CdTe-2.4 which were used as morphological controls of healthy adhered cells and un-healthy non-adhered cells in the co-culture experiments. Scale bars are 200 μm.

Co-Culture Experiments. Co-culture experiments were carried out with HEK 293T cells and DH5α *E. coli* transformed with pFPV-mCherry plasmid. pFPV-mCherry was a gift from Olivia Steele-Mortimer (Addgene plasmid # 20956) and was used in these experiments for the constitutive production of fluorescent protein mCherry for imaging purposes.[34] 9,000 HEK 293T cells were seeded per well into 96 well plates and allowed to grow for 36 h to reach 80% confluency. The 96 well plates were pretreated with 0.01% poly-L-lysine (Sigma Aldrich) for one hour and rinsed twice with dPBS prior to seeding. Separate 96 well plates were used for the light and dark conditions. pFPV-mCherry *E. coli* were grown for 16 h from a single colony under above described bacterial cell culture conditions and with 100 μg/mL ampicillin sodium salt to maintain the plasmid. DMEM was removed from the HEK-293T cultures and supplemented with

DMEM containing approximately 10^5 bacterial cells mL^{-1}, 100 μg/mL ampicillin sodium salt, and respective q uantum dots. Plates were then placed in an incubator with 5% CO_2 at 37°C for 24 h either illuminated or shielded from light with tin foil.

Mammalian cells were then stained with the following procedure. Cells were washed twice with dPBS and fixed in 4% methanol-free formaldehyde for 5 min. The cells were again rinsed twice with dPBS and treated with 0.1% triton x-100 for 3-5 min. The cells were then rinsed with dPBS two times and stained with a 1x dilution of Phalloidin CruzFluor 488 Conjugate (Santa Cruz Biotechnology) for 20 min at room temperature. The cells were rinsed twice with warm dPBS and treated with 300 nM DAPI (Santa Cruz Biotechnology) for 5 min at room temperature. The cells were rinsed two final times with warm dPBS and covered with tin foil to protect the stains. All wash steps were carried out with pre-warmed 37°C dPBS. The fluorescence microscopy was complimented by morphological characterization using transmission (Figure 6.8), which was used to find the QD concentration tolerance of the HEK-293T cells.

Symbols and Abbreviations

AMP	-	Ampicillin	
CAMHB	-	Cation adjusted Mueller Hinton broth	
CFU	-	Colony-forming unit	
CHL	-	Chloramphenicol	
CLI	-	Clindamycin	
CRE	-	Carbapenem-resistant Enterobacteriaceae	
DAPI	-	4',6-diamidino-2-phenylindole	
DMEM	-	Dubelco's modified eagle medium	
dPBS	-	Dubelco's phosphate buffered saline.	
ESBL	-	Extended-spectrum β-lactamases	
FITC	-	Fluorescein isothiocyanate	
FRX	-	Ciprofloxacin	
GEN	-	gentamicin	
I_I	-	Inherent-inhibition	eq. 6.2
I_P	-	Photoinhibition	eq. 6.3
KAN	-	Kanamycin	
LB	-	Luria broth	
MDR	-	Multi-drug resistant	
MPA	-	3-mercaptopropionic acid	
OD_0	-	Optical density at the initial time point	eq. 6.1-3
OD_{DT}	-	Optical density of treated dark culture	eq. 6.2
OD_{DNT}	-	Optical density of untreated dark culture	eq. 6.2
OD_{LT}	-	Optical density of treated light culture	eq. 6.3
OD_{LNT}	-	Optical density of untreated light culture	eq. 6.3
OD_t	-	Optical density after *t* hours of treatment	eq. 6.1-3
PBS	-	Phosphate-buffered saline	
QD	-	Quantum dot	
RIF	-	Rifampicin	
S	-	Saturation bacterial growth	eq. 6.1
STM	-	Scanning Tunneling Microscopy	
STR	-	Streptomycin	
STS	-	Scanning Tunneling Spectroscopy	
t	-	Time	eq. 6.1-3
TET	-	Tetracycline	
λ	-	Lag-time	eq. 6.1
μ	-	Growth rate	eq. 6.1

References

1) LeClerc J. E., et al. *Science* **1996**, *274*, 1208-1211.
2) Chatterjee A., et al. *Proc. Natl. Acad. Sci. USA* **2011**, *108*, 9721-9726.
3) Courtney C. M., Chatterjee A. *ACS Infect. Dis.* **2015**, *1*, 253-263.
4) World Health Organization. Global Tuberculosis Report **2012**.
5) Centers for Disease Control and Prevention. Antibiotic Resistance Threats **2013**.
6) He M., et al. *Nat. Genet.* **2013**, *45*, 109-113.
7) Chang H., et al. Lipsitch. *Microbiol. Mol. Biol. Rev.* **2015**, *79*, 101-116.
8) Blair J. M. A., et al. *Nature Rev. Microbiol.* **2015**, *13*, 42-51.
9) Falgas M. E., Bliziotis I. A. *Int. J. Antimicrob. Agents* **2007**, *29*, 630-636.
10) Lu Z., et al. *Langmuir* **2008**, *24*, 5445-5452.
11) Brayner R., et al. *Nano Lett.* **2006**, *6*, 866-870.
12) Medintz I. L., Mattoussi H. *Phys. Chem. Chem. Phys.* **2009**, *11*, 17-45.
13) Huang X., et al. *J. Am. Chem. Soc.* **2006**, *128*, 2115-2120.
14) Lee C., et al. *Nano Lett.* **2005**, *5*, 709-711.
15) Connor E. E., et al. *Small* **2005**, *1*, 325-327.
16) Yu B. P. *Physiol. Rev.* **1994**, *74*, 139-162.
17) Thannickal V. J., Fanburg B. L. *Am. J. Physiol. Lung Cell. Mol. Physiol.* **2000**, *279*, L10005-L1028.
18) Imlay J. A. *Nature Rev. Microbiol.* **2013**, *11*, 443-454.
19) Valko M., et al. *Int. J. Biochem. Cell Biol.* **2007**, *39*, 44-84.
20) Apel K., Hirt H. *Annu. Rev. Plant Biol.* **2004**, *55*, 373-399.
21) Kohanski M. A., et al. *Cell* **2007**, *130*, 797-810.
22) Dwyer D. J., et al. *Proc. Natl. Acad. Sci. USA* **2014**, *111*, E2100-E2109.
23) Ipe B. I., et al. *Small* **2005**, *1*, 706-709.
24) Rengifo-Herrera J. A., et al. *J. Sol. Energy Eng.* **2007**, *129*, 135-140.
25) Walker G. C. *Microbiol. Rev.* **1984**, *48*, 60-93.
26) Sun Q., et al. *Nano Lett.* **2014**, *14*, 101-106.
27) Courtney C. M., et al. *Nat. Mater.* **2016**, *15*, 529-534.
28) Zwietering M. H. et al. *Appl. Environ. Microbiol.* **1990**, *56*, 1875-1881.
29) EUCAST. Breakpoint Tables for Interpretation of MICs and Zone Diameters Version 5.0. http://www.eucast.org (accessed Oct. 20, 2015).
30) Yu W. W., et al. *Chem. Mater.* **2003**, *125*, 2854-2860.

Chapter 7
The Mechanism of CdTe's Therapeutic Action

The size-controllable optical properties of cadmium chalcogenide quantum dots (QDs), especially their bright and tunable emission spectrum, have prompted their investigation as biological probes and markers.[1] There have been concerns about the inherent toxicity of these particles due to their constituent elements,[2–4] mostly coalescing around fears of leaching.[5] However, the available literature indicates that leaching is a minor contributor to overall toxicity, with the primary effect potentially arising due to the perturbation of the redox homeostasis of the targeted cells.[6–10] This has been observed to be tied to photostimulation of the quantum dots, with an increased light flux lowering the LD_{50} of exposed cells,[11] the implication being that the excited charge carriers can be transferred to different aqueous targets. This chapter investigates the mechanism of action induced by CdTe QDs, which Chapter 6 has shown to be readily phototoxic when exposed to visible light.[12]

The identity of the species formed by CdTe upon light stimulation is hinted at using the redox-active dye DCFH-DA. When

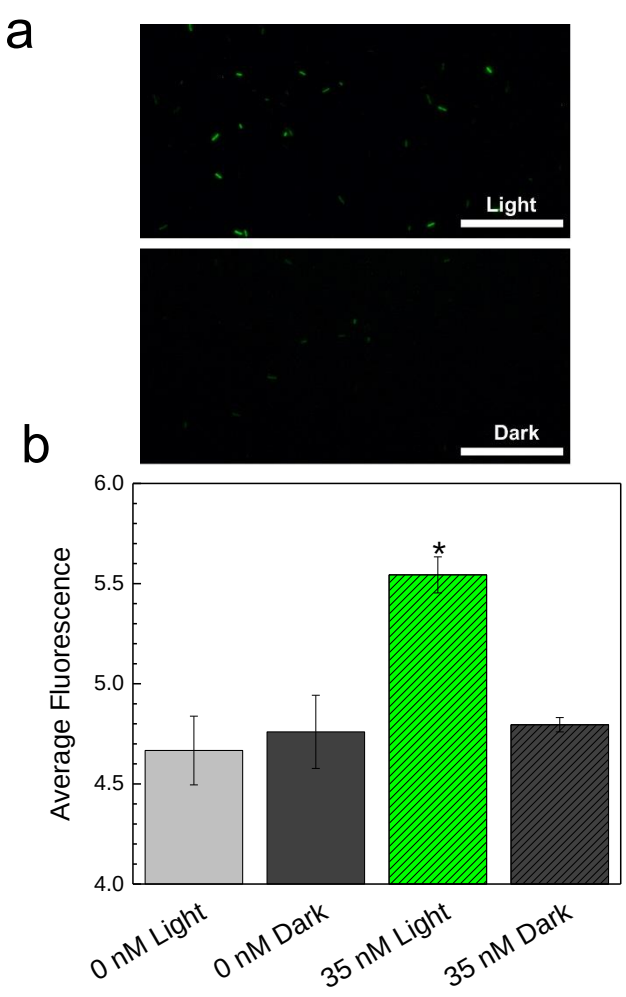

Figure 7.1 – **a.** Images of *E. coli* stained with DCFH-DA and exposed to CdTe in light and dark (60 μm scale bars). **b.** Result of FACS at various conditions.

this molecule is exposed to a variety of oxidizing agents it reacts to form a fluorescein derivative exhibiting bright green emission (Figure 7.1a). When cell cultures are rigorously maintained in dark conditions there is minimal background fluorescence from the dye, but when exposed to light the QD-generated species lead to significant emission. Flow cytometry was used to confirm that only only those cells exposed to both light and CdTe-2.4 exhibited significant increases in reactive oxidative species (Figure 7.1b). While this indicates that the charge carriers excited upon light stimulation lead to the formation of redox-active species, their precise identities are not readily apparent from this assay.

Given the previous observations of radicals being generated by CdS,[13,14] QD suspensions were investigated by electron paramagnetic resonance spectroscopy (EPR) to quantify any formation from CdTe. Due to the short lifetimes (ns-μs) of the initially formed species in aqueous media, the spin trap 5,5-dimethyl-1-pyrroline *N*-oxide (DMPO) was used to make them visible at the necessary time scales.[15–17] In this scheme, radicals react with the resonance double bond of DMPO to form a stable oxygen-centered radical (Figure 7.2a). Each adduct will yield an

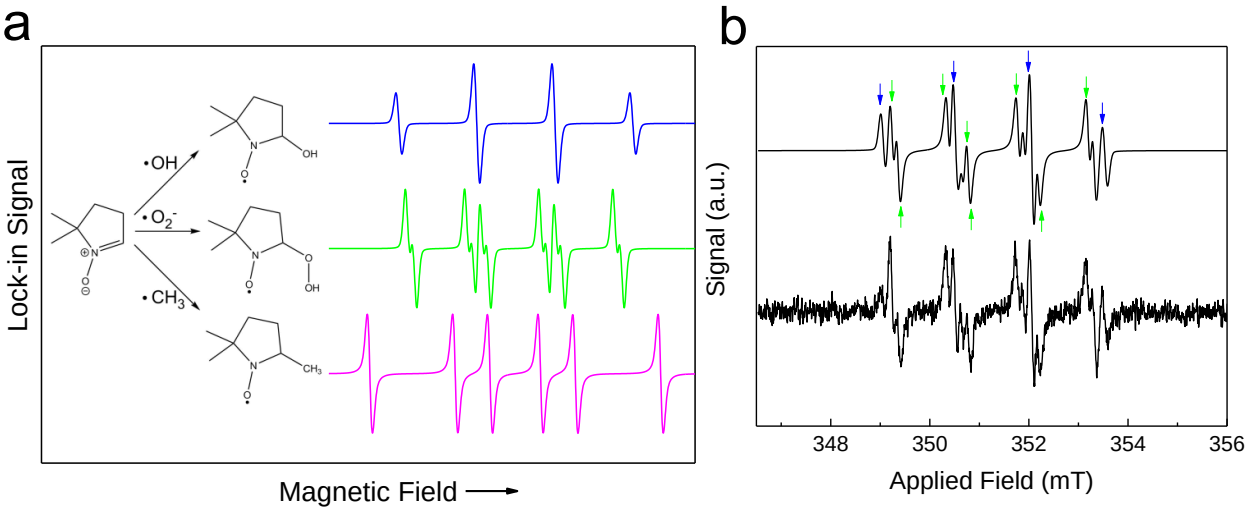

Figure 7.2 – **a.** Common DMPO-radical adducts and their simulated EPR spectra. **b.** Measured spectra of CdTe-2.4 in dark and after light exposure with simulated spectra as a linear combination of hydroxyl and superoxide radicals (marked features).

identifiable EPR spectrum based on the spin coupling with nearby spin-active nuclei, which can be simulated and fit to acquired spectra.

The first EPR measurements of CdTe were conducted under nominally dark conditions to provide a baseline for comparison after stimulation (see methods for sample preparation). Aside from a SiO_2 E' defect arising from the quartz capillaries (subtracted in all spectra), there is a strong quartet of peaks whose hyperfine coupling well match the theoretical spectrum of hydroxyl radical-DMPO adducts (DMPO-OH, not shown). Such a signal likely arises due to the incomplete sequestering of the particles from light during sample preparation, and confirms that the long-term products of CdTe upon stimulation are hydroxyl radicals. Irradiating the same sample with 365 nm light results in an overall increase in radical signal and the addition of new features to the previous hydroxyl adducts (all reported spectra are the light spectrum with the dark spectrum subtracted). Simulating the obtained spectrum as a linear combination of hydroxyl and superoxide radicals yields a matching curve which predicts all of the observed features (Figure 7.2b). An experiment utilizing the singlet oxygen trap TEMPO matched previous

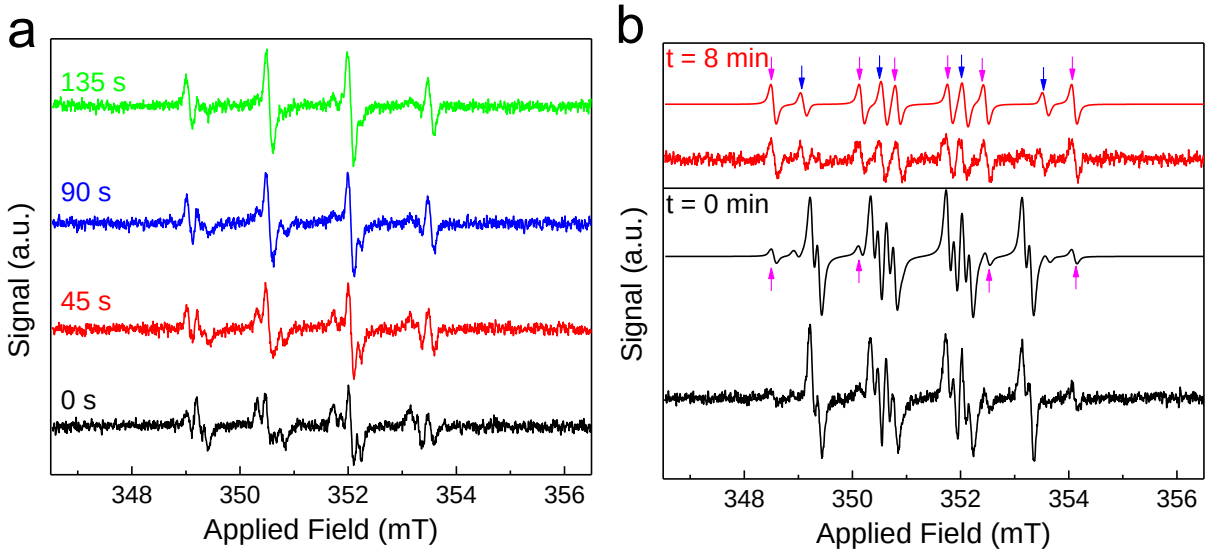

Figure 7.3 – **a.** Time evolution of the EPR spectra after the illumination of CdTe. **b.** Observed and simulated EPR spectra of illuminated CdTe in the presence of 10vol% DMSO initially and over time.

reports[18] showing no detectable formation by EPR implying the generation of these radicals only. Thus, while it is clear that both hydroxyl and superoxide radicals are formed upon light stimulation, the exact electron transfer reactions deserve further investigation.

Tracking the EPR signal post-illumination allows the quantification of the relative contribution of each radical as a function of time. For CdTe, this is reflected in the increasing signal contribution from DMPO-OH and the attenuation in the quantity of DMPO-OOH, such that after 2-3 min superoxide is present in minimal amounts (Figure 7.3a). Repeating the experiment in the presence of dimethyl sulfoxide (DMSO) can determine whether the hydroxyl radicals are formed from dismutation of the DMPO-OOH adduct to the more stable DMPO-OH, or if they are formed externally in solution through acid/base and fenton chemistry. In the latter case, hydroxyl radicals will bind to the sulfur of DMSO and release methyl radicals into solution, which can then be detected by DMPO (equation 7.1). Immediately after light stimulation there are characteristic features of DMPO-CH_3 in the acquired spectra, which become dominant over time at the expense of DMPO-OH and superoxide radicals (Figure 7.3b, pink arrows). Thus, it is likely that superoxide radicals are formed first using the photoexcited electrons of CdTe, which over time dismute in solution to hydroxyl radicals.

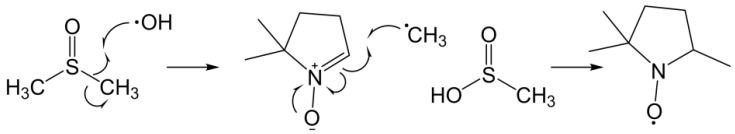

(7.1)

Though oxygen-centered radicals are toxic in their own right, it is necessary to confirm whether they are the direct actors or if a further oxidized species is the specific source of the phototoxicity. As Luria broth (LB) is a complex medium, it is not possible to determine which of the sugars, proteins, or lipids would be involved, therefore a control experiment was devised where *E. coli* were suspended in phosphate buffered saline (PBS) only. Measurements by EPR

show that the same radical species are formed in this medium, which only accelerates the conversion of superoxide to hydroxyl radicals due to the increased concentration of metal cations. Because no growth is occuring in this medium, an endpoint metabolic assay was used to quantify cell viability (Figure 7.4a). As the same photoeffect is present as was previously shown in Chapter 6 under these conditions (Figure 7.4b), these radicals are apparently directly responsible for the phototoxic outcome.

While direct oxidation of water is unlikely given the bandgap of the CdTe particles, to confirm that the initial font of radicals consists of solely superoxide a measurement was conducted in the presence of the superoxide dismustase (SOD) enzyme. Immediately, there is a strong attenuation in the total radical signal under these conditions, with a 95% decrease (Figure 7.5a). Over time, the signal is further reduced such that the number of spins is near the detection limit of the spectrometer. As both superoxide and hydroxyl radical signals were diminished, it can be concluded that the hydroxyl radicals are formed through pathways starting from superoxide, and not through direct oxidation of water via the photogenerated CdTe hole.

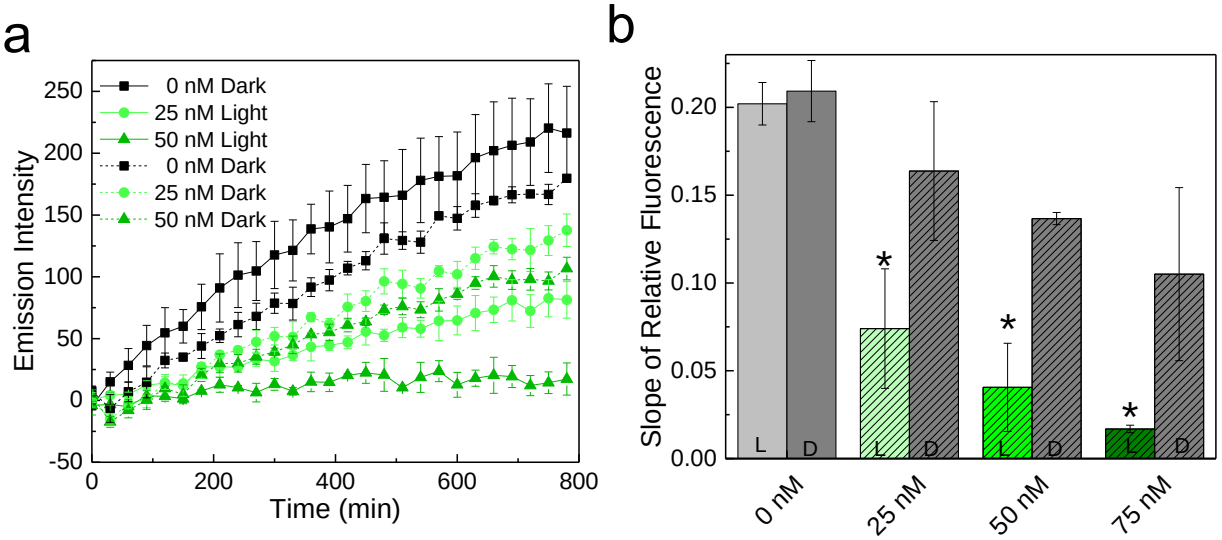

Figure 7.4 – **a.** Resazurin metabolic assay of *E. coli* post-exposure to CdTe-2.4 at specified conditions in PBS media. **b.** Relative slope of the emission curves with asterisks indicating significant differences between light and dark cultures.

The simplest route of superoxide formation would involve the direct electron transfer from CdTe quantum dots to advantageous dissolved oxygen. To confirm this hypothesis, water was partially degassed under flowing nitrogen and used as the suspending medium. As in the presence of SOD, the initial radical signal was strongly attenuated under the same measuring conditions, thus confirming the initial radical source (Figure 7.5b). Taken together, these results explain previous observations that cell cultures grown in anaerobic environments are significantly less susceptible to phototoxicity in the presence of CdTe.[12]

While the photoexcited hole is incapable of directly oxidizing water, it must also be involved in a half reaction to complete the redox cycle. While potential hole quenchers are available in cellular media, the observation of radical production in distilled water implies other sources. As the only other major component in those experiments was the ligand, an experiment was conducted where excess MPA was added to a CdTe suspension that was periodically measured by NMR spectroscopy (Figure 7.6a). Under illumination, this resulted in the conversion of MPA to the correspoding disulfide dimer. Thus, the bound ligands will over time act as sacrificial reducing agents during radical produciton, and will be consumed first due to

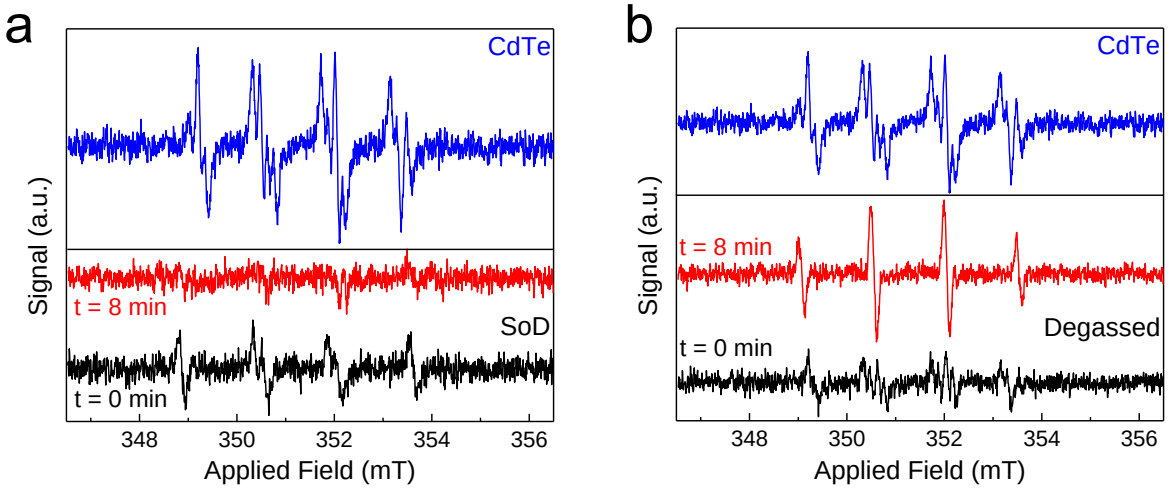

Figure 7.5 – Attenuating the number of available radicals compared to nominal production via the addition of **a.** superoxide dismutase and **b.** by partially removing dissolved oxygen.

their close proximity to both the quantum dots and adjacent ligands. The complete cycle can then be drawn as in Figure 7.6b.

Of the two species, hydroxyl radicals are generally viewed as the more toxic,[19] which arises from several mechanisms of action. All four of the DNA bases are susceptible to hydroxyl attack[20,21] through proton abstraction, adduct formation, ring breaking, and strand cleavage, and are likely the source of CdTe-induced DNA damage reported in the literature (Figure 7.6b).[22] Cell membranes are also susceptible to hydroxyl radical attack through lipid peroxidation,[23] which is an effect that has sometimes been reported during experiments with CdTe QDs.[24–26] The resulting membrane damage is self-propagating, and may then allow additional quantum dots access within the cells.

All of the previous experiments were done with one size of CdTe, with an average bandgap of 2.4 eV (CdTe-2.4), due to its previously observed phototoxicity. One of the most readily apparent consequences of quantum confinement is the blue-shifting of a particle's optical properties as it becomes smaller (Figure 7.7a). A consequence of this change that is rarely mentioned is the concomitant change of the bandedge redox potentials. As electron transfer from

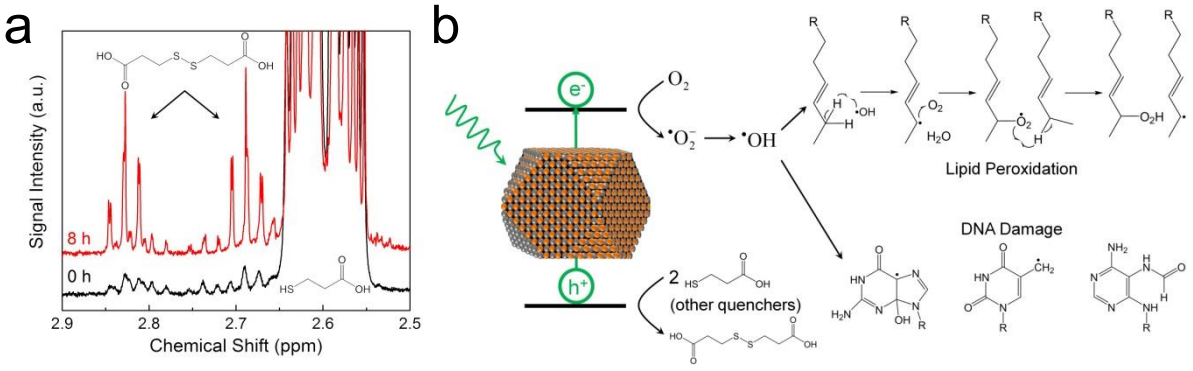

Figure 7.6 – **a.** NMR spectra of a CdTe/MPA solution under illumination. **b.** Complete redox system with potentially toxic reactions in cells.

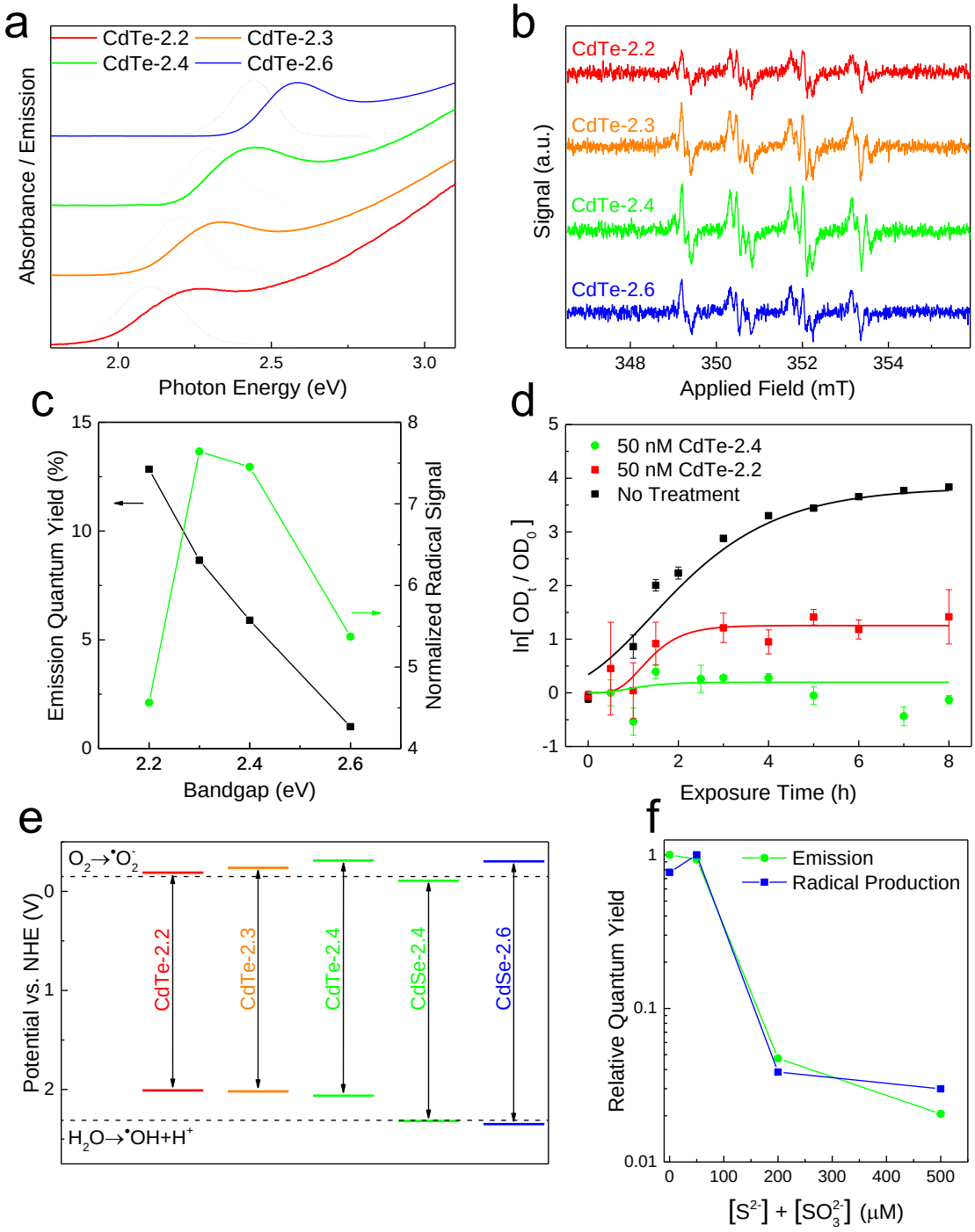

Figure 7.7 – **a.** Absorbance and emission spectra of different sized CdTe quantum dots. **b.** Un-normalized EPR spectra of the CdTe sizes after 30 s of UV stimulation. **c.** Photoluminescence quantum yield and integrated EPR signal as a function of quantum dot bandgap. **d.** Growth curves of E. coli exposed to different quantum dot sizes at the same concentration versus untreated controls. **e.** Conduction and valence band positions for the CdTe and CdSe quantum dots on the NHE scale. The potentials of pertinent redox half-reactions are marked by dashed lines. **f.** Effect of hole quenchers on the photoluminescence and radical quantum yields.

CdTe to dissolved oxygen will depend on the specific QD potential, the size of the particle can thus have a significant impact on the level of radical production. To quantify this, a range of visible light-absorbing CdTe quantum dots were synthesized and their radical production under light stimulation was quantified.

While the nature of the radical species does not change with particle size, it appears the total number of spins reaches a maximum between the 2.3 and 2.4 eV particles (Figure 7.7b). The total integrated signal from these measurements, normalized by sample absorbance at the exciting wavelength, was used to calculate the relative number of spins (N_S) produced by each particle size (Figure 7.7c). To obtain the total radical signal, the obtained EPR spectra were integrated twice with respect to the magnetic field (B), with the first integration yielding a curve directly proportional to the absorbance spectrum and the total integral of that being proportional to the total number of spins in solution (eq. 7.2). The normalization factor is the absorbance of each sample at 365 nm rather than concentration due to the changing extinction coeffients for each size at the exciting wavelength, which makes the result analagous to a quantum yield. This analysis shows that there is indeed an ideal size range where CdTe can efficiently transfer its excited electrons to dissolved oxygen. This result is consistent with the observation that particles outside of that range have a diminished phototoxic effect (Figure 7.6d).

$$N_S = A_{365}^{-1} \iint S(B)\, dB dB \tag{7.2}$$

Plotting the redox potentials of each particle size against the half-cell reactions for reducing oxygen and oxidizing water it becomes clear why this occurs (Figure 7.7e).[27] The valence bands of each CdTe size, which remain relatively constant, are well out of range of water oxidation and supports the observation that CdTe cannot form hydroxyl radicals directly. The majority of the potential shift with size occurs in the valence band,[28] with smaller sizes achieving

larger over-potentials with respect to oxygen reduction. The significant reduction in signal from CdTe-2.2 thus results from almost half of the particles in the synthesized size distribution lacking the necessary energy to facilitate the electron transfer.

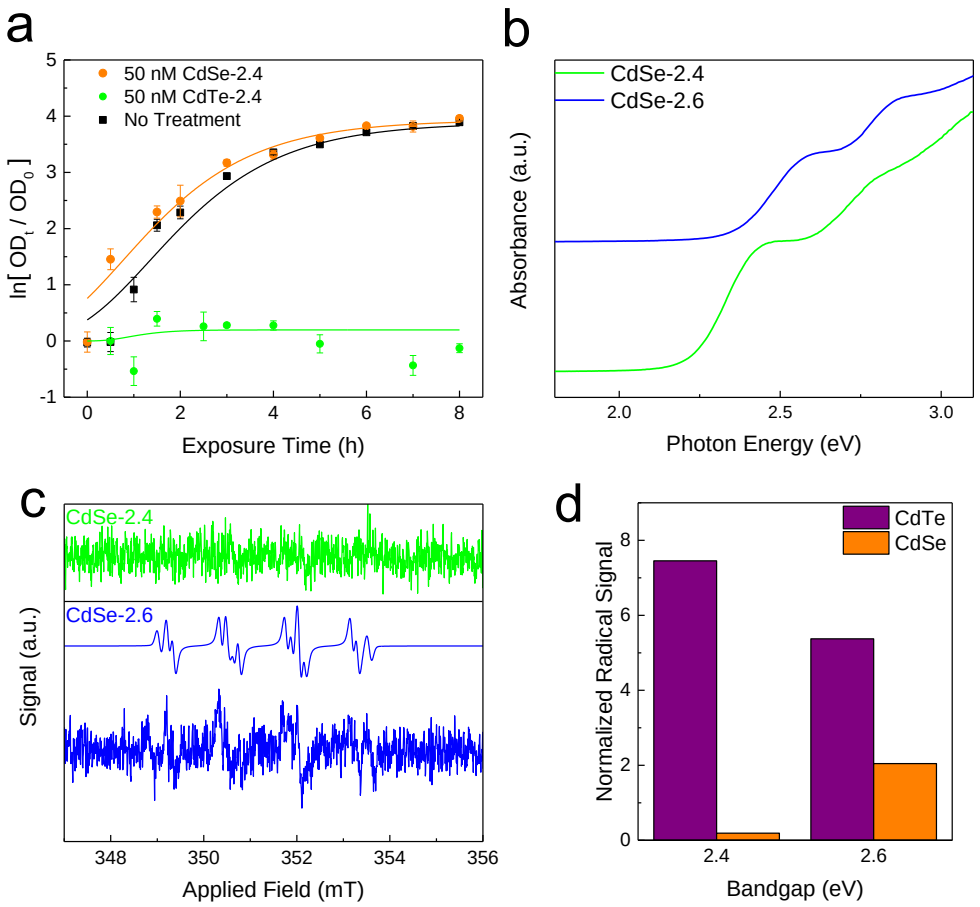

Figure 7.8 – **a.** Growth curves of E. coli exposed to CdSe-2.4 and CdTe-2.4 at the same concentration versus untreated controls. **b.** Absorbance n spectra of different sized CdSe quantum dots. **c.** Un-normalized EPR spectra of the CdSe sizes after 30 s of UV stimulation. Simulated spectra are shown above the experimental. **d.** Integrated EPR signal as a function of quantum dot bandgap comparing CdSe to CdTe.

A difference arises when comparing CdTe-2.3 and CdTe-2.4. The latter has a larger over-potential, and should thus be better able to have more of the synthesized particles align with oxygen reduction, but both sizes produce nearly the same number of spins. The primary difference between the two, other than size, is that CdTe-2.3 has a significantly higher emission quantum yield, which indicates more charge carriers are available at the long lifetimes required

for the kinetics of the electron transfer (Figure 7.7c). This principle is exemplified by CdTe-2.6, which has the highest overall reduction potential but lowest quantum yield, and thus diminished radical production. The link between emission quantum yield and radical yield can be easily visualized using quenching species that reduce both simultaneously (Figure 7.7f), and show that, provided the potentials are equal, a more emissive nanoparticle should be better able to generate radicals.

Measuring redox potentials in this way can help predict why otherwise similar quantum dots can have disparate effects. For example, while both possess the same bandgap, CdTe-2.4 and CdSe-2.4 have completely different light-activated effects on *E. coli* (Figure 7.8a).[12,29] Based on their potential, the CdSe-2.4 particles are incapable of donating electrons to dissolved oxygen or of oxidizing water and hence have no effect, which matches previous EPR reports investigating the material.[13,30] However, like CdTe, the conduction band of CdSe changes with size such that blue-absorbing CdSe-2.6 (Figure 7.8b) possess the proper redox potential for oxygen reduction. Measuring both by EPR reveals minimal superoxide radical production from CdSe-2.4 as expected, while significant quantities are produced by CdSe-2.6 (Figure 7.8c). The overall number is still quite low compared to CdTe of the same potential (Figure 7.7 d), likely due to the poor emission quantum yield of aqueous CdSe, but demonstrates the size-dependent redox character of quantum dots and the important effect that size has on redox chemistry and antimicrobial applications.

In this chapter the role of aqueous cadmium chalcogenide QDs in producing radical species has been clarified and expanded upon. CdTe was shown to produce superoxide radicals upon electron donation to dissolved oxygen, and this latter species then dismutes to hydroxyl radicals as typically seen in previous reports on QDs. The significant dependence of radical

generation on material and size was also shown, which demonstrates the necessity of properly tuning the electronic structure of quantum dots for engaging in desired redox reactions. The tunability of quantum dots can thus potentially recommend the same nano-scaled material for interacting with a variety of different targets.

Methods

Quantum Dot Synthesis. CdTe was synthesized using the same method as described in Chapter 6 with different sizes obtained by changing the reaction time. CdSe was synthesized using the same general protocol only using 25 mg of selenium powder and 20 mg of sodium borohydride at the appropriate steps.

Quantum Dot Characterization. Absorbance spectra were measured on a VWR UV-1600PC UV/VIS spectrophotometer. Emission spectra were obtained on a calibrated PTI fluorimeter with quantum yields calculated relative to a fluorescein isothiocyanate standard (Sigma). A Philips CM 100 microscope was used to obtain TEM images of the nanoparticles, the size distributions of which were analyzed using ImageJ (Figure 7.9). The resolution and noise level of the microscope did not allow the discrimination of the CdSe samples by size, resulting in the same average diameter for both. Based on optical correlations CdSe-2.6 should have a diameter of 2.1 nm with CdSe-2.4 at 2.5 nm.

Redox Staining. Cultures of *E. coli* were exposed to CdTe-2.4 for 2 h in light and dark conditions and then incubated with 2',7'-dichlorofluorescin diacetate for 5 min. When exposed to oxidizing species like hydroxyl radicals the dye reacts to a green florescent form. The sample was then diluted 1:10 into PBS and measured using a CyAn ADP Analyzer Cytometer (488/530) to evaluate the relative fluorescence, and therefore oxidative species, in the treated cells. Samples were kept on ice throughout the procedure. From each sample 30,000 cells were counted. Flow

cytometry data was analyzed using MATLAB and excel software. Images shown in Figure 7.1a were acquired using a Zeiss inverted microscope with a camera affixed to the eyepiece.

Non-Growth Media Experiment. MG1655 *E. coli* cells were diluted 1:100 into M9 media and allowed to grow for 3 h. After 3 h the cells were centrifuged for 10 min at 5,000 rpm and rinsed with PBS twice. The cells were then re-suspended in PBS with respective CdTe-2.4 in light and dark. After 6 h, resazurin sodium salt solution (Sigma Aldrich) was added and the fluorescence (485/610) was measured where an increase in red fluorescence was an indicator of cell viability.

Redox Potentials. The values of the reduction and oxidation potentials of the various nanoparticles were determined using the same STS methods as described in Chapter 2. The error

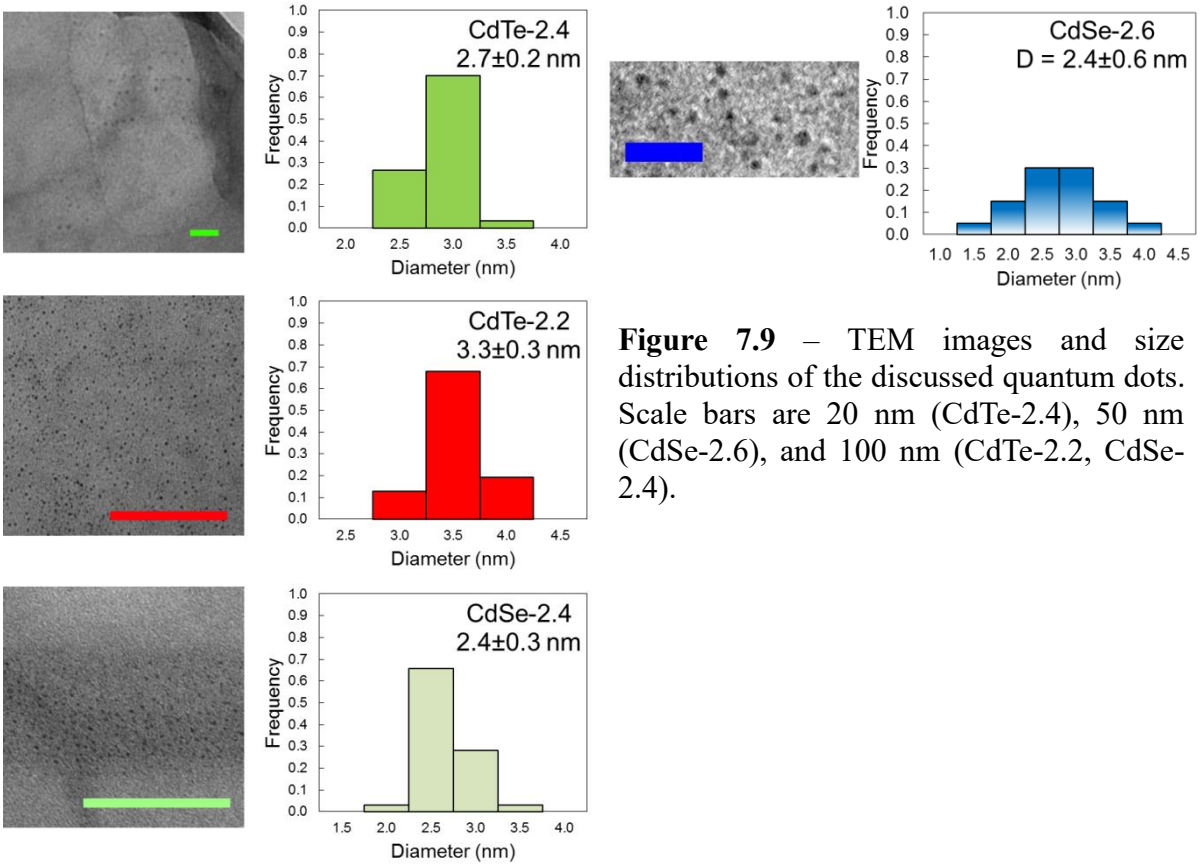

Figure 7.9 – TEM images and size distributions of the discussed quantum dots. Scale bars are 20 nm (CdTe-2.4), 50 nm (CdSe-2.6), and 100 nm (CdTe-2.2, CdSe-2.4).

associated with the average values reported in Figures 7.7 are summarized in Table 7.1.

Table 7.1

	CdTe			CdSe	
E_g (eV)	2.2	2.3	2.4	2.4	2.6
CB (V)	-0.2±0.1	-0.2±0.1	-0.3±0.1	-0.1±0.1	-0.3±0.2
VB (V)	2.0±0.1	2.0±0.1	2.1±0.1	2.3±0.1	2.3±0.1

Electron Paramagnetic Resonance. In order to observe all radical species on the required timescales the quantum dots were initially filtered using 3k centrifuge filters and washed three times with pH 11 water and once with double-distilled water (DDW) in an attempt to remove any transition metal cations which are capable of Fenton chemistry. Without this step the observed superoxide dismutase to hydroxyl radicals so quickly that their adducts with DMPO are not visible by EPR. A trial using pentetic acid as a chelator, as is commonly used in the literature, to sequester metal ions resulted in no radical signal due to the fact that its addition completely quenched the QD emission, indicative of competitive interactions with the dots themselves. 10vol% DMSO in DDW was used in the experiment reported in Figure 2a to test the source of hydroxyl radicals. The experiment utilizing SoD (Sigma) was prepared by dissolving

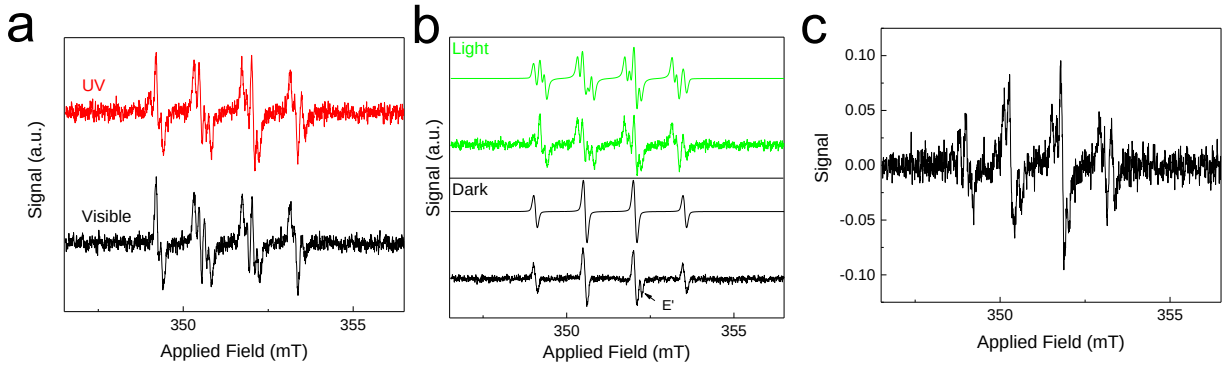

Figure 7.10 – **a.** EPR spectra acquired after exposure of CdTe-2.4 to UV and visible light. **b.** Comparison of light and dark acquired spectra for CdTe. **c.** Spectrum of CdSe-2.4 in light with 350% higher concentration, 160% higher microwave flux, and 4 additional capillary tubes compared to Figure 7.8.

1-2 mg of the enzyme in 100 μL DDW which was used to re-disperse the filtered QDs. The degassed water was prepared by bubbling nitrogen through DDW for 1 h and using a portion of it to re-disperse the filtered QDs.

All spectra were acquired using a Bruker Elexsys Elexsys E 500 spectrometer equipped with an SHQE cavity. Aqueous samples containing 1vol% DMPO (Dojindo) were loaded into three quartz capillaries for each experiment. A control measurement using a visible light source was used to confirm that the same radical species are formed during EPR studies and cell culture (Figure 7.10a). The signal under dark conditions was first quantified to provide a baseline of comparison for each sample (Figure 7.10b). Radicals were photogenerated by exposure to 365 nm light for 30 s unless otherwise specified (Figure 7.10c), and were immediately re-measured. Spectra were simulated using Spinfit (Bruker) which fit the measured curves to linear combinations of specified theoretical radical signals. None of the reported spectra have been re-scaled.

Quantum Yield and Quenching. A stock solution of fluorescein isothiocyanate (FITC) was prepared by diluting 0.8 mg in in 1 mL pH 11 water. This was subsequently diluted 50x to yield the reference solution. The quantum dot samples were filtered in the same manner as discussed previously and diluted 10x to yield solutions with absorbances at 475 nm between 0.03-0.05. The emission spectrum was measured on a Photon Technologies International fluorimeter for each solution starting at 485 nm using 475 nm excitation with three independent replicates for each sample. Recorded intensities were corrected with a NIST calibration file to account for detector sensitivity. Quantum yield was calculated using equation 7.3, where Φ_X is the quantum yield of x, A_X is the absorbance of x, I_X is the measured intensity spectrum, and λ is

the wavelength. Measured quantum yields range from 4-5(±1)% in this size range with no significant size dependence.

$$\frac{\Phi_{QD}}{\Phi_{FITC}} = \frac{A_{FITC}\int_{\lambda_1}^{\lambda_2} I_{QD}\lambda d\lambda}{A_{QD}\int_{\lambda_1}^{\lambda_2} I_{FITC}\lambda d\lambda} \tag{7.3}$$

Interactions with redox targets were probed by tracking fluorescence quantum yield upon the addition of electron and hole quenching small molecules. Emission was quenched by adding 2 μL of quencher solution to 100 μL of QD stock (quantum yield was within measurement error when 2 μL of water was added as a control). Silver nitrate (electron quencher), a 1:1 mixture of sodium sulfite and sodium sulfide (hole quenchers), and methylene blue (redox indicator) all exhibit concentration dependent quenching of the QD photoluminescence (Figure 7.11a). With a high light fluence the photoluminescence quantum yield can recover over time as the quencher in solution is used up, and indicates that the interactions between QDs and redox targets is reversible (Figure 7.11b, using 365 nm light, spectra recorded with a calibrated Ocean Optics USB 4000 detector).

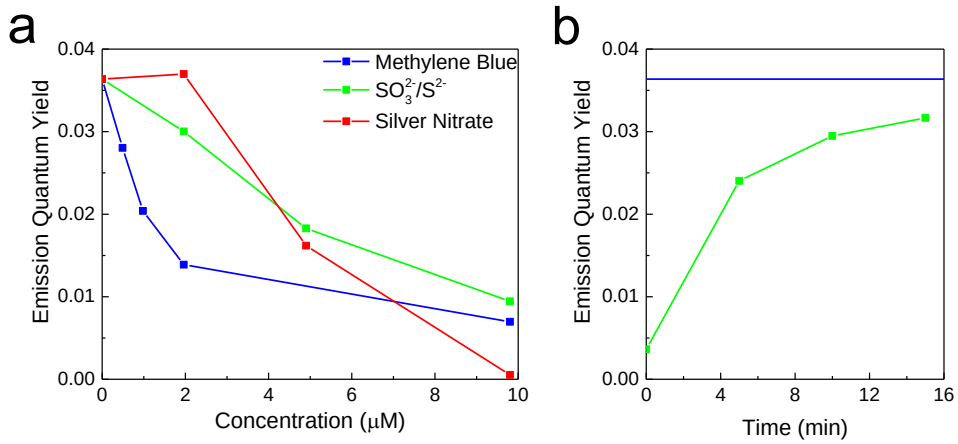

Figure 7.11 – **a.** Effect of emission quenchers on the emission quantum yield of CdTe-2.4. **b.** Emission recovery after exposure to high concentrations of methylene blue during constant stimulation.

Though of very low intensity there was still detectable emission from the CdSe QDs in aqueous media (Figure 7.12). For both, the spectra exhibitied far red-shifted peaks which were significantly broadened, indicative of primarily defect-mediated emission. The overall quantum yield was difficult to determine accurately due to the signal strength being below the linear range of the instrument, though an order of magnitude estimate of ~0.2% was applicably for both.

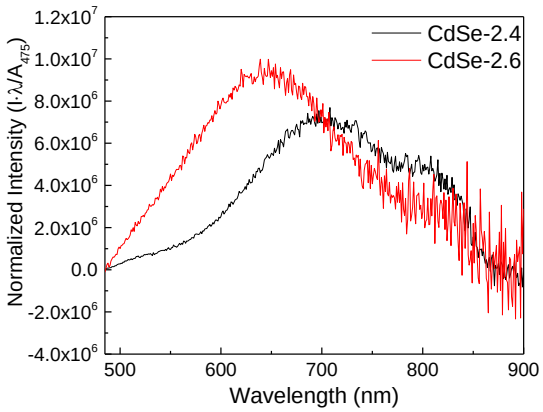

Figure 7.12 – Normalized emission spectra for the two CdSe sizes.

Cyclic Votammetry. Cyclic voltammetry (CV) measurements were carried out in a three-electrode configuration with a glassy carbon plate electrode, platinum wire electrode, and Ag/AgCl (1M KCl) as working, counter, and reference electrode, respectively using a Bio-Logic SP-200 Research Potentiostat.PBS was used as an electrolyte. Typical scan rates ranged from 0.1-1 V/s. All the voltammograms were corrected using the NHE scale. For CV measurements with MG1655 *E. coli* cells, the solution was sonicated to lyse the cells so membrane penetration was not a factor.

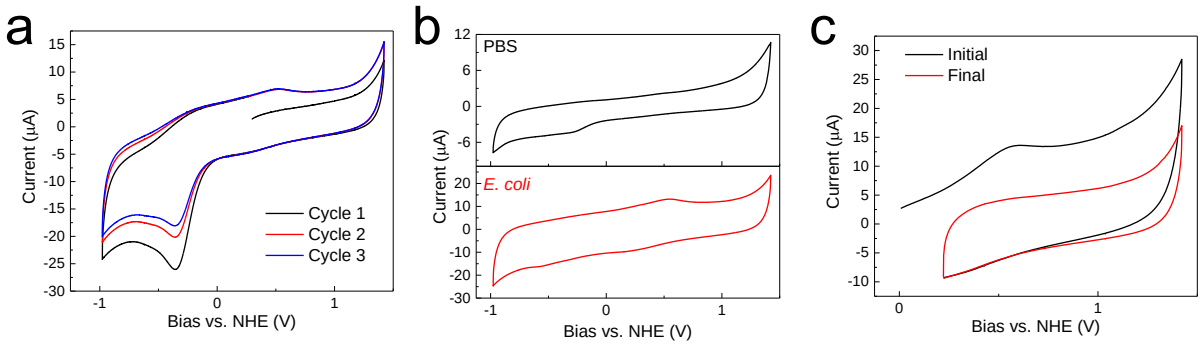

Figure 7.13 – **a.** CVs of PBS solutions exhibiting decreased superoxide signal with successive scans. **b.** CVs of PBS and *E. coli* suspended in PBS. **c.** Successive scans of suspended *E. coli* exhibiting rapid loss of superoxide-to-hydroxyl radical interconversion signal.

Cycling CdTe-2.4 QDs through complete redox cycle shows dual peaks corresponding to superoxide and hydroxyl radicals (-0.38 and +0.5 V, Figure 7.13a). Both peaks remain visible when the particles are incorporated into cells (Figure 7.13b). However, direct hole injection into CdTe QDs does not lead to the broad peak attributed to water oxidation, and removing the redox half-cycle for the formation of superoxide radicals leads to rapid decay in the hydroxyl peak (Figure 7.13c).

Symbols and Abbreviations

A	-	absorbance	eq. 7.2-3
B	-	applied magnetic field	eq. 7.2
CB	-	conduction band	
CV	-	cyclic voltammetry	
DCFH-DA	-	2',7'-dichlorofluorescin diacetate	
DDW	-	double-distilled water	
DMPO	-	5,5-dimethyl-1-pyrroline *N*-oxide	
DMSO	-	dimethyl sulfoxide	
E_g	-	bandgap	
EPR	-	electron paramagnetic resonance	
FACS	-	fluorescence-activated cell sorting	
I_X	-	emission intensity spectrum of x	eq. 7.3
LB	-	Luria broth	
LD_{50}	-	dose at which 50% of a population die	
NHE	-	normal hydrogen electrode	
NMR	-	nuclear magnetic resonance	
N_S	-	number of spins	eq. 7.2
PBS	-	phosphate-buffered saline	
QD	-	quantum dot	
S	-	EPR signal	eq. 7.2
SoD	-	superoxide dismutase	
STS	-	scanning tunneling spectroscopy	
TEMPO	-	(2,2,6,6-tetramethylpiperidin-1-yl)oxyl	
VB	-	valence band	
λ	-	wavelength	eq. 7.3
Φ_X	-	emission quantum yield of x	eq. 7.3

References

1) Michalet X., et al. *Science* **2005**, *307*, 1208-1211.
2) Emmerson B. T. *Ann. Inter. Med.* **1970**, *73*, 854-855.
3) Schroeder H. A., et al. *J. Chronic Dis.* **1970**, *23*, 227-243.
4) Ba L. A., et al. *Org. Biomol. Chem.* **2010**, *8*, 4203-4216.
5) Derfus A. M., et al. *Nano Lett.* **2004**, *4*, 11-18.
6) Bakalova R., et al. *Nano Lett.* **2004**, *4*, 1567-1573.
7) Nagy A., et al. *ACS Nano* **2012**, *6*, 4748-4762.
8) Cho S. J., et al. *Langmuir* **2007**, *23*, 1974-1980.
9) Bruneau A., et al. *Environ. Toxicol.* **2013**, *30*, 9-25.
10) Gagné F., et al. *J. Environ. Monit.* **2010**, *12*, 1556-1565.
11) Schneider R., et al. *Nanotechnology* **2009**, *20*, 225101.
12) Courtney C. M., et al. *Nat. Mater.* **2016**, *15*, 529-534.
13) Ipe B. I., et al. *Small* **2005**, *1*, 706-709.
14) Harbour J. R., Hair M. L. *J. Phys. Chem.* **1977**, *81*, 1791-1793.
15) Bhattacharjee S. *Curr. Sci.* **2005**, *89*, 1113-1121.
16) Buettner G. R., Mason R. P. *Methods Enzymol.* **1990**, *186*, 127-133.
17) Buettner G. R. *Free Radic. Biol. Med.* **1987**, *3*, 259-303.
18) Dumas E., et al. *Environ. Sci. Technol.* **2010**, *44*, 1464-1470.
19) Watts R. J., et al. *Adv. Environ. Res.* **2003**, *7*, 961-968.
20) Cadet J., et al. *Mutat. Res. Fund. Mol. Mech. Mut.* **1999**, *424*, 9-21.
21) Burrows C. J., Muller J. G. *Chem. Rev.* **1998**, *98*, 1109-1152.
22) Wang C., et al. *Talanta* **2010**, *80*, 1228-1233.
23) Mylonas C., Kouretas D. *In Vivo* **1999**, *13*, 295-309.
24) Lu Z., et al. *Langmuir* **2008**, *24*, 5445-5452.
25) Gagné F., et al. *Aquat. Toxicol.* **2008**, *86*, 333-340.
26) Choi A. O., et al. *J. Nanobiotechnology* **2007**, *5*, 1.
27) Buettner G. R. *Arch. Biochem. Biophys.* **1993**, *300*, 535-543.
28) Goodman S. M., et al. *Appl. Phys. Lett.* **2015**, *106*, 083109.
29) Wang L., et al. *J. Hazard. Mater.* **2010**, *177*, 1134-1137.
30) Kauffer F. A., et al. *J. Hazard. Mater.* **2014**, *268*, 246-255.

Chapter 8
Improving the Stability and Efficacy of CdTe Therapeutics

One of the observed limitations of the light-activated therapy presented in Chapter 6 is that the length of time over which the particles are active is between 4-6 h, after which arrested bacterial growth can resume (Figure 8.1a). While the inhibition quantified at eight hours (Figure 8.1b) reflects the decreased extent of bacterial growth, over time the cultures will recover under the tested conditions. This means that the nanoparticles are becoming inactivated either due to light exposure or as an effect of the biological medium. To first examine the degradation kinetics of the therapeutic action, an experiment was conducted where the emission and absorbance spectra of CdTe cores were measured in phosphate-buffered saline with and without light stimulation (no bacterial cells).

The absorbance spectra during light exposure reveal schanging features indicative of several degradation processes (Figure 8.1c). At six hours, there was notable scattering at longer wavelengths which is indicative of aggregation. As the particles are electrostatically stabilized, this is only possible when the ligands are sufficiently removed.[1] Because the carboxylic acid group of the 3-mercaptopropionic acid (MPA) ligands, which electrostatically stabilize the particles, remains un-protonated at pH 7.4 (pKa 4-4.5),[2] this instability is likely due to the desorption of the ligands either through re-protonation (pKa > 10)[3] or photocatalyzed dimerization of the thiol termini.[4] Both processes are likely contributors as it has been shown that ligand binding is a meta-stable state near neutral pH,[1] which explains why the same end result is obtained in dark after twenty four hours, while light exposure accelerates degradation through thiol oxidation.

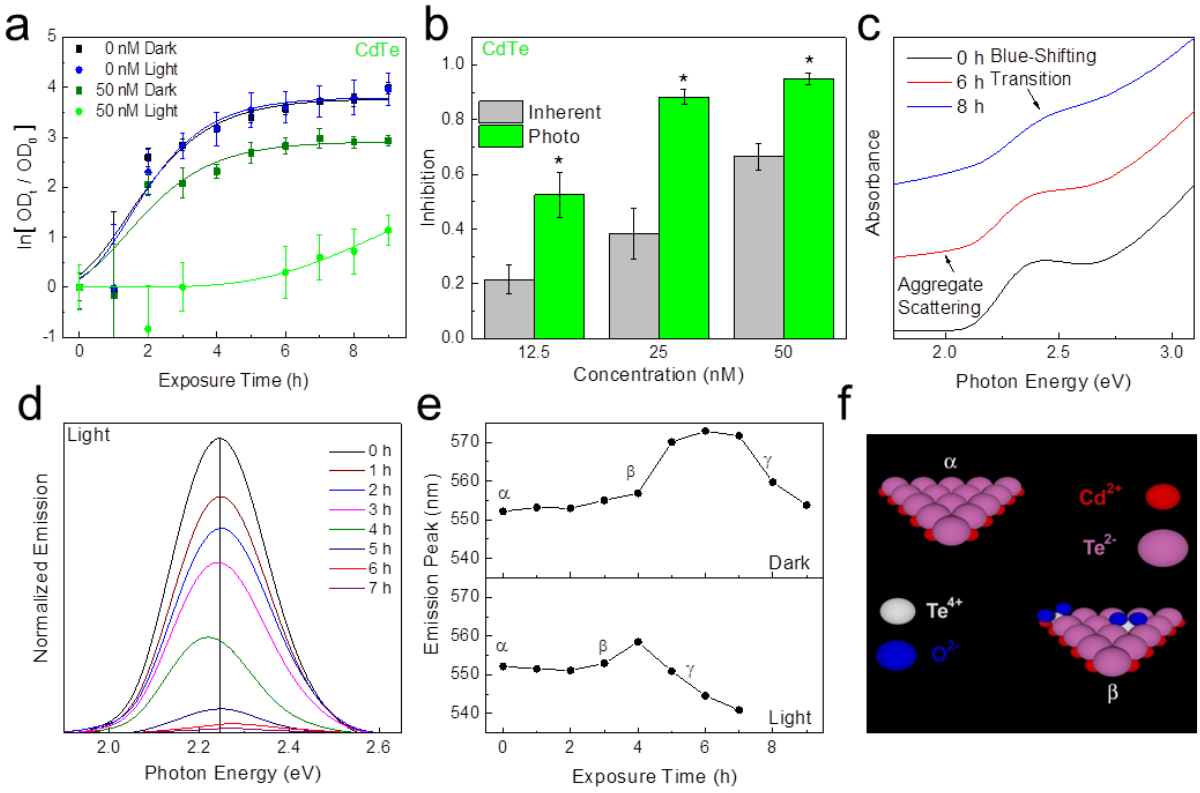

Figure 8.1 – **a.** Growth curves of *E. coli* exposed to CdTe-2.4 in light and dark. **b.** Inhibition as a function of CdTe concentration. Significant photoinhibition is denoted by an asterisk. **c.** Absorbance spectra of CdTe-2.4 during light exposure in PBS. **d.** Emission spectra over time during the degradation experiments. The original peak position is marked by the line. **e.** Degradation profiles of CdTe in light and dark with different phases labeled. **f.** Visualization of the oxidation of Te rich facets.

From the photoluminescence spectra obtained concurrently (Figure 8.1d), there is a clear attenuation in signal intensity over time and significant shifts in peak position, both of which are representative of chemical instability in a biologically relevant medium. Tracking the position of the emission peak reveals different regimes of particle degradation (Figure 8.1e). Starting from the initial state (α), there is a region of general red-shifting (β) which lasts until 4 and 6 h in light and dark. This behavior, which has previously been observed *in vitro*,[5] likely corresponds to the creation of oxygen defects on the surface of the nanoparticles which act as lower energy recombination centers. Long duration XPS studies of bulk CdTe exposed to aqueous environments report an oxygen rich surface, consisting primarily of CdO and TeO_2 (Figure

8.1f).[6] The initial defects are favored to form on the tellurium-rich facets due to the lack of ligands which could provide a diffusion barrier for incoming oxygen,[7] and the general instability of anionic tellurium in an aqueous environment.

After a maximum redshift, there is a rapid blue-shifting regime (γ), which indicates that the diameter of the emissive CdTe core is steadily shrinking. This is reflected directly in the absorbance spectrum, which exhibits a blue-shifting excitonic peak. Concomitantly, this regime produces the largest reduction in luminescence intensity, such that by seven hours no emission was detectable in the light-exposed sample, and indicates that the oxidized shell makes non-radiative recombination the kinetically favored relaxation pathway due to the plethora of defects. The accelerated changes probably correlate with the loss of protecting ligands as well. While the change in photoluminescence intensity may indicate that fewer photoexcited charge carriers are

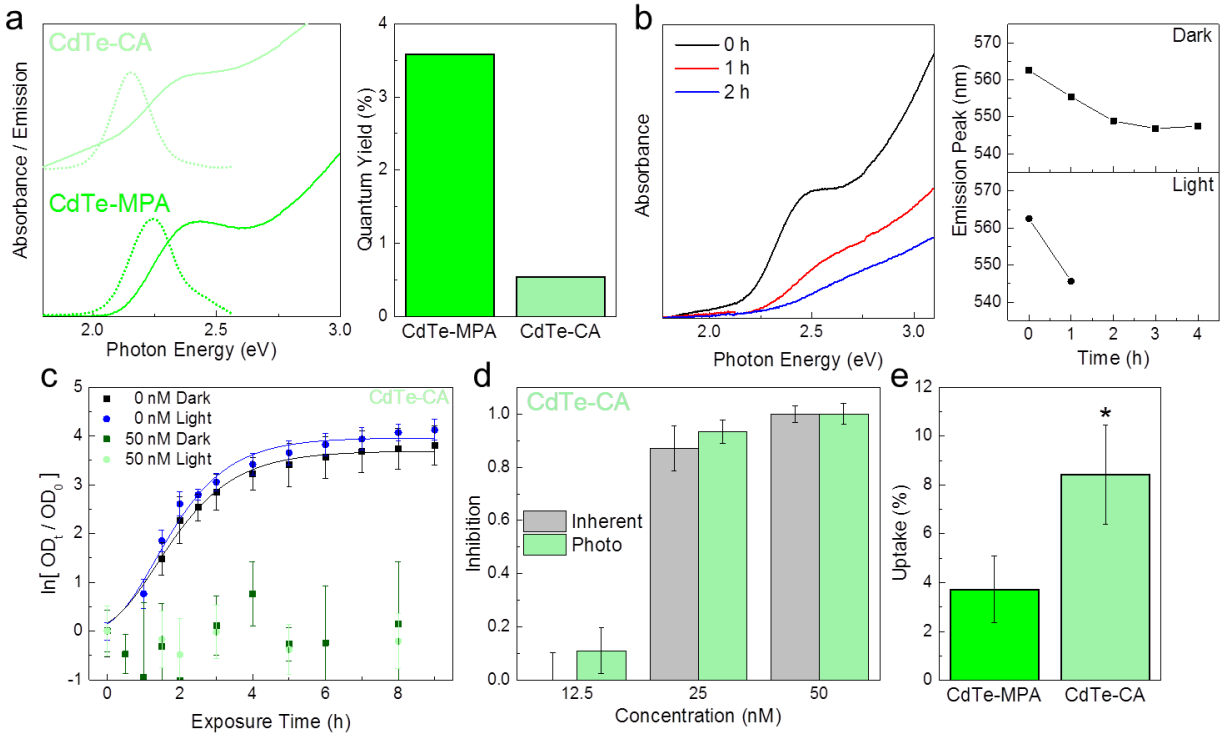

Figure 8.2 – **a.** Optical properties of CdTe-2.4 before and after ligand exchange. **b.** Absorbance and emission degradation profiles of CdTe-CA. **c.** Growth curves of *E. coli* exposed to CdTe-CA. **d.** Inhibition as a function of concentration. **e.** Relative QD uptake.

available for the therapeutic mechanism, the main result of the degradation is the shifting of the redox potentials and the formation of a barrier for interacting with the external medium. Thus, it is the goal of this chapter to evaluate different methods of increasing the stability of photoactive nanoparticles while retaining their anti-microbial effect upon light stimulation.

Ligand charge can have a significant effect on nanoparticle uptake and toxicity (Chapter), so the effect of these interactions and the resulting changes in phototoxicity initiated by switching from positive to negative ligands was investigated. CdTe with positive cysteamine ligands (CdTe-CA) were synthesized through ligand exchange of MPA coated dots as described previously.[8] The initial stocks were filtered and re-dispersed in pH 6 medium containing excess cysteamine, and were allowed to react overnight. The emission was characteristically attenuated as has been previously reported, and there were indications of aggregation even after a bulk-centrifuge step for removing poorly-stabilized particles (Figure 8.2a).

The degradation profiles of these particles were quantified in the same manner as the MPA-coated analogues (Figure 8.2b). Instead of the two-regime curve shown previously, the CA coated particles exhibited only blue-shifting emission and a rapid loss of emission intensity. After two hours of light exposure, the photoluminescence was below the detection limit of the instrument, while the population kept in dark was non-luminescent between four and five hours. This is reflected in the absorbance spectra, which show a rapid loss of colloidal stability with the increasing contributions of scattering, and chemical instability through the loss of the primary excitonic feature. Thus, it seems that in biologically-relevant media, positively charged ligands lead to lower stability overall than those coated with MPA.

From the observed growth curves the positively charged particles also exhibit far greater inherent toxicity than their negatively charged counterparts (Figure 8.2c). Above concentrations

of 12.5 nM, there are no significant changes in OD up to 9 h of exposure, and the inhibition in both light and dark approach the maximum value of 1 (Figure 8.2d). The increased toxicity of using such ligands has been discussed previously in the literature,[9] with the explanation that the positively charged coating can more strongly interact with the cellular membrane (and

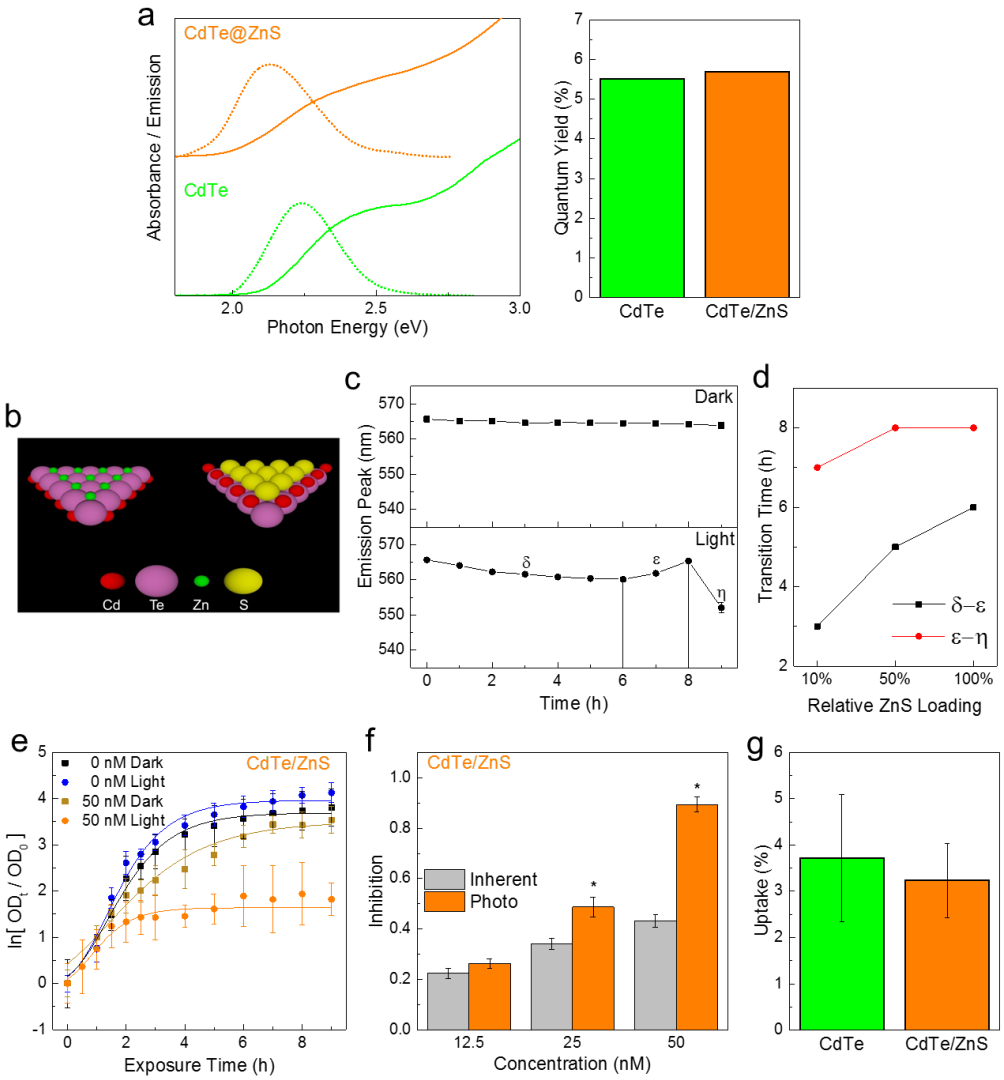

Figure 8.3 – **a.** Optical properties of CdTe/ZnS. **b.** Visualization of Cd and Te-rich facets post-deposition. **c.** Degradation profiles of CdTe/ZnS in light and dark. **d.** Transition times during degradation as a function of ZnS used in the syntheses. 100% is the shell thickness used in all other panels. **e.** Optical density growth curves of *E. coli* exposed to CdTe/ZnS. **f.** Inhibition as a function of concentration. Significant differences between inherent and photo-inhibition are marked with an asterisk. **g.** Relative QD uptake.

mitochondria in eukaryotes), which creates a much higher local concentration of nanoparticles around the cell. To test this idea, the uptake of CdTe-CA versus CdTe-MPA was measured.

Overnight cultures of MG1655 *E. coli* were diluted 1:10 into PBS with respective quantum dots, where the final concentration was 100 nM. The cultures were placed in a 37°C incubator and were shaken for 1 h to allow for uptake. The culture medium was then removed and the cells were pelleted, then washed twice with PBS and once with double-distilled water (DDW). After re-suspension in DDW the cells were diluted and submitted for ICP-MS analysis which quantified the elemental composition. By comparison to known standards, the total number of QDs associated with the cells was calculated as a total percentage of the initial number in each culture, represented in Figure 8.2e as the percent uptake. Comparing the negative and positively charged particles reveals that the CA-coated dots had over twice the association with cells, which is likely the source of the high inherent-inhibition. Thus, their poor stability and increased toxicity precluded positively-charged particles from being further considered.

In addition to lowering the colloidal stability of the particles, loss of the capping ligands allows oxygen more free access to the nanoparticle surface. One method of potentially increasing chemical stability regardless of ligand presence is to coat the particles with a thin shell of a more inherently stable material. In the past, several reports examining dots for fluorescent labeling have utilized type-I heterostructures consisting of an emissive CdX core enveloped in a thin shell of ZnS, which protects the emission intensity and decreases overall toxicity.[10–12] For therapeutic applications, the goal of increased stability with thicker shells is weighed against the increasing tunneling barrier for moving photogenerated charges from the core material to the intended targets.[13] There is also the potential effect of different chemical binding affinities between the core and shell metals, which could change the ability of the particles to efficiently interact with

the necessary species in the medium. Thus, for these experiments, ZnS shells were investigated which have sub-monolayer thicknesses.

CdTe-2.4 particles were filtered to remove unreacted starting materials and diluted to 2 μM in pH 11 water. Stock solutions containing zinc(II) nitrate and thiourea (sulfur source) were mixed in a 1:1 ratio with the quantum dot stock and fresh MPA, then allowed to react at 98°C for 1 h. The deposition of the shell material was identified optically by changes in the absorbance features and by red-shifting emission with greater coverage (Figure 8.3a). Similar behavior has been previously reported.[14-16] In the sub-monolayer regime, the most likely deposition mode is where the sulfur atoms deposit on cadmium-rich facets, while the zinc passivates the tellurium-rich areas (Figure 8.3b).

Quantifying the elemental composition of the ZnS coated core shells allows the calculation of the total surface coverage of the CdTe cores. A maximum coverage of about ~43% ZnS was obtained when the shell precursor solutions contained zinc and sulphur at concentrations of two mono-layers equivalent (MLE, 100%) ZnS relative to the cores. Shell formation does not have an appreciable impact on the fluorescence quantum yield in relation to the cores alone (Figure 8.3a), indicating that any benefit due to increased surface passivation is offset by the electronic structure changes at low loadings. Based on other reports,[17,18] these changes appear to have lesser impacts for CdSe/ZnS hybrids as the ZnSe bulk band positions are in a type-I alignment with CdSe naturally which allows increased luminescence due to passivation defects while limiting changes to the electronic structure at the interface.

Characterizing the degradation profile of the ZnS core-shells reveals different regimes of changes than the cores, and a greater innate stability (Figure 8.3c). There is an initial regime of slowly blue-shifting emission (δ), and while higher energy emission has been documented[19] for

the bulk transformation of ZnS to ZnO, the exact kinetic process for the oxidation of shell materials at or below the monolayer level is unclear. The observed blue-shifting effect is temporary, and similar red-shifting behavior as seen in the cores begins to take place (ε), followed by a rapid blue-shift and collapse of the emission intensity (η). These measurements support the hypothesis that the core-shell particles degrade significantly slower than the naked cores, lasting about twice as long. Persistence of the emission implies that CdTe/ZnS are able to continue generating redox species as well. In dark, there is enhanced stability as well, such that the small blue-shifting in the measurement time frame may be due to the application of UV light used to test the emission. The degree of ZnS coverage has an appreciable impact on degradation,

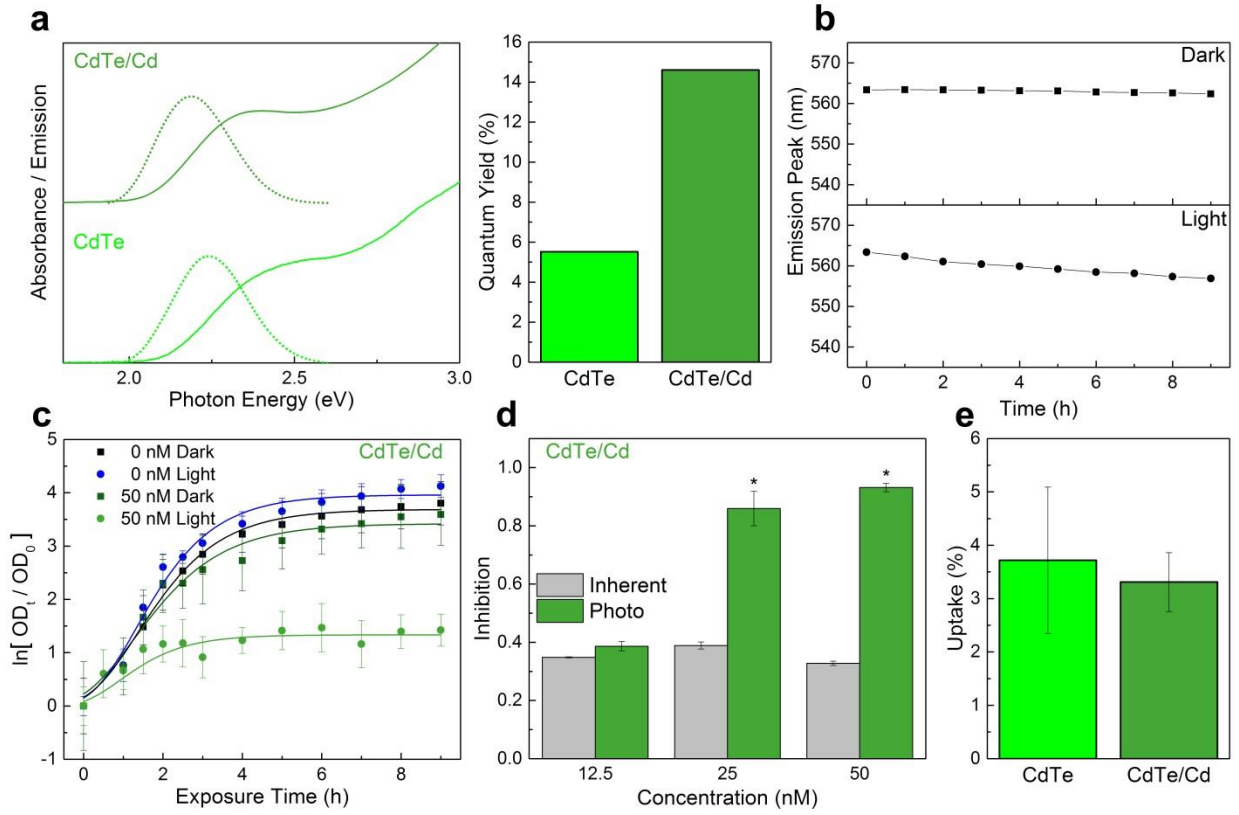

Figure 8.4 – **a.** Optical properties of CdTe/Cd. **b.** Degradation profiles of CdTe/Cd in light and dark. **c.** Optical density growth curves of *E. coli* exposed to CdTe/Cd. **d.** Inhibition as a function of concentration. Significant differences between inherent and photoinhibition are marked with an asterisk. **e.** Relative QD uptake.

with the transitions between phases occurring more rapidly with lower loading (Figure 8.3d), which supports the hypothesis that the observed changes are due to oxidation of the shell materials.

Like the cores, the CdTe/ZnS particles have a phototoxic effect on *E. coli* (Figure 8.3e) and a concentration-dependent inherent-toxicity similar to the cores (Figure 8.3f). There is, however, a decrease in the photoeffect at lower concentrations, likely due to the shell material interfering with charge utilization. This is reflected in the growth curves, where there are about two hours of comparable growth for the light exposed cultures which then flattens out to a lower saturation growth extent. Thus, it seems that a portion of the coating shell needs to be oxidized (δ) before the particles can reach their full therapeutic potential at later times. Because this was observed at sub-monolayer coverage, increasing the thickness will only serve to further attenuate the therapeutic efficacy even though the stability will be undoubtedly increased. It was also confirmed that these changes were not due to different levels of uptake between the cores and core-shells, because the core-shells are slightly larger than their uncoated counterparts (2.9±0.3 versus 3.2±0.5 nm, Figure 8.3g). There was no significant difference between the two samples with regard to the percent uptake under the conditions as previously described, and is thus indicative that the primary motivator for cell-association in this size regime is the ligand charge regardless of nanoparticle material.

An alternative to using a heterojunction for passivation would be to deposit additional cadmium on the tellurium rich facets. The only effect this would have on the electronic structure of the particles would be a slight decrease in bandgap due to the larger diameter, while the stability would likely increase due to the larger number of sites to which ligands could bind.[7] CdTe/Cd particles were synthesized by mixing a stock of CdTe cores (2 μM) with a mixture of

$CdCl_2$ and additional MPA in a 1:1 ratio, followed by reacting at 98°C for 15 min. Elemental analysis of these particles indicates there is a 42% increase in cadmium content compared to the cores, which translates to a 0.2 MLE coverage, implying near-complete passivation of the tellurium facets for a cation-rich quantum dot. The reduction in defects[20] is reflected in the photoluminescence quantum yield of the overcoated particles, which is over twice that of the untreated cores, while the slight absorbance red-shift confirms the larger dimeter of the particles (Figure 8.4a).

In terms of stability, the cadmium overcoated samples consistently outperform both the cores and CdTe/ZnS core shells (Figure 8.4b). Unlike any competitor, and most samples in dark, the overcoat particles were still luminescent after 24 h of irradiation and underwent much slower rates of degradation during the first nine hours. The degradation curve also consists of a single monotonic phase of slow blue shifting which appears to be characteristic of this type of treated sample. As there are no exposed tellurium facets to readily oxidize, degradation only consists of the buildup of CdO on the surface followed by slow inward diffusion. There was also minimal macro-aggregation observed during emission measurements (settling or distinct sources of emission) which is indicative of the greater number of capping ligands which can bind over the entire surface, and predicts a superior colloidal stability in biological media.

When tested *in vitro*, the overcoat quantum dots induce a stronger phototoxic effect (Figure 8.4c) than the ZnS counterparts while the inherent-toxicity remains consistent within the measured concentration range (Figure 8.4d). In addition to the higher phototoxicity than CdTe/ZnS, there is also less of an effectiveness lag, as evidenced by the OD curves showing stronger deviations from the dark and no treatment cultures at shorter exposure times. The more constant inherent inhibition is also reflective of the greater ligand passivation, which better

protects the cells from dark-catalyzed reactions and toxicity. As with the ZnS core-shells there is also no difference in uptake between the CdTe/Cd and core particles (Figure 8.4e), further emphasizing the dependence of uptake on the capping ligand.

While the cores and both of the core-shell particles exhibit a phototoxic response, it was necessary to determine whether the same mechanism applied in all cases. As shown in previous studies[13,21] and Chapter 7 the formation of radicals upon light stimulation of nanoparticles was quantified with electron paramagnetic resonance (EPR). From the obtained spectra in light there remain the same features consistent with superoxide and hydroxyl radicals (Figure 8.5a).[22] This was confirmed by simulating a combination of the two adducts which matches the features in the observed curves. These features are consistent for the cores and both of the core-shell particles, indicating that neither the interface states in the CdTe/ZnS or the slightly increased size of the CdTe/Cd are altering the electronic structure sufficiently to significantly change to phototoxic mechanism. When normalized by the sample absorbance, it is apparent that the CdTe core QDs have significantly higher yield of radical species compared to CdTe/ZnS core-shell QDs, which

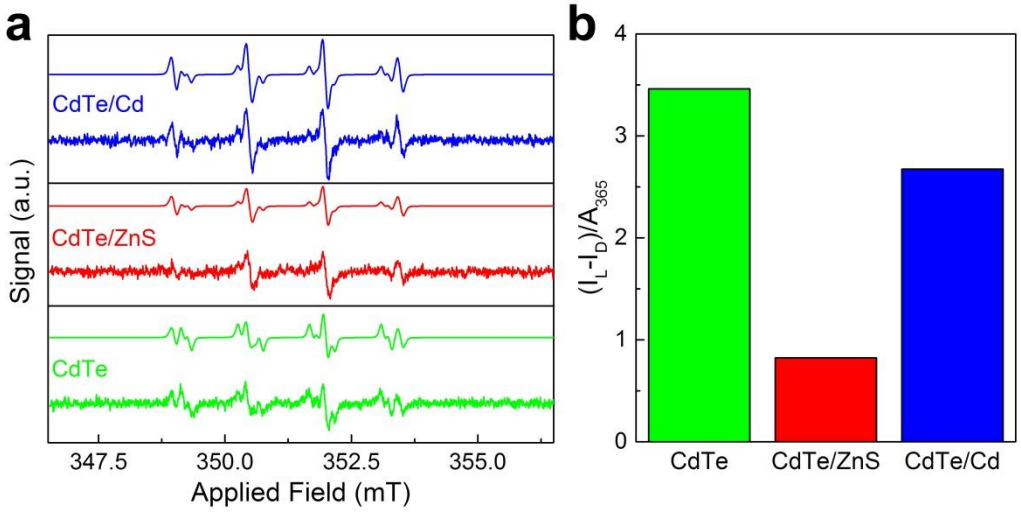

Figure 8.5 – **a.** EPR spectra of the cores and core-shells with simulations consisting of a linear combination of hydroxyl and superoxide radicals. **b.** Relative radical production for the three samples.

explains the observed difference in their respective photoeffect (Figure 8.5b). The production from CdTe/Cd shows similar attenuation though to a lesser degree, and explains why the observed growth curves fall between the effectiveness of the cores and CdTe/ZnS core-shells.

To further understand this behavior and elucidate the radical formation kinetics electrochemical impedance spectroscopy (EIS) mreasurments were completed for all three samples. This technique measures how photogenerated charges are transported to the QD surface, and their subsequent injecting into the adsorbed relevant species which forms the observed redox products (Figure 8.6a). Using analysis of Bode (Figure 8.6b) and Nyquist (Figure 8.6c) plots to fit an equivalent circuit diagram it is possible to obtain the solution resistance, resistance to adsorbate charge injection (R_{CT}), capacitance of the electrical double layer (C_{DL}),

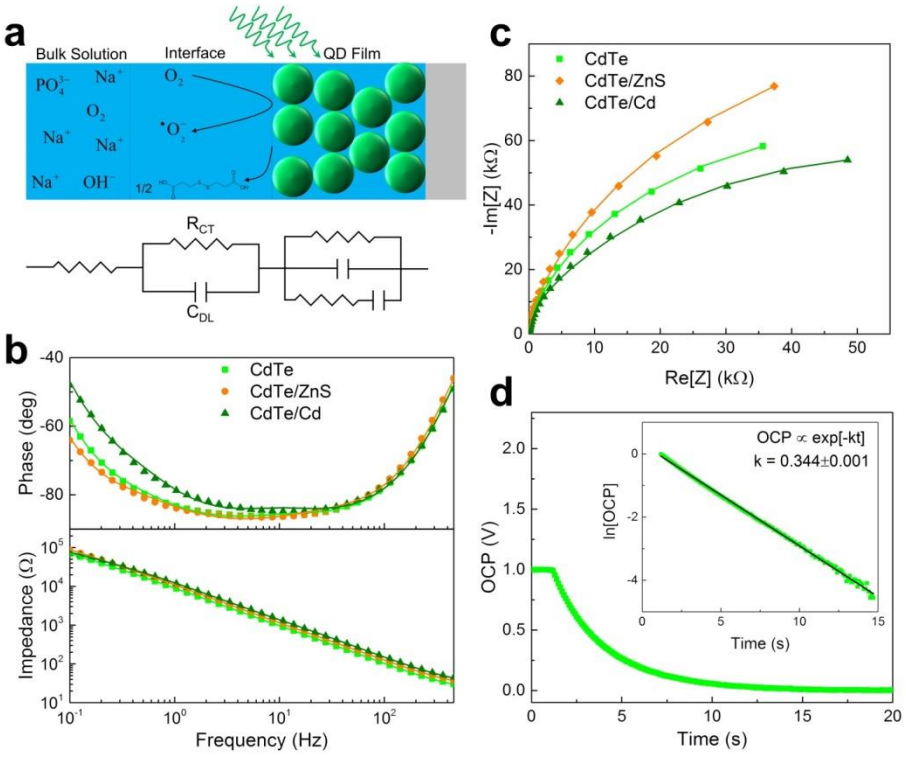

Figure 8.6 – **a.** Schematic illustrating EIS measurements and the equivalent circuit components for each part. **b.** Bode and **c.** Nyquist plots used to determine the interfacial parameters reported in Table 8.1. **d.** Open circuit potential decay of the cores with the linearized plot used to extract the rate of charge injection inset.

and inherent resistance to charge transport and QD defect state density. Comparing resistance to charge injection between the three morphologies it was observed that core QDs have the lowest resistance, with CdTe/ZnS and CdTe/Cd having 5- and 8-fold higher resistance to charge injection (Table 8.1). Also, the double layer capacitance of CdTe and CdSe/ZnS is higher than CdTe/Cd, normally indicating easier of transport of redox species even though the interfacial charge injection resistance is higher. This can likely be explained because the greater ligand coverage of the CdTe/Cd decreases the water to form a double layer between the ions and solution whereas the exposed anionic facets of CdTe and CdTe/ZnS yielded gaps. There is also the effect of increased hydrophobic spacing with the two methylene groups of MPA potentially causeing a decrease in the double layer capacitance as was shown on carbon nanotubes.[23] Overall O_2 may not be greatly affected by the local electric field in this situation anyway as it lacks charge.

The open circuit potential (OCP) decay was also tracked in the respective QDs as a function of time to extract the charge carrier lifetime kinetics (Figure 8.6d). The of OCP decay curves show that the overall photochemical process is faster in cores compared to the CdTe/ZnS core-shell QDs (Table 8.1). This observation is consistent with the quantified ROS radical generation observed via EPR and phototherapeutic effect *in vitro*. In CdTe/Cd, two modes of decay were observed: the faster recombination between photogenerated charge carriers, and the generation of radical species. This observation explains the anomaly betweena higher quantum yield and depressed radical generation observed by EPR (Chapter 7). While CdTe/Cd overcoated QDs improve the quantum yield and have higher number of photogenerated charges for ROS radical formation, the increased resistance to charge injection leads to recombination before they can be injected into the adsorbed oxygen to form superoxide radicals.

Table 8.1

	CdTe	CdTe/ZnS	CdTe/Cd
k (ms^{-1})	0.344±0.001	0.317±0.002	0.31±0.01 0.92±0.05
R_{CT} ($k\Omega \cdot cm^2$)	1.02±0.02	5.03±0.01	8.74±0.03
C_{DL} ($\mu F \cdot cm^{-2}$)	73.4±0.4	63.5±0.2	35.0±0.1

In this chapter modifications were made to phototoxic CdTe-2.4 with the goal of improving the overall therapeutic efficacy through stabilization. Positive ligands were found to be ineffective for this endeavor with enhanced degradation and inherent toxicity. Of the two core-shell style treatments CdTe/Cd proved to be the superior choice compared to CdTe/ZnS in both regards. In any case, the surface modifications did not have a significant impact on the phototherapeutic mechanism, only its efficiency. The effect of each treatment was to decrease the overall rate of radical production through greater charge injection resistance at the nanoparticle adsorbate interface. For CdTe/ZnS, this is likely due to the hetero-layer acting as a barrier for charge injection from the active core, while for CdTe/Cd it is plausible that the increased Cd coverage allows greater ligand coverage, which serves as an adsorption barrier for oxygen. Observations of core-shell interface interactions, while of limited relevance to therapeutics, raises interesting questions about nanostructured electronics and even bulk interfaces, such as whether a true type-I heterojunction is even possible for certain material combinations. Hypotheses about the formation of the interface defect states could be probed by STS (Chapter 2), though the ambiguity of how to characterize sub-monolayer shells remains a potential problem, as well as isolating single heteroatoms on a facet for probing.

Methods

Protocols not unique to this chapter may be found in Chapters 6 and 7.

Cysteamine Ligand Exchange. A stock of cysteamine-hydrochloride (CA) was created by dissolving CA (7.7 mg, 0.10 mmol) in 1 mL of pH 6 water. This was used to re-disperse CdTe-2.4 cores which were filtered, and washed twice with double-distilled water (DDW). The QDs were then kept in the dark at room temperature overnight. Prior to use the particles were bulk-centrifuged at 10 krpm for 5 min to remove poorly-passivated QDs, and washed in a similar manner using PBS.[8]

ZnS Core-Shell Synthesis. A stock 100X solution of zinc and sulphur sources was created by dissolving $Zn(NO_3)_2 \cdot 6H2O$ (609 mg, 5.57 mmol) and thiourea (75 mg, 1.0 mmol) in 10 mL DDW. For a synthesis, 100 µL of the 100X stock was diluted into 10 mL of freshly de-gassed DDW which served as the zinc-sulphur precursor stock. 200 µL

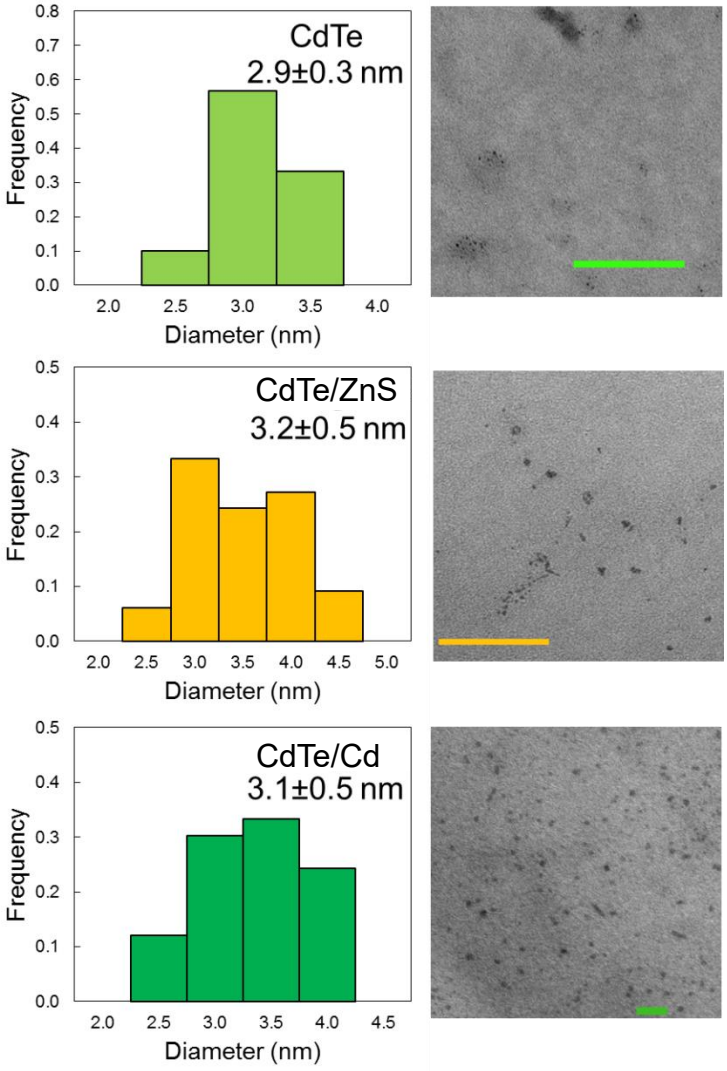

Figure 8.7 – TEM images and size distribution histograms of the core and core-shell particles. Distributions and average diameters are the result of the analysis of 30 particles. Scale bars are 100 nm for CdTe and CdTe/ZnS and 20 nm for CdTe/Cd.

of CdTe-2.4 stock were filtered, washed twice, and re-dispersed with pH 11 water. This solution was then diluted to 2 μM. The reaction solution consisted of the filtered quantum dots and the precursor stock in a 1:1 ratio, with 10 μL of 0.5 M NaOH per 500 μL of reaction volume. This mixture was then divided into 100 μL PCR tubes and reacted at 98°C for 1 h. Prior to use in cell cultures they were filtered and washed as previously described. Due to changes in the optical properties the absorbance after synthesis was used to calculate the extinction coefficient at 400 nm for the 1 μM stock, which was then used to calculate the concentrations post-filtering.

Cd-Overcoat Synthesis. A Cd-MPA stock was prepared and degassed as previously described for the core syntheses. 200 μL of CdTe-2.4 stock were filtered, washed twice, re-dispersed with pH 11 water, then diluted to 2 μM. The QD and Cd-MPA stocks were mixed in equal volumes with 10 μL of 0.5 M NaOH per 500 μL of reaction volume. The reaction solution was then divided into 100 μL PCR tubes and reacted at 98°C for 15 min.

Particle Characterization. All absorbance, emission, and quantum yield data were obtained from the batch of cores which was used to make the surface treated samples for consistency. Transmission electron micrographs were obtained to confirm morphology and size (Figure 8.6). Due to the low contrast with the available instrument the analysis procedure was modified so that the individual particles were manually isolated before size analysis. This introduced some bias to the analysis, though it was done systematically to retain comparability. Cores exhibited an average diameter of 2.9±0.3 nm, with the core-shells being slight larger with CdTe/ZnS and CdTe/Cd averaging 3.2±0.5 nm and 3.1±0.5 nm, which matches the ICP observations of single monolayer regime coverage.

Degradation Studies. QDs were centrifuged and filtered in the same manner used to prepare stocks for biological assays. Two samples of each type were prepared in PBS to simulate

a biologically relevant medium. One was kept in dark, while the other was illuminated using the same light intensity as the assays. Emission spectra were recorded using 365 nm excitation and a calibrated Ocean Optics USB4000 detector every hour until no signal was detectable. LB media was not used due to its tendency to fluoresce and obscure the quantum dot signal.

Uptake Studies. Three cultures were grown overnight and diluted 1:10 into phosphate-buffered saline with the quantum dots at 100 nM total concentration. The cultures were then shaken for 1 h at 37°C and collected into centrifuge tubes. The tubes were spun at 15 krpm at 3 min and the supernatant was removed. The cell pellet was then washed twice with PBS and once with double-distilled water using this procedure. The pellet was then dispersed in ~300 µL double-distilled water for storage (final volume was recorded after dispersion).

ICP-MS samples were prepared by diluting 25 µL of the samples to 1 mL total volume. Standards were prepared within the limits of the possible concentration range for comparison (Figure 8.8). This analysis provided the raw element composition of the samples, which was used to calculate the signal corresponding to specific concentrations. In all cases the sensitivity to tellurium was relatively low, requiring the use of the cadmium concentration exclusively for determining uptake (Table 8.2). The percentage uptake reported in the figures are defined using a mass balance comparing the total number of particles associated with the cells with the initial number introduced into the cultures.

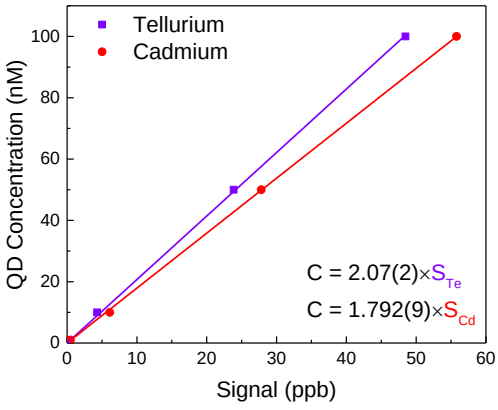

Figure 8.8 – Calibration curves for determining QD concentration from ICP-MS signal. Numbers in parentheses represent the error in the final digit.

The monolayers equivalent addition of Cd and Zn for the CdTe/ZnS and CdTe/Cd samples was calculated by comparing the signal to the number of

atoms in the untreated core (eq. 8.1-4). For ZnS, this entailed converting the ppb signal (S) to number of atoms using the molecular weight (M_{Zn}), which is normalized to the total cadmium signal to compensate for total QD concentration. Due to the high background signal of Zn (Table 8.1) the blank is subtracted from the measured value; this had a negligible effect on the Cd calculation and was neglected. The total atoms were calculated by multiplying the relative signal to the number of Cd atoms in the core ($n_{Cd,core}$ eq. 8.3), which is based on the number of Cd-Te units within that volume. The number of zinc atoms is then compared to the number in 1 ML of zinc calculated using the projected area of a Zn^{2+} over the surface area of a 2.9 nm nanoparticle (eq. 8.4) to yield the MLE coverage. The surface coverage was calculated by correlating the signal from the known concentration standards to the observed signal using the number of atoms in a 2.9 nm diameter CdTe core as a reference. For the CdTe/Cd overcoat the difference in Cd signal relative to that predicted by the Te signal is used to calculate the number of Cd atoms in the shell, which is converted to MLE in the same way as CdTe/ZnS (eq. 8.2).

$$\mathrm{MLE_{Zn}} = \frac{S_{Zn}}{S_{Cd}} \frac{M_{Cd}}{M_{Zn}} \frac{n_{Cd,core}}{n_{Zn,ML}} \tag{8.1}$$

$$\mathrm{MLE_{Cd}} = \left(\frac{S_{Cd,meas.}}{S_{Cd,pred.}} - 1 \right) \frac{n_{Cd,core}}{n_{Cd,ML}} \tag{8.2}$$

$$n_{Cd,core} \approx \frac{4\pi}{3} \left[\frac{r_{QD}}{r_{Cd^{2+}} + r_{Te^{2+}}} \right]^3 \tag{8.3}$$

$$n_{XY,ML} \approx 4 \left[\frac{r_{QD}}{r_{X^{2+}} + r_{Y^{2-}}} \right]^2 \tag{8.4}$$

Table 8.2

Uptake	Te	Cd	Zn	Calibration	Te	Cd	Zn
No. Trt.	--	0.05±0.01	0.38±0.09	1 nM Core	--	0.5	1.3
CdTe-MPA	0.3±0.3	2.9±0.8	0.35±0.02	10 nM Core	4.3	6.2	1.6
CdTe-CA	2±1	8±4	0.3±0.2	50 nM Core	23.9	27.9	1.3
CdTe/Cd	--	2.8±0.7	0.37±0.09	100 nM Core	48.5	55.9	1.5
CdTe/ZnS	0.3±0.3	2.5±0.8	1.1±0.7	1 μM Core	409.8	580.8	1.4
CdTe-2.2	--	2.5±0.6	0.1±0.1	10% ZnS	341.5	476.1	7.6
CdSe-2.4	--	0.8±0.3	--	50% ZnS	270.7	401.9	24.8
				100% ZnS	232.5	307.4	23.3
				100% Cd	318.5	595.4	1.5

All Values in ppb. --: below detection limit

Symbols and Abbreviations

CA	-	cysteamine	
DDW	-	double distilled water	
EIS	-	electrochemical impedence spectroscopy	
EPR	-	electron paramagnetic resonance	
ICP-MS	-	inductively coupled plasma mass spectrometry	
LB	-	luria broth	
M_x	-	molecular weight of x	eq. 8.1
MLE	-	monolayers equivalent	
MPA	-	3-mercaptopropionic acid	
$n_{x,y}$	-	number of atoms x at location y	eq. 8.1-4
OD	-	optical density	
PBS	-	phosphate-buffered saline	
QD	-	quantum dot	
r_x	-	radius of x	eq. 8.3-4
S_x	-	ICP-MS signal of atom x	eq. 8.1-2
$S_{meas.}$	-	measured Cd signal	eq. 8.2
$S_{pred.}$	-	predicted Cd signal based on Te signal	eq. 8.2
TEM	-	transmission electron microscopy	
α	-	initial quantum dot state	
β	-	core surface defect state	
γ	-	core shrinkage state	
δ	-	initial ZnS oxidation state	
ε	-	CdTe/ZnS defect state	
η	-	CdTe/ZnS core shrinkage state	

References

1) Aldana J., et al. *J. Am. Chem. Soc.* **2005**, *127*, 2496-2504.
2) Song X., et al. *Electrophoresis* **2006**, *27*, 1341-1346.
3) Keire D. A., et al. *J. Org. Chem.* **1992**, *57*, 123-127.
4) Aldana J., et al. *J. Am. Chem. Soc.* **2001**, *123*, 8844-8850.
5) Lu Z., et al. *Langmuir* **2008**, *24*, 5445-5452.
6) Zeng C., et al. *J. Environ. Manage.* **2015**, *154*, 78-85.
7) Katari J. E. B., et al. *J. Phys. Chem.* **1994**, *98*, 4109-4117.
8) Lovrić J., et al. *J. Mol. Med.* **2005**, *83*, 377-385.
9) Nagy A., et al. *ACS Nano* **2012**, *6*, 4748-4762.
10) Kirchner C., et al. *Nano Lett.* **2005**, *5*, 331-338.
11) Chan W., et al. *Toxicol. Lett.* **2006**, *167*, 191-200.
12) Cho S. J., et al. *Langmuir* **2007**, *23*, 1974-1980.
13) Ipe B. I., et al. *Small* **2005**, *1*, 706-709.
14) Tsay J. M., et al. *J. Am. Chem. Soc.* **2004**, *126*, 1936-1927.
15) van de Walle C. G., Neugebauer J. *Nature* **2003**, *423*, 626-628.
16) Thuy U. T. D. T., et al. *Opt. Mater.* **2016**, *53*, 34-38.
17) Dabbousi B. O., et al. *J. Phys. Chem. B* **1997**, *101*, 9463-9475.
18) Talapin D. V., et al. *Nano Lett.* **2001**, *1*, 207-211.
19) Zhang X. T., et al. *J. Appl. Phys.* **2002**, *92*, 3293-3298.
20) Glozman A., et al. *Isr. J. Chem.* **2001**, *41*, 39-44.
21) Gao L., et al. *ACS Nano* **2014**, *8*, 7260-7271.
22) Finkelstein E., et al. *Arch. Biochem. Piophys.* **1980**, *200*, 1-16.

Bibliography

21CFR73.575; **2015**.

Achtstein A. W., Schliwa A., Prudnikau A., Hardzei M., Artemyev M. V., Thomsen C., Woggon U. Electronic structure and exciton-phonon interaction in two-dimensional colloidal CdSe nanosheets. *Nano Lett.* **2012**, *12*, 3151-3157.

Adegoke O., Chidawanyika W., Nyokong T. Interaction of CdTe quantum dots with 2,2-diphenyl-1-picrylhydrazyl free radical: a spectroscopic, fluorimetric and kinetic study. *J. Fluoresc.* **2012**, *22*, 771-778.

Ahmad A., et al. Enzyme mediated extracellular synthesis of CdS nanoparticles by the fungus, *Fusarium oxysporum*. *J. Am. Chem. Soc.* **2002**, *124*, 12108-12109.

Ahmed T., Kilina S., Das T., Haraldsen J. T., Rehr J. J. Balatsky S. V. Electronic fingerprints of DNA bases on graphene. *Nano Lett.* **2012**, *12*, 927-931.

Åkerman M. E., Chan W. C. W., Laakkonen P., Bhatia S. N., Ruoslahti E. Nanocrystal targeting *in vivo*. *Proc. Natl. Acad. Sci. U.S.A.* **2002**, *99*, 12617-12621.

Al-Hajaj N. A., Moquin A., Neibert K. D., Soliman G. M., Winnik F. M., Maysinger D. Short ligands affect modes of QD uptake and elimination in human cells. *ACS Nano* **2011**, *5*, 4909-4918.

Albanese A., Tang P. S., Chan W. C. W. The effect of nanoparticle size, shape, and surface chemistry on biological systems. *Annu. Rev. Biomed. Eng.* **2012**, *14*, 1-16.

Aldana J., Lavelle N., Wang Y., Peng X. Size-dependent dissociation pH of thiolate ligands from cadmium chalcogenide nanocrystals. *J. Am. Chem. Soc.* **2005**, *127*, 2496-2504.

Aldana J., Wang Y. A., Peng X. Photochemical instability of CdSe nanocrystals coated by hydrophilic thiols. *J. Am. Chem. Soc.* **2001**, *123*, 8844-8850.

Aldeek F., Mustin C., Balan L., Medjahdi G., Roques-Carmes T., Arnoux P., Schneider R. Enhanced photostability from CdSe(S)/ZnO core/shell quantum dots and their use in biolabeling. *Eur. J. Inorg. Chem.* **2011**, 794-801.

Algar W. R., Krull U. J. Luminescence and stability of aqueous thioalkyl acid capped CdSe/ZnS quantum dots correlated to ligand ionization. *ChemPhysChem* **2007**, *8*, 561-568.

Algar W. R., Tavares A. J., Krull U. J. Beyond labels: a review of the application of quantum dots as integrated components of assays, bioprobes, and biosensors utilizing optical transduction. *Anal. Chim. Acta.* **2010**, *673*, 1-25.

Alivisatos A. P. Semiconductor Clusters, Nanocrystals, and Quantum Dots. *Science* **1996**, *271*, 933-937.

Alivov Y., Singh V., Ding Y., Cerkovnik L. J., Nagpal P. Doping of wide-bandgap titanium-dioxide nanotubes: optical, electronic and magnetic properties. *Nanoscale* **2014**, *6*, 10839-10849.

Ambrosone A., Mattera L., Marchesano V., Quarta A., Susha A. S., Tino A., Rogach A. L., Tortiglione C. Mechanisms underlying toxicity induced by CdTe quantum dots determined in an invertebrate model organism. *Biomaterials* **2012**, *33*, 1991-2000.

Amelia M., Lincheneau C., Silvi S., Credi A. Electrochemical properties of CdSe and CdTe quantum dots. *Chem. Soc. Rev.* **2012**, *41*, 5728-5743.

Anas A., Akita H., Harashima H., Itoh T., Ishikawa M., Biju V. Photosensitized breakage and damage of DNA by CdSe-ZnS quantum dots. *J. Phys. Chem. B* **2008**, *112*, 10005-10011.

Apel K., Hirt H. Reactive oxygen species: metabolism, oxidative stress, and signal transduction. *Annu. Rev. Plant Biol.* **2004**, *55*, 373-399.

Aranda A., Sequedo L., Tolosa L., QUintas G., Burello E., Castell J. V., Gombau L. Dichloro-dihydro-fluorescein diacetate (DCFH-DA) assay: a quantitative method for oxidative stress assessment of nanoparticle-treated cells. *Toxicol. In Vitro* **2013**, *27*, 954-963.

Arvizo R. R., Miranda O. R., Thompson M. A., Pabelick C. M., Bhattacharya R., Robertson J. D., Rotello V. M., Prakash Y. S., Mukherjee. Effect of nanoparticle surface charge at the plasma membrane and beyond. *Nano Lett.* **2010**, *10*, 2543-2548.

Ba L. A., Döring M., Jamier V., Jacob C. Tellurium: an element with great biological potency and potential. *Org. Biomol. Chem.* **2010**, *8*, 4203-4216.

Bai H. J., Zhang Z. M., Guo Y., Yang G. E. Biosynthesis of cadmium sulfide nanoparticles by photosynthetic bacteria *Rhodopseudomonas palustris*.*Colloids Surf. B Biointerfaces* **2009**, *70*, 142-146.

Bailon-Ruiz S., Perales-Perez O. UV-enhanced toxicity of water-stable quantum dots in human pancreatic carcinoma cells. *J. Exp. Nanosci.* **2014**, *9*, 942-956.

Bakalova R., Ohba H., Zhelev Z., Nagase T., Jose R., Ishikawa M., Baba Y. Quantum dot anti-CD conjugates: Are they potential photosensitizers or potentiators of classical photosensitizing agents in photodynamic therapy of cancer? *Nano Lett.* **2004**, *4*, 1567-1573.

Bakueva L., Gorelikov I., Musikhin S., Zhao X. S., Sargent E. H., Kumacheva E. PbS quantum dots with stable efficient luminescence in the near-IR spectra range. *Adv. Mater.* **2004**, *16*, 926-929.

Balandin A. A., Lazarenkova O. L. Mechanism for thermoelectric figure-of-merit enhancement in regimented quantum dot superlattices. *Appl. Phys. Lett.* **2003**, *82*, 415-417.

Ballou B., Lagerholm B. C., Ernst L. A., Bruchez M. P., Waggoner A. S. Noninvasive imaging of quantum dots in mice. *Bioconjug. Chem.* **2004**, *15*, 79-86.

Bao H., Lu Z., Cui X., Qiao Y., Guo J., Anderson J. M., Li C. M. Extracellular microbial synthesis of biocompatible CdTe quantum dots. *Acta Biomater.* **2010**, *6*, 3534-3541.

Baral S., Fojtik A., Weller H., Henglein A. Photochemistry and radiation chemistry of colloidal semiconductors. 12. Intermediates of the oxidation of extremely small particles of CdS, ZnS, and Cd_3P_2 and size quantization effects. *J. Am. Chem. Soc.* **1986**, *108*, 375-378.

Baroli B. Penetration of nanoparticles and nanomaterials in the skin: fiction or reality? *J. Pharm. Sci.* **2010**, *99*, 21-50.

Beebe J. M., Kim B., Gadzuk J. W., Frisbie C. D., Kushmerick J. G. Transition from direct tunneling to field emission in metal-molecule-metal junctions. *Phys. Rev. Lett.* **2006**, *97*, 026801.

Bentzen E. L., Tomlinson I. D., Mason J., Gresch P., Warnement M. R., Wright D,m Sanders-Bush E., Blakely R., Rosenthal S. J. Surface modification to reduce nonspecific binding of quantum dots in live cell assays. *Bioconjug. Chem.* **2005**, *16*, 1488-1494.

Bertin G., Averbeck D. Cadmium: cellular effects, modifications of biomolecules, modulation of DNA repair and genotoxic consequences (a review). *Biochimie* **2006**, *88*, 1549-1559.

Bhattacharjee S. Reactive oxygen species and oxidative burst: roles in stress, senescence and signal transduction in plants. *Curr. Sci.* **2005**, *89*, 1113-1121.

Binnig G., Quate C. F., Gerber C. Atomic force microscope. *Phys. Rev. Lett.* **1986**, *56*, 930-933.

Binnig G., Rohrer H., Gerber C., Weibel E. Surface studies by scanning tunneling microscopy. *Phys. Rev. Lett.* **1982**, *49*, 57-61.

Biver M., Filella M. Bulk dissolution rates of cadmium and bismuth tellurides as a function of pH, temperature and dissolved oxygen. *Environ. Sci. Technol.* **2016**, *50*, 4675-4681.

Blair J. M. A., Webber M. A., Baylay A. J., Ogbolu D. O., Piddock L. J. V. Molecular mechanisms of antibiotic resistance. *Nature Rev. Microbiol.* **2015**, *13*, 42-51.

Bleaney B., Stevens K. W. H. Paramagnetic resonance. *Rep. Prog. Phys.* **1953**, *16*, 108-159.

Blum J. L., Xiong J. W., Hoffman C., Zelikoff J. T. Cadmium associated with inhaled cadmium oxide nanoparticles impacts fetal and neonatal development and growth. *Toxicol. Sci.* **2012**, *126*, 478-486.

Bode B. M., Gordon M. S. Macmolplt: a graphical user interface for GAMESS. *J. Mol. Graph. Model.* **1998**, *16*, 133-138.

Boisselier E., Astruc D. Gold nanoparticles in nanomedicine: preparations, imaging, diagnostics, therapies and toxicity. *Chem. Soc. Rev.* **2009**, *38*, 1759-1782.

Boldt K., Bruns O. T., Gaponik N., Eychmüller A. Comparative examination of the stability of semiconductor quantum dots in various biochemical buffers. *J. Phys. Chem. B* **2006**, *110*, 1959-1963.

Booth M., Brown A. P., Evans S. D., Critchley K. Determining the concentration of $CuInS_2$ quantum dots from the size-dependent molar extinction coefficient. *Chem. Mater.* **2012**, *24*, 2064-2070.

Bouet C., Mahler B., Nadal B., Abecassis B., Tessier M. D., Ithurria S., Xu X., Dubertret B. Two-dimensional growth of CdSe nanocrystals, from nanoplatelets to nanosheets. *Chem. Mater.* **2013**, *25*, 639-645.

Bottrill M., Green M. Some aspects of quantum dot toxicity. *Chem. Commun.* **2011**, *47*, 7039-7050.

Bouldin J. L., Ingle T. M., Sengupta A., Alexander R., Hannigan R. E., Buchanan R. A. Aqueous toxicity and food chain transfer of Quantum DOTs in freshwater algae and *Ceriodaphnia dubia*. *Environ. Toxicol. Chem.* **2008**, *27*, 1958-1963.

Brayner R., Dahoumane S. A., Nguyen J. N., Yéprémain C., Djediat C., Couté A., Fiévet F. Ecotoxicological studies of CdS nanoparticles on photosynthetic microorganisms. *J. Nanosci. Nanotechnol.* **2011**, *11*, 1852-1858.

Brayner R., Ferrari-Iliou R., Brivois N., Djediat S., Benedetti M. F., Fiévet F. Toxicological impact studies based on *Escherichia coli* bacteria in ultrafine ZnO nanoparticles colloidal medium. *Nano Lett.* **2006**, *6*, 866-870.

Brown K. A., Dayal S., Ai X., Rumbles G., King P. W. Controlled assembly of hydrogenase-CdTe nanocrystal hybrids for solar hydrogen production. *J. Am. Chem. Soc.* **2010**, *132*, 9672-9680.

Brown K. A., Wilker M. B., Boehm M., Dukovic G., King P. W. haracterization of photochemical processes for H_2 production by CdS nanorod-[FeFe] hydrogenase Complexes. *J. Am. Chem. Soc.* **2012**, *134*, 5627-5636.

Bruchez M., Moronne M., Gin P., Weiss S., Alivisatos A. P. Semiconductor nanocrystals as fluorescent biological labels. *Science* **1998**, *281*, 2013-2016.

Bruneau A., Fortier M., Gagné F., Gagnon C., Turcotte P., Tayabali A., Davis T. A., Auffret M., Fournier M. *In vitro* immunotoxicology of quantum dots and comparison with dissolved cadmium and tellurium. *Environ. Toxicol.* **2013**, *30*, 9-25.

Brus L. E. A simple model for the ionization potential, electron affinity, and aqueous redox potentials of small semiconductor crystallites. *J. Chem. Phys.* **1983**, *79*, 5566-5571.

Brust M., Walker M., Bethell D., Schiffrin D. J., Whyman R. Tynthesis of thiol-derivatised gold nanoparticles in a two-phase liquid-liquid system. *J. Chem. Soc., Chem. Commun.* **1994**, 801-802.

Bube R. H. Photoconductivity of the sulfide, selenide, and telluride of zinc or cadmium. *Proc. IRE* **1955**, *43*, 1836-1850.

Buettner G. R. Spin trapping: ESR parameters of spin adducts. *Free Radic. Biol. Med.* **1987**, *3*, 259-303.

Buettner G. R. The pecking order of free radicals and antioxidants: lipid peroxidation, alpha-tocopherol, and ascorbate. *Arch. Biochem. Biophys.* **1993**, *300*, 535-543.

Buettner G. R., Mason R. P. Spin-trapping methods for detecting superoxide and hydroxyl free radicals *in vitro* and *in vivo*. *Methods Enzymol.* **1990**, *186*, 127-133.

Bui H., Onodera C., Kidwell C., Tan Y., Graugnard E., Kuang W., Lee J., Knowlton W. B., Yurke B., Hughes W. L. Programmable periodicity of quantum dot arrays with DNA origami nanotubes. *Nano Lett.* **2010**, *10*, 3367-3372.

Burrows C. J., Muller J. G. Oxidative nucleobase modifications leading to strand scission. *Chem. Rev.* **1998**, *98*, 1109-1152.

Cadet J., Delatour T., Douki T., Gasparutto D., Pouget J., Ravanat J., Sauvaigo S. Hydroxyl radicals and DNA base damage. *Mutat. Res. Fund. Mol. Mech. Mut.* **1999**, *424*, 9-21.

Centers for Disease Control and Prevention. Antibiotic Resistance Threats. **2013**.

Chae Y., Kim S. W., An Y. *In vivo* visual evaluation of nanoparticle transfer in a three-species terrestrial food chain. *Chemosphere* **2016**, *151*, 101-107.

Chan W., Shiao N., Lu P. Z. CdSe quantum dots induce apoptosis in human neuroblastoma cells via mitochondrial-dependent pathways and inhibition of survival signals *Toxicol. Lett.* **2006**, *167*, 191-200.

Chang H., Cohen T., Grad Y. H., Hanage W. P., O'Brien T. F., Lipsitch M. Origin and proliferation of multiple-drug resistance in bacterial pathogens. *Microbiol. Mol. Biol. Rev.* **2015**, *79*, 101-116.

Chang S., Dai Y., Kang B., Han W., Mao L., Chen D. UV-enhanced cytotoxicity of thiol-capped CdTe quantum dots in human pancreatic carcinoma cells. *Toxicol. Lett.* **2009**, *188*, 104-111.

Chang E., Thekkek N, Yu W. W., Colvin V. L., Drezek R. Evaluation of quantum dot cytotoxicity based on intracellular uptake. *Small* **2006**, *2*, 1412-1417.

Chatterjee A., Johnson C. M., Shu C. C., Kaznessis Y. N., Ramkrishna D., Dunny G. M., Hu W. S. Convergent transcription confers a bistable switch in *Enterococcus faecalis* conjugation. *Proc. Natl. Acad. Sci. USA* **2011**, *108*, 9721-9726.

Chen F., Gerion D. Fluorescent CdSe / ZnS nanocrystal−peptide conjugates for long-term, nontoxic imaging and nuclear targeting in living cells. *Nano Lett.* **2004**, *4*, 1827-1832.

Chen H., Gong Y., Han R. Cadmium telluride quantum dots (CdTe-QDs) and enhanced ultraviolet-B (UV-B) radiation trigger antioxidant enzyme metabolism and programmed cell death in wheat seedlings. *PLoS One* **2014**, *9*, e110400.

Chen Z., Moore J., Radtke G., Sirringhaus H., O'Brien S. Binary nanoparticle superlattices in the semiconductor-semiconductor system: CdTe and CdSe. *J. Am. Chem. Soc.* **2007**, *129*, 15702-15709.

Chen G., Roy I., Yang C., Prasad P. N. Nanochemistry and nanomedicine for nanoparticle-based diagnostics and therapy. *Chem. Rev.* **2016**, *116*, 2826-2885.

Chen C.,Wu D., Chan Y., Lin C. C., Chung P., Hsiao M., Liu R. Evaluations of the chemical stability and cytotoxicity of $CuInS_2$ and $CuInS_2$/ZnS core/shell quantum dots. *J. Phys. Chem. C* **2015**, *119*, 2852-2860.

Cho S. J., Maysinger D., Jain M., Röder B., Hackbarth S., Winnik F. M. Long-term exposure to CdTe quantum dots causes functional impairments in live cells. *Langmuir* **2007**, *23*, 1974-1980.

Choi A. O., Brown S. E., Szyf M., Maysinger D. Quantum dot-induced epigenetic and genotoxic changes in human breast cancer cells. *J. Mol. Med.* **2008**, *86*, 291-302.

Choi A. O., Cho S. J., Desbarats J., Lovrić J., Maysinger D. Quantum dot-induced cell death involves Fas upregulation and lipid peroxidation in human neuroblastoma cells. *J. Nanobiotechnology* **2007**, *5*, 1.

Choi J. H., Fafarman A. T., Oh S. J., Ko D. K., Kim D. K., Diroll B. T., Muramoto S., Gillen J. G., Murray C. B., Kagan C. R. Bandlike transport in strongly coupled and doped quantum dot solids: a route to high-performance thin-film electronics. *Nano Lett.* **2012**, *12*, 2631-2638.

Choi S. H., Kim B. S., Frisbie C. D. Electrical resistance of long conjugated molecular wires. *Science* **2008**, *320*, 1482-1486.

Choi H. S., Liu W., Misra P., Tanaka W., Zimmer J. P., Ipe B. I., Bawendi M. G., Frangioni J. V. Renal clearance of quantum dots. *Nat. Biotechnol.* **2007**, *25*, 1165-1170.

Chu I. H., Radulaski M., Vukmirovic N., Cheng H. P., Wang L. W. Charge transport in a quantum dot supercrystal. *J. Phys. Chem. C* **2011**, *115*, 21409-21415.

Chu M., Wu Q., Wang J., Hou S., Miao Y., Peng J., Sun Y. *In vitro* and *in vivo* transdermal delivery capacity of quantum dots through mouse skin. *Nanotechnology* **2007**, *18*, 455103.

Chu M., Wu Q., Yang H., Yuan R., Hou S., Yang Y., Zou Y., Xu S., Xu K., Ji A., Sheng L. Transfer of quantum dots from pregnant mice to pups across the placental barrier. *Small* **2010**, *6*, 670-678.

Clapp A. R., Medintz I. L., Mauro J. M., Fisher B. R., Bawendi M. G., Mattoussi H. Fluorescence resonance energy transfer between quantum dot donors and dye-labeled protein acceptors. *J. Am. Chem. Soc.* **2004**, *126*, 301-310.

Clarke S. J., Hollmann C. A., Aldaye F. A., Nadeau J. L. Effect of ligand density on the spectral, physical, and biological characteristics of CdSe/ZnS quantum dots. *Bioconjug. Chem.* **2008**, *19*, 562-568.

Clarke S. J., Hollmann C. A., Zhang Z., Suffern D., Bradforth S. E., Dimitrijevic N. M., Minarik W. G., Nadeau J. L. Photophysics of dopamine-modified quantum dots and effects on biological systems. *Nat. Mater.* **2006**, *5*, 409-417.

Clever J. L., Derrick M. E., Johnson S. A. The solubility of some sparingly soluble salts of zinc and cadmium in water and in aqueous electrolyte solutions. *J. Phys. Chem. Ref. Data* **1992**, *21*, 941-1004.

Clift M. J. D., Rothen-Rutishauser B., Brown D. M., Duffin R., Donaldson k., Proudfoot L., Guy K., Stone V. The impact of different nanoparticle surface chemistry and size on uptake and toxicity in a murine macrophage cell line. *Toxicol. Appl. Pharmacol.* **2008**, *232*, 418-427.

Coe S., Woo W. K., Bawendi M., Bulović V. Electroluminescence from single monolayers of nanocrystals in molecular organic devices. *Nature* **2002**, *420*, 800-803.

Cohen H., Nogues C., Naaman R., Porath D. Direction measurement of electrical transport through single DNA molecules of complex sequence. *Proc. Natl. Acad. Sci. U.S.A.* **2005**, *102*, 11589-11593.

Connor E. E., Mwamuka J., Gole A., Murphy C. J., Wyatt M. D. Gold nanoparticles are taken up by human cells but do not cause acute cytotoxicity. *Small* **2005**, *1*, 325-327.

Cooper D. R., Dimitrijevic N. M., Nadeau J. L. Photosensitization of CdSe/ZnS QDs and reliability of assays for reactive oxygen species production. *Nanoscale* **2010**, *2*, 114-121.

Cordero S. R.,Carson P. J., Estabrook R. A., Strouse G. F., Buratto S. K. Photoactivated luminescence of CdSe quantum dot monolayers. *J. Phys. Chem. B* **2000**, *104*, 12137-12142.

Courtney C. M., Chatterjee A. Sequence-specific peptide nucleic acid-based antisense inhibitors of TEM-1 β-lactamase and mechanism of adaptive resistance. *ACS Infect. Dis.* **2015**, *1*, 253-263.

Courtney C. M., Goodman S. M., McDaniel J. A., Madinger N. E., Chatterjee A., Nagpal P. Photoexcited quantum dots for killing multidrug-resistant bacteria. *Nat. Mater.* **2016**, *15*, 529-534.

Crane M., Handy R. D., Garrod J., Owen R. Ecotoxicity test methods and environmental hazard assessment for engineered nanoparticles. *Ecotoxicology* **2008**, *17*, 421-437.

Crookes-Goodson W. J., Slocik J. M., Naik R. R. Bio-directed synthesis and assembly of nanomaterials. *Chem. Soc. Rev.* **2008**, *37*, 2403-2412.

Dabbousi B. O., Rodriguez J., Mikulec F. V., Heine J. R., Mattoussi H., Ober R., Jensen K. F., Bawendi M. G. (CdSe)ZnS Core-shell quantum dots: synthesis and characterization of a size series of highly luminescent nanocrystallites. *J. Phys. Chem. B* **1997**, *101*, 9463-9475.

Dameron C. T., Reeses R. N., Mehra R. K., Kortan A. R., Carrol P. J., Steigerwald M. L., Brus L. E., Winge D. R. Biosynthesis of cadmium sulphide quantum semiconductor crystallites. *Nature* **1989**, *338*, 596-597.

Dao T. D., Hafez M. E., Beloborodov I. S., Jeong H. D.. Thioacetic-acid capped PbS quantum dot solids exhibiting thermally activated charge hopping transport. *Bull. Korean. Chem. Soc.* **2014**, *35*, 457-465.

de Souza G. C. S., Ribeiro D., Rodrigues S. S. M., Paim A. P. S., Lavorante A. F., da Silva V. L., Santos J. L. M., Araújo A. N., Montenegro M. C. B. S. M. Clean photoinduced generation of free reactive oxygen species by silica films embedding MPA-CdTe quantum dots. *RSC Adv.* **2016**, *6*, 8563-8571.

Delehanty J. B., Medintz I. L., Pons T., Brunel F. M., Dawson P. E., Mattoussi H. Self-assembled quantum dot- peptide bioconjugates for selective intracellular delivery. *Bioconjug Chem.* **2006**, *17*, 920-927.

Derfus A. M., Chan W. C. W., Bhatia S. N. Probing the cytotoxicity of semiconductor quantum dots. *Nano Lett.* **2004**, *4*, 11-18.

Dhawan A., Sharma V. Toxicity assessment of nanomaterials: methods and challenges. *Anal. Bioanal. Chem.* **2010**, *398*, 589-605.

Diaconescu B., Padilha L. A., Nagpal P., Swartzentruber B. S., Klimov V. I. Measurement of electronic states of PbS nanocrystal quantum dots using scanning tunneling spectroscopy: the role of parity selection rules in optical absorption. *Phys. Rev. Lett.* **2013**, *110*, 127406.

Díaz E. C., Cases M. V. Analytical methodologies for nanotoxicity assessment. *Trends Anal. Chem.* **2016**, *84*, 160-171.

Dirkse T. P. The solubility product constant of ZnO. *J. Electrochem. Soc.* **1986**, *133*, 1656-1657.

Dobrovolskaia M. A., McNeil S. E. Immunological properties of engineered nanomaterials. *Nat. Nanotechnol.* **2007**, *2*, 469-478.

Domingos R. F., Simon D. F., Hauser C., Wilkinson K. J. Bioaccumulation and effects of CdTe/CdS quantum dots on *Chlamydomonas reinhardtii* – nanoparticles or the free ions? *Environ. Sci. Technol.* **2011**, *45*, 7664-7669.

Doña J. M., Herrero J. Chemical-bath deposition of ZnSe thin films. *J. Electrochem Soc.* **1995**, *142*, 764-770.

Donaldson K., Tran L., Jimenez L. A., Duffin R., Newby D. E., Mills N., MacNee W., Stone V. Combustion-derived nanoparticles: a review of their toxicology following inhalation exposure. *Part. Fibre Toxicol.* **2005**, *2*.

Dong A., Chen J., Vora P. M., Kikkawa J. M., Murray C. B. Binary nanocrystal superlattice membranes self-assembled at the liquid-air interface. *Nature* **2010**, *466*, 474-477.

Dou Y., Egdel R. G., Walker T., Law D. S. L., Beamson G. N-type doping in CdO ceramics: a study by EELS and photoemission spectroscopy. *Surf. Sci.* **1998**, *298*, 241-258.

Dougherty D., Kittel K., Meeks J., McGlynn S. P. Photoelectron spectroscopy of carbonyls. Ureas, uracils, and thymine. *J. Am. Chem. Soc.* **1976**, *98*, 3815-3520.

Dougherty D., Younathan E. S., Voll R., Abdulnur S., McGlynn S. P. Photoelectron spectroscopy of some biological molecules. *J. Electron. Spectrosc. Relat. Phenom.* **1978**, *13*, 379-393.

Duan H., Nie S. Cell-penetrating quantum dots based on multivalent and endosome-disrupting surface coatings. *J. Am. Chem. Soc.* **2007**, *129*, 3333-3336.

Dubertret B., Skourides P., Norris D. J., Noireaux V., Brivanlou A. H., Libchaber A. *In vivo* imaging of quantum dots encapsulated in phospholipid micelles. *Science* **2002**, *298*, 1759-1762.

Dutton W. A., Cooper W. C. The oxides and oxyacids of tellurium. *Chem. Rev.* **1966**, *66*, 657-675.

Dukes A. D., McBride J. R., Rosenthal S. J. Synthesis of magic-sized CdSe and CdTe nanocrystals with diisooctylphosphinic acid. *Chem. Mater.* **2010**, *22*, 6402-6408.

Dumas E., Gao C., Suffern D., Bradforth S. E., Dimitrijevic N. M. Nadeau J. L. Interfacial charge transfer between CdTe quantum dots and gram negative vs gram positive bacteria. *Environ. Sci. Technol.* **2010**, *44*, 1464-1470.

Dumas E., Ozenne V., Mielke R. E., Nadeau J. L. Toxicity of CdTe quantum dots in bacterial strains. *IEEE Trans. Nanobioscience* **2009**, *8*, 58-64.

Dvoranová D., Barbieriková Z., Brezová V. Radical intermediates in photoinduced reactions on TiO_2 (an EPR spin trapping study). *Molecules* **2014**, *19*, 17279-17304.

Dwyer D. J., Belenky P. A., Yang J. H., MacDonald I. C., Martell J. D., Takahashi N., Chan C. T., Lobritz M. A., Braff D., Schwarz E. G., Ye J. D., Pati M., Vercruysse M., Ralifo P. S., Allison K. R., Khalil A. S., Ting A. Y., Walker G. C., Collins J. J. Antibiotics induce redox-related physiological alterations as part of their lethality. *Proc. Natl. Acad. Sci. USA* **2014**, *111*, E2100-E2109.

Eda G., Yamaguchi H., Voiry D., Fujita T., Chen M., Chhowalla M. Photoluminescence from chemically exfoliated MoS_2. *Nano Lett.* **2011**, *11*, 5111-5116.

Egerton R. F. Electron energy-loss spectroscopy in the TEM. *Rep. Prog. Phys.* **2009**, *72*, 016502.

Ema M., Gamo M., Honda K. Developmental toxicity of engineered nanomaterials in rodents. *Toxicol. Appl. Pharmacol.* **2016**, *299*, 47-52.

Emmerson B. T. "Ouch-ouch" disease: the osteomalacia of cadium nephrpathy. *Ann. Inter. Med.* **1970**, *73*, 854-855.

Endres R. G., Cox D. L., Singh R. R. P. The quest for high-conductance DNA. *Rev. Mod. Phys.* **2004**, *76*, 195-214.

Epe B. Genotoxicity of singlet oxygen. *Chem. Biol. Interact.* **1991**, *80*, 239-260.

Erb R. E., Ehlers M. H. Resazurin reducing time as an indicator of bovine semen fertilizing capacity. *J. Dairy Sci.* **1950**, *33*, 853-864.

EUCAST. Breakpoint Tables for Interpretation of MICs and Zone Diameters Version 5.0. http://www.eucast.org (accessed Oct. 20, 2015).

Falgas M. E., Bliziotis I. A. Pandrug-resistant Gram-negative bacteria: the dawn of the post-antibiotic era? *Int. J. Antimicrob. Agents* **2007**, *29*, 630-636.

Falvo M. R., Taylor R. M., Helser A., Chi V., Brooks F. P., Washburn S., Superfine R. Nanometre-scale rolling and sliding of carbon nanotubes. *Nature* **1999**, *397*, 236-238.

Fan H., Leve E. W., Scullin C., Gabaldon J., Tallant D., Bunge S., Boyle T., Wilson M. C., Brinker C. J. Surfactant-assisted synthesis of water-soluble and biocompatible semiconductor quantum dot micelles. *Nano Lett.* **2005**, *5*, 645-648.

Fan J., Sun Y., Wang S., Li Y., Zeng X., Cao Z., Yang P., Song P., Wang Z., Xian Z., Gao H., Chen Q., Cui D., Ju D. Inhibition of autophagy overcomes the nanotoxicity elicited by cadmium-based quantum dots. *Biomaterials* **2016**, *78*, 102-114.

Fang T., Li X., Wang Q., Zhang Z., Liu P., Zhang C. Toxicity evaluation of CdTe quantum dots with different size on *Escherichia coli*. *Toxicol. In Vitro* **2012**, *26*, 1233-1239.

Ferrer I. J., Díaz-Chao P., Pascual A., Sánchez C. An investigation on palladium sulphide (PdS) thin films as a photovoltaic material. *Thin Solid Films* **2007**, *515*, 5783-5786.

Feynman R P. There's plenty of room at the bottom. *Engineering and Science* **1960**, 22-36.

Finkelstein E., Rosen G. M., Rauckman E. J. Spin trapping of superoxide and hydroxyl radical: Practical aspects. *Arch. Biochem. Piophys.* **1980**, *200*, 1-16.

Fischer H. C., Liuy L., Pang K. S., Chan W. C. W. Pharmacokinetics of nanoscale quantum dots: *in vivo* distribution, sequestration, and clearance in the rat. *Adv. Funct. Mater.* **2006**, *16*, 1299-1305.

Fitzpatrick J. A. J., Andreko S. K., Ernst L. A., Waggoner A. S., Ballou B., Bruchez M. P. Long-term persistence and spectral blue shifting of quantum dots *in vivo*. *Nano Lett.* **2009**, *9*, 2736-2741.

Fontes A., Santos B S. Quantum dots: applications in biology. Springer **2014**.

Förster T. 10th Spiers Memorial Lecture. Transfer mechanisms of electronic excitation. *Discuss. Faraday Soc.* **1959**, *27*, 7-17.

Fowler R. H., Nordheim L. Electron emission in intense electric fields. *Proc. R. Soc. London* **1928**, *119*, 173-181.

Franzl T., Klar T. A., Schietinge S., Rogach A. L., Feldmann J. Exciton recycling in graded gap nanocrystal structures. *Nano. Lett.* **2004**, *4*, 1599-1603.

Gagné F., Auclair J., Turcotte P., Fournier M., Gagnon C., Sauvé S., Blaise C. Ecotoxicity of CdTe quantum dots to freshwater mussels: Impacts on immune system, oxidative stress and genotoxicity. *Aquat. Toxicol.* **2008**, *86*, 333-340.

Gagné F., Fortier M., Yu L., Osachoff H. L. Skirrow R. C., van Aggelen G., Gagnon C., Fournier M. Immunocompetence and alterations in hepatic gene expression in rainbow trout exposed to CdS/CdTe quantum dots. *J. Environ. Monit.* **2010**, *12*, 1556-1565.

Gao X., Cui Y., Levenson R. M., Chung L. W. K., Nie S. *In vivo* cancer targeting and imaging with semiconductor quantum dots. *Nat. Biotechnol.* **2004**, *22*, 969-976.

Gao L., Liu R., Gao F., Wang Y., Jiang X., Gao X. Plasmon-mediated generation of reactive oxygen species from near-infrared light excited gold nanocages for photodynamic therapy in vitro. *ACS Nano* **2014**, *8*, 7260-7271.

Gaponik N., Talapin D. V., Rogach A. L., Hoppe K., Shevchenko E. V., Komowski A., Eychmüller A., Weller H. Thiol-capping of CdTe nanocrystals : an alternative to organometallic synthetic routes. *J. Phys. Chem. B* **2002**, *106*, 7177-7185.

Garnett M. C., Kallinteri P. Nanomedicines and nanotoxicology: some physiological principles. *Occup. Med.* **2006**, *56*, 307-311.

Genereux J. C., Barton J. K. Mechanisms for DNA charge transport. *Chem. Rev.* **2010**, *110*, 1642-1662.

Gerlier D., Thomasset N. Use of MTT colorimetric assay to measure cell activation. *J. Immunol. Methods* **1986**, *94*, 57-63.

Geys J., Nemmar A., Verbeken E., Smolders E., Ratoi M., Hoylaerts M. F., Nemery B., Hoet P. H. M. Acute toxicity and prothrombotic effects of quantum dots: impact of surface charge. *Environ. Health Perspect.* **2008**, *116*, 1607-1613.

Gill S. S., Tuteja N. Reactive oxygen species and antioxidant machinery in abiotic stress tolerance in crop plants. *Plant Physiol. Biochem.* **2010**, *48*, 909-930.

Glozman A., Lifshitz E., Hoppe K., Rogach A. L., Weller H., Echymüller. Optically detected magnetic resonance of thiol-capped CdTe nanocrystals. *Isr. J. Chem.* **2001**, *41*, 39-44.

Gogoi S. K., Gopinath P., Paul A., Ramesh A., Ghosh S. S., Chattopadhyay A. Green fluorescent protein-expressing *Escherichia coli* as a model system for investigating the antimicrobial activities of silver nanoparticles. *Langmuir* **2006**, *22*, 9322-9328.

Gomes S. A. O., Vieira C. S., Almeida D. B., Santos-Mallet J. R., Menna-Barreto R. F. S., Cesar C. L., Feder D. CdTe and CdSe quantum dots cytotoxicity: a comparative study on microorganisms. *Sensors* **2011**, *11*, 11664-11678.

Goodman A. M. Evaporated metallic contacts to conducting cadmium sulfide single crystals. *J. Appl. Phys.* **1964**, *35*, 573-580.

Goodman S. M., Noh H., Singh V., Cha J. N., Nagpal P. Charge transport through exciton shelves in cadmium chalcogenide quantum dot-DNA nano-bioelectronic thin films. *Appl. Phys. Lett.* **2015**, *106*, 083109.

Goodman S. M., Singh V., Ribot J. C., Chatterjee A., Nagpal P. Multiple energy exciton shelves in quantum-dot-DNA nanobioelectronics. *J. Phys. Chem. Lett.* **2014**, *5*, 3909-3913.

Goodman S. M., Siu A., Singh V., Nagpal P. Long-range energy transfer in self-assembled quantum dot-DNA cascades. *Nanoscale* **2015**, *7*, 18435-18440.

Gopee N. V., Roberts D. W., Webb P., Cozart C. R., Siitonen P. H., Warbritton A. R., Yu W. V., Colvin V. L., Walker J. J., Howard P. C. Migration of intradermally injected quantum dots to sentinel organs in mice. *Toxicol. Sci.* **2007**, *98*, 249-257.

Gratton S. E. A., Ropp P. A., Pohlhaus P. D., Luft J. C., Madden V. J., Napier M. E., DeSimone J. M. The effect of particle design on cellular internalization pathways. *Proc. Natl. Acad. Sci. U. S. A.* **2008**, *105*, 11613-11618.

Green M., Haigh S. J., Lweis E. A., Sandiford L., Burkitt-Gray M., Fleck R., Vizcay-Barrena G., Jensen L., Mirzai H., Curry R. J., Dailey L. The biosynthesis of infrared-emitting quantum dots in *Allium fistulosum*. *Sci. Rep.* **2016**, *6*, 20480.

Green M., Howman E. Semiconductor quantum dots and free radical induced DNA nicking. *Chem. Commun.* **2005**, 121-123.

Gregory M. W. The infectiousness of pompous prose. *Nature* **1992**, *360*, 11-12.

Gur I., Fromer N. A., Geier M. L., Alivisatos A. P. Air-stable all-inorganic nanocrystal solar cells processed from solution. *Science* **2005**, *310*, 462-465.

Han D., Pal S., Nangreave J., Deng Z., Liu Y., Yan H. DNA origami with complex curvatures in three-dimensional space. *Science* **2011**, *332*, 342-346.

Han Y., Xie G., Sun Z., Mu Y., Han S., Xiao Y., Liu N., Wang H., Guo C., Shi Z., Li Y., Huang P. Plasma kinetics and biodistribution of water-soluble CdTe quantum dots in mice: a comparison between Cd and Te. *J. Nanoparticle Res.* **2011**, *13*, 5373-5380.

Harbour J. R., Hair M. L. Superoxide generation in the photolysis of aqueous cadmium sulfide dispersions. Detection by spin trapping. *J. Phys. Chem.* **1977**, *81*, 1791-1793.

Hardman R. A toxicologic review of quantum dots: toxicity depends on physicochemical and environmental factors. *Environ. Health Perspect.* **2006**, *114*, 165-172.

Hauck T. S., Anderson R. E., Fischer H. C., Newbigging S., Chan W. C. W. *In vivo* quantum-dot toxicity assessment. *Small* **2010**, *6*, 138-144.

He Y., Lu H., Sai L. M., Su Y., Hu M., Fan C., Huang W., Wang L. Microwave synthesis of water-dispersed CdTe/CdS/ZnS core-shell-shell quantum dots with excellent photostability and biocompatibility. *Adv. Mater.* **2008**, *20*, 3416-3421.

He Y., Lu H., Su Y., Sai L., Hu M., Fan C., Wang L. Ultra-photostable, non-cytotoxic, and highly fluorescent quantum nanospheres for long-term, high-specificity cell imaging. *Biomaterials* **2011**, *32*, 2133-2140.

He M., Miyajima F., Roberts P., Ellison L., Pickard D. D., Martin M. J., Connor T. R., Harris S. R., Fairley D., Bamford K. B., D'Arc S., Brazier J., Brown D., Coia J. E., Douce G., Gerding D., Kim H. J., Koh T. H., Kato H., Senoh M., Louie T., Michell S., Butt E., Peacock S. J., Brown N. M., Riley, T., Songer G., Wilcox M., Pirmohamed M., Kuijper E., Hawkey P., Wren B. W., Dougan G., Parkhill J., Lawley T. D. Emergence and global spread of epidemic healthcare-associated *Clostridium difficile*. *Nat. Genet.* **2013**, *45*, 109-113.

He Y., Sai L., Lu H., Hu M., Lai W., Fan Q., Wang L., Huang W. Microwave-assisted synthesis of water-dispersed CdTe nanocrystals with high luminescent efficiency and narrow size distribution. *Chem. Mater.* **2007**, *19*, 359-365.

Henderson D. O., Mu R., Ueda A., Wu M. H., Gordon E. M., Tung Y. S., Huang M., Keay J., Feldman L. C., Hollingsworth J. A. Optical and structural characterization of copper indium disulfide thin films. *Mater. Des.* **2001**, *22*, 585-589.

Ho C., Chang H., Tsai H., Tsai M., Yang C., Ling Y., Lin P. Quantum dot 705, a cadmium-based nanoparticle, induces persistent inflammation and granuloma formation in the mouse lung. *Nanotoxicology* **2013**, *7*, 105-115.

Holmes J. D., Smith P. R., Evans-Gowing R., Richardson D. J., Russel D. A., Sodeau J. R. Bacterial photoprotection through extracellular cadmium sulfide crystallites. *Photochem. Photobiol.* **1995**, *62*, 1022-1026.

Hoshino A., Fujioka K., Oku T., Suga M., Sasaki Y. F., Ohta T., Yasuhara M., Suzuki K., Yamamoto K. Physicochemical properties and cellular toxicity of nanocrystal quantum dots depend on their surface modification. *Nano Lett.* **2004**, *4*, 2163-2169.

Hoshino A., Hanaki K., Suzuki K., Yamamoto K. Applications of T-lymphoma labeled with fluorescent quantum dots to cell tracing markers in mouse body. *Biochem. Biophys. Res. Commun.* **2004**, *314*, 46-53.

Hoshino A., Hanada S., Yamamoto K. Toxicity of nanocrystal quantum dots: the relevance of surface modifications. *Arch. Toxicol.* **2011**, *85*, 707-720.

Hossain S. T., Das P., Mukherjee S. K. Toxicity of cadmium nanoparticles to *Bacillus subtilis*. *Toxicol. Environ. Chem.* **2013**, *95*, 1748-1756.

Hossain S. T., Mukherjee S. K. CdO nanoparticle toxicity on growth, morphology, and cell division in *Escherichia coli*. *Langmuir* **2012**, *28*, 16614-16622.

Hossain S. T., Mukherjee S. K. Toxicity of cadmium sulfide (CdS) nanoparticles against *Escherichia coli* and HeLa cells. *J. Hazard. Mater.* **2013**, *260*, 1073-1082.

Hsieh S., Wang F., Lin C., Chen Y., Hung S., Wang Y. The inhibition of osteogenesis with human bone marrow mesenchymal stem cells by CdSe/ZnS quantum dot labels. *Biomaterials* **2006**, *27*, 1656-1664.

Hu M., Chen J., Li Z., Au L., Hartland G. V., Li X., Marquez M., Xia Y. Gold nanostructures: engineering their plasmonic properties for biomedical applications. *Chem. Soc. Rev.* **2006**, *35*, 1084-1094.

Huang X., El-Sayed I. H., Qian W., El-Sayed M. A. Cancer cell imaging and photothermal therapy in the near-infrared region by using gold nanorods. *J. Am. Chem. Soc.* **2006**, *128*, 2115-2120.

Hung A. M., Micheel C. M., Bozano L. D., Osterbur L. W., Wallraff G. M., Cha J. N. Large-area spatially ordered arrays of gold nanoparticles directed by lithographically confined DNA origami. *Nat. Nanotechnol.* **2010**, *5*, 121-126.

Hussain S. M., Hess K. L., Gearhart J. M., Geiss K. T., Schlager J. J. *In vitro* toxicity of nanoparticles in BRL 3A rat liver cells. *Toxicol. In Vitro.* **2005**, *19*, 975-983.

Hyeon T. Chemical synthesis of magnetic nanoparticles. *Chem. Commun.* **2003**, 927-934.

Imlay J. A. The molecular mechanisms and physiological consequences of oxidative stress: lessons from a model bacterium. *Nature Rev. Microbiol.* **2013**, *11*, 443-454.

Ipe B. I., Lehnig M., Niemeyer C. M. On the generation of free radical species from quantum dots. *Small* **2005**, *1*, 706-709.

Issa I. M., Awad S. A. The amphoteric properties of tellurium dioxide. *J. Phys. Chem.* **1954**, *58*, 948-951.

Jacob J. M., Lens P. N. L., Balakrishnan R. M. Microbial synthesis of chalcogenide semiconductor nanoparticles: a review. *Microb. Biotechnol.* **2016**, *9*, 11-21.

Jacobsen N. R., Møller P., Jensen K. A., Vogel U., Ladefoged O., Loft S., Wallin H. Lung inflammation and genotoxicity following pulmonary exposure to nanoparticles in ApoE-/- mice. *Part. Fibre Toxicol.* **2009**, *6*, 2.

Jain M. P., Vaisheva F., Maysinger D. Metalloestrogenic effects of quantum dots. *Nanomedicine* **2012**, *7*, 23-37.

Jaiswal J. K., et al. Long-term multiple color imaging of live cells using quantum dot bioconjugates. *Nat. Biotechnol.* **2003**, *21*, 47-51.

Jalili N., Laxminarayana K. A review of atomic force microscopy imaging systems: application to molecular metrology and biological sciences. *Mechatronics* **2004**, *14*, 907-945.

Jaques S. L. Optical properties of biological tissues: a review *Phys. Med. Biol.* **2013**, *58*, R37-R61.

Jenny D. A., Bube R. H. Semiconducting cadmium telluride. *Phys. Rec.* **1954**, *96*, 1190-1191.

Jiang W., Mashayakhi H., Xing B. Bacterial toxicity comparison between nano- and micro-scaled oxide particles. *Environ. Pollut.* **2009**, *157*, 1619-1625.

Jiang X., Röcker C., Hafner M., Brandholt S., Dörlich R. M., Nienhaus G. U. Endo- and exocytosis of zwitterionic quantum dot nanoparticles by live HeLa cells. *ACS Nano* **2010**, *4*, 6787-6797.

Jin T., Sun D., Su J. Y., Zhang H., Sue H. Antimicrobial efficacy of zinc oxide quantum dots against *Listeria monocytogenes*, *Salmonella Enteritidis*, and *Escherichia coli* O157:H7. *J. Food Sci.* **2009**, *74*, M46-M52.

Johari-Ahar M., Barar J., Alizadeh A. M., Davaran S., Omidi Y., Rashidi M. Methotrexate-conjugated quantum dots: synthesis, characterisation and cytotoxicity in drug resistant cancer cells. *J. Drug Target.* **2015**, *24*, 120-133.

Kagan C., Murray C., Nirmal M., Bawendi M. Electronic energy transfer in CdSe quantum dot solids. *Phys. Rev. Lett.* **1996**, *76*, 1517-1520.

Kalyanaraman B., Darley-Usmar V., Davies K. J. A., Dennery P. A., Forman H. J., Grisham M. B., Mann G. E., Moore K., Roberts J. L., Ischiropoulos H. Measuring reactive oxygen and nitrogen species with fluorescent probes: challenges and limitates. *Free Radic. Biol. Med.* **2012**, *52*, 1-6.

Kamat P. V. Quantum dot solar cells. Semiconductor nanocrystals as light harvesters. *J. Phys. Chem. C* **2008**, *112*, 18737-18753.

Kang Z., Tsang C. H. A., Wong N., Zhang Z., Lee S. Silicon quantum dots: A general photocatalyst for reduction, decomposition, and selective oxidation reactions. *J. Am. Chem. Soc.* **2007**, *129*, 12090-12091.

Katari J. E. B., Colvin V. L, Alivisatos A. P. X-ray photoelectron spectroscopy of CdSe nanocrystals with applications to studies of the nanocrystal surface. *J. Phys. Chem.* **1994**, *98*, 4109-4117.

Katsumiti A., Gilliland D., Arostegui I., Cajaraville M. P. Cytotoxicity and cellular mechanisms involved in the toxicity of CdS quantum dots in hemocytes and gill cells of the mussel *Mytilus galloprovincialis*. *Aquat. Toxicol.* **2014**, *153*, 39-52.

Kauffer F. A., Merlin C., Balan L., Schneider R. Incidence of the core composition on the stability, the ROS production and the toxicity of CdSe quantum dots. *J. Hazard. Mater.* **2014**, *268*, 246-255.

Keire D. A., Strauss E., Guo W., Noszal B., Rabenstein D. L. Kinetics and equilibria of thiol disulfide interchange reactions of selected biological thiols and related molecules with oxidized glutathione. *J. Org. Chem.* **1992**, *57*, 123-127.

Kelley S. O., Barton J. K. Electron transfer between bases in double helical DNA. *Science* **1999**, *283*, 375-381.

Kensova R., Blazkova I., Vaculovicova M., Milosvljevic V., Blazkova L., Hynek D., Kopel P., Novotna M., Zehnalek J., Pohanka M., Trnkova L., Adam V., Kizek R. The effect of cadmium ions and cadmium nanoparticles on chicken embryos and evaluation of organ accumulation. *Int. J. Electrochem. Sci.* **2015**, *10*, 3623-3634.

Khalil W. K. B., Girgis E., Emam A. N., Mohamed M. B., Rao K. V. Genotoxicity evaluation of nanomaterials: DNA damage, micronuclei, and 8-hydroxy-2-deoxyguanosine induced by magnetic doped CdSe quantum dots in male mice. *Chem. Res. Toxicol.* **2011**, *24*, 640-650.

King P. W. Designing interfaces of hydrogenase-nanomaterial hybrids for efficient solar conversion. *Biochim. Biophys. Acta* **2013**, *1827*, 949-952.

Kim Y., Cook S., Tuladhar S. M., Choulis S. A., Nelson J., Durrant J. R., Bradley D. D. C., Giles M., McCulloch I., Ha C., Ree M. A strong regioregularity effect in self-organizing conjugated polymer films and high-efficiency polythiophene: fullerene solar cells. *Nat. Mater.* **2006**, *5*, 197-203.

Kim Y., Lee D. D., Cha H. G., Kim C. W., Kang Y. C., Kang Y. S. Preparation and characterization of the antibacterial Cu nanoparticle formed on the surface of SiO_2 nanoparticles. *J. Phys. Chem. B* **2006**, *110*, 24923-24928.

Kim S., Park J., Jang Y., Chung Y., Hwang S., Hyeon T. Synthesis of monodisperse palladium nanoparticles. *Nano Lett.* **2003**, *3*, 1289-1291.

Kim J., Park Y., Yoon T. H., Yoon C. S., Choi K. Phototoxicity of CdSe/ZnSe quantum dots with surface coatings of 3-mercaptopropionic acid or tri-n-octylphosphine oxide/gum arabic in *Daphnia magna* under environmentally relevant UV-B light. *Aquat. Toxicol.* **2010**, *97*, 116-124.

King-Heiden T. C., Wiecinski P. N., Mangham A., N., Metz K. M., Nesbit D., Pedersen J. A., Hamers R. J., Heideman W., Peterson R. E. Quantum dot nanotoxicity assessment using the zebrafish embryo. *Environ. Sci. Technol.* **2009**, *43*, 1605-1611.

Kirchner C., Javier A. M., Susha A. S., Rogach A. L., Kreft O., Sukhorukov G. B., Parak W. J. Cytotoxicity of colloidal CdSe and CdSe/ZnS nanoparticles. *Nano Lett.* **2005**, *5*, 331-338.

Klaassen C. D., Liu J., Diwan B. A. Metallothionein protection of cadmium toxicity. *Toxicol. Appl. Pharmacol.* **2009**, *238*, 215-220.

Klaper R., Arndt D., Bozich J., Dominguez G. Molecular interactions of nanomaterials and organisms: defining biomarkers for toxicity and high-throughput screening using traditional and next-generation sequencing approaches. *Analyst* **2014**, *139*, 882-895.

Kleopfer J. A., Mielke R. E., Nadeau J. L. Uptake of CdSe and CdSe/ZnS quantum dots into bacteria via purine-dependent mechanisms. *Appl. Environ. Microbiol.* **2005**, *71*, 2548-2557.

Kohanski M. A., Dwyer D. J., Hayete B., Lawrence C. A., Collins J. J. A common mechanism of cellular death induced by bactericidal antibiotics. *Cell* **2007**, *130*, 797-810.

Kongkanand A., Tvrdy K., Takechi K., Kuno M., Kamat P. V. Quantum dot solar cells. Tuning photoresponse through size and shape control of CdSe – TiO_2 architecture. *J. Am Chem. Soc.* **2008**, *130*, 4007-4015.

Konstantatos G., Howard I., Fischer A., Hoogland S., Clifford J., Klem E., Levina L., Sargent E. H. Ultrasensitive solution-cast quantum dot photodetectors. *Nature* **2006**, *442*, 180-183.

Kreibig U. Electronic properties of small silver particles: the optical constants and their temperature dependence. *J. Phys. F: Metal Phys.* **1974**, *4*, 999-1014.

Kroto H. W., Heath J. R., O'Brien S. C., Curl R. F., Smalley R. E. C_{60}: buckmisterfullerene. *Nature* **1985**, *318*, 162-163.

Kruk M., Jaroniec M. Gas adsorption characterization of ordered organic-inorganic nanocomposite materials. *Chem. Mater.* **2001**, *13*, 3169-3183.

Kubař T., Gutiérrez R., Kleinekathöfer U., Cuniberti G., Elstner M. Modeling charge transport in DNA using multi-scale methods. *Phys. Status Solidi B* **2013**, *250*, 2277-2287.

Kubena R. L., Joyce R. J., Ward J. W., Garvin H. L., Stratton F. P., Brault R. G. Dot lithography for zero-dimensional quantum wells using focused ion beams. *Appl. Phys. Lett.* **1987**, *50*, 1589-1591.

Kuo T., Lee C., Lin S., Dong C., Chen C., Tan H. Studies of intracorneal distribution and cytotoxicity of quantum dots: risk assessment of eye exposure. *Chem. Res. Toxicol.* **2011**, *24*, 253-261.

Ladhar C., Geffroy B., Cambier S., Treguer-Delapierre M., Durand E., Brèthes D., Bourdineaud J. Impact of dietary cadmium sulphide nanoparticles on *Danio rerio* zebrafish at very low contamination pressure. *Nanotoxicology* **2014**, *8*, 676-685.

Lai L., Jin J., Xu Z., Ge Y., Jiang F., Liu Y. Spectroscopic and microscopic studies on the mechanism of mitochondrial toxicity induced by CdTe QDs modified with different ligands. *J. Membr. Biol.* **2015**, *248*, 727-740.

Lai L., Lin C., Xiao C., Xu Z., Han X., Fu L., Li D., Mei P., Jiang F., Guo Q., Liu Y. Adhesion of quantum dots-induced membrane damage of *Escherichia coli*. *J. Colloid Interface Sci.* **2013**, *389*, 61-70.

Lakowitcz J. R. Principles of Fluorescence Spectroscopy 3rd ed. Springer **2006**.

Lampert M. A. Simplified theory of space-charge-limited currents in an insulator with traps. *Phys. Rev.* **1956**, *103*, 1648-1656.

Lampis S., Zonaro E., Bertolini C., Cecconi D., Monti F., Micaroni M., Turner R. J., Butler C. S., Vallini G. Selenite biotransformation and detoxification by *Stenotrophomonas maltophilia* SeITE02: novel clues on the route to bacterial biogenesis of selenium nanoparticles. *J. Hazard. Mater.* **2016**, *in press*.

Landry M. L., Morrell T. E., Karagounis T. K., Hsia C., Wang C. Simple syntheses of CdSe quantum dots. *J. Chem. Educ.* **2014**, *91*, 274-279.

Lankoff A., Sandberg W. J., Wegierek-Ciuk A., Lisowska H., Refsnes M., Sartowska B., Schwarze P. E., Meczynska-Wielgosz S>, Wojewodzka M., Kruszewski M. The effect of agglomeration state of silver and titanium dioxide nanoparticles on cellular response of HepG2, A549 and THP-1 cells. *Toxicol. Lett.* **2012**, *208*, 197-213.

Larson D. R., Zipfel W. R., Williams R. M., Clark S. W., Bruchez M. P., Wise F. W., Webb W. W. Water-soluble quantum dots for multiphoton fluorescence imaging *in vivo*. *Science* **2003**, *300*, 1434-1436.

Law M., Luther J. M., Song Q., Hughes B. K., Perkins C. L., Nozik A. J. Optical and electrical properties of PbSe nanocrystal solids treated thermally or with simple amines. *J. Am. Chem. Soc.* **2008**, *130*, 5974-5985.

Law W., Yong K., Roy I., Ding H., Hu R., Zhao W., Prasad P. N. Aqueous-phase synthesis of highly luminescent CdTe/ZnTe core/shell quantum dots optimized for targeted bioimaging. *Small* **2009**, *5*, 1302-1310.

L'Azou B., Passagne I., Mounicou S., Tréguer-Delapierra M., Puljalté I., Szpunar J., Lobinski R., Ohayon-Courtès C. Comparative cytotoxicity of cadmium forms ($CdCl_2$, CdO, CdS micro- and nanoparticles) in renal cells. *Toxciol. Res.* **2014**, *3*, 32-41.

LeBel C. P., Bondy S. C. Sensitive and rapid quantification of oxygen ractive species formation in rat synaptosomes. *Neurochem. Int.* **1990**, *17*, 435-440.

LeClerc J. E., Li B., Payne W. L., Cebula T. A. High mutation frequencies among *Escherichia coli* and salmonella pathogens. *Science* **1996**, *274*, 1208-1211.

Lee Y., Lo Y. Highly efficient quantum-dot-sensitized solar cell based on co-sensitization of CdS/CdSe. *Adv.Funct. Mater.* **2009**, *19*, 604-609.

Lee C., Lowery A., Halas N., West J., Drezek R. Immunotargeted nanoshells for integrated cancer imaging and therapy. *Nano Lett.* **2005**, *5*, 709-711.

Lee H., Shin D., Song H., Yuk J., Lee Z., Lee S., Hwang S. M., Kim J., Lee C., Jo E. Nanoparticles up-regulate tumor necrosis factor-alpha and CXCL8 via reactive oxygen species and mitogen-activated protein kinase activation. *Toxicol. Appl. Pharmacol.* **2009**, *238*, 160-169.

Lewinski N., Colvin V., Drezek R. Cytotoxicity of nanopartides. *Small* **2008**, *4*, 26-49.

Li K. G., Chen J. T., Bai S. S., Wen X., Song S. Y., Yu Q., Li J., Wang Y. Q.. Intracellular oxidative stress and cadmium ions release induce cytotoxicity of unmodified cadmium sulfide quantum dots. *Toxicol. In Vitro* **2009**, *23*, 1007-1013.

Li X., Chen N., Su Y., He Y., Yin M., Wei M., Wang L., Huang W., Fan C., Huang Q. Autophagy-sensitized cytotoxicity of quantum dots in PC12 cells. *Adv. Healthc. Mater.* **2014**, *3*, 354-359.

Li H., Li M., Shih W. Y., Lelkes P. I., Shih W. Cytotoxicity tests of water soluble ZnS and CdS quantum dots. *J. Nanosci. Nanotechnol.* **2011**, *11*, 3543-3551.

Li L., Pandey A., Werder D. J., Khanal B. P., Peityga J. M., Klimov V. I. Efficient synthesis of highly luminescent copper indium sulfide-based core/shell nanocrystals with surprisingly long-lived emission. *J. Am. Chem. Soc.* **2011**, *133*, 1176-1179.

Li L., Qian H., Fang N., Ren J. Significant enhancement of the quantum yield of CdTe nanocrystals synthesized in aqueous phase by controlling the pH and concentrations of precursor solutions. *J. Lumin.* **2006**, *116*, 59-66.

Li Y., Zhang W., Niu J., Chen Y. Mechanism of photogenerated reactive oxygen species and correlation with the antibacterial properties of engineered metal-oxide nanoparticles. *ACS Nano* **2012**, *6*, 5164-5173.

Li J., Zhang Y., Xiao Q., Tian F., Liu X., Li R., Zhao F., Jiang F., Liu Y. Mitochondria as target of quantum dots toxicity. *J. Hazard. Mater.* **2011**, *194*, 440-444.

Liang J., He Z., Zhang S., Huang S., Ai X., Yang H., Han H. Study on DNA damage induced by CdSe quantum dots using nucleic acid molecular "light switches" as probe. *Talanta* **2007**, *71*, 1675-1678.

Liang X., Wang H., Zhu Y., Zhang R., Cogger V. C., Liu X., Xu Z. P., Grice J. E., Roberts M. S. Short- and long-term tracking of anionic ultra-small nanoparticles in kidney. *ACS Nano* **2016**, *10*, 387-395.

Lin S., Bhattacharya P., Rajapakse N. C., Brune D. E., Ke P. C. Effects of quantum dots adsorption on algal photosynthesis. *J. Phys. Chem. C* **2009**, *113*, 10962-10966.

Link S., El-Sayed M. A. Size and temperature dependence of the plasmon absorption of colloidal gold nanoparticles. *J. Phys. Chem. B* **1999**, *103*, 4212-4217.

Liu Z., Ada E. T., Shamsuzzoha M., Thompson G. B., Nikles D. E. Synthesis and activation of PtRu alloyed nanoparticles with controlled size and composition. *Chem. Mater.* **2006**, *18*, 4946-4951.

Liu Y., Chen W., Joly A. G., Wang Y., Pope C., Zhang Y., Bovin J., Sherwood P. Comparison of water-soluble CdTe nanoparticles synthesized in air and in nitrogen. *J. Phys. Chem. B* **2006**, *110*, 16992-17000.

Liu J., Hu R., Liu J., Zhang B., Wang Y., Liu X., Law W., Liu L., Ye L., Yong K. Cytotoxicity assessment of functionalized CdSe, CdTe and InP quantum dots in two human cancer cell models. *Mater. Sci. Eng. C* **2015**, *57*, 222-231.

Liu N., Mu Y., Chen Y., Sung H., Han S., Wang M., Wang H., Li Y., Xu Q., Huang P., Sung Z. Degradation of aqueous synthesized CdTe/ZnS quantum dots in mice: differential blood kinetics and biodistribution of cadmium and tellurium. *Part. Fibre Toxicol.* **2013**, *10*, 37.

Liu T., Xing R., Zhou Y., Zhang J., Su Y., Zhang K., He Y., Sima Y., Xu S. Hematopoiesis toxicity induced by CdTe quantum dots determined in an invertebrate model organism. *Biomaterials* **2014**, *35*, 2942-2951.

Liu Z., Zhou X., Wu Q., Zhao Y., Wang D. Crucial role of intestinal barrier in the formation of transgenerational toxicity in quantum dots exposed nematodes *Caenorhabditis elegans*. *RSC Adv.* **2015**, *5*, 94257-94266.

Longothetidis S., Cardona M., Lautenschlager P., Garriga M. Temperature dependence of the dielectric function and the interband critical points of CdSe. *Phys. Rev. B* **1986**, *34*, 2458-2469.

Lonhienne T. G. A., Sagulenko E., Webb R. I., Lee K., Franke J., Devos D. P., Nouwens A., Carroll B. J., Fuerst J. A. Endocytosis-like protein uptake in the bacterium *Gemmata obscuriglobus*. *Proc. Natl. Acad. Sci. U.S.A.* **2010**, *107*, 12883-12888.

Lopez-Sanchez J. A., Dimitratos N., Hammond C., Brett G. L., Kesavan L., White S., Miedziak P., Tiruvalam R., Jenkins R. L., Carley A. F., Knight D., Kiely C. J., Hutchings G. J. Facile removal of stabilizer-ligands from supported gold nanoparticles. *Nat. Chem.* **2011**, *3*, 551-556.

Lovrić J., Bazzi H. S., Cuie Y., Fortin G. R. A., Winnik F. M., Maysinger D. Differences in subcellular distribution and toxicity of green and red emitting CdTe quantum dots. *J. Mol. Med.* **2005**, *83*, 377-385.

Lovrić J., Cho S. J., Winnik F. M., Maysinger D. Unmodified cadmium telluride quantum dots induce reactive oxygen species formation leading to multiple organelle damage and cell death. *Chem. Biol.* **2005**, *12*, 1227-1234.

Lu Z., Li C. M., Bao H., Qiao Y., Toh Y. Mechanism of antimicrobial activity of CdTe quantum dots. *Langmuir* **2008**, *24*, 5445-5452.

Luo Y. H., Wu S., Wei Y., Chen Y., Tsai M., Ho C., Lin S., Yang C., Lin P. Cadmium-based quantum dot induced autophagy formation for cell survival via oxidative stress. *Chem. Res. Toxicol.* **2013**, *26*, 662-673.

Luo Z., Wu Q., Zhang M., Li P., Ding Y. Cooperative antimicrobial activity of CdTe quantum dots with rocephin and fluorescence monitoring for *Escherichia coli*. *J. Colloid Interface Sci.* **2011**, *362*, 100-106.

Ma J., Chen J., Guo J., Wang C. C., Yang W. L., Xu L., Wang P. N. Photostability of thiol-capped CdTe quantum dots in living cells: the effect of photooxidation. *Nanotechnology* **2006**, *17*, 2083-2089.

Ma J., Chen J., Zhang Y., Wang P., Guo J., Yang W., Wang C. Photochemical instability of thiol-capped CdTe quantum dots in aqueous solution and living cells: Process and mechanism. *J. Phys. Chem. B* **2007**, *111*, 12012-12016.

Ma-Hock L., Brill S., Wihlleben W., Farias P. M. A., Chaves C. R., Tenório D. P. L. A., Fontes A., Santos B. S., Landsiedel R., Strauss V., Treumann S., van Ravenzwaay B. Short term inhalation toxicity of a liquid aerosol of CdS/$Cd(OH)_2$ core shell quantum dots in male Wistar rats. *Toxicol. Lett.* **2012**, *208*, 115-124.

Madelung O. Semiconductors: Data Handbook, 3rd ed. Springer **2004**.

Mahendra S., Zhu H., Colvin V. L., Alvarez P. J. Quantum dot weathering results in microbial toxicity. *Environ. Sci. Technol.* **2008**, *42*, 9424-9430.

Mahto S. K., Park C., Yoon T. H., Rhee S. W. Assessment of cytocompatibility of surface-modified CdSe/ZnSe quantum dots for BALB/3T3 fibroblast cells. *Toxicol. In Vitro* **2010**, *24*, 1070-1077.

Mallajosyula S. S., Pati S. K. Toward DNA conductivity: a theoretical perspective. *J. Phys. Chem. Lett.* **2010**, *1*, 1881-1894.

Manabe N., Hoshino A., Liang Y., Goto T., Kato N., Yamamoto K. Quantum dot as a drug tracer *in vivo*. *IEEE Trans. Nanobioscience* **2006**, *5*, 263-267.

Mancini M. C., Kairdolf B. A., Smith A. M., Nie S. Oxidative quenching and degradation of polymer-encapsulated quantum dots: new insights into the long-term fate and toxicity of nanocrystals *in vivo*. *J. Am. Chem. Soc.* **2008**, *130*, 10836-10837

Medintz I. L., Mattoussi H. Quantum dot-based resonance energy transfer and its growing application in biology. *Phys. Chem. Chem. Phys.* **2009**, *11*, 17-45.

Mei J., Yang L., Lai L., Xu Z., Wang C., Zhao J., Jin J., Jiang F., Liu Y. The interactions between CdSe quantum dots and yeast *Saccharomyces cerevisiae*: adhesion of quantum dots to the cell surface and the protection effect of ZnS shell. *Chemosphere* **2014**, *112*, 92-99.

Michael P. W. Cadmium carcinogenesis in review. *J. Inorg. Biochem.* **2000**, *79*, 241-244.

Michalet X., Pinaud F. F., Bentolil L. A., Tsay J. J., Doose S., Li J. J., Sundaresan G., Wu A. M., Gambhir S. S., Weiss S. Quantum dots for live cells, *in vivo* imaging and diagnostics. *Science* **2005**, *307*, 1208-1211.

Migita S., Moquin A., Fujishiro H., Himeno S., Maysinger D., Winnik F. M., Taniguchi A. Quantum dots induce heat shock-related cytotoxicity at intracellular environment. *In Vitro Cell. Dev. Biol. Anim.* **2014**, *50*, 367-372.

Mirkin C. A., Letsinger R. L., Mucic R. C., Storhoff J. J. A DNA-based method for rationally assembling nanoparticles into macroscopic materials. *Nature* **1996**, *382*, 607-609.

Mitchell G. P., Mirkin C. A., Letsinger R. L. Programmed assembly of DNA functionalized quantum dots. *J. Am. Chem. Soc.* **1999**, *121*, 8122-8123.

Monthious M., Kuznetsov V. L. Who should be given the credit for the discovery of carbon nanotubes? *Carbon* **2006**, *44*, 1621-1623.

Morella G., De Giorgi M., Kudera S., Manna L., Cingolani R., Anni M. Temperature and size dependence of nonradiative relaxation and exciton-phonon coupling in colloidal CdTe quantum dots. *J. Phys. Chem. C* **2007**, *111*, 5846-5849.

Mortensen L. J., Oberdörster G., Pentland A. P., Delouise L. A. *In vivo* skin penetration of quantum dot nanoparticles in the murine model: the effect of UVR. *Nano Lett.* **2008**, *8*, 2779-2787.

Mosmann T. Rapid colorimetric assay for cellular growth and survival: application to proliferation and cytotoxicity assays. *J. Immunol. Methods* **1983**, *65*, 55-63.

Moulick A., Blazkova I., Milosavljevic V., Fohlerova Z., Hubalek J., Kopel P., Vaculovicova M., Adam V., Kizek R. Application of CdTe/ZnSe quantum dots in *in vitro* imaging of chicken tissue and embryo. *Photochem. Photobiol.* **2015**, *91*, 417-423.

Mu Q., Jiang G., Chen L., Zhou H., Fourches D., Tropsha A., Yan B. Chemical basis of interactions between engineered nanoparticles and biological systems. *Chem. Rev.* **2014**, *114*, 7740-7781.

Murphy C. B., Zhang Y., Troxler T., Ferry V., Martin J. J., Jones W. E. Probing Förster and Dexter energy-transfer mechanisms in fluorescent conjugated polymer chemosensors. *J. Chem. B* **2004**, *17*, 1537-1543.

Murray C. B. Kagan C. R., Bawendi M. G. Self-organization of CdSe nanocrystallites into three-dimensional quantum dot superlattices. *Science* **1995**, *270*, 1335-1338.

Murray C. B., Kagan C. R., Bawendi M. G. Synthesis and characterization of monodisperse nanocrystals and close-packed nanocrystal assemblies. *Annu. Rev. Mater. Sci.* **2000**, *30*, 545-610.

Murray C. B., Norris D. J., Bawendi M. G. Synthesis and characterization of nearly monodisperse CdE (E = sulfur, selenium, tellurium) semiconductor nanocrystallites. *J. Am. Chem. Soc.* **2005**, *115*, 8706.

Mylonas C., Kouretas D. Lipid peroxidation and tissue damage. *In Vivo* **1999**, *13*, 295-309.

Mytilinaios I.,Salih M., Schofield H. K., Lambert R. J. W. Growth curve prediction from optical density data. *Int. J. Food Microbiol.* **2012**, *154*, 169-176.

Nabiev I., Mitchell S., Davies A., Williams Y., Kelleher D., Moore R., Gun'ko Y. K., Byme S., Rakovich Y. P., Donegan J. F., Sukhanova A., Conroy J., Cottell D., Gaponik N., Rogach A., Volkov Y. Nonfunctionalized nanocrystals can exploit a cell's active transport machinery delivering them to specific nuclear and cytoplasmic compartments. *Nano Lett.* **2007**, *7*, 3452-3461.

Nagpal P., Klimov V. I. Role of mid-gap states in charge transport and photoconductivity in semiconductor nanocrystal films. *Nat. Commun.* **2011**, *2*.

Nagy A., Hollingsworth J. A., Hu B., Steinbrück A., Stark P. C., Rios-Valdez C., Vuyisich M., Steward M. H., Atha D. H., Nelson B. C., Iyer R. Functionalization-dependent induction of cellular survival pathways by CdSe quantum dots in primary normal human bronchial epithelial cells. *ACS Nano* **2013**, *7*, 8397-8411.

Nagy A., Steinbrück A., Gao J., Doggett N., Hollingsworth J. A., Iyer R. Comprehensive analysis of the effects of CdSe quantum dot size, surface charge, and functionalization on primary human lung cells. *ACS Nano* **2012**, *6*, 4748-4762.

Nagy A., Zane A., Cole S. L., Severance M., Dutta P. K., Waldman W. J. Contrast of the biological activity of negatively and positively charged microwave synthesized CdSe/ZnS quantum dots. *Chem. Res. Toxicol.* **2011**, *24*, 2176-2188.

National Renewable Energy Laboratory. Reference Solar Spectral Irradiance: Air Mass 1.5. http://rredc.nrel.gov/solar/spectra/am1.5/ (accessed Aug 15, 2013).

Neibert K. D., Maysinger D. Mechanisms of cellular adaptation to quantum dots--the role of glutathione and transcription factor EB. *Nanotoxicology* **2012**, *6*, 249-262.

Nguyen C. C., Rippstein P., Tayabali A. F., Willmore W. G. Mitochondrial toxicity of cadmium telluride quantum dot nanoparticles in mammalian hepatocytes. *Toxicol. Sci.* **2015**, *146*, 31-42.

Nguyen K. C., Seligy V. L., Tayabali A. F. Cadmium telluride quantum dot nanoparticle cytotoxicity and effects on model immune responses to *Pseudomonas aeruginosa*. *Nanotoxicology* **2013**, *7*, 202-211.

Nielsen P. E., Eghold M., Berg R. H., Buchardt O. Sequence-selective recognition of DNA by strand displacement with a thymine-substituted polyamide. *Science* **1991**, *254*, 1497-1500.

Nies D. H., Silver S. Ion efflux systems involved in bacterial metal resistances. *J. Ind. Microbiol. Biotechnol.* **1995**, *14*, 186-199.

Nobusada K., Yamaki T. Electronic properties of palladium-thiolate complexes with tiara-like structures. *J. Phys. Chem. A* **2004**, *108*, 1813-1817.

Noh H., Goodman S. M., Mohan P., Goodwin A. P., Nagpal P., Cha J. N. Direction conjugation of DNA to quantum dots for scalable assembly of photoactive thin films. *RSC Adv.* **2014**, *4*, 8064-8071.

Noh H., Hung A. M., Cha J. N. Surface-driven DNA assembly of binary cubic 3D nanocrystal superlattices. *Small* **2011**, *7*, 3021-3025.

Nordberg M. Studies on metallothionein and cadmium. *Environ. Res.* **1978**, *15*, 381-404.

Norris D. J., Bawendi M. G. Measurement and assignment of the size-dependent optical spectrum in CdSe quantum dots. *Phys. Rev. B* **1996**, *53*, 16338-16346.

Novoselov K. S., Geim A. K., Morozov S. V., Jiang D., Zhang Y., Dubonos S. V., Grigorieva I. V., Firsov A. A. Electric field effect in atomically thin carbon films *Science* **2004**, *306*, 666-669.

Nozik A. J. Quantum dot solar cells. *Physica E* **2002**, *14*, 115-120.

Nykypanchuk D., Maye M. M., Lelie D. V., Gang O. DNA-guided crystallization of colloidal nanoparticles. *Nature* **2008**, *451*, 549-552.

Oberdörster G., Maynard A., Donaldson K., Castranova V., Fitzpatrick J., Ausman K., Carter J., Karn B., Kreyling W., Lai D, Olin S., Monteiro-Riviere N., Warheit D., Yang H. Principles for characterizing the potential human health effects from exposure to nanomaterials: elements of a screening strategy. *Part. Fibre Toxicol.* **2005**, *2*, 8.

Oberdörster G., Oberdörster E., Oberdörster J. Nanotoxicology: an emerging discipline evolving from studies of ultrafine particles. *Environ. Health Perspect.* **2005**, *113*, 823-839

Oh S., Lim S. A rapid and transient ROS generation by cadmium triggers apoptosis via caspase-dependent pathway in HepG2 cells and this is inhibited through N-acetylcysteine-mediated catalase upregulation. *Toxicol. Appl. Pharmacol.* **2006**, *212*, 212-223.

Oh E., Liu R., Nel A., Gemill K. B., Bilal M., Cohen Y., Medintz I. L. Meta-analysis of cellular toxicity for cadmium containing quantum dots. *Nat. Nanotechnol.* **2016**, *11*, 479-486.

Pace H. E., Lesher E. K., Ranville J. F. Influence of stability on the acute toxicity of CdSe/ZnS nanocrystals to *Daphnia magna*. *Environ. Toxicol. Chem.* **2010**, *29*, 1338-1344.

Padilha L. A., Robel I., Lee D. C., Nagpal P., Pietryga J. M., Klimov V. I. Spectral dependence of nanocrystal photoionization probability: the role of hot-carrier transfer. *ACS Nano* **2011**, *5*, 5045-5055.

Pal S.,Tak Y. K., Song J. M. Does the antibacterial activity of silver nanoparticles depend on the shape of the nanoparticle? A study of the gram-negative bacterium *Escherichia coli*. *Appl. Environ. Microbiol.* **2007**, *73*, 1712-1720.

Pandey A., Guyot-Sionnest P. Slow electron cooling colloidal quantum dots. *Science* **2008**, *322*, 929-932.

Panthani M. G., Akhavan V., Goodfellow B., Schmidtke J. P., Dunn L., Dodabalapur A., Barbara P. F., Korgel B. A. Synthesis of $CuInS_2$, $CuInSe_2$, and $Cu(In_xGa_{1-x})Se_2$ (CIGS) nanocrystal "inks" for printable photovoltaics. *J. Am. Chem. Soc.* **2008**, *130*, 16770-16777.

Park C., Do H. K., Min J. K., Tae H. Y. Preparation, characterization and toxicological impacts of monodisperse quantum dot nanocolloids in aqueous solution. *Bull. Korean Chem. Soc.* **2008**, *29*, 303-304.

Park S. Y., Lytton-Jean A. K. R., Lee B., Weigand S., Schatz G. C., Mirkin C. A. DNA-programmable nanoparticle crystallization. *Nature* **2008**, *451*, 553-556.

Pattnaik P. Surface plasmon resonance applications in understanding receptor-ligand interactions. *Appl. Biochem. Biotechnol.* **2005**, *126*, 79-92.

Pelley J. L., Daar A. S., Saner M. A. State of academic knowledge on toxicity and biological fate of quantum dots. *Toxicol. Sci.* **2009**, *112*, 276-296.

Peng S., Padva A., LeBreton P. R. Ultraviolet photoelectron studies of biological purines: the valence electronic structure of adenine. *Proc. Natl. Acad. Sci. U.S.A.* **1976**, *73*, 2966-2968.

Peng A. A., Peng X. Formation of high-quality CdTe, CdSe, and CdS nanocrystals using CdO as precursor. *J. Am. Chem. Soc.* **2001**, *123*, 183-184.

Peshavariya H. M., Dusting G. J., Selemidis S. Analysis of dihydroethidium fluorescence for the detection of intracellular and extracellular superoxide produced by NADPH oxidase. *Free Radic. Res.* **2007**, *41*, 699-712.

Peynshaert K., Manshian B. B., Joris F., Braeckmans K., De Smedt S. C., Demeester J., Soenen S. J. Exploiting intrinsic nanoparticle toxicity: the pros and cons of nanoparticle-induced autophagy in biomedical research. *Chem. Rev.* **2014**, *114*, 7581-7609.

Pillai S., Catchpole K. R., Trupke T., Green M. A. Surface plasmon enhanced silicon solar cells. *J. Appl. Phys.* **2007**, *101*, 093105.

Pinaud B. A., Chen Z., Abram D. N., Jaramillo T. F. Thin films of sodium birnessite-type MnO_2: optical properties, electronic band structure, and solar photoelectrochemistry. *J. Phys. Chem. C* **2011**, *115*, 11830-11838.

Prasad K., Jha A. K. Biosynthesis of CdS nanoparticles: an improved green and rapid procedure. *J. Colloid Interface Sci.* **2010**, *342*, 68-72.

Priester J. H., Stoimenov P. K., Mielke R. E., Webb S. M., Ehrhardt C., Zhang J. P., Stucky G. D., Holden P. A. Effects of soluble cadmium salts versus CdSe quantum dots on the growth of planktonic *Pseudomonas aeruginosa*. *Environ. Sci. Technol.* **2009**, *43*, 2589-2594.

Pullar J. M., Vissers M. C., Winterbourn C. C. Living with a killer: the effects of hypochlorous acid on mammalian cells. *IUMB Life* **2000**, *50*, 259-266.

Ramadan S. E., Razak A. A., Ragab A. M., El-Meleigy M. Incorporation of tellurium into amino acids and proteins in a tellurium-tolerant fungi. *Biol. Trace Elem. Res.* **1989**, *20*, 225-232.

Rengifo-Herrera J. A., Sanabria J., Machuca F., Dierolf C. F., Pulgarin C., Orellana G. A comparison of solar photocatalytic inactivation of waterborne *E. coli* using tris(2,2'-bipyridine)ruthenium(II), rose bengal, and TiO_2. *J. Sol. Energy Eng.* **2007**, *129*, 135-140.

Resch U., Weller H., Henglein A. Photochemistry and radiation chemistry of colloidal semiconductors. 33. Chemical changes and fluorescence in CdTe and ZnTe. *Langmuir* **1989**, *5*, 1015-1020.

Ribot J. C., Chatterjee A., Nagpal P. Measurements of single nucleotide electronic states as nanoelectronic fingerprints for identification of DNA nucleobases, their protonated and unprotonated states, isomers, and tautomers. *J. Phys. Chem B* **2015**, *119*, 4968-4974.

Rikans L. E., Yamano T. Mechanisms of cadmium-mediated acute hepatotoxicity. *J. Biochem. Mol. Toxicol.* **2000**, *14*, 110-117.

Rincón A., Pulgarin C. Use of coaxial photocatalytic reactor (CAPHORE) in the TiO_2 photoassisted treatment of mixed *E. coli* and *Bacillus sp.* and bacterial community present in wastewater. *Catal. Today* **2005**, *101*, 331-344.

Roberts J. R., Antonini J. M., Porter D. W., Chapman R. S., Scabilloni J. F., Young S., Schwegler-Berry D., Castranova V., Mercer R. R. Lung toxicity and biodistribution of Cd/Se-ZnS quantum dots with different surface functional groups after pulmonary exposure in rats. *Part. Fibre Toxicol.* **2013**, *10*.

Rose A. Space-charge-limited currents in solids. *Phys. Rev.* **1955**, *97*, 1538-1544.

Rowe D. M. Thermoelectrics, an environmentally-friendly source of electric power. *Renew. Energy* **1999**, *16*, 1251-1256.

Ryman-Rasmussen J. P., Riviere J. E., Monteiro-Riviere N. A. Penetration of intact skin by quantum dots with diverse physicochemical properties. *Toxicol. Sci.* **2006**, *91*, 159-165.

Ryman-Rasmussen J. P., Riviere J. E., Monteiro-Riviere N. A. Surface coatings determine cytotoxicity and irritation potential of quantum dot nanoparticles in epidermal keratinocytes. *J. Invest. Dermatol.* **2007**, *127*, 143-153.

Rzigalinski B. A., Stobl J. S. Cadmium-containing nanoparticles: perspectives on pharmacology and toxicology of quantum dots. *Toxicol. Appl. Pharmacol.* **2009**, *238*, 280-288.

Sadaf A., Zeshan B., Wang Z., Zhang R., Xu S., Wang C., Cui Y. Toxicity evaluation of hydrophilic CdTe quantum dots and CdTe/SiO_2 nanoparticles in mice. *J. Nanosci. Nanotechnol.* **2012**, *12*, 8287-8292.

Sahu A., Khare A., Deng D. D., Norris D. J. Quantum confinement in silver selenide semiconductor nanocrystals. *Chem. Commun.* **2012**, *48*, 5458-5460.

Sakimoto K. K., Wong A. B., Yang P. Self-photosensitization of nonphotosynthetic bacteria for solar-to-chemical production. *Science* **2016**, *351*, 74-77.

Samia A. C., Chen X., Burda C. Semiconductor quantum dots for photodynamic therapy. *J. Am. Chem. Soc.* **2003**, *125*, 15736-15737.

Samia A. C. S., Dayal S., Burda C. Quantum dot-based energy transfer: perspectives and potential for applications in photodynamic therapy. *Photochem. Photobiol.* **2006**, *82*, 617-625.

Sanghi R., Verma P. A facile green extracellular biosynthesis of CdS nanoparticles by immobilized fungus. *Chem. Eng. J.* **2009**, *155*, 886-891.

Sayes C. M., Marchione A. A., Reed K. L., Warheit D. B. Comparative pulmonary toxicity assessments of C_{60} water suspensions in rats: few differences in fullerene toxicity *in vivo* in contrast to *in vitro* profiles. *Nano Lett.* **2007**, *7*, 2399-2406.

Sayes C. M., Reed K. L., Warheit D. B. Assessing toxicology of fine and nanoparticles: comparing in vitro measurements to *in vivo* pulmonary toxicity profiles. *Toxicol. Sci.* **2007**, *97*, 163-180.

Schaadt D. M., Feng B., Yu E. T. Enhanced semiconductor optical absorption via surface plasmon excitation in metal nanoparticles. *Appl. Phys. Lett.* **2005**, *86*, 063106.

Schaller R. D., Klimov V. I. High Efficiency carrier multiplication in PbSe nanocrystals: implications for solar energy conversion. *Phys. Rev. Lett.* **2004**, *92*, 186601.

Schmidt M. W., Baldridge K. K., Boatz J. A., Elbert S. T., Gordon M. S., Jensen J. H., Koseki S., Matsunaga N., Nguyen K. A., Su S., Windus T. L., Dupuis M., Montgomery J. A. General atomic and molecular electronic structure system. *J. Comput. Chem.* **1993**, *14*, 1347-1363.

Schneider M., Stracke F., Hansen S., Schaefer U. F. Nanoparticles and their interactions with the dermal barrier. *Dermatoendocrinol.* **2009**, *1*, 197-206.

Schneider R., Wolpert C., Guilloteau H., Balan L., Lambert J., Merlin C. The exposure of bacteria to CdTe-core quantum dots: the importance of surface chemistry on cytotoxicity. *Nanotechnology* **2009**, *20*, 225101.

Schroeder H. A., Frost D. V., Balass J. J. Essential metals in man: selenium. *J. Chronic Dis.* **1970**, *23*, 227-243.

Schumacher W., Nagy A., Waldman W. J., Dutta P. K. Direct synthesis of aqueous CdSe/ZnS-based quantum dots using microwave irradiation. *J. Phys. Chem. C* **2009**, *113*, 12132-12139.

Seleverstov O.,Zabimyk O., Zschamack M., Bulavina L., Nowicki M., Heinrich J. M., Yezhelyev M., Emmrich F., O'Reagan R., Bader A. Quantum dots for human mesenchymal stem cells labeling. A size-dependent autophagy activation. *Nano Lett.* **2006**, *6*, 2826-2832.

Selvan S. T., Tan T. T., Ying J. Y. Robust, non-cytotoxic, silica-coated CdSe quantum dots with efficient photoluminescence. *Adv. Mater.* **2005**, *17*, 1620-1625.

Semonin O. E., Luther J. M., Choi S., Chen H. Y., Gao J., Nozik A. J., Beard M. C. Peak external photocurrent quantum efficiency exceeding 100% via MEG in a quantum dot solar cell. *Science* **2011**, *334*, 1530-1533.

Shiohara A., Hoshino A., Hanaki K., Suzuki K., Yamamoto K. On the cyto-toxicity caused by quantum dots. *Microbiol. Immunol.* **2004**, *48*, 669-675.

Shockley W., Queisser H. J. Detailed balance limit of efficiency of p-n junction solar cells. *J. Appl. Phys.* **1961**, *32*, 510-519.

Silva A. C. A., Silva M. J. B., da Luz F. A. C., Silva D. P., de Deus S. L. V., Dantas N. O. Controlling the cytotoxicity of CdSe magic-sized quantum dots as a function of surface defect density. *Nano. Lett.* **2014**, *14*, 5452-5427.

Silver S. Bacterial resistances to toxic metal ions - a review. *Gene* **1996**, *179*, 9-19

Singh V., Beltran I. J. C., Ribot J. C., Nagpal P. Photocatalysis deconstructed: design of a new selective catalyst for artificial photosynthesis. *Nano. Lett.* **2014**, *14*, 597-603.

Singh V., Yu Y., Sun Q., Korgel B., Nagpal P. Pseudo-direct bandgap transitions in silicon nanocrystals: effects on optoelectronics and thermoelectrics. *Nanoscale* **2014**, *6*, 14643-14647.

Sinha P., Balas R., Krueger L., Wade A. Fate and transport evaluation of potential leaching risks from cadmium telluride photovoltaics. *Environ. Toxicol. Chem.* **2012**, *31*, 1670-1675.

Slaveykova V. I., Startchev K., Roberts J. Amine- and carboxyl- quantum dots affect membrane integrity of bacterium *Cupriavidus metallidurans* CH34. *Environ. Sci. Technol.* **2009**, *43*, 5117-5122.

Slinker J. D., Mann N. B., Renfrew S. E., Barton J. K. DNA charge transport over 34 nm. *Nat. Chem.* **2011**, *3*, 228-233.

Smith A. M., Mancini M. C., Nie S. Bioimaging: second window for *in vivo* imaging. *Nat. Nanotechnol.* **2009**, *4*, 710-711.

Soler M., McCusker J. K. Distinguishing between Dexter and rapid sequential electron transfer in covalently linked donor-acceptor assemblies. *J. Am. Chem. Soc.* **2008**, *130*, 4708-4724.

Song X., Li L., Qian H., Fang N., Ren J. Highly efficient size separation of CdTe quantum dots by capillary gel electrophoresis using polymer solution as sieving medium. *Electrophoresis* **2006**, *27*, 1341-1346.

Su Y., He Y., Lu H., Sai L., Li Q., Li W., Wang L., Shen P., Huang Q., Fan C. The cytotoxicity of cadmium based, aqueous phase-synthesized, quantum dots and its modulation by surface coating. *Biomaterials* **2009**, *30*, 19-25.

Su Y., Hu M., Fan C., He Y., Li Q., Li W., Wang L., Shen P., Huang Q. The cytotoxicity of CdTe quantum dots and the relative contributions from released cadmium ions and nanoparticle properties. *Biomaterials* **2010**, *31*, 4829-4834.

Su Y., Peng F., Jiang Z., Zhong Y., lu Y., Jiang X., Huang Q., Fan C., Lee S. T., He Y. *In vivo* distribution, pharmacokinetics, and toxicity of aqueous synthesized cadmium-containing quantum dots. *Biomaterials* **2011**, *32*, 5855-5862.

Sukhovatkin V., Hinds S., Brzozowski L., Sargent E. H. Colloidal quantum-dot photodetectors exploiting multiexciton generation. *Science* **2009**, *324*, 1542-1544.

Sun Q., Ding Y., Goodman S. M., Funke H. H., Nagpal P. Copper plasmonics and catalysis: role of electron-phonon interactions in dephasing localized surface plasmons. *Nanoscale* **2014**, *6*, 12450-12457.

Sun C., Lee J. S. H., Zhang M. Magnetic nanoparticles in MR imaging and drug delivery. *Adv. Drug Deliv. Rev.* **2008**, *60*, 1252-1265.

Sun B., Marx E., Greenham N. C. Photovoltaic devices using blends of branched CdSe nanoparticles and conjugated polymers. *Nano Lett.* **2003**, *3*, 961-963.

Sun Q., Mundoor H., Ribot J. C., Singh V., Smalyukh I. I., Nagpal P. Plasmon-enhanced energy transfer for improved upconversion of infrared radition in doped-lanthanide nanocrystals. *Nano Lett.* **2014**, *14*, 101-106.

Sun Y., Xia Y. Shape-controlled synthesis of gold and silver nanoparticles. *Science* **2002**, *298*, 2176-2179.

Sun Y., Zhou B., Lin Y., Wang W., Fernando K. A. S., Pathak P., Meziani M. J., Harruff B. A., Wang X., Wang H., Luo P. G., Yang H., Kose M. E., Chen B., Veca L. M., Xie S. Quantum-sized carbon dots for bright and colorful photoluminescence. *J. Am. Chem. Soc.* **2006**, *128*, 7756-7757.

Sweeney R. Y., Mao C., Gao X., Burt J. L., Belcher A. M., Georgiou G., Iverson B. L. Bacterial biosynthesis of cadmium sulfide nanocrystals. *Chem. Biol.* **2004**, *11*, 1553-1559.

Sze S. M. Physics of Semiconductor Devices, 2nd ed. Wiley-Interscience **1981**.

Talapin D. V., Lee J. S., Kovalenko M. V., Shevchenko E. V. Prospects of colloidal nanocrystals for electronic and optoelectronic applications. *Chem. Rev.* **2010**, *110*, 389-458.

Talapin D. V., Murray C. B. PbSe Nanocrystal solids for n-and p-channel thin film field-effect transistors. *Science* **2005**, *310*, 86-89.

Talapin D. V., Rogach A. L., Kornowski A., Haase M., Weller H. Highly luminescent monodisperse CdSe and CdSe/ZnS nanocrystals synthesized in a hexadecylamine-trioctylphosphine oxide−trioctylphospine mixture. *Nano Lett.* **2001**, *1*, 207-211.

Tang J., Brzozowski L., Barkhouse D. A. R., Wang X., Debnath R., Wolowiec R., Palmiano E., Levina L., Pattantyus-Abraham A. G., Jamakosmanovic D., Sargent E. H. Quantum dot photovoltaics in the extreme quantum confinement regime: the surface-chemical origins of exceptional air- and light-stability. *ACS Nano* **2010**, *4*, 869-878.

Tang J., Kemp K. W., Hoogland S., Jeong K. S., Liu H., Levina L., Furukawa M., Wang X., Debnath R., Cha D., Chou K. W., Fischer A., Amassian A., Asbury J. B., Sargent E. H. Colloidal-quantum-dot photovoltaics using atomic-ligand passivation. *Nat. Mater.* **2011**, *10*, 765-771.

Tang M., Li Z., Chen L., Xing T., Hu Y., Yang B., Ruan D., Sun F., Wang M. The effect of quantum dots on synaptic transmission and plasticity in the hippocampal dentate gyrus area of anesthetized rats. *Biomaterials* **2009**, *30*, 4948-4955.

Tang S. F., Lin S. Y., Lee S. C. Near-room temperature operation of an InAs/GaAs quantum-dot infrared photodetector. *Appl. Phys. Lett.* **2001**, *78*, 2428-2430.

Tang M., Wang M., Xing T., Zeng J., Wang H., Ruan D. Mechanisms of unmodified CdSe quantum dot-induced elevation of cytoplasmic calcium levels in primary cultures of rat hippocampal neurons. *Biomaterials* **2008**, *29*, 4383-4391.

Tang M., Xing T., Zeng J., Wang H., Li C., Yin S., Yan D., Deng H., Liu J., wang M., Chen J., Ruan D. Unmodified CdSe quantum dots induce elevation of cytoplasmic calcium levels and impairment of functional properties of sodium channels in rat primary cultured hippocampal neurons. *Environ. Health Perspect.* **2008**, *116*, 915-922.

Teranishi T., Miayake M. Size control of palladium nanoparticles and their crystal structures. *Chem. Mater.* **1998**, *10*, 694-600.

Thannickal V. J., Fanburg B. L. Reactive oxygen species in cell signaling. *Am. J. Physiol. Lung Cell. Mol. Physiol.* **2000**, *279*, L10005-L1028.

Thomas D. G., Hopfield J. J. Exciton spectrum of cadmium sulfide. *Phys. Rev.* **1959**, *116*, 573-582.

Thuy U. T. D. T., Tu L. A., Loan N. T., Chi T. T. K., Liem N. Q. Comparative photoluminescence properties of type-I and type-II CdTe/CdS core/shell quantum dots. *Opt. Mater.* **2016**, *53*, 34-38.

Tikhomirov G., Hoogland S., Lee P. E., Fischer A., Sargent E. H., Kelly S. O. DNA-based programming of quantum dot valency, self-assembly and luminescence. *Nat. Nanotechnol.* **2011**, *6*, 485-490.

Tisdale W. A., Williams J. K., Timp B. A., Norris D. J., Aydil E. S., Zhu X. Y. Hot-electron transfer from semiconductor nanocrystals. *Science* **2010**, *328*, 1543-1547.

Tsay J. M., Pflughoefft M., Bentolila L. A., Weiss S. Hybrid approach to the synthesis of highly luminescent CdTe/ZnS and CdHgTe/ZnS nanocrystals. *J. Am. Chem. Soc.* **2004**, *126*, 1936-1927.

Tsoi K. M.,Dai Q., Alman B. A., Chan W. C. W. Are quantum dots toxic? Exploring the discrepancy between cell culture and animal studies. *Acc. Chem. Res.* **2013**, *46*, 663-671.

Tyagi A., Rawat K., Verma A. K., Bohidar H. B. Mechanistic evaluation of the size dependent antimicrobial activity of water soluble QDs. *Anal. Methods* **2016**, *8*, 1060-1068.

Ulusoy M., Lavrentieva A., Walter J., Sambale F., Green M., Stahl F., Scheper T. Evaluation of CdTe/CdS/ZnS core/shell/shell quantum dot toxicity on three-dimensional spheroid cultures. *Toxicol. Res.* **2015**, *5*, 126-135.

Ulusoy M., Walter J., Lavrentieva A., Kretschmer I,m Sandiford L., Le Marois A., Bongartz R., Aliuos P., Suhling K., Stahl F., Green M., Scheper T. One-pot aqueous synthesis of highly strained CdTe/CdS/ZnS nanocrystals and their interactions with cells. *RSC Adv.* **2015**, *5*, 7485-7494.

Urano S., Yang X., LeBreton P. R. UV photoelectron and quantum mechanical characterization of DNA and RNA bases: valence electronic structures of adenine, 1,9-dimethyl-guanine, 1-methylcytosine, thymine and uracil. *J. Mol. Struct.* **1989**, *214*, 315-328.

Urban J. J., Talapin D. V., Shevchenko E. V., Murray C. B. Self-assembly of PbTe quantum dots into nanocrystal superlattices and glassy films. *J. Am. Chem. Soc.* **2006**, *128*, 3248-3255.

Valko M., Leibfritz D., Moncol J., Cronin M. T., Mazur M., Telser J. Free radicals and antioxidants in normal physiological functions and human disease. *Int. J. Biochem. Cell Biol.* **2007**, *39*, 44-84.

van de Walle C. G., Neugebauer J. Universal alignment of hydrogen levels in semiconductors and insulators. *Nature* **2003**, *423*, 626-628.

van Sark W. G. J. H. M., Frederix P. L. T. M., Van den Heuvel D. J., Gerritsen H. C., Bol A. A., Van Linger J. N. J., De Mello Donegá C., Meijerink A. Photooxidation and photobleaching of single CdSe/ZnS quantum dots probed by room-temperature time-resolved spectroscopy. *J. Phys. Chem. B* **2001**, *105*, 8281-8284.

Verma S., Das S., Khanagrot B. S. Effects of CdO nanoparticles on the development and hatching of a freshwater pulmonate snail *Lymnaea Luteola L*. *J. Biomed. Nanotechnol.* **2011**, *7*, 197-198.

Vernon-Parry K. D. Scanning electron microscopy: an introduction. *III-Vs Rev.* **2000**, *13*, 40-44.

Viana O., Ribeiro M., Rodas A., Rebouças J., Fontes A., Santos B. Comparative study on the efficiency of the photodynamic inactivation of *Candida albicans* using CdTe quantum dots, Zn(II) porphyrin and their conjugates as photosensitizers. *Molecules* **2015**, *20*, 8893-8912.

Voura E. B., Jaiswal J. K., Mattoussi H., Simon S. M. Tracking metastatic tumor cell extravasation with quantum dot nanocrystals and fluorescence emission-scanning microscopy. *Nat. Med.* **2004**, *10*, 993-998.

Vratny F., Micale F. Reflectance spectra of non-stoichiometric titanium oxide, niobium oxide, and vanadium oxide. *Trans. Faraday Soc.* **1963**, *59*, 2739-2749.

Wagner C. J. Investigations of silver sulfide. *J. Chem. Phys.* **1953**, *21*, 1819-1827.

Waitkins G. R., Clark C. W. Selenium dioxide: preparation, properties, and use as oxidizing agent. *Chem. Rev.* **1945**, *36*, 235-289.

Walker G. C. Mutagenesis and inducible responses to deoxyribonucleic acid damage in *Escherichia coli*. *Microbiol. Rev.* **1984**, *48*, 60-93.

Wang Q., Fang T., Liu P., Min X., Li X. Study of the bioeffects of CdTe quantum dots on *Escherichia coli cells*. *J. Colloid Interface Sci.* **2011**, *363*, 476-480.

Wang C., Gao X., Su X. Study the damage of DNA molecules induced by three kinds of aqueous nanoparticles. *Talanta* **2010**, *80*, 1228-1233.

Wang G., Yang X., Qian F., Zhang J. Z., Li Y. Double-sided CdS and CdSe quantum dot co-sensitized ZnO nanowire arrays for photoelectrochemical hydrogen generation. *Nano Lett.* **2010**, *10*, 1088-1092.

Wang J., Zhang X., Chen Y., Sommerfeld M., Hu Q. Toxicity assessment of manufactured nanomaterials using the unicellular green alga *Chlamydomonas reinhardtii*. *Chemosphere* **2008**, *73*, 1121-1128.

Wang L., Zheng J., Long Y., Gao M., Hao J., Du J., Mao X., Zhou D. Rapid determination of the toxicity of quantum dots with luminous bacteria. *J. Hazard. Mater.* **2010**, *177*, 1134-1137.

Wang L., Zhang J., Zheng Y., Yang J., Zhang Q., Zhu X. Bioeffects of CdTe quantum dots on human umbilical vein endothelial cells. *J. Nanosci. Nanotechnol.* **2010**, *10*, 8591-8596.

Warheit D. B. How meaningful are the results of nanotoxicity studies in the absence of adequate material characterization? *Toxicol. Sci.* **2008**, *101*, 183-185.

Warnement M. R., Tomlinson I. D., Chang J. C., Schreuder M. A., Luckabaugh C. C., Rosenthal S. J. Controlling the reactivity of ampiphilic quantum dots in biological assays through hydrophobic assembly of custom PEG derivatives. *Bioconjug. Chem.* **2008**, *19*, 1404-1413.

Watts R. J., Washington D., Howsawkeng J., Loge F. J., Teel A. L. Comparative toxicity of hydrogen peroxide, hydroxyl radicals, and superoxide anion to *Escherichia coli*. *Adv. Environ. Res.* **2003**, *7*, 961-968.

Wei C., Lin W., Zainal Z., Williams N. E., Zhu K., Kruzic A. P., Smith R. L., Rajeshwar K. Bactericidal activity of TiO_2 photocatalyst in aqueous media: toward a solar-assisted water disinfection system. *Environ. Sci. Technol.* **1994**, *28*, 934-938.

Werlin R., Priester J. H., Mielke R. E., Krämer S., Jackson S., Stoimenov P. K., Stucky G. D., Cherr G. N., Orias E., Holden P. A. Biomagnification of cadmium selenide quantum dots in a simple experimental microbial food chain. *Nat. Nanotechnol.* **2011**, *6*, 65-71.

Wijtmans M., Rosenthal S. J., Zwanenburg B., Porter N. A. Visible light excitation of CdSe nanocrystals triggers the release of coumarin from cinnamate surface ligands. *J. Am. Chem. Soc.* **2006**, *128*, 11720-11726.

Willard D. M., Carillo L. L., Jung J., Van Orden A. CdSe−ZnS quantum dots as resonance energy transfer donors in a model protein−protein binding assay. *Nano Lett.* **2001**, *1*, 469-474.

Willets K. A., van Duyne R. P. Localized surface plasmon resonance spectroscopy and sensing. *Annu. Rev. Phys. Chem.* **2007**, *58*, 267-297.

Williams Y.,Sukhanova A., Nowostawska M., Davies A. M., Mitchell S., Oleinikov V., Gun'ko Y., Nabiev I., Kelleher D., Volkov Y. Probing cell-type-specific intracellular nanoscale barriers using size-tuned quantum dots. *Small* **2009**, *5*, 2581-2588.

Winnik F. M., Maysinger D. Quantum dot cytotoxicity and ways to reduce it. *Acc. Chem. Res.* **2013**, *46*, 672-680.

World Health Organization. Global Tuberculosis Report. **2012**.

Wu T., He K., Zhan Q., Ang S., Ying J., Zhang S., Zhang T., Xue Y., Chen Y., Tang M. Partial protection of N-acetylcysteine against MPA-capped CdTe quantum dot-induced neurotoxicity in rat primary cultured hippocampal neurons. *Toxicol. Res.* **2015**, *4*, 1613-1622.

Wu T., He K., Zhan Q., Ang S., Ying J., Zhang S., Zhang T., Xue Y., Tang M. MPA-capped CdTe quantum dots exposure causes neurotoxic effects in nematode *Caenorhabditis elegans* by affecting the transporters and receptors of glutamate, serotonin and dopamine at the genetic level, or by increasing ROS, or both. *Nanoscale* **2015**, *7*, 20460-20473.

Wu T., Tang M. Toxicity of quantum dots on respiratory system. *Inhal. Toxicol.* **2014**, *26*, 128-139.

Xi W., Pattanayak S., Wang C., Fairbanks B., Gong T., Wagner J., Kloxin C. J., Bowman C. N. Clickable nucleic acids: sequence-controlled periodic copolymer/oligomer synthesis by orthogonal thiol-x reactions. *Angew. Chem. Int. Ed.* **2015**, *54*, 14462-14467.

Xiao Y., Forry S. P., Gao X., Holbrook R. D., Telford W. G., Tona A. Dynamics and mechanisms of quantum dot nanoparticle cellular uptake. *J. Nanobiotechnology* **2010**, *8*, 13.

Xu M., Deng G., Liu S., Chen S., Cui D., Yang L., Wang Q. Free cadmium ions released from CdTe-based nanoparticles and their cytotoxicity on *Phaeodactylum tricornutum*. *Metallomics* **2010**, *2*, 469-473.

Xu G., Mahajan S., Roy I., Yong K. Theranostic quantum dots for crossing blood-brain barrier in vitro and providing therapy of HIV-associated encephalopathy. *Front. Pharmacol.* **2013**, *4*, 140.

Yan M., Zhang Y., Xu K., Fu T., Qin H., Zheng X. An *in vitro* study of vascular endothelial toxicity of CdTe quantum dots. *Toxicology* **2011**, *282*, 94-103.

Yang R. S., Chang L. W., Wu J., Tsai M., Wang H., Kuo Y., Yeh T., Yang C. S., Lin P. Persistent tissue kinetics and redistribution of nanoparticles, quantum dot 705 in mice: ICP-MS quantitative assessment. *Environ. Health Perspect.* **2007**, *115*, 1339-1343.

Yang C., Xie H., Li Q., Sun E., Su B. Adherence and interaction of cationic quantum dots on bacterial surfaces. *J. Colloid. Interface Sci.* **2015**, *450*, 388-395.

Ye L., Yong K., Liu L., Roy I., Hu R., Zhu J., Cai H., Law W., Liu J., Wang K., Liu J., Liu Y., Hu Y., Zhang X., Swihart M. T. A pilot study in non-human primates shows no adverse response to intravenous injection of quantum dots. *Nat. Nanotechnol.* **2012**, *7*, 453-458.

Yoffe A. D. Low-dimensional systems: quantum size effects and electronic properties of semiconductor microcrystallites (zero-dimensional systems) and some quasi-two-dimensional systems. *Adv. Phys.* **1993**, *42*, 173-262.

Yong K., Law W., Ru R., Ye L., Liu L., Swihart M. T., Prasad P. N. Nanotoxicity assessment of quantum dots: from cellular to primate studies. *Chem. Soc. Rev.* **2013**, *42*, 1236-1250.

Yong K., Roy I., Law W., Hu R. Synthesis of cRGD-peptide conjugated near-infrared CdTe/ZnSe core-shell quantum dots for in vivo cancer targeting and imaging. *Chem. Commun.* **2010**, *46*, 7136-7138.

Yu B. P. Cellular defenses against damage from reactive oxygen species. *Physiol. Rev.* **1994**, *74*, 139-162.

Yu W. W., Qu L., Guo W., Peng X. Experimental determination of the extinction coefficient of CdTe, CdSe, and CdS nanocrystals. *Chem. Mater.* **2003**, *15*, 2854-2860.

Zeng C., Ramos-Ruiz A., Field J. A., Sierra-Alvarez R. Cadmium telluride (CdTe) and cadmium selenide (CdSe) leaching behavior and surface chemistry in response to pH and O_2. *J. Environ. Manage.* **2015**, *154*, 78-85.

Zenkevich E. I., Sagun E. I., Knyukshto V. N., Stasheuski A. S., Galievsky V. A., Stupak A. P., Blaudeck T., von Borczyskowski C. Quantitative analysis of singlet oxygen ($^1O_2$) generation via energy transfer in nanocomposites based on semiconductor quantum dots and porphyrin ligands. *J. Phys. Chem. C* **2011**, *115*, 21535-24545.

Zhang Y., Chen W., Zhang J., Liu J., Chen G., Pope C. *In vitro* and *in vivo* toxicity of CdTe nanoparticles. *J. Nanosci. Nanotechnol.* **2007**, *7*, 497-503.

Zhang Y., Hu B., Huang Y. Polyethylenimine/grapefruit peel hybrid biosorbent for the removal of toxic CdTe quantum dots from water. *RSC Adv.* **2015**, *5*, 57082-57089.

Zhang H., Hyun B., Wise F. W., Robinson R. D. A generic method for rational scalable synthesis of monodisperse metal sulfide nanoparticles. *Nano. Lett.* **2012**, *12*, 5856-5860.

Zhang X. T., Liu Y. C., Zhang L. G., Zhang J. Y., Lu Y. M., Shen D. Z., Xu W., Zhong G. Z., Fan X. W. Kong X. G. Structure and optically pumped lasing from nanocrystalline ZnO thin films prepared by thermal oxidation of ZnS thin films. *J. Appl. Phys.* **2002**, *92*, 3293-3298.

Zhang S., Metin O., Su D., Sun S. Monodisperse AgPd alloy nanoparticles and their superior catalysis for the dehydrogenation of formic acid. *Angew. Chem. Int. Ed.* **2013**, *52*, 3681-3684.

Zhang L. W., Monteiro-Riviere N. A. Assessment of quantum dot penetration into intact, tape-stripped, abraded and flexed rat skin. *Skin Pharmacol. Physiol.* **2008**, *21*, 166-180.

Zhang L. W., Monteiro-Riviere N. A. Mechanisms of quantum dot nanoparticle cellular uptake. *Toxicol. Sci.* **2009**, *110*, 138-155.

Zhang T., Stilwell J. L., Gerion D., Ding L., Elboudwarej O., Cooke P. A., Gray J. W., Alivisatos A. P., Chen F. F. Cellular effect of high doses of silica-coated quantum dot profiled with high throughput gene expression analysis and high content cellomics measurements. *Nano Lett.* **2006**, *6*, 800-808.

Zhang Y., Xu Z. Direct observation of the size dependence of Dexter energy transfer from polymer to small PbS quantum dots. *Appl. Phys. Lett.* **2008**, *93*, 083106.

Zhang L. W., Yu W. W., Colvin V. L., Monteiro-Riviere N. A. Biological interactions of quantum dot nanoparticles in skin and in human epidermal keratinocytes. *Toxicol. Appl. Pharmacol.* **2008**, *228*, 200-211.

Zhang Y., Zhang H., Ma M., Guo X., Wang H. The influence of ligands on the preparation and optical properties of water-soluble CdTe quantum dots. *Appl. Surf. Sci.* **2009**, *255*, 4747-4753.

Zhao Y., Wang X., Qu Q., Li Y., Tang M., Wang D. Quantum dots exposure alters both develppment and function of D-type GABAergic motor neurons in nematodes *Caenorhabditis elegans*. *Toxicol. Res.* **2015**, *4*, 399-408.

Zhao Y., Wang X., Wu Q., Li Y., Wang D. Translocation and neurotoxicity of CdTe quantum dots in RMEs motor neurons in nematode *Caenorhabditis elegans*. *J. Hazard. Mater.* **2015**, *283*, 480-489.

Zhao F., Zhao Y., Liu Y., Chang X., Chen C., Zhao Y. Cellular uptake, intracellular trafficking, and cytotoxicity of nanomaterials. *Small* **2011**, *7*, 1322-1337.

Zhou C., Vitiello V., Pellegrini D., Wu C., Morelli E., Buttino. oxicological effects of CdSe/ZnS quantum dots on marine planktonic organisms. *Ecotoxicol. Environ. Saf.* **2016**, *123*, 26-31.

Zhu Z., Yeh Y., Tang R., Yan B., Tamayo J., Vachet R. W., Rotello V. M. Stability of quantum dots in live cells. *Nat. Chem.* **2011**, *3*, 963-968.

Zwietering M. H., Jongenburger I., Rombouts F. M., Van't Riet K. Modeling of the bacterial growth curve. *Appl. Environ. Microbiol.* **1990**, *56*, 1875-1881.

Zeng C., Ramos-Ruiz A., Field J. A., Sierra-Alvarez R. Cadmium telluride (CdTe) and cadmium selenide (CdSe) leaching behavior and surface chemistry in response to pH and O_2. *J. Environ. Manage.* **2015**, *154*, 78-85.

Appendix

This section contains analytical, synthetic, and calibration procedures not already discussed in previous chapters.

Photoluminescence Detector Calibration. The Ocean Optics USB 4000 detector (OO) was calibrated in order to correct measured spectra. Monochromatic light was provided from 410-1,000 nm using a tungsten filament lamp projecting into a monochromator which directly illuminated the detector, which was kept in a box to prevent other incident light from being measured (Figure A.1a). The monochromator slits were adjusted to limit the bandwidth as much as possible while illuminating the entire detector area. Three replicate spectra were measured every 10 nm using the OO with the integration time (t) being adjusted to have the maximum intensity at ~60,000 counts (Figure A1b). Once complete, the power spectrum was recorded using a NIST-calibrated Newport detector at the same wavelengths (Figure A.1c). A bandpass filter (315 – 710 nm) and a longpass filter (715 nm cutoff) were used in their respective ranges to prevent the detection of second order wavelengths.

Total counts as a function of wavelength (λ) as measured by the Newport were calculated from the measured power (P) using equation A.1. The total counts as measured by the OO were calculated by first subtracting the measured baseline, then smoothing the entire spectrum using a 0.01 window Loess, and by integrating the total area. This area was normalized by the aperture diameter and the integration time to yield the total signal (equation A.2).

$$\text{Counts}_N(\lambda) = P\left(\mu\text{W}\cdot\text{cm}^{-2}\right)\times 10^{-6}\left(\text{J}\cdot\mu\text{J}^{-1}\right)\times\left[\frac{\lambda(\text{nm})}{1239.8(\text{nm}\cdot\text{eV})\times 1.60218\cdot 10^{-19}\left(\text{J}\cdot\text{eV}^{-1}\right)}\right] \quad \text{(A.1)}$$

$$\text{Counts}_{OO}(\lambda) = \frac{\int_{350}^{1050} I(\lambda)\, d\lambda}{\frac{\pi}{4}\left(0.44(\text{cm})\right)^2 t} \tag{A.2}$$

The responsivity of the OO detector was calculated by dividing the OO counts by the Newport counts at each wavelength. The relative sensitivity was then calculated by dividing the measured spectrum by the maximum observed responsivity, placing the resulting correction values on a scale from 0 – 1. To interpolate all of the individual points measured by the OO detector, a series of bigaussian functions (on the eV scale, *E*) were summed to fit the data which yielded calibration curve shown in Figure A.1d (equations A.3-11).

$$f_1 = 0.00647 + 0.555 \exp\left[\frac{-(E-2.37783)^2}{2\cdot(0.31477)^{1/2}}\right] \quad 1.55 < E < 2.37783 \tag{A.3}$$

$$f_2 = 0.00647 + 0.555 \exp\left[\frac{-(E-2.37783)^2}{2\cdot(0.1715)^{1/2}}\right] \quad 2.37783 \le E \tag{A.4}$$

$$f_3 = 0.00647 + 0.43567 \exp\left[\frac{-(E-2.01575)^2}{2\cdot(0.31149)^{1/2}}\right] \quad 1.55 < E < 2.01575 \tag{A.5}$$

$$f_4 = 0.00647 + 0.43567 \exp\left[\frac{-(E-2.01575)^2}{2\cdot(9.44613\cdot 10^{14})^{1/2}}\right] \quad 2.01575 \le E \tag{A.6}$$

$$f_5 = 0.07938 + 0.0612 \exp\left[\frac{-(E-1.32185)^2}{2\cdot(0.06576)^{1/2}}\right] \quad E < 1.32185 \tag{A.7}$$

$$f_6 = 0.07938 + 0.0612 \exp\left[\frac{-(E-1.32185)^2}{2\cdot(0.04293)^{1/2}}\right] \quad 1.32185 \le E < 1.55 \tag{A.8}$$

$$f_7 = 0.07938 + 0.11534 \exp\left[\frac{-(E-1.50438)^2}{2\cdot(0.06485)^{1/2}}\right] \quad E < 1.50438 \tag{A.9}$$

$$f_8 = 0.07938 + 0.11534 \exp\left[\frac{-(E-1.50438)^2}{2\cdot(0.15581)^{1/2}}\right] \quad 1.50438 \le E < 1.55 \tag{A.10}$$

$$S(\lambda) = \sum_{k=1}^{8} f_k(\lambda) \tag{A.11}$$

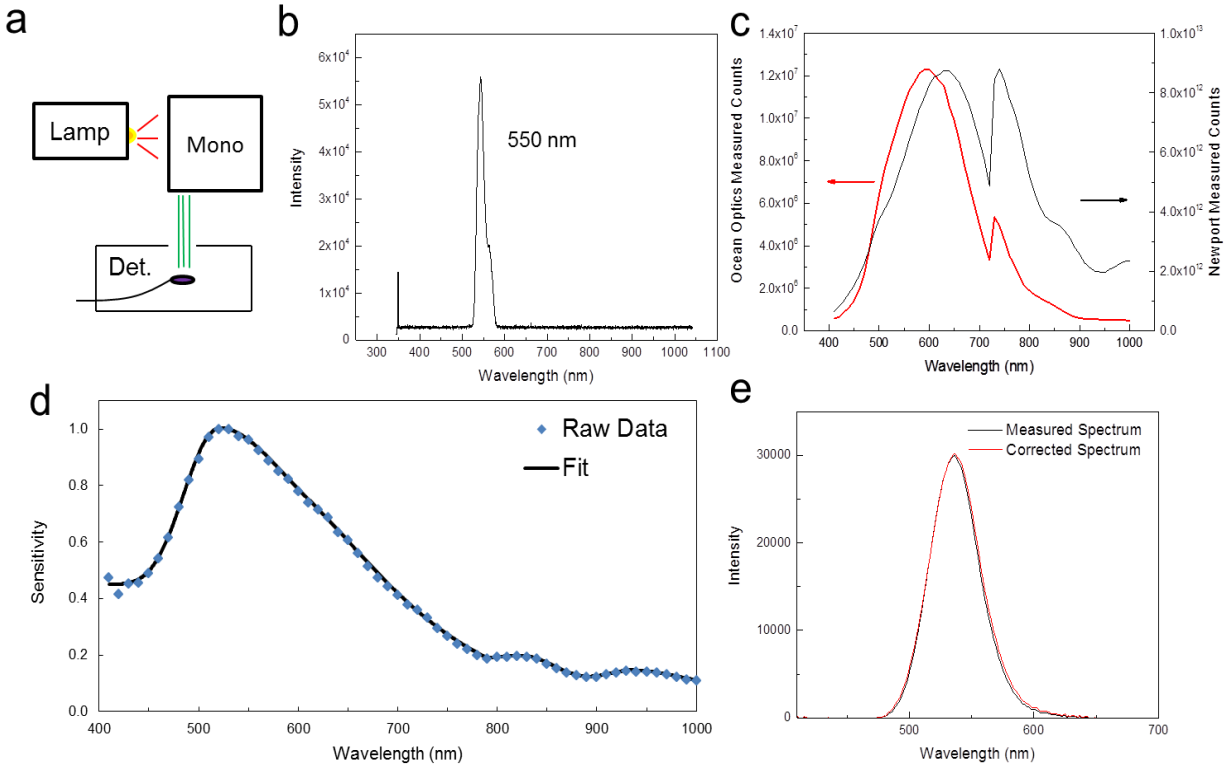

Figure A.1 – **a.** Schematic of detector setup. **b.** Example spectrum measured by the Ocean Optics USB400 at 550 nm. **c.** Lamp power spectra measured by the Ocean Optics and the calibrated Newport detector. **d.** Measured sensitivity (points) and fit values (curve). **e.** Example emission spectrum before and after correction.

To use this calibration, first truncate a measured spectrum from 410-1,000 nm (there was insufficient signal outside of this range to yield usable calibration data). Then subtract the background and smooth with a 0.01 window Loess, or another appropriate algorithm. Then, divide each measured wavelength by the corresponding value of the calibration curve to yield the corrected spectra (Figure A.1e).

Image Analysis Using ImageJ. The following procedure is known to be valid for ImageJ 1.46r for clearly resolved TEM images of quantum dots for size distribution analysis. Words in

italics are commands and menu locations of the various necessary functions, arrows represent moving within a sub-menu or window.

- Crop desired image to a region of well separated particles with good contrast against the background and a uniform intensity. Remove any caption as well.
- Open image in ImageJ.
- *Analyze → Set Scale*: input pixel dimensions.
- *Image → Type → 8-Bit*
- *Image → Adjust → Brightness/Contrast → Auto → Apply → Close Window*
- *Image → Adjust → Threshold*
    - Move top slide all the way to the left.
    - Adjust bottom slider until the majority of nanoparticles are distinctly separate
    - *Apply → Close Window*
- *Process → Noise → Despeckle*: repeat until no changes observed.
- *Analyze → Analyze Particles → OK*
- Copy data table into Excel.
- Delete all but second column.
- Calculate diameter: '=2*sqrt("Area"/PI())'
- Enter column of BIN steps
- *Data → Analysis → Data Analysis → Histogram → OK*
    - Select diameter column in *Input Range* box.
    - Select BIN column in *BIN Range* box.
    - Select 1x2 matrix of cells as *Output Range → OK*

Aqueous Synthesis of Magic-Size CdTe. While the aqueous CdTe synthesis described in the preceding chapters is capable of yielding highly luminescent particles, it is limited to creating stable particles with an absorption peak of 495 nm or greater. To create smaller dots the synthesis was modified slightly, so instead of reacting for several hours at 98°C the mixture was kept at room temperature and allowed to react for days. Within 24 hours a defined peak at 446 nm has developed (Figure A.2a) which indicates the formation of ~1.8 nm particles.[1] After 23 days of reacting at room temperature in dark conditions weak emission was observed (Figure A.2b). This emergence of emission has been reported in the literature also at these sizes.[2] The rapid formation of the particles followed by slow red-shifting spectra indicate that the majority of the starting materials nucleate in the first few hours of growth, if not immediately, and all subsequent growth is due to Ostwald ripening. As the peak positions are relatively constant after thirty days of reaction it would appear that the available thermal energy at room temperature is insufficient to

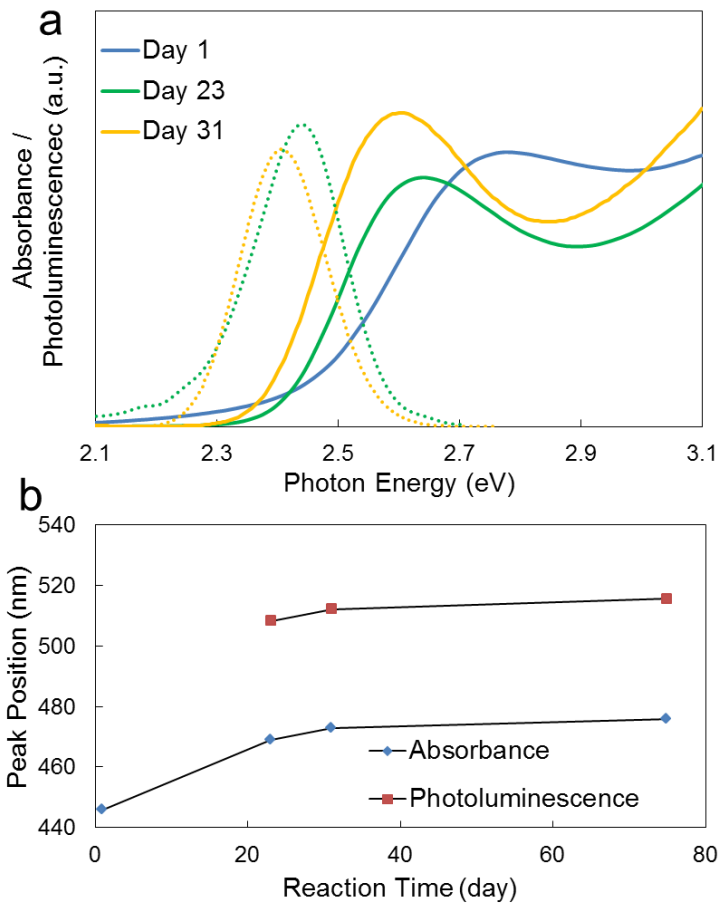

Figure A.2 – **a.** Absorbance and photoluminescence spectra of the magic CdTe as a function of reaction time. **b.** Peak positions as a function of reaction time.

continue this process once the particles become larger than ~2 nm. Alternatively, the particles may be too similar in size to continue the ripening process, with the system reaching a size equilibrium. However, the large size dispersion suggested by the width of the absorbance peak would

Solvent-Dependent CdTe Photoluminescence. In an early particle sterilization method the quantum dots were initially filtered to dryness and re-dispersed in 100% ethanol several times (in this section all percents are vol%). This was always accompanied by a red-shift in the observed emission, which would return to the nominal value once re-dispersed in 100% aqueous media. This effect was examined by vacuum drying samples of CdTe and re-dispersing them in various organic solvents (Figure A.3a). For the three tested there are strong red-shifts, with ethanol yielding the greatest in magnitude. In all cases this also translated to lower values of the full-half-maximum of the emission spectrum which inversely correlates with the observed red-shift (Figure A.3b). Qualitatively it appeared that in the ethanol case the particles were forming distinct aggregates instead of evenly dispersing in solution. This likely means the observed shifts are likely due to energy

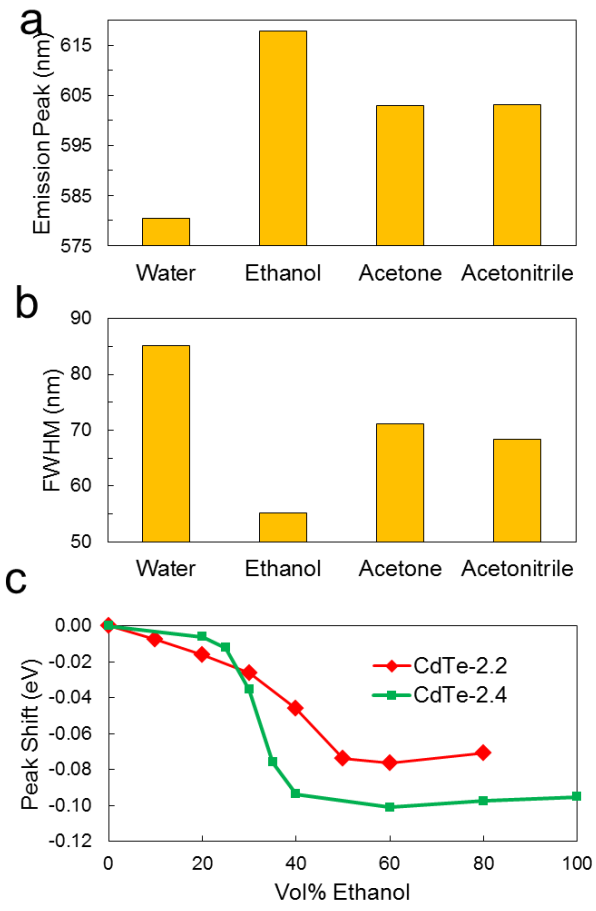

Figure A.3 – **a.** Effect of solvent on CdTe emission energy. **b.** Effect of solvent on the emission broadness. **c.** Change in emission peak as a function of ethanol content in the medium.

transfer, with smaller dots in the aggregates transferring their absorbed energy to the larger dots.[3] The acetone and acetonitrile samples did not appear to show similarly large aggregates to the naked eye, though the observed shifts do indicate some aggregation. As different solvents lead to different levels of aggregation and emission changes it may be possible to use this effect to develop an inefficient analytical technique, or at least a tech demo.

Any amount of aggregation is undesirable when preparing quantum dots for integration with cultures due to their greater observed inherent toxicity. A test was performed to determine at what ethanol concentration the aggregation begins (Figure A.3c). Minimal shifts are observed in CdTe-2.4 until ~30% ethanol, after which the peak rapidly shifts to the previously observed position by 40% ethanol. Slightly larger CdTe-2.2 are better able to tolerate the ethanol, fully aggregating at 50% and undergoing a more gradual change than the CdTe-2.2. This may be due to the greater number of ligands on the surface which would provide a greater barrier for aggregation. In typical laboratory practice, at least 70% ethanol is used to sanitize materials, indicating that ethanol washes will not be usable for yielding sterile dots without aggregation. A similar effect has been noted for methanol-precipitated dots, which retained some shifts even after re-dispersal in 100% water.[4] These experiments prompted the development of the inherently sterile syntheses described in the preceding chapters.

Analysis of Inhibition. The inhibition parameters Chapter 6 are defined using OD values due to their more accurate determination against other derived values. It was considered using the growth rates obtained by fitting the OD growth curves to eq. 6.1 in a similar function form (eq. A.12). However, the error associated with the growth rate was very dependent on the early time points, which tended to have higher uncertainty due to the detection limits of the available instruments. This is exacerbated for the light-treated samples as the complete curve shape is

usually not visible within the measured time span, or at all, and without an accurate value of the saturation level the growth rate cannot be reliably extracted. Thus, inhibition was defined as the extent of growth over a certain time period.

$$I = 1 - \frac{\mu_T}{\mu_{NT}} \tag{A.12}$$

Complex-Decomposition Synthesis of Palladium Sulfide Quantum Dots. The desire to investigate other, potentially less toxic, metal sulfide particles for the LARS investigations required the development of alternate syntheses. In organic media, it has been shown that thiol ligands are capable of serving as a sulfur source, though this is typically operated at higher temperatures than is possible in aqueous media.[5] For palladium sulfide this is accomplished using the decomposition of Pd-thiol complexes, and has been shown previously for aliphatic ligands.[6]

The first step in the preparation of aqueous PdS involved the conversion of insoluble $PdCl_2$ to tetra-chloride species (Figure A.4a). In acidic and neutral media, there are similar absorbance features, which changes upon addition of sodium hydroxide. While desirable to de-protonate the tiol ligands to promote binding, the Pd-hydroxide complex is so stable that it does not change upon addition of MPA. Adding MPA to the acidic or neutral samples yields a change in absorbance features with a broadening of the previously observed transition (Figure A.4b). Analysis of this sample with MALDI-MS reveals that the primary components are low-molecular weight complexes of somewhat ambiguous composition and stoichiometry. (Figure A.4c).

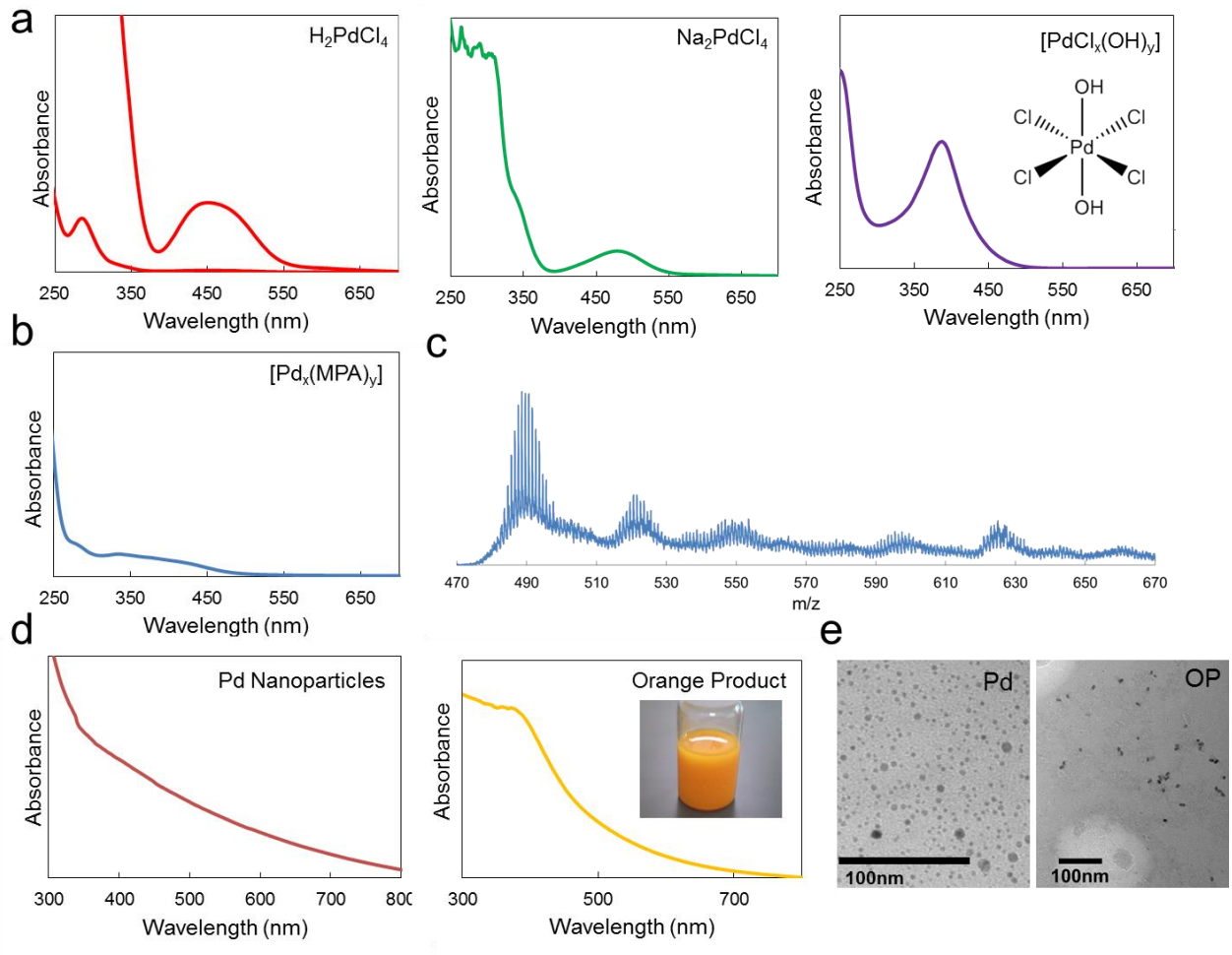

Figure A.4 – **a.** Absorbance spectra of palladium chloride precursors under various pH conditions. **b.** Absorbance spectrum of the presumed Pd-MPA complexes. **c.** MALDI-MS spectrum of the MPA complexes. **d.** Absorbance spectra of palladium nanoparticles and the obtained orange product. **e.** TEM images of the samples shown in **d.**

The resulting orange product of the MPA addition will gradually settle out and result in a clear orange suspension with a primary transition at ~450 nm (Figure A.4d). This is much higher in energy than the bulk bandgap of PdS (1.6 eV) and is comparable to magic size CdSe and CdTe.[7] The feature is also different than the absorbance spectrum of Pd^0 nanoparticles which matches expected trends for metallic dots, and show that the Pd is likely not reduced by the thiol ligands (Pd particles were synthesized in an aqueous environment using ethanol as a reducing agent).[8] TEM images show that in some cases the addition of MPA leads to the formation of anisotropic nanoparticles (Figure A4.e). The yield and size are not altered by the application of

heat however, and their appearance is not reliably reproducible. Thus, the attempted method of ligand decomposition does not seem to be a viable procedure for producing PdS in an aqueous environment.

Properties of Metal Sulfides. During efforts to identify different photoeffects a variety of metal sulfide nanoparticles were synthesized and analyzed. To test the general synthetic method, cadmium sulfide was made first.[9] In this reaction, $CdCl_2$ (3.5 mg, 20 μmol) was dissolved in 5 mL degassed water with 1.8 μL MPA. 750 μL of this solution and water were mixed, in addition to 30 μL of 0.5 M NaOH and placed in an ice bath. 50 μL of ammonium sulfide solution (6.3 M, Sigma-Aldrich) was diluted with 950 μL of water to yield a stock solution, 3 μL of which was added to the Cd precursor yield a clear solution exhibiting an absorbance shoulder above 3 eV, and visible emission with a large Stoke's shift characteristic of CdS (Figure A.7a, LT). Heating a portion of the sample improved the resolution of the absorbance peak, (HT) and increased the particle size to 3±1 nm (Figure A.5b). After two days, the particles were still stable and luminescent. Due to their high-energy band gap these particles were not considered for cell assays.

The same procedure was used to make PbS nanoparticles. $Pb(NO_3)_2$ (10.5 mg, 32 μmol) was dissolved in 5 mL water with 2.5 μL MPA, with 375 μL of this solution being mixed with 1,125 μL of water (all else the same as CdS synthesis). Upon addition of the $(NH_3)_2S$ the solution turned brown, and after 1 h revealed an apparently exponential absorbance curve and an emission profile consisting of two overlapping features from two different size populations (average diameter 3.3±0.3 nm, Figure A.5b).[10] Heating a portion of the particles yielded a clear solution, while holding the remaining particles for two days yielded a white precipitate. In both cases the particles likely degraded to PbO, and due to this instability were not considered for cell

studies, also being precluded by the lack of toxicological improvement over cadmium-containing nanoparticles.

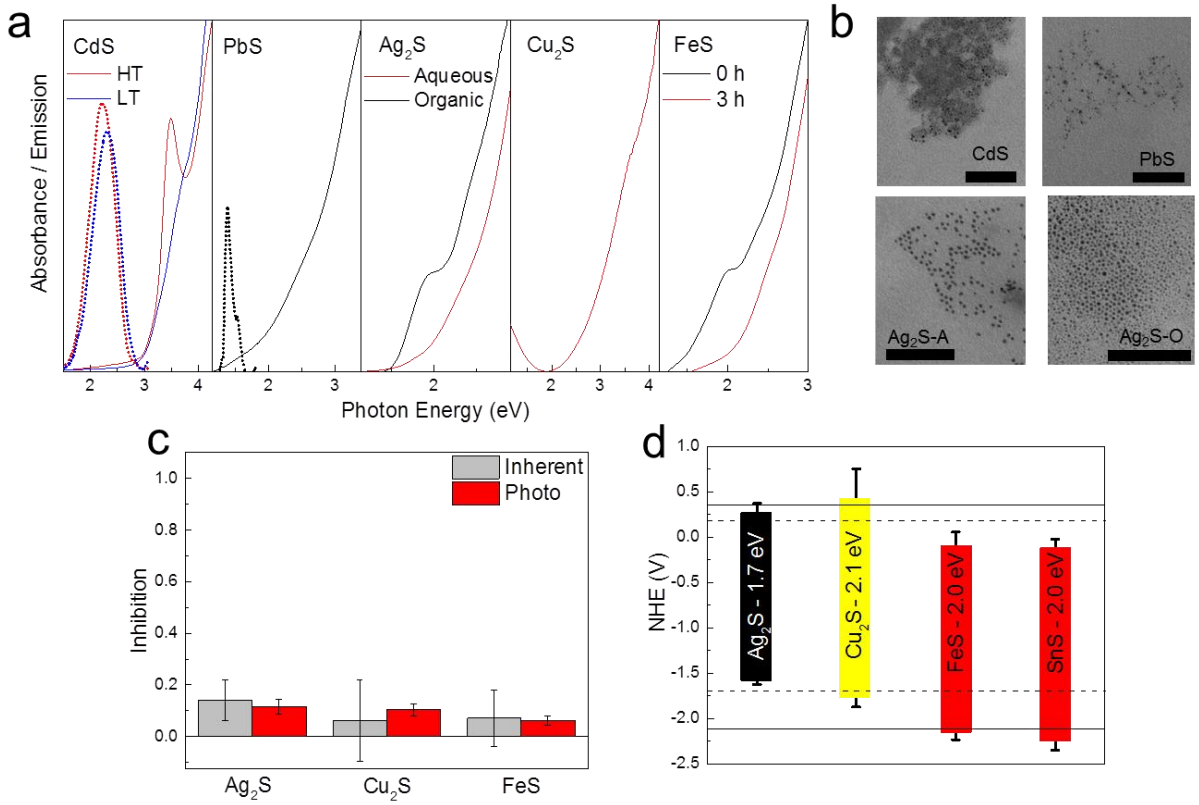

Figure A.5 – **a.** Optical spectra of the nanoparticles synthesized using Na_2S. Absorbance spectra are solid lines, emission are dotted. **b.** TEM images of the synthesized quantum dots. Scale bars are 100 nm in each image. **c.** Inhibition values for the particles tested against ESBL *K. pneumoniae*. **d.** Measured bandedge positions of the tested materials. Solid lines are reference to the levels of CdTe-2.4.

Two different methods were attempted to make silver(I) sulfide nanoparticles. The first was conducted in organic medium, where AgCl (150 mg, 1.05 mmol) was heated to 80°C to complex with trioctylphosphine (3 mL). Oleylamine (3 mL, OA) was then added and the solution was brought down to 30°C. Ammonium sulfide (62 µL, 6.3 M) was mixed with 3 mL OA and dried over 4 Å molecular sieves, which was accompanied by the solution turning darker yellow and vapor evolution. 1 mL of this dried solution was injected in the silver precursor which resulted in an immediate color change to black. It was allowed to react for 5 min, following

which methanol was added to precipitate the particles, and was centrifuged for 4 min at 5 krpm. Following another methanol wash the final product was re-suspended in chloroform. An aqueous method was also employed using the previously described method starting with $AgNO_3$ (11.0 mg, 76.8 μmol) in 5 mL water with 2.5 μL MPA, 375 μL of which were mixed with 1,125 μL water. Upon addition of ammonium sulfide, the solution turned light brown, which remained constant after 1 h or 98°C heating. There were differences between the two batches, most notably the presence of an absorbance feature in the organic sample which is absent from the aqueous (Figure A.5a). The sizes of the aqueous and organic samples were on the same order of magnitude, 4.4±0.6 and 3.7 ± 0.4 nm, though the organic synthesized were somewhat smaller on average (Figure A.7b). Because of their need for a ligand exchange step, the organic-synthesized silver sulfide particles were not considered for cell culture assays.

Copper(I) sulfide was made using the standard ammonium sulfide procedure in water with one caveat. Due to the low solubility of CuCl in water a saturated solution was used as the metal precursor solution. The absorbance post-synthesis also revealed one half of a plasmonic peak below 2 eV, which is likely indicative of the partial oxidation of Cu^+ to Cu^{2+} on the surface (Figure A.5a).[11] This was reflected in the STS measurements exhibiting a large number of defect states, and which contributed to the large spread in observed conduction band positions (Figure A.5d). Because of copper's low atomic weight the small particles formed were not visible by the available TEM.

Iron(II) sulfide was made using $FeCl_2$ (4 mg, 32 μmol in 10 mL) and was somewhat unique among the light transition metal sulfides synthesized in an aqueous environment in that two hours after injection it exhibited a true absorbance peak at 630 nm, though without detectible emission (Figure A.5a). Over time though, the particles began to precipitate, and the absorbance

feature was eventually lost to an exponential curve. This is likely due to the oxidation of Fe^{2+} to Fe^{3+} which is favorable in aqueous environments. Attempts to synthesize Fe_2S_3 particles directly using this method resulted in an immediate bulk precipitate with a dark black color. Like Cu_2S, these particles were not visible with the available TEM.

Other synthesized particles included tin(II) sulfide, which was not used further due to the similar redox potentials as FeS (Figure A.5d), and palladium(II) sulfide. Because the previous attempts with PdS revealed an incompatibility with MPA, an alternate synthesis was used. $PdCl_2$ (3.5 mg, 20 μmol) was dissolved in NaCl/water with poly(vinylpyrrolidone) (20 mg, 40 kDa molecular weight) to create the stock solution, which yielded a brown solution upon addition of ammonium sulfide. Due to the expense of the starting materials PdS was not considered for therapeutic applications.

Because the synthesized materials could not be wholly made in sterile environments those tested *in vitro* were first sanitized. Typically, 150 μL of a QD stock was washed with 75 μL of ethanol and re-dispersed in 150 μL PBS. Due to the lack of published extinction-concentration calibration curves for these materials serial dilutions were made to cover different concentration regimes. The concentration shown in Figure A.5c was a 1:10 dilution from the sterilized stock. The use of mass concentration (mg/mL) was considered but the low amount of material in each batch largely precluded the accurate estimation of that value.

None of these other materials were able to induce a statistically significant effect in any of the previously tested strains which were susceptible to CdTe-2.4 (Figure A.5c). This is likely due to the misalignment of the redox states of these particles with those associated with radical formation (Figure A.5d). Thus, the search for cadmium-free phototherapeutics continues.

CdTe/Te Core-Shells. As an analogue to the cadmium-overcoated particles presented in Chapter 8, CdTe with overcoated tellurium was synthesized in a similar manner. Unlike the cation treated samples, the emission from these dots was immediately lost upon the addition of more tellurium, and the absorbance spectrum exhibited a loss of peak resolution and indicated aggregation (Figure A.6). These observations square with the proposed poor ligand passivation of anionic facets and the resulting trapping behavior inherent to exposed tellurium atoms. The red-shifting peak at low Te loadings confirm that the observed changes are due to deposition and not simply tellurium precipitates in solution.

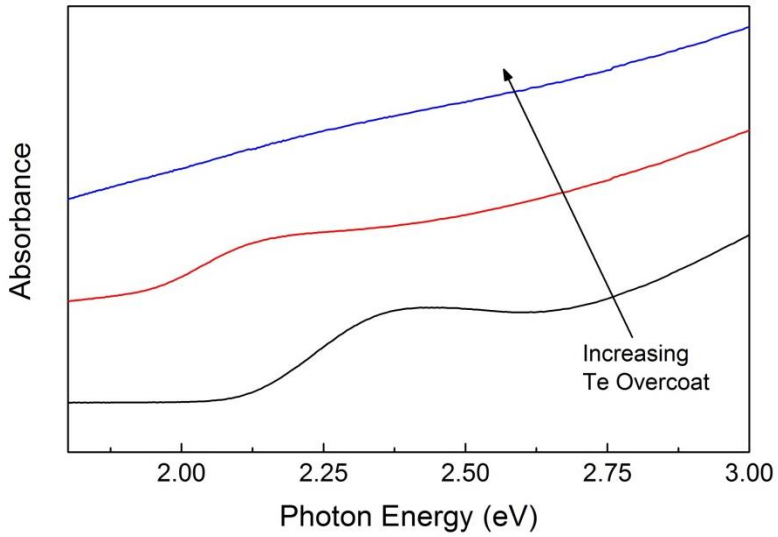

Figure A.6 – Absorbance spectra of CdTe/Te particles.

Citation Format. The end-of chapter references are listed using a modified version of the ACS style notably without all of the superfluous punctuation, and are truncated to either two authors or one author et al for brevity and to prevent redundancy, as the full citation is provided in the bibliography for completeness. Though seemingly popular in many biological journals, the Harvard system of in-line citation is abandoned in favor of numbered endnotes due to the inherent lack of clarity in the former style.[12]

Symbols and Abbreviations

CdTe-X	-	CdTe particles with a bandgap of X	
E	-	photon energy	eq. A.3-11
f_x	-	piecewise fitting function	eq. A.3-11
I	-	measured light intensity spectrum	eq. A.2
I	-	inhibition	eq. A.12
MPA	-	3-mercaptopropionic acid	
N	-	Newport detector	eq. A.1
OA	-	oleylamine	
OO	-	Ocean Optics USB 4000 detector	eq. A.2
P	-	light power	eq. A.1
S	-	*OO sensitivity function*	eq. A.11
t	-	Integration time	eq. A.2
λ	-	wavelength	eq. A.1-2
μ	-	treated (T) and untreated (NT) growth rates	eq. A.12

References

1) Dukes A. D., et al. *Chem. Mater.* **2010**, *22*, 6402-6408.
2) Li L., et al. *J. Lumin.* **2006**, *116*, 59-66.
3) Kagan C. R., et al. *Phys. Rev. Lett.* **1996**, *76*, 1517-1520.
4) Zhang Y., et al. *J. Nanosci. Nanotechnol.* **2007**, *7*, 497-503.
5) Li L., et al. *J. Am. Chem. Soc.* **2011**, *133*, 1176-1179.
6) Nobusada K., Yamaki T. *J. Phys. Chem. A* **2004**, *108*, 1813-1817.
7) Ferrer I. J., et al. *Thin Solid Films* **2007**, *515*, 5783-5786.
8) Teranishi T., Miayake M. *Chem. Mater.* **1998**, *10*, 694-600.
9) Zhang H., et al. *Nano. Lett.* **2012**, *12*, 5856-5860.
10) Bakueva L., et al. *Adv. Mater.* **2004**, *16*, 926-929.
11) Sun Q., et al. *Nanoscale* **2014**, *6*, 12450-12457.
12) Gregory M. W. *Nature* **1992**, *360*, 11-12.